

Study of intermolecular interactions in hetero-organic thin films

Benjamin Stadtmüller



Study of intermolecular interactions in hetero-organic thin films

Von der Fakultät für Mathematik, Informatik und Naturwissenschaften der RWTH Aachen University zur Erlangung des akademischen Grades eines Doktors der Naturwissenschaften genehmigte Dissertation

vorgelegt von

Master of Science

Benjamin Stadtmüller

aus Aschaffenburg

Berichter: Universitätsprofessor Dr. Christian Kumpf Universitätsprofessor Dr. Matthias Wuttig

Tag der mündlichen Prüfung: 09.04.13

Diese Dissertation ist auf den Internetseiten der Hochschulbibliothek online verfügbar.

Forschungszentrum Jülich GmbH Peter Grünberg Institute (PGI) Functional Nanostructures at Surfaces (PGI-3)

Study of intermolecular interactions in hetero-organic thin films

Benjamin Stadtmüller

Schriften des Forschungszentrums Jülich Reihe Schlüsseltechnologien / Key Technologies Bibliographic information published by the Deutsche Nationalbibliothek. The Deutsche Nationalbibliothek lists this publication in the Deutsche Nationalbibliografie; detailed bibliographic data are available in the Internet at http://dnb.d-nb.de.

Publisher and Forschungszentrum Jülich GmbH

Distributor: Zentralbibliothek

52425 Jülich

Tel: +49 2461 61-5368 Fax: +49 2461 61-6103

Email: zb-publikation@fz-juelich.de www.fz-juelich.de/zb

Cover Design: Grafische Medien, Forschungszentrum Jülich GmbH

Printer: Grafische Medien, Forschungszentrum Jülich GmbH

Copyright: Forschungszentrum Jülich 2013

Schriften des Forschungszentrums Jülich Reihe Schlüsseltechnologien / Key Technologies, Band / Volume 61

D 82 (Diss., RWTH Aachen, University, 2013)

ISSN 1866-1807 ISBN 978-3-89336-871-6

The complete volume is freely available on the Internet on the Jülicher Open Access Server (JUWEL) at www.fz-juelich.de/zb/juwel

Neither this book nor any part of it may be reproduced or transmitted in any form or by any means, electronic or mechanical, including photocopying, microfilming, and recording, or by any information storage and retrieval system, without permission in writing from the publisher.

Abstract

In this work we present a systematic study of the structure formation in hetero-organic systems consisting of the prototype molecules 3,4,9,10-perylene-tetra-carboxylic-dianhydride (PTCDA) and copper-II-phthalocyanine (CuPc) adsorbed on the Ag(111) surface. The geometric structure of these systems is investigated with established surface science techniques like low energy electron diffraction, scanning tunneling microscopy or the X-ray standing wave technique. The electronic structure of the individual molecules in the mixed films is revealed by angle resolved photoemission spectroscopy data which are analyzed in the orbital tomography approach introduced recently [PBF+09, PRU+11].

Laterally mixed films of CuPc and PTCDA were studied in order to reveal the influence of the substrate mediated intermolecular interaction on the geometric and electronic properties of the mixed film. The lateral order, i.e., the size and shape of the unit cell, can be tuned by changing the relative coverage of the molecules on the surface. A highly surprising finding is that the charge transfer between the individual molecules in the mixed film and the substrate is no longer reflected by their adsorption height on the surface. We explain this finding by a coupling of the electronic levels of the molecules via a hybrid state, which results in an additional population of the PTCDA LUMO and a complete depopulation of the CuPc LUMO level.

Vertically stacked bilayer films allow to study both the intermolecular interaction strength along the vertical stacking direction and the influence of the second organic layer on the properties of the metal organic interface. For the adsorption of CuPc on a closed PTCDA layer on Ag(111), a smooth organic-organic interface was formed. CuPc adsorbs in the second layer on PTCDA and does not destroy the lateral order of the PTCDA layer. The vertical distance between the organic layers indicates a mainly electrostatic and van der Waals interaction across the hetero-organic interface. However, the chemical bonding between PTCDA and the silver surface is changed upon the adsorption of CuPc. This is reflected in an enhanced charge transfer into the PTCDA LUMO level coinciding with an altered vertical adsorption height of PTCDA which depends on the CuPc coverage. These findings can be explained by an additional screening effect, induced by the adsorption of CuPc.

For the reversed system, PTCDA on a closed layer of CuPc/Ag(111), no hetero-organic interface is formed at RT. Instead, a certain amount of PTCDA penetrates into the CuPc layer and exchanges CuPc molecules. The CuPc molecules, which remain at the silver surface, form a disordered mixed structure with PTCDA, the others move to the second organic layer. We believe that the molecular exchange is enabled by a missing attractive intermolecular interaction in the CuPc film and a larger adsorption energy gain for PTCDA compared to CuPc when the molecules make direct contact to the Ag(111) surface.

List of acronyms

CBE constant binding energy
CuPc copper-II-phthalocyanine
DFT density functional theory

DOS density of states

FHWM full width half maximum

HC high coverage

HOMO highest occupied molecular orbital

LC low coverage

LEED low energy electron diffraction

LT low temperature

LUMO lowest occupied molecular orbital

M1°1 Mixed One-to-One
MBW Mixed Brick Wall
MZZ Mixed Zig-Zag
ML monolayer

NIXSW normal incidence X-ray standing wave

PDOS projected density of states

p.o.l. point-on-lineRT room temperatureSB Stacked-Bilayer

PES photoelectron spectroscopy

PTCDA 3,4,9,10-perylene-tetra-carboxylic-dianhydride

QMS quadrupole mass spectrometer

SPA-LEED spot profile analysis low energy electron diffraction

STM scanning tunneling microscopy
STS scanning tunneling spectroscopy
TPD temperature programmed desorption

(AR)UPS (angle resolved) ultraviolet photoelectron spectroscopy

XSW X-ray standing wave

Contents

1	Intro	oductio	n	1		
2	Experimental techniques 2.1 (High-resolution)-Low energy electron diffraction					
3	Mor	10-orgai	nic thin films	25		
	3.1	PTCD 3.1.1 3.1.2	A/Ag(111)	25 26		
	3.2	CuPc/ 3.2.1 3.2.2	PTCDA on $Ag(111)$	29 40 40 43		
4		Lateral intermolecular interaction: CuPc and PTCDA on Ag(111) 49				
	4.1		l order: Long range order and local adsorption geometry Modeling the CuPc-PTCDA interaction by pair potential calculations Formation of mixed structures Mixed Brick Wall Structure Mixed One-to-One Phase Mixed Zig-Zag Phase Conclusion	50 51 53 57 60 62 64		
	4.2	Electro 4.2.1 4.2.2 4.2.3	Onic structure Global electronic structure - (AR)UPS Local electronic structure - STS Conclusion	65 65 77 80		
	4.3		al adsorption geometry: The Mixed Brick Wall structure	80 81		

Contents

		4.3.2 Adsorption heights	85
		4.3.3 Conclusion	90
	4.4	Influence of the lateral intermolecular interaction on the adsorption behavior	90
	4.5	Conclusion	92
	4.6	Outlook	94
5	Vort	ical intermolecular interaction:	
3		c on PTCDA on Ag(111)	97
	5.1	Lateral order: Long range order and local adsorption geometry	98
	5.2	Electronic structure	106
	5.3	Vertical adsorption geometry	115
	0.0	5.3.1 Core level models	115
		5.3.2 Vertical adsorption geometry at different coverages	121
		5.3.3 Vertical adsorption geometry at different temperatures	126
	F 4	5.3.4 Conclusion	132
	5.4	Modification of the PTCDA/Ag(111) interaction by the adsorption of CuPc .	133
	5.5	Thermally induced molecular exchange at the hetero-organic interface	136
	5.6	Conclusion	139
6	Mol	ecular exchange at a hetero-organic bilayer: PTCDA on CuPc on Ag(111)	143
	6.1	Lateral order: Long range order	143
	6.2	Electronic structure	147
	6.3	Vertical adsorption geometry	150
		6.3.1 Core level models	150
		6.3.2 Adsorption heights	152
	6.4	The metal-organic interface: The basis for the hetero-organic growth	158
	6.5	Conclusion	159
	6.6	Outlook	160
7	Sum	mary and conclusion	163
•	Jun	mary and conclusion	100
Sa	mple	preparation	167
Bi	bliog	тарну	169
Lis	st of	Figures	181
Lis	st of	publications	193
Ac	know	rledgements	197

1 Introduction

The interest in exploring the basic properties of large aromatic molecules is based on their great potential to serve as active materials in organic electronic devices. In particular, this class of materials allows to fabricate new types of electronic elements such as flexible organic light emitting diodes (OLED) [HLC⁺12] or organic photovoltaic cells (OPVC) [LYJ⁺12], which is not possible using conventional inorganic semiconductors like silicon and germanium. Furthermore, the large spectrum of applications for these organic devices and their low production costs already attracted the attention of the industry which resulted in the first commercially available ultra-thin displays based on organic LEDs.

While realizing and improving these organic devices it became evident, that the performance of such electronic assemblies depends crucially on the physical properties of the interfaces between the active materials [BCK05, WMPL07]. The interface between a metal contact and the organic film does not only dominate the charge injection into the organic material, but also acts as a template layer for the subsequent organic film growth. Hence, it determines the crystalline quality and the molecular arrangement in the molecular solid grown on top, which in turn affects the charge transport properties within the organic film [WW04].

Therefore the adsorption behavior of aromatic prototype molecules on highly crystalline surfaces was extensively investigated during the last decades [For97, GG10]. They represent model systems for the metal-organic interfaces. In order to directly access the interface chemistry, many studies focused on (sub)monolayer films on noble metal surfaces. Such metal substrates were commonly used due to their relatively low surface reactivity. The intermolecular interaction within these adsorbate films has a comparable influence on the structure formation at the metal-organic interface as the bonding of each molecule to the noble metal surface. The complex interplay between these interaction mechanisms results in different growth behaviors in the submonolayer regime depending on the relative interaction strengths which are usually intrinsic properties of the adsorbate system, i.e., of the aromatic adsorbate and the noble metal surface [Tau07, SHK $^+$ 09].

Although these fundamental studies contributed significantly to a comprehensive understanding of the intermolecular interactions between equal molecules and their consequences on the

organic film growth, only a few aspects of the interaction between different types of molecules have been revealed yet [BWBM03, HGS⁺10]. This is rather surprising since hetero-organic interfaces play a major role for the efficiency of organic devices [OWB⁺10]. In addition, laterally mixed organic films containing at least two different types of molecules on metal surfaces might allow to intentionally modify the structural properties by changing the ratio of both coverages of the aromatic components. In this way the size and shape of the metal-hetero-organic template layer can be tailored in order to control the subsequent film growth.

In order to realize these possible applications for hetero-organic adsorbate systems, the basic interaction mechanisms between two different types of molecules have to be characterized in detail. This gap in our knowledge is tackled in this work by a systematic study of laterally mixed organic films and vertically stacked ultra-thin hetero-organic bilayer films adsorbed on the (111)-oriented silver surface (Ag(111)). While the organic-organic bilayer films provide mainly information about the intermolecular interaction in vertical stacking direction, the laterally mixed films allow to study the direct as well as the substrate mediated interaction between the molecules. The prototype molecules 3,4,9,10-perylene-tetra-carboxylic-dianhydride (PTCDA) and copper-II-phthalocyanine (CuPc), which are used in this study, have both been studied extensively on the Ag(111) surface [Tau07, KSS+10]. The attractive interaction between PTCDA molecules leads to the formation of ordered islands, while the intermolecular repulsion between CuPc molecules results in a diluted 2D gas phase with a continuously increasing molecular density with rising coverage [Tau07, KSS+10]. This different intermolecular interactions might induce new effects for the hetero-organic systems, which can be identified since the pure adsorbate systems are well known.

The ambitious goal of characterizing the lateral and vertical intermolecular interactions between different types of molecules requires a combination of various experimental approaches. After this short introduction, these experimental approaches are introduced in chapter 2. The geometric structure in these mixed organic systems is explored by well established surface science techniques like low energy electron diffraction (LEED), scanning tunneling microscopy (STM) and the X-ray standing wave technique (XSW). The electronic structure of the individual molecules in the mixed films is accessed by angle resolved photoemission spectroscopy (ARPES) which is combined with the orbital tomography approach that was introduced only recently [PBF+09, PRU+11]. Since the latter method has up to now only been employed to low symmetric surfaces, chapter 3 presents the first experimental evidence that this technique is also applicable to more complex surfaces as, e.g., Ag(111). Furthermore, a short review of the individual adsorption properties of CuPc and PTCDA on Ag(111) is presented in the same chapter.

A detailed view on laterally mixed films containing CuPc and PTCDA on the Ag(111) sur-

face is presented in chapter 4. The attractive electrostatic interaction between the molecules results in the formation of different mixed organic structures in the (sub)monolayer regime. The parameters of the mixed organic lattice can be tuned by changing the relative coverage of the molecules on the surface. Furthermore, a new effect was found, which was not expected from the experience with established adsorption models for individual molecules on Ag(111): The charge transfer into the molecules is no longer correlated with their bonding distance to the surface, i.e., with their adsorption height. Instead the electronic levels of the individual molecules are coupled via a hybrid state which results in a common electronic structure.

In the subsequent chapters of this work we focus on vertically stacked hetero-organic bilayers of CuPc and PTCDA directly adsorbed on the Ag(111) surface. In chapter 5, the adsorption behavior of submonolayer films of CuPc on a closed PTCDA monolayer film on Ag(111) is discussed. A smooth interface is formed between the CuPc and PTCDA layers which interact mainly by electrostatic and van der Waals forces. Most remarkable, the chemical bonding between PTCDA and the silver surface is modified upon adsorption of CuPc which results in an enhanced charge transfer into the PTCDA LUMO. This finding can be correlated with an additional screening effect induced by the CuPc layer.

The reversed hetero-organic system, PTCDA on a monolayer CuPc/Ag(111), is discussed in chapter 6. The structure formation of this system allows to identify the influence of the metal-organic interface on the properties of the subsequent organic film growth. However, no interface between CuPc and PTCDA layers is formed. Instead, PTCDA replaces CuPc and forms a disordered mixed film. This result is correlated with the intermolecular interactions in the CuPc and PTCDA monolayer film and the interaction strength of these molecules with the Ag(111) surface.

Finally, all our findings are concluded in chapter 7.

2 Experimental techniques

In this work the geometric as well as the electronic properties of organic adsorbates on noble metal surfaces are studied by a variety of different experimental techniques and theoretical approaches. Only in this way a comprehensive understanding of the metal-organic interface can be obtained. This chapter introduces briefly the basic principles of the employed experimental techniques and theoretical approaches. Since all these methods are well established, this section does not provide a full review of their physical basics, but focuses on the specific aspects which are crucial for understanding the experimental results presented in this work.

2.1 (High-resolution)-Low energy electron diffraction

Low energy electron diffraction (LEED) is one of the most common experimental methods for studying the lateral order of crystalline surfaces. Monoenergetic electrons hit the sample surface under normal incidence and are diffracted by the first few atomic layers of the sample. The angular distribution of the backscattered electrons is detected on a fluorescence screen. The kinetic energy $E_{\rm kin}$ of the electrons is in the range of 20 to 500 eV. The corresponding de Broglie wavelengths $\lambda_{\rm dB}$ are between 0.6 and 2.7 Å, i.e., comparable to the atomic distances in a solid state crystal. The low kinetic energies of the electrons lead to a small inelastic mean free path below 10 Å which causes the high surface sensitivity of this experimental method as most electrons are diffracted by the topmost layer. In the simplest approximation (geometric diffraction theory) the reciprocal lattice of the quasi 2-dimensional crystal can be described by Ewald rods in reciprocal space, which are arranged perpendicular to the surface. The positions of these Ewald rods \bar{a}_i^* in reciprocal space are directly related to the lattice parameter of the surface grid in real space \vec{a}_i by the equation $\vec{a}_i \cdot \vec{a}_i^* = 2\pi \delta_{ij}$ [VHWC86, OLS⁺03]. In this geometric approximation the lateral lattice parameters of the surface structure can be determined by analyzing the positions of the diffraction maxima in reciprocal space. Furthermore, the lateral profile of the diffraction spots yields information about the surface morphology [HvH99, VHWC86].

In a more sophisticated description the finite penetration depth of the electrons into the crystalline film as well as multiple scattering of the electrons is considered [JSY82, VHWC86,

Pen93, Pen94]. This results in an intensity modulation along the otherwise homogeneous Ewald rods which contains information of the exact position and height of each atomic scatterer within the surface unit cell. This modulation can be accessed by LEED-IV measurements recording the intensity distribution along the Ewald rods and provides information of the complete structure of the surface layers which contribute to the diffraction pattern.

SPA-LEED

The spot profile analysis (SPA-)LEED instrument [ZHvH02, HvH99] is the high resolution alternative to a conventional LEED setup which explains why it is also referred to as "high resolution-LEED". A schematic cross section is shown in Fig. 2.1(a). In contrast to the conventional LEED setup, the SPA-LEED unit uses a single electron multiplier (channeltron) as a detector which is installed at a fixed angle with respect to the electron gun. In order to record a two dimensional diffraction pattern, which is equivalent to a conventional LEED image, the angle of the incoming electrons as well as of the diffracted electrons needs to be continuously modified. This is illustrated in the modified Ewald construction in Fig. 2.1(b). The momentum vector of the incoming electrons is shown in dark green, the one for the diffracted electrons in light green. In this way, the diffraction vector \vec{K} (red vector) is scanned through reciprocal space. Note that for large deflections of the electron beam in the SPA-LEED device the electron path is influenced by inhomogeneities in the electrostatic octupole field. This leads to distortions in the detected diffraction pattern [Bay08].

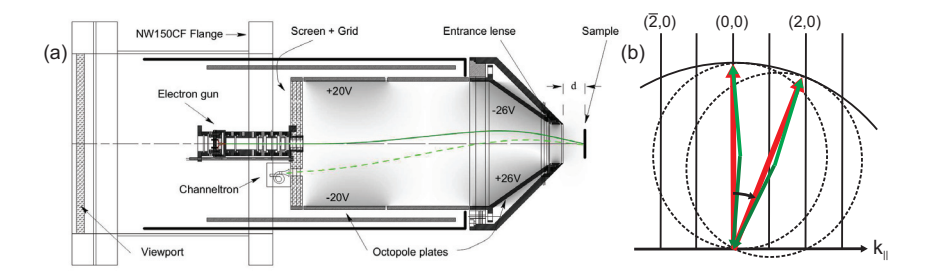


Figure 2.1: (a) Cross section of a SPA-LEED instrument [HvH99] and modified Ewald construction (b).

An important advantage of the channeltron detector is its large dynamic detection range which allows to use a much lower electron flux compared to a conventional LEED. This reduces the radiation damage for sensitive samples which is especially crucial when studying organic adsorbates.

The lateral resolution $\Delta k/k$ of any diffraction experiment is determined by the ratio between the aperture in front of the detector (LEED: $\approx 0.5\,\mathrm{mm}$, SPA-LEED: $\approx 0.1\,\mathrm{mm}$) and the distance between the sample and the detector (LEED: $\approx 75\,\mathrm{mm}$, SPA-LEED: $\approx 300\,\mathrm{mm}$) [Krö11, Sta09a]. As a consequence, the nominal resolution of a SPA-LEED instrument is 20 times higher than for a conventional LEED. For a Si(111) crystal an experimental resolution of $\delta D = 0.0004~\text{Å}^{-1}$ was reported [HvH99] which is equal to a "transfer width" of $T = 2\pi/\delta D = 15700~\text{Å}$. However, such a high resolution can not be achieved on metal surfaces due to the high mosaicity of the surface [HvH99, Sta09a]. This effect results in an enhanced width of the Ewald rods for increasing electron energies. For the instrument used in this work (Omicron SPA-LEED, serial no. 52), a momentum resolution of $\Delta k = 0.01~\text{Å}^{-1}$, which corresponds to a transfer width of 630 Å could be achieved at a kinetic energy of $E_{\rm kin} = 27.2\,\mathrm{eV}$.

The superstructure matrix

In order to determine the unit cell size of a diffraction pattern, the k-space segment of the pattern at first has to be calibrated [Sta09b, Krö11]. As a reference, the diffraction pattern of the well known commensurate PTCDA monolayer structure on Ag(111) has been used [KUS04]. The calibrated diffraction pattern was analyzed using the software *Spotplotter* by Patrick Bayersdorfer [Bay08]. This software calculates a diffraction pattern based on a given superstructure matrix as well as the substrate symmetry and superimposes this simulated pattern onto the experimental diffraction data. The superstructure matrix

$$\begin{pmatrix} \vec{A} \\ \vec{B} \end{pmatrix} = \begin{pmatrix} m_{11} & m_{12} \\ m_{21} & m_{22} \end{pmatrix} \cdot \begin{pmatrix} \vec{a} \\ \vec{b} \end{pmatrix}$$
 (2.1)

provides a distinct relation between the adsorbate lattice with the unit cell vectors \vec{A} and \vec{B} and the substrate grid (unit cell vectors \vec{a} and \vec{b}) and hence describes the parameters of the adsorbate lattice.

The superstructure matrix is optimized manually by achieving a coincidence between the positions of the simulated and the experimentally obtained diffraction spots. The absolute uncertainty of this data analysis method is estimated to by ± 0.04 for each number in the superstructure matrix. This error is propagated to the lattice parameters.

2.2 Photoelectron spectroscopy

Photoelectron spectroscopy (PES) is very extensively used for studying the electronic properties of surfaces and crystals. It is based on the photoelectric effect, which was first discovered by Hertz [Her87] and Hallwachs [Hal88] and a few years later explained by Einstein as a consequence of the quantum nature of light [Ein05]. In a photoemission experiment, the sample is illuminated by (monochromatic) light of a certain energy $\hbar\omega$ and the kinetic energy distribution of the emitted photoelectrons is recorded by an electron analyzer.

Photoemission process

In the following the basic concept of the photoemission process is described. In a photoemission experiment an incoming photon of the energy $\hbar\omega$ hits an initial state i with wave function ψ_i and transforms it into a final state f with a wave function ψ_f . Note that the photoelectron, which is emitted, is also described by ψ_f . In the sudden approximation it is assumed, that the remaining (N-1) electron system immediately responds to the created photohole and that the emitted photoelectron does not interact with the photohole. Hence, the transition probability w between the N-electron state ψ_i and the N-electron state ψ_f is given by Fermi's Golden Rule [Hüf03]:

$$w \propto \frac{2\pi}{\hbar} \left| \left\langle \psi_f | \hat{\Delta} | \psi_i \right\rangle \right|^2 \delta(E_f - E_i - \hbar \omega) \tag{2.2}$$

The δ -function in equation (2.2) ensures the energy conservation in the photoexcitation process. The operator $\hat{\Delta}$ describes the coupling of the incoming photon to the N-electron system. In a general approach this operator has the form

$$\hat{\Delta} = \frac{e}{2mc} (\mathbf{A}\hat{\mathbf{p}} + \hat{\mathbf{p}}\mathbf{A}) + \frac{e^2}{2mc^2} \mathbf{A}\mathbf{A} = \frac{e}{mc} \mathbf{A}\hat{\mathbf{p}}.$$
 (2.3)

The photon is described by the vector potential \mathbf{A} which interacts with the momentum operator $\hat{\mathbf{p}}=i\hbar\vec{\nabla}$ of the electron system. In the Coulomb gauge $\vec{\nabla}\mathbf{A}=0$ this expression can be simplified by neglecting two photon transitions. For photon energies smaller than $\hbar\omega\approx 50\,\mathrm{eV}$, the wavelength of the incoming light is much larger than the size of the excited molecular orbital. Therefore the spacial modulation of the vector field \mathbf{A} can also be neglected, which results in a constant vector potential \mathbf{A}_0 (Dipole approximation). The latter vector yields information about the polarization of the incoming photon.

In the simplest approximation, the wave function ψ_i of the initial state can be written as the product of the wave function of the electron which is excited Φ_k and the wave function of the rest of the electron system $\psi_{i,R}^k(N-1)$. In the same way, the final state is expressed by the product of the wave function of the electron system $\psi_{f,R}^k(N-1)$ and the wave function of the emitted photoelectron $\Phi_{f,\mathrm{kin}}$. This leads to a reformulation of Fermi's Golden Rule:

$$w \propto \left| \langle \Phi_{f, \text{kin}} | \mathbf{A} \hat{\mathbf{p}} | \Phi_k \rangle \right|^2 \left| \langle \psi_{f, R}^k(N-1) | \psi_{i, R}^k(N-1) \rangle \right|^2 \delta(E_{\text{kin}} + E_f(N-1) - E_i(N) - \hbar \omega) \tag{2.4}$$

Hence, the photocurrent depends on the product of a one electron matrix element (first term) and the overlap integral for the initial and final state of the residual (N-1) electron system (second term). In the so called frozen approximation [Hüf03], the relaxation of the (N-1) electron system is not considered, i.e. $\psi_{f,R}^k(N-1) = \psi_{i,R}^k(N-1)$. Consequently the overlap integral is 1. In this case, we can derive a simple relation between the kinetic energy of the photoelectron and the binding energy $E_{\rm b}$ of the emitting orbital. When the wave functions (and hence also energies) of initial and final state of the (N-1) electron system are identical $(E_f(N-1)=E_i(N-1))$, the condition of a vanishing argument of the δ -function in equation (2.4) can be written as

$$E_{\rm kin} = \hbar\omega - (E_f(N-1) - E_i(N)) = \hbar\omega - E_{\rm b} - \Phi.$$
 (2.5)

In a second step, this relation is adapted for photoemission arising from metal crystals with work function Φ .

In order to understand the binding energies of the molecular orbitals for organic molecules adsorbed on noble metal surfaces correctly, a description beyond the frozen approximation is necessary. Due to the high polarizability of the organic films as well as of the metal substrate, the created photohole can be screened effectively by the surrounding material. Consequently, the entire electron system relaxes to an energetically more favored configuration and the relation $\psi_{f,R}^k(N-1) = \psi_{i,R}^k(N-1)$ is not valid anymore. The binding energy positions of specific electronic levels can therefore be different, depending on the screening abilities of the surrounding material [FTFP08, Krö11]. This influence of the electronic reorganization on the binding energy obtained for a specific electronic level is called a final state effect.

In this work the valence orbital structure of organic molecules was studied with angle integrated UPS. The valence states were excited using a monochromatized UV-source which provides photons of the He-I $_{\alpha}$ emission line $E_{\hbar\omega}=21.218\,\mathrm{eV}$ and the kinetic energy distribution was recorded with a hemispherical electron analyzer (VG Scienta R4000, 30° acceptance angle). All spectra are normalized only by the number of scans, and the energy scale was calibrated to the Fermi level E_{F} . The latter was obtained by a least square fit of an errorfunction to the Fermi edge [Wei05], which was proven to be a suitable approximation of the Fermi distribution. This model function contains an effective temperature T_{eff} which accounts

for a broadening of the Fermi distribution function due to the instrumental resolution and the sample temperature. The background of the photoemission spectra close to the Fermi level was modeled by an exponential increase with rising binding energy.

The work function of the metal-organic interfaces was determined from the secondary electron cutoff in normal emission geometry. During the data accumulation the sample was biased to $-9\,\mathrm{V}$ in order to increase the kinetic energy of the cutoff electrons. The cutoff energy E_{Cut} was determined from the derivative of the cutoff spectrum. The onset energy of the secondary electron cutoff was defined as the highest binding energy value that revealed a value significantly different from zero for the derivative of the cutoff spectrum.

Angle resolved PES and orbital tomography

In this work the electronic structure of the molecular adsorbates on noble metal surfaces was not only studied by conventional (angle integrated) UPS, but also by angle resolved photo-electron spectroscopy (ARPES). The ARPES data were analyzed with the so called *orbital tomography* technique which was introduced by Puschnig et al. [PBF⁺09]. This data evaluation procedure allows to identify the emitting molecular orbital by the angular distribution of its photoelectron yield.

The angular dependence of the photoemission intensity at a certain binding energy $I(E_b, \vartheta, \varphi)$ can be obtained from the one electron matrix element in equation (2.4). In the simplest approximation, the final state of the photoemission process can be described as a plane wave of a free electron [FE74]:

$$I(E_{\rm b}, \vartheta, \varphi) \propto w \propto \left| \left\langle e^{i\vec{k}\vec{r}} |\mathbf{A}\hat{\mathbf{p}}| \Phi_k \right\rangle \right|^2 = |\mathbf{A}\mathbf{k}|^2 \cdot \left| \tilde{\Phi}_k \right|^2$$
 (2.6)

Here the photocurrent is proportional to the square of the Fourier transform of the initial wave function $\tilde{\Phi}_k$. The term $|\mathbf{Ak}|^2$ scales the intensity of the pure orbital emission pattern according to the angle between the direction of the photoelectron and the incoming radiation. Although this approach is considered to be too simple to describe the angular distribution of a photoemission experiment correctly, it has been successfully applied to ARPES data recorded for organic molecules on noble metal surfaces [PBF⁺09, PRU⁺11, SWR⁺12, WHS⁺12].

The orbital tomography approach uses the plane wave approximation for the final state of the photoemission process. For a molecular adsorbate, the initial state is equivalent to a molecular orbital. In Fig. 2.2 the calculation of the theoretical photoemission momentum distribution is illustrated in three steps. First, the wave function of the molecular orbital shown in panel (a) is calculated for the free molecule by density functional theory (DFT). This wave

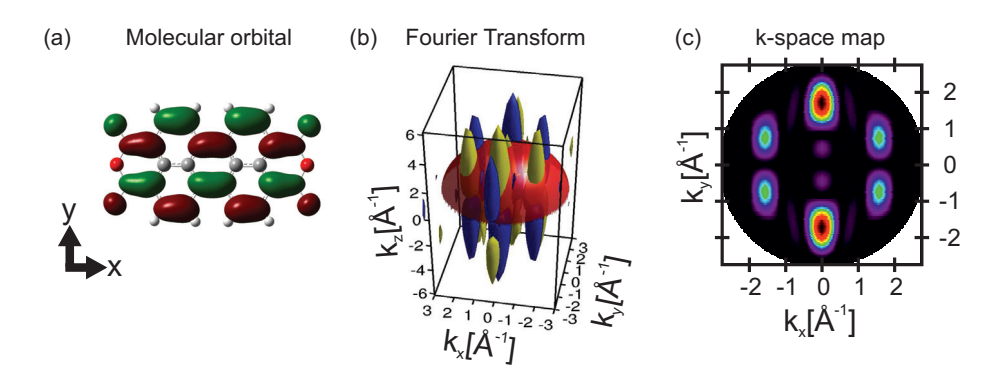


Figure 2.2: (a) PTCDA orbital (LUMO) for a free molecule in the gas phase (DFT calculation, B3LYP, basis set: LANL2DZ [FTS⁺]). (b) 3D Fourier Transform of the PTCDA LUMO wave function. The red dome represents a hemispherical cut at constant $k = \sqrt{(2m/\hbar^2) \cdot E_{\rm kin}}$ for $E_{\rm kin} = 35\,{\rm eV}$ (image created by Daniel Lüftner, University of Graz). (c) Resulting constant binding energy map of the PTCDA LUMO level.

function is Fourier transformed and the result is shown in Fig. 2.2(b). Since the ARPES data is accumulated for a constant kinetic energy $E_{\rm kin}$, the Fourier transform has to be evaluated on a hemispherical sphere of radius $k = \sqrt{(2m/\hbar^2) \cdot E_{\rm kin}}$ which is indicated by a red dome in panel (b). The resulting two dimensional intensity distribution on this sphere is presented in Fig. 2.2(c) as a function of the parallel momentum components k_x and k_y . The shape of this so called constant binding energy (CBE) maps is characteristic for each molecular orbital and can be compared to the experimental ARPES data recorded in the same k-space range. However, it has to be considered additionally that molecules often adsorb on the surface in different orientations. These rotations are also reflected and lead to a more complex emission pattern compared to the CBE in Fig. 2.2(b). How this effect is handled is shown in detail in

section 3.1.2.

The ARPES experiments were performed using the synchrotron radiation source BESSY II (beamline U125/2-SGM) located at the Helmholtz Zentrum Berlin (HZB). A schematic overview of the ARPES experiment is shown in Fig. 2.3(a). The sample is illuminated by monochromatic radiation of the energy $\hbar\omega=35\,\mathrm{eV}$ with a fixed incident angle of 40° between the incoming light and the surface normal. The excited photoelectrons $\Phi_f(E_{\mathrm{kin}},k_\parallel)$ are detected as a function of the polar ϑ , the azimuthal angle φ and the kinetic energy E_{kin} . The photoelectron yield was recorded with a toroidal electron analyzer having a polar acceptance angle ϑ of $\pm 80^\circ$ and an energy dispersion range of 1.0 eV at a pass energy of 10 eV [BTH+05]. For this experimental parameters, the energy resolution of the setup was estimated to be better than 150 meV from the broadening of the Fermi edge. The azimuthal angular distribution φ was accessed by rotating the sample around its surface normal in steps of 1° in a range of at least

130°. This range is sufficient to create a CBE map for a surface structure with a threefold symmetry. The angle resolved photoemission data is transformed from polar and azimuthal emission angles into reciprocal space coordinates k_x and k_y by

$$k_x = \sqrt{(2m_e/\hbar^2) \cdot E_{\rm kin}} \sin(\vartheta) \cos(\varphi)$$
 and (2.7)

$$k_y = \sqrt{(2m_e/\hbar^2) \cdot E_{\rm kin}} \sin(\vartheta) \sin(\varphi).$$
 (2.8)

Considering the threefold symmetry of the silver bulk crystal and calibrating the energy scale to the Fermi level yields a three dimensional ARPES data cube $I(k_x, k_y, E_b)$ which is illustrated in Fig. 2.3(b). To account for the substrate contribution, ARPES data of the clean substrate were also recorded for the entire valence band region. From the experimental data cubes $I(k_x, k_y, E_b)$ CBE maps can be extracted for comparison with theoretical maps calculated for specific molecular orbitals. This allows to correlate the recorded spectral features with molecular orbitals.

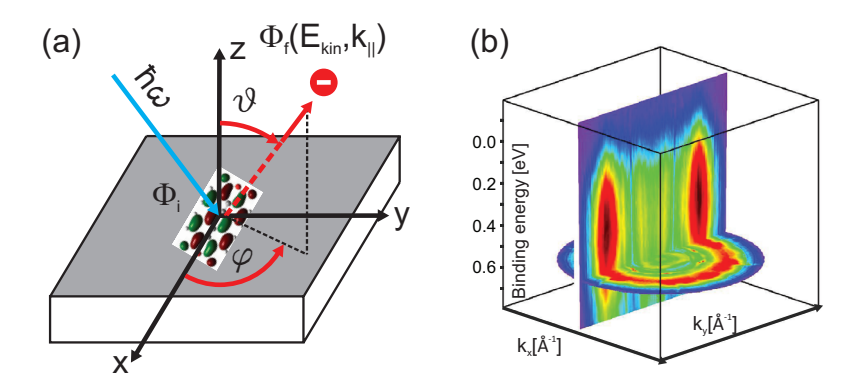


Figure 2.3: (a) Schematic overview of the ARPES experiment. (b) Illustration of an ARPES data cube $I(k_x, k_y, E_b)$.

The comparison of the theoretical and experimental CBE maps can be done qualitatively by just comparing experimental ARPES data and calculated CBE maps or by an advanced procedure called tomographic deconvolution. The latter allows to separate the contributions of specific molecular orbitals to experimental ARPES data. This is achieved by a two dimensional fit of the theoretical CBE maps to the ARPES data performed at every binding energy in the region of interest. The resulting fitting parameters can be interpreted as the density of states projected on the corresponding molecular orbital (PDOS). Up to now, this approach has only been applied to low symmetric fcc(110) surfaces [BKF⁺09, PBF⁺09, ZFS⁺10, PRU⁺11, WHS⁺12], since it was believed that on high-symmetric surfaces, where usually a large number of different molecular orientations occurs, the results will not be unambiguous.

However, in section 3.1.2 it is proven experimentally by studying the well known model system PTCDA/Ag(111) [ZKS+06, SWR+12], that this method is also applicable to fcc(111) surfaces. More details of the tomographic deconvolution procedure including an estimation of the experimental uncertainties are given in section 3.1.2.

2.3 The normal incidence X-ray standing wave technique

The adsorption height of a molecule on a surface is a quite direct measure for the bonding strength of the molecule with the substrate. Using a standing wave field as a probe, this bonding distance can be accurately measured ($\Delta z < 0.04\,\text{Å}$) by the normal incidence X-ray standing wave (NIXSW or XSW) technique. The great potential of this method resulted in a large number of NIXSW studies in the last decade which contributed significantly to a comprehensive understanding of the adsorption properties of mono-organic films adsorbed on different surfaces [Sta09a, Krö11, Mer12, HBL+07, GSS+07, SHK+09, HTS+10, MMM+10, GHD+11, KSK+11]. By comparing the adsorption distance between the surface and the molecule with the sum of the van der Waals radii of the involved atomic species the character of the molecule-metal bond can be classified. Adsorption distances smaller than this reference value indicate (at least partial) chemical bonding of the molecule to the surface which coincides with charge redistribution at the interface. In contrast, a larger bonding distance is an indication for a weak, mostly van der Waals induced interaction, i.e., physisorption. Based on this classification, a better understanding of the electronic level alignment at the metal-organic interface can be achieved [DGS+08].

Basic principles of the NIXSW method

This section provides a very brief introduction into the mathematical concept of the NIXSW method based on the reviews of Batterman [BC64], Zegenhagen [Zeg93] and Woodruff [Woo05, Woo98]. A more detailed description of the method can also be found in [Sta09a, Mer12]. In an NIXSW experiment, the electromagnetic wave field of the incoming radiation $\Sigma_0 = E_0 e^{-2\pi i \vec{k}_0 \vec{r}}$ illuminates a crystalline sample perpendicular to a set of Bragg planes which are used to generate the standing wave field. E_0 is the complex amplitude of the incoming wave and \vec{k}_0 represents its wave vector. For photon energies close to the Bragg condition, this wave generates a second, Bragg reflected, wave field $\Sigma_H = E_H e^{-2\pi i \vec{k}_H \vec{r}}$. Since both wave fields are coherent to each other, they can interfere and form a standing wave field. The intensity of this standing wave field is obtained by the square of the absolute value in

equation (2.9).

$$I = \left| E_0 e^{-2\pi i \vec{k}_0 \vec{r}} + E_H e^{-2\pi i \vec{k}_H \vec{r}} \right|^2 = \left| E_0 \right|^2 \left| 1 + \frac{E_H}{E_0} e^{-2\pi i \vec{H} \vec{r}} \right|^2$$
 (2.9)

 $|E_0|^2$ is the intensity of the incoming beam and \vec{H} is the reciprocal lattice vector of the Bragg reflection used to create the standing wave field. The coherence between both wave fields allows to express the ratio of the complex wave field amplitudes E_H/E_0 as a complex number with a phase ν . Furthermore, this ratio can be calculated in the framework of the dynamic scattering theory [BC64] as

$$\frac{E_H}{E_0} = \sqrt{R}e^{i\nu} = -\sqrt{\left(\frac{F_H}{F_{\bar{H}}}\right)} \left(\eta \pm \sqrt{\eta^2 - 1}\right). \tag{2.10}$$

For centrosymmetric crystals $(F_H = F_{\bar{H}})$ this ratio depends mainly on the complex structure factors F_0 and F_H for the forward scattered and the Bragg reflected wave and a complex value

$$\eta = \frac{-2(\Delta E/E_{\text{Bragg}})(\sin(\theta_B))^2 + \Gamma F_0}{|P|\Gamma F_H}, \text{ with}$$
 (2.11)

$$\eta = \frac{-2(\Delta E/E_{\text{Bragg}})(\sin(\theta_B))^2 + \Gamma F_0}{|P|\Gamma F_H}, \text{ with}$$

$$\Gamma = \frac{e^2/(4\pi\epsilon_0 mc^2)\lambda_{\text{Bragg}}^2}{\pi V_{\text{UC}}}.$$
(2.11)

This complex parameter η is a function of the energy difference ΔE between the actual photon energy $\hbar\omega$ and the Bragg energy $E_{\rm Bragg}=hc/\lambda_{\rm Bragg}$ at a certain Bragg angle θ_B . Furthermore, V_{UC} is the volume of the crystal unit cell and P is the polarization factor. In our case, P=1 since we use σ polarized light for our NIXSW experiment.

For an ideal, non-absorbing crystal, the reflectivity $R = |E_H/E_0|^2$ is plotted in Fig. 2.4 as a dashed line versus the real part η' of the parameter η , which depends linearly on the photon energy difference ΔE . When neglecting the absorption within the crystal, all structure factors are real numbers. The reflectivity profile reveals a characteristic shape with a constant value in the range between $\eta'=1$ and $\eta'=-1$. Consequently, the standing wave field does not change its intensity in this energy range which is also known as the Darwin width of the reflectivity profile R. According to equation (2.10), the relative phase of the incoming and Bragg reflected wave shifts within this Darwin width from $\nu = \pi$ to $\nu = 0$. This results in a shift of the standing wave field inside the crystal perpendicular to the Bragg planes. Furthermore, different refraction indices for X-ray photons in the crystal and in vacuum result in a small energy difference of the Bragg energy and the center of the reflectivity profile [BC64].

Considering the adsorption of the wave field in the crystal results in the reflectivity profile

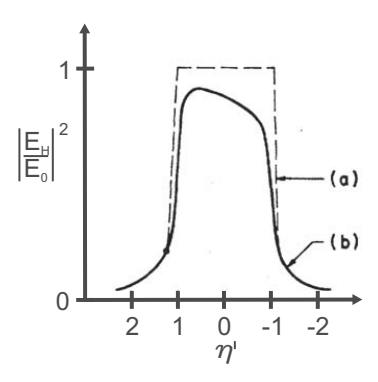


Figure 2.4: Shape of the reflectivity profile for a perfect crystal as a function of the real part η' of the parameter η [BC64]. The dashed curve (a) is obtained for zero absorption while for (b) the adsorption of the standing wave field in the crystal is considered.

which is included in Fig. 2.4 as a solid line. The asymmetric shape is attributed to the spacial shift of the standing wave field towards the atomic planes which results in a stronger adsorption of the wave field when approaching $\eta' = -1$.

Combining equations (2.9) and (2.10) allows to calculate the intensity distribution of the standing wave field:

$$I_{SW}(E,z) = 1 + R(E) + 2\sqrt{R(E)} \cdot \cos(\nu(E) - 2\pi z/d_{hkl})$$
 (2.13)

The intensity is normalized to the intensity I_0 of the incoming beam. Assuming that the photon absorption Y_{SW} of an atom within the standing wave field is proportional to the local photon intensity $I_{SW}(E,z)$, the vertical adsorption position of the atom can be analyzed using equation (2.13). The photon absorption Y_{SW} can be quantified by recording secondary emission processes. The most commonly used signals for this purpose are fluorescence, Auger electrons or photoelectrons. Fitting measured yield curves Y_{SW} together with the calculated reflectivity R and phase ν allows to determine the vertical position z of a single atom with respect to the nearest Bragg plane underneath.

The coherent fraction ${\cal F}^H$ and position ${\cal P}^H$

The adsorption height of a single atom on the surface can be obtained by equation (2.13). In order to describe the vertical position of more than one atom of the same species, several effects have to considered. Even though the averaged adsorption height of all atoms is similar, they reveal a certain vertical height distribution due to vertical disorder, surface

defects or thermally induced vibrations. In addition, different adsorption sites with different vertical positions can occur in complex adsorbate systems. In order to account for these aspects, in equation (2.13), a distribution function f(z) for the vertical position z is introduced, which describes the vertical position of all atoms of one species (normalization: $\int_0^{d_H} f(z)dz = 1$).

$$I_{SW}(E,z) = 1 + R(E) + 2\sqrt{R(E)} \cdot \int_0^{d_H} f(z) \cos(\nu(E) - 2\pi z/d_{hkl}) dz \qquad (2.14)$$

$$= 1 + R(E) + 2\sqrt{R(E)} \cdot F^{H} \cos(\nu(E) - 2\pi P^{H})$$
 (2.15)

The resulting expression can be simplified by introducing two new structural parameters: the coherent position P^H and coherent fraction F^H . The coherent position P^H reflects the averaged vertical position in fractions of the Bragg plane distance $P^H = \frac{D^H}{d_{hkl}}$ above the nearest Bragg plane. Hence the position D^H is ambiguous and can only be determined modulo the periodicity of the standing wave field. The coherent fraction F^H specifies the fraction of objects which are found at the position P^H . It can be interpreted as a vertical ordering parameter with values between 0 and 1. $F^H = 0$ indicates a homogeneous distribution of the adsorbates relative to the Bragg planes while $F^H = 1$ demonstrates that all objects are located exactly at the same height D^H corresponding to the coherent position P^H .

While the influence of statistical effects like vertical disorder or thermally induced vibrations on the coherent fraction and position is difficult to analyze, the impact of multiple adsorption sites can be calculated by a Fourier analysis. The coherent fraction F^H and position P^H can be understood as amplitude and phase of one Fourier component H. In case of multiple adsorption sites we have to deal with coherent fractions F^H_k and coherent positions P^H_k for each site, which average to F^H and P^H according to

$$F^{H} \cdot e^{2\pi i P^{H}} = \sum_{k=1}^{N} n_{k} \cdot F_{k}^{H} \cdot e^{2\pi i P_{k}^{H}}$$
(2.16)

The sum of the relative contributions n_k of all adsorption sites has to be normalized to 1.

$$\sum_{k=1}^{N} n_k = 1 \tag{2.17}$$

Since this Fourier analysis is used several times in this work, we illustrate it in a simple example in Fig. 2.5. The XSW parameter $(F^H; P^H)$ are plotted in a polar coordinate system (the Argand diagram) as a vector \mathbf{Z} . The coherent fraction determines the length (i.e., the absolute value) of this vector \mathbf{Z} , its polar angle is given by $2\pi P^H$. In the example chosen here, we assume two distinct adsorption heights A and B which are equally populated, i.e.,

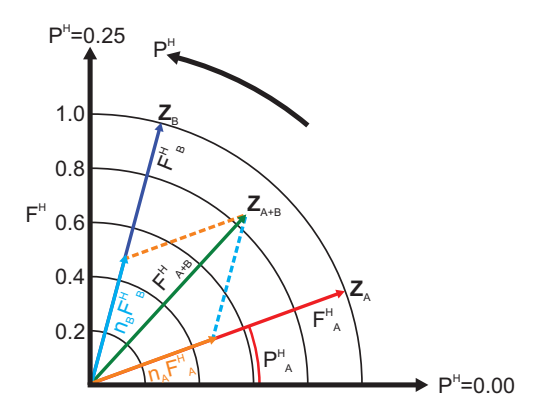


Figure 2.5: Argand diagram with hypothetical data demonstrating the Fourier analysis for two different adsorption sites A and B which are equally occupied.

 $n_A = n_B = 0.5$. The vectors $\mathbf{Z}_{\text{A/B}}$ have therefore to be scaled with 0.5 and summed up to $\mathbf{Z}_{\text{A+B}}$ with the corresponding parameters $P_{\text{A+B}}$ and $F_{\text{A+B}}$. These are the values which one obtains in an experiment for such a two level system. This Fourier analysis or vector analysis is used in chapter 5 and 6 in order to disentangle the contributions of molecules in different adsorption heights to the averaged experimental yield signal.

The NIXSW experiment and data analysis

The NIXSW experiments were performed at the Hard X-Ray Photoemission (HAXPES) and XSW end station ID32 at the European Synchrotron Radiation Facility (ESRF) in Grenoble, France. The photoelectron core level signals were detected with a hemispherical electron analyzer (PHOIBOS 225, SPECS) which was mounted in an angle of 90° with respect to the incoming photon beam. For the NIXSW experiment, the (111)-reflection of a Ag(111) single crystal was used in order to generate a standing wave field perpendicular to the sample surface. The reflectivity of the Bragg reflected beam and the photoemission yield were recorded at 25 different photon energies in a range of 5 eV around the Bragg condition. The reflectivity profile and the integrated yield curves were analyzed with the software *Torricelli* by Giuseppe Mercurio [Mer12].

The core level emission lines were analyzed with the commercial software CASAXPS. The chemical sensitivity of the photoemission signal allows to separate the photoemission yield of chemically different atomic species within one molecules. This allow to determine the adsorption height of all different species in the molecule and hence to estimate the molecular bending on the surface.

2.4 Scanning tunneling microscopy and spectroscopy

The introduction of the first scanning tunneling microscope (STM) in 1981 by Binning and Rohrer opened a new field of opportunities in surface science [BRGW82, Wie94, Che93]. For the first time it was possible to image surface structures with atomic resolution in real space. This experimental technique takes advantage of the quantum mechanical tunneling effect which is illustrated in Fig. 2.6. A sharp metallic tip shown in red in panel (a), is placed only a few Ångstroms above a non-insulating surface. A potential difference U_{Bias} is applied between the probe and the sample which results in a small tunneling current I in the vacuum barrier. This is illustrated in the potential diagram in Fig. 2.6(b). The sample surface and the metallic tip are separated by a potential barrier Φ which is mainly attributed to the work function of the material. According to basic quantum mechanics the substrate wave functions decay exponentially in the barrier. If the vacuum gap d is small enough, the wave function still exhibits a significant contribution at the position of the tip and can be detected in the tip as a small electric current. This tunnel current is proportional to the probability of the substrate wave function at the position of the tip $(|\psi(d)|^2 = |\psi(0)|^2 e^{2\kappa d})$ and hence to the overlap of the substrate wave function with the ones of the metallic tip.

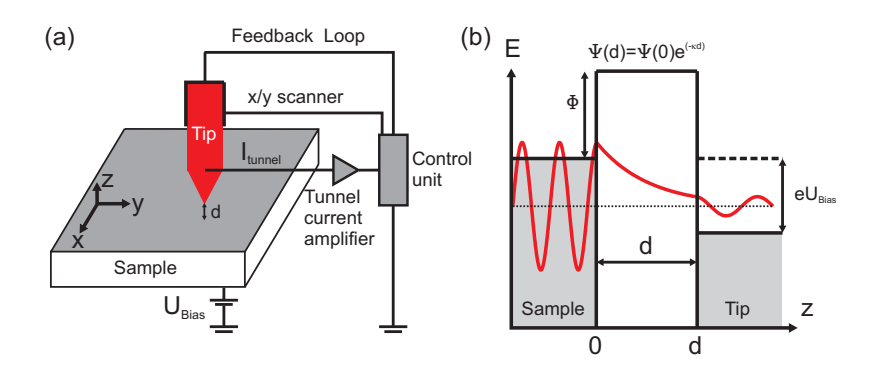


Figure 2.6: (a) Schematic working principle of a scanning tunneling microscope. (b) Potential diagram illustrating the quantum mechanic tunneling effect.

This approach can be employed in order to image surface structures. The tip is scanned laterally over the surface with piezoelectric drives and the tunneling current I is recorded as a function of the lateral tip positions (x,y). In the constant-current mode, the current between the sample and the tip is kept constant for a selected bias voltage U_{Bias} while scanning the surface. This is done by a feedback loop which compensates changes in the tunneling current by modifying the vertical position z of the tip with piezoelectric drives. The piezo voltage necessary to adapt the vertical tip position is recorded for all lateral positions (x,y) and

results in a topological contrast of the surface structure.

Besides imaging the surface topology, the tunneling process also allows to study the local density of states (LDOS) of a surface by scanning tunneling spectroscopy (STS). This local spectroscopic technique accesses the occupied as well as unoccupied electronic states by changing the applied sample bias $U_{\rm Bias}$. For recording an STS spectrum, the tip is placed at a selected position on the surface while the bias voltage $U_{\rm Bias}$ is continuously ramped in a certain voltage range. The resulting tunneling current as well as its first derivative dI/dU are recorded as a function of the binding energy $e \cdot U_{\rm Bias}$. The latter is proportional to the local density of states. For a better signal quality, the dI/dU signature is accessed by using a lockin amplifier. This device modulates the bias voltage $U_{\rm Bias}$ with a high frequency sinusoidal signal V_{LIA} , which induces a sinusoidal response in the tunneling current. The amplitude of this response is sensitive to the slope of the tunneling current.

Mathematical basics of scanning tunneling microscopy (STM) and spectroscopy (STS)

In analogy to the photoelectric yield discussed in section 2.2, the tunneling current in an STM experiment can be described by Fermi's Golden Rule [Wie94, Bar61]. However, this approach is rather challenging since it requires the knowledge of the electronic structure of the tip. In the simplified Tersoff-Hamann model, this problem is neglected by assuming a spherically shaped tip with curvature R [TH85] which only exhibits spherical s-wave functions. For low sample temperature ($kT \ll \Delta U_{\rm resolution}$) and low sample bias U, the tunneling current is

$$I \propto U \cdot n_t(E_F) \cdot e^{2\kappa R} \sum_{\nu} |\psi_{\nu}(r_0)|^2 \delta(E_{\nu} - E_F). \tag{2.18}$$

Even in this simple model, the tunneling current still depends on microscopic tip properties like its curvature R as well as its density of states $n_t(E_F)$ right at the Fermi level. Since the substrate wave functions ψ_{ν} decay exponentially within the vacuum gap, $\psi_{\nu}(r_0) \propto \psi_{\nu}(E_{\nu})e^{-\kappa(s+R)}$, the relation in equation (2.18) transforms into

$$I \propto U \cdot n_t(E_F) \cdot n_s(E_F) \cdot e^{-2\kappa s}$$
 (2.19)

In this context, s is the distance between the tip apex and the surface, and κ is the inverse decay length in the vacuum gap. It is revealed that the density of states of the surface $n_s(E_F)$ is proportional to the tunneling current and hence reflected in the STM contrast. This contrast depends exponentially on the distance s between the surface and the tip.

For finite bias voltages U, equation (2.19) can be generalized by an integration over all bias voltages dU in the energy gap between the Fermi level and U.

$$I(U) \propto \int_{E_F}^{eU} n_t(-eU + E) \cdot n_s(E) \cdot T(z, E, eU) dE$$
 (2.20)

In this equation (2.20) the transmission function T(z, E, eU) describes the probability for an electron to tunnel between the sample and the tip. For small bias voltages U the transmission function T(z, E, eU) as well as the density of states within the tip n_t can be considered to be constant. Hence, the contrast in the STM image is proportional to the density of states in the sample integrated over an energy window $E_F + eU$. This finding indicates that the tunneling contrast in a constant-current image is not only of topological nature but also contains information about the electronic structure.

From the tunneling current (equation (2.20)), the differential conductance dI/dU can be calculated. Assuming that the transmission function T(z, E, eU) as well as the DOS of the tip $n_t(E_F)$ are bias independent, this results in

$$\frac{dI(U)}{dU} = \propto n_t(E_F) \cdot n_s(E_F + eU) \cdot T(z, E_F + eU, eU). \tag{2.21}$$

This term reveals a linear relation between the differential conductance dI/dU and the local density of states of the substrate $n_s(E_F + eU)$. Hence, the scanning tunneling spectroscopy allows direct access to the local density of states at an energy eU with respect to the Fermi level.

Tunneling process through organic molecules on metal surfaces

In this work, the adsorption of organic molecules on metal surfaces is studied by the STM and STS-technique. The presence of a molecule in the junction between the surface and the tip leads to the appearance of additional electronic states within this gap which can be assigned to the molecular orbitals. This is illustrated in the energy diagrams in Fig. 2.7, in which the energy positions of the molecular levels are fixed with respect to the Fermi level of the substrate. The electrons tunneling between the sample and the tip also travel through those molecular orbitals that are energetically located between the Fermi level and the applied bias voltage $U_{\rm Bias}$. Consequently the contrast of the STM images resembles the electronic density of states of the molecular orbitals involved in the tunneling process. For negative (positive) sample bias, the occupied (unoccupied) molecular levels are responsible for the tunneling contrast (Fig. 2.7(a) and (c))

For scanning tunneling spectroscopy, the bias voltage is scanned through the energy positions

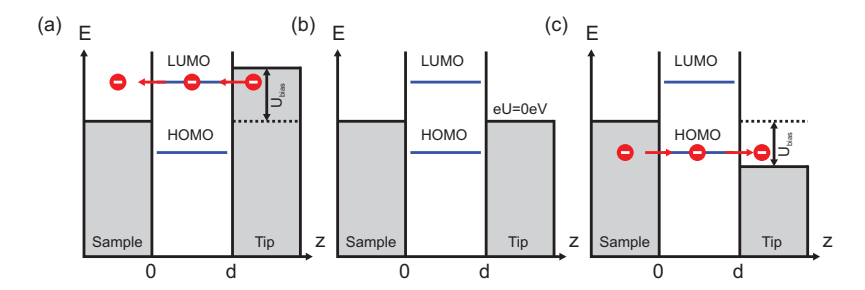


Figure 2.7: Energy diagrams illustrating the role of the molecular orbitals for the tunneling process. The energetic positions of the molecular energy levels are fixed with respect to the substrate Fermi level. The sample bias is negative (a) zero (b) and positive (c).

of the orbitals. In case of an overlap, a resonant current through the corresponding molecular state occurs. This results in a peak in the differential conductance dI/dU. The energy position of this spectroscopic feature reflects the binding energy of the molecular level. For the occupied molecular orbitals STS and photoelectron spectroscopy should reveal equal binding energy positions [KHT⁺08, SWR⁺12].

2.5 The pair potential approach

The pair potential approach is a simple theoretical model for describing the lateral structure formation of organic thin films. Since this method only considers van der Waals and electrostatic interactions between the molecules and no interaction to the surface, it provides most reliable results for weakly interacting surfaces like Au(111) [MF05, WKG⁺10, KSW⁺11, Krö11].

The parametrization as well as the implementation of the pair potential approach, which is introduced in this section, is based on the previous work of Kröger et al. [Krö11, KSW⁺11]. The interaction energy between two molecules A and B, which is also referred to as the pair potential Φ , is defined as

$$\Phi(\mathbf{r}) = \sum_{i} \sum_{j} \left(\phi_{ij}^{\text{vdW}}(r_{ij}) + \phi_{ij}^{\text{ec}}(r_{ij}) \right). \tag{2.22}$$

Electrostatic $\phi_{ij}^{\text{ec}}(r_{ij})$ as well as the van der Waals interaction $\phi_{ij}^{\text{vdW}}(r_{ij})$ between all pairs of atoms ij are considered. Since both potentials are centrosymmetric, they only depend on the inter atomic distance r_{ij} . The indices i and j number all atoms in molecules A and B.

The electrostatic potential $\phi_{ij}^{ec}(r_{ij})$ is parametrized as the Coulomb potential between two

partially charged atoms (i, j) at a distance r_{ij} :

$$\phi_{ij}^{\text{ec}}(r_{ij}) = \frac{Z_i Z_j}{4\pi\epsilon_0 r_{ij}} \tag{2.23}$$

Since surface interactions are not taken into account, image charges created in the metal surface are also neglected in the electrostatic potentials. The partial charges of the atoms within the molecule are obtained from a DFT calculation for the free molecule. More details can be found in [Krö11, KSW⁺11].

The parametrization of the van der Waals interaction is given by

$$\phi_{ij}^{\text{vdW}}(r_{ij}) = a_{ij}e^{-b_{ij}r_{ij}} - \frac{c_{ij}}{r_{ij}^6}.$$
(2.24)

This potential consists of two parts: the Pauli repulsion is described by an exponential function and the attractive London force is proportional to r_{ij}^{-6} . The so called "non-bonding parameters" a_{ij} , b_{ij} and c_{ij} are element specific and hence depend on the interacting atoms. For pairs of equal types of atoms, the parameters $b_{ij} = b_n$ and $c_{ij} = c_n$ can be found in literature [SS65, SBS79, FZ94]. $a_{ij} = a_n$ is optimized in order to reveal the minimum energy at a distance corresponding to the van der Waals radius of the element n. The element specific parameters used in this work are summarized in table 2.1. For atomic pairs of different elements n and m, the van der Waals parameters are calculated as the geometric mean of the symmetric pairs (e.g., $a_{nm} = \sqrt{a_n a_m}$).

n	$a_n [eV]$	$b_n [\mathring{\mathbf{A}}^{-1}]$	$c_n [\text{eV Å}^6]$	r_{vdW} [Å]
Н	432	4.52	1.96	1.30
С	34000	4.59	15.7	1.77
N	9000	4.59	12.70	1.55
О	5600	4.59	9.41	1.50
Cu	550	2.95	94.93	1.40

Table 2.1: Element specific van der Waals parameters and van der Waals radii used for the pair potential calculations. While b_n , c_n and r_{vdW} were reported in literature [SS65, SBS79, FZ94, Bon64], a_n was optimized to create the potential minimum at the van der Waals radius of the corresponding element.

Based on this parametrization, the intermolecular interaction between two or more organic molecules can be calculated by the pair potential approach. For simplification, the molecules are treated as rigid objects with a fixed internal structure which is optimized beforehand by a DFT calculation for the free molecule in the gas phase. This assumption neglects a possible relaxation of the internal molecular structure caused by the interaction between the

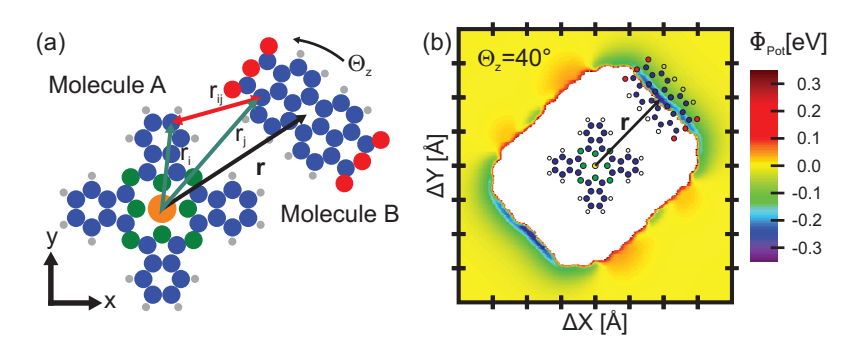


Figure 2.8: Illustration of the pair potential approach. (a) The relative displacement vector ${\bf r}$ between the center of masses of the molecules is shown as ablack arrow, the atomic distance r_{ij} used in the pair potential equation (2.22) as red arrow . (b) Pair potential map for a constant rotation vector $\Theta = (\Theta_x, \Theta_y, \Theta_z)$ as a function of the lateral displacement ${\bf r} = (\Delta X, \Delta Y, \Delta Z)$ with $\Delta Z = 0$.

molecules. Consequently, the positions of all atoms within the molecule are fully characterized by the location of the molecular center of mass and the molecular orientation. The pair potential between two molecules A and B is calculated as a function of the relative displacement vector $\mathbf{r} = (\Delta X, \Delta Y, \Delta Z)$ and the relative molecular orientation vector $\Theta = (\Theta_x, \Theta_y, \Theta_z)$. The angle Θ_k indicates a rotation of molecule B relative to molecule A around an axis in k-direction through the center of mass of molecule B. The pair potential energy is usually presented in two dimensional maps as a function of two independent coordinates while the other coordinates are kept constant. This is illustrated in Fig. 2.8 for the interaction between CuPc and PTCDA as a function of the lateral displacement vector $\mathbf{r} = (\Delta X, \Delta Y, \Delta Z)$ with $\Delta Z = 0$. All other coordinates are fixed at zero or at a predefined value like in the case of the relative in plane rotation. which is set to $\Theta_z = 40^{\circ}$ in this example. The corresponding arrangement of the molecules is shown in panel (a). For each displacement $\mathbf{r} = (\Delta X, \Delta Y, 0)$, the overall pair potential is calculated and plotted according to a defined color code as a function of the displacement vector, see Fig. 2.8(b). While areas of negative pair potential energy in this map indicate an attractive interaction between the molecules, areas of positive pair potential energy indicate intermolecular repulsion. Favorable adsorption configurations for the molecules are usually reflected in deep minima in the pair potential energy map.

3 Mono-organic thin films

The geometric and electronic properties of large organic molecules on metal surfaces is determined by a delicate interplay between the molecule-substrate as well as the intermolecular interaction. For this reason organic model molecules like 3,4,9,10-perylenetetra-carboxylic-dianhydride (PTCDA) or copper-II-phthalocyanine (CuPc) on the Ag(111) surface have been studied during the last decades. This surface is of particular interest since the interaction strength between the molecules as well as their bonding to the surface are in the same energy range. Therefore, both forces compete with each other resulting in a variety of different geometric arrangements of the molecules on the surface.

Combining experimental and theoretical studies for those model systems leads to a comprehensive understanding of the adsorption mechanisms at metal-organic interfaces. This knowledge on mono-organic films is mandatory in order to investigate the adsorption of hetero-organic films consisting of two different types of molecules. It allows to predict the interface properties of mixed organic films on noble metal surfaces and unmasks new effects induced by the intermolecular interaction. For this reason, CuPc and PTCDA, two of the most frequently studied molecules on noble metal surfaces were chosen in order to create mixed organic interfaces.

Since in the following chapters the findings for hetero-organic thin films will be compared with the adsorption properties of bare CuPc and PTCDA films on Ag(111), this chapter summarizes important results for both mono-organic systems. In addition new experimental results for those systems are presented in sections 3.1.2 and 3.2.2.

3.1 PTCDA/Ag(111)

In Fig. 3.1 a schematic picture of perylene derivative PTCDA ($C_{24}O_6H_8$) is shown in a ball model. This planar molecule consists of a perylene core which is terminated by two anhydride groups containing two different types of oxygen atoms. The sp²-hybridization of the carbon atoms results in π -conjugated and delocalized orbitals which expand mainly over the perylene core of the molecule. The high electron negativity of the oxygen atoms in the anhydride

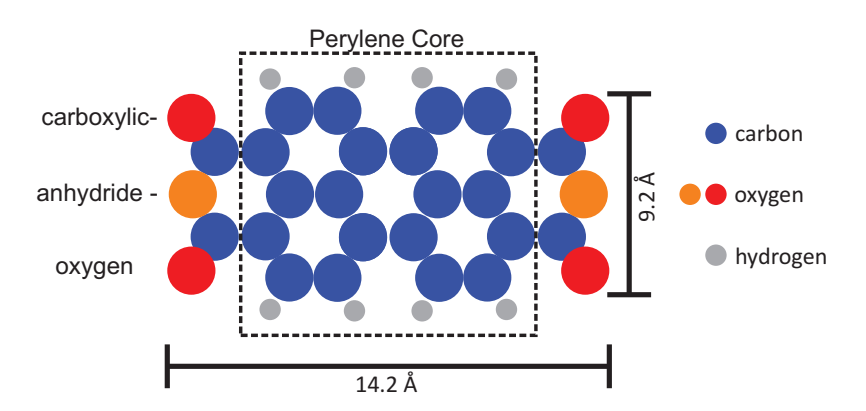


Figure 3.1: Chemical structure of PTCDA presented in a ball model. The molecule consists of a perylene core which is terminated by two anhydride groups.

group leads to a quadrupole moment on the molecule with negative partial charges on the oxygen atoms and positively charged hydrogen atoms. This electrostatic moment has a strong influence on the structure formation of PTCDA films and crystals.

After a short presentation of the adsorption behavior of PTCDA on Ag(111) in section 3.1.1, which mainly stems from literature, a new approach for analyzing angle resolved photoemission data is discussed for the well studied PTCDA/Ag(111) monolayer structure in section 3.1.2. The latter results were also published recently in Ref. [SWR⁺12].

3.1.1 A short introduction

The adsorption behavior of PTCDA on noble metal surfaces and particular on Ag(111) is experimentally [KUS04, HKC⁺05, KTH⁺06, ZKS⁺06, HBL⁺07, Tau07, DGS⁺08, KHT⁺08, SSM⁺08] and theoretically [RTT07, AS09, RNP⁺09, DP10] one of the best characterized adsorbate systems. This introduction about the properties of the PTCDA/Ag(111) metalorganic interface is focused on experimental results, which are crucial for studying the formation of mixed organic films in the following chapters 4,5 and 6.

In the submonolayer regime, the electrostatic moment of the PTCDA molecule results in the clustering of the molecules in ordered islands [MGS⁺06], revealing the commensurate monolayer structure. The corresponding diffraction pattern of this structure is shown in Fig. 3.2(a). The red circles in the lower part of the image mark the positions of calculated diffraction maxima based on the superstructure matrix $(\frac{7}{2}\frac{1}{5})$. The almost rectangular unit cell $(\gamma = (89.0 \pm 0.4)^{\circ})$ with unit cell vector lengths of $|\vec{A}| = (19.0 \pm 0.1)$ Å and $|\vec{B}| = (12.6 \pm 0.1)$ Å is very similar to the molecular arrangement in the (102)-plane of the α or β phase of the PTCDA molecular bulk crystal [KDR⁺02]. The unit cell on Ag(111) is only slightly smaller,

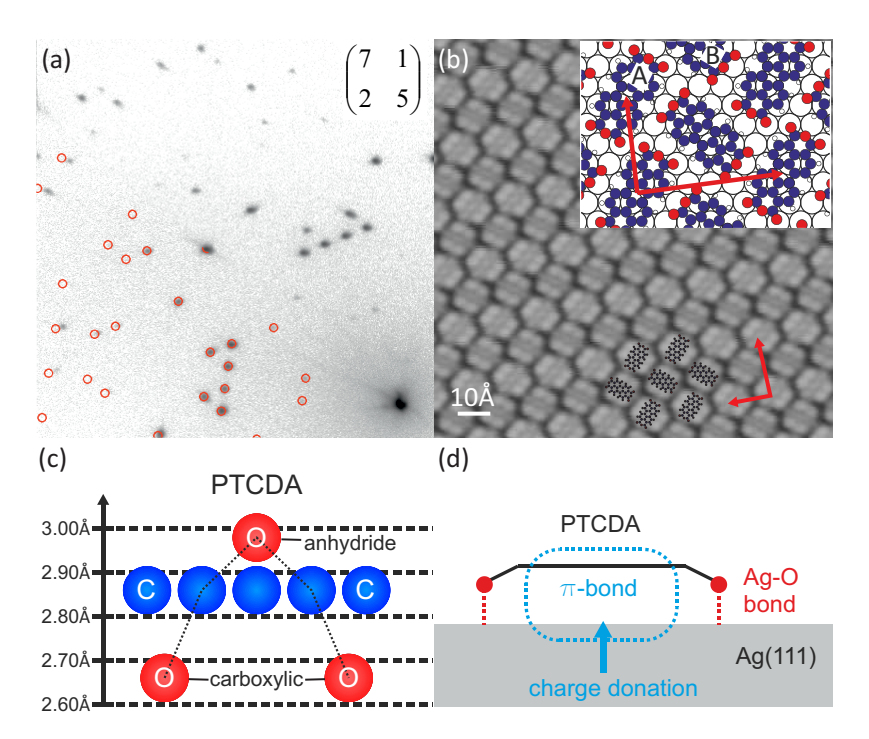


Figure 3.2: (a) LEED pattern ($E_{\rm kin}=27.2\,{\rm eV}$) and (b) STM image ($U_{\rm Bias}=-0.34\,{\rm V},~I=0.2\,{\rm nA}$) of the PTCDA monolayer structure on Ag(111). The inset of panel (b) shows the lateral adsorption geometry of the PTCDA molecules in the unit cell. (c) Vertical adsorption geometry of PTCDA/Ag(111) [HTS+10]. The molecule is shown in a front view along the molecular axes. (d) Schematic model of the interaction channels between PTCDA and the Ag(111) surface.

caused by the interaction between PTCDA and the underlying substrate.

In the monolayer structure, the PTCDA molecules are arranged in a herringbone pattern. This was found in submolecular resolved LT-STM images similar to the one shown in panel (b), which reveals two differently aligned PTCDA molecules. The exact orientation of the molecules in the unit cell as well as their adsorption site is illustrated in the inset in Fig. 3.2(b) in a structural model. One PTCDA molecule, labeled with "A", is aligned with its long axes along the silver rows, i.e., along the $[\bar{1}01]$ high symmetry direction of the substrate. The second molecule "B" is rotated 77° with respect to molecule A. As a consequence, the relative position of the functional anhydride group with respect to the substrate is different for the molecules A and B even though the center of both carbon backbone is located above a bridge site of the Ag(111) surface $[KTH^{+}06]$. The relative orientation of the molecules in the unit cell is strongly influenced by the $O\cdots H$ interaction between the different PTCDA molecules in the unit cell.

The adsorption height of PTCDA on Ag(111) was determined by the X-ray standing waves method [HTS+10]. The resulting vertical adsorption geometry is illustrated in a front view representation of the molecule along its long axis in Fig. 3.2(c). The PTCDA carbon backbone (shown as blue circles) adsorbs on the Ag(111) surface in an almost flat geometry and exhibits a distance of $d_{\text{Backbone}}^H = 2.86 \,\text{Å}$ to the silver surface. This distance is much smaller than the sum of the van der Waals radii of silver and carbon [Bon64] and hence points to a significant overlap of the π -conjugated electronic system of the molecule with electronic states of the substrate. This finding suggests a chemical interaction between PTCDA and the silver surface, which is supported by the strong geometric distortion of the molecule upon adsorption. The carboxylic oxygen atoms bend towards the silver surface, while the anhydride oxygen species is located above the perylene core. In addition, the carboxylic oxygen atoms are found directly above silver atoms, which suggests the formation of a second more localized bond between the carboxylic oxygen atoms and the silver atoms below. The displacement of the anhydride oxygen above the molecular plane may be the result of stress on the molecule due to the strong bending of the carboxylic oxygen atoms to the surface.

Combining the experimental findings with density functional theory (DFT) calculations [RTT07, RNP+09] allows to characterize the different interaction mechanisms which are present at the PTCDA/Ag(111) interface. Those interaction channels are illustrated in Fig. 3.2(d). The overlap of the molecular π -orbitals with substrate states leads to the formation of a π -bond between the molecule and the substrate. This causes a charge redistribution at the interface which results in a partial filling of the PTCDA LUMO level. Experimental evidence for this charge transfer into the LUMO level of the molecule is found in literature [ZKS+06], and discussed in the next section 3.1.2. In addition, a more localized bond is formed between the carboxylic oxygen atoms and the underlying silver which explains the bending of the PTCDA molecule. For this bond the specific adsorption site of the molecule is crucial. This can explain the commensurate registry between the molecular film and the silver surface. Both interaction channels between the molecule and the surface coincide with a charge redistribution at the metal-organic interface which results in an effective charge transfer of ≈ 0.35 electrons (≈ 0.47 electrons) into each PTCDA molecule [RTT07] ([RNP+09]). Since an orbital-resolved electron transfer analysis revealed a much larger charge in the PTCDA LUMO level, a certain amount of charge has also to be transfered back from the molecule into the substrate. However, this does not result in a depopulation of a particular molecular level, but effects up to ≈ 20 orbitals which are localized mainly at the carboxylic oxygen atoms [RNP+09]. This charge donation and backdonation between PTCDA and the silver surface, found in DFT, again illustrates the chemical character of the molecule-substrate interaction.

3.1.2 Tomographic deconvolution on a highly symmetric surface: PTCDA on Ag(111)

Although, the appearance of a new state at the Fermi level was conclusively demonstrated for PTCDA/Ag(111) by conventional angle integrated photoelectron spectroscopy [ZKS⁺06], the assignment of this feature to the PTCDA LUMO level was only possible due to further knowledge of the adsorbate system. This general limitation of UPS can be overcome by recording the angular distribution of the photoelectron yield (ARPES/ARUPS). Analyzing the momentum distribution of the photoemission intensity with the orbital tomography approach, described in section 2.2, allows to identify the emitting molecular orbital.

However, up to now, this approach has only been applied to (110)-oriented surfaces of face centered cubic crystals [BKF⁺09, PBF⁺09, ZFS⁺10, PRU⁺11, WHS⁺12]. This is clearly due to the fact that this surface shows only low symmetry (p2mm). As a result, most molecules (especially elongated molecules) tend to align along high symmetry directions of the substrate surface. Hence, the angular distribution of the photoelectron yield for the complete organic layer is comparable to the emission of one single molecule.

This section provides evidence that the orbital tomography approach is not only limited to low symmetry surfaces but can also be extended to surfaces exhibiting, e.g., p3m1 symmetry as the Ag(111) surface. The monolayer structure of PTCDA on Ag(111) discussed in the previous section 3.1.1 is an ideal benchmark system for this method since the unit cell contains two structurally inequivalent PTCDA molecules A and B with distinct azimuthal orientations [KTH+06]. The three rotational domains, each having one additional mirror domain, result in twelve molecules with different orientations on the surface. Moreover, the local density of states of both inequivalent PTCDA molecules has been studied by scanning tunneling spectroscopy (STS) [KTH+06] and can be used as a reference for the projected density of states (PDOS) obtained by orbital tomography.

The orbital tomography approach takes advantage of the plane wave approximation for the final state of the photoemission process. As a consequence, the momentum distribution of the photoemission intensity from a specific molecular orbital can be obtained from a hemispherical cut through the three dimensional Fourier transform of the molecular wave function at a radius k, which is determined by the kinetic energy of the electrons in the final state. For this reason, the molecular wave functions of the HOMO and LUMO level for a single PTCDA molecule are displayed in Fig. 3.3(a)+(b). The corresponding theoretical momentum maps are included in panels (c)+(d). The HOMO momentum map reveals four distinct main features and four additional side features with significantly lower intensity. The positions of these maxima can be directly correlated to the nodal structure of the HOMO. Since the HOMO

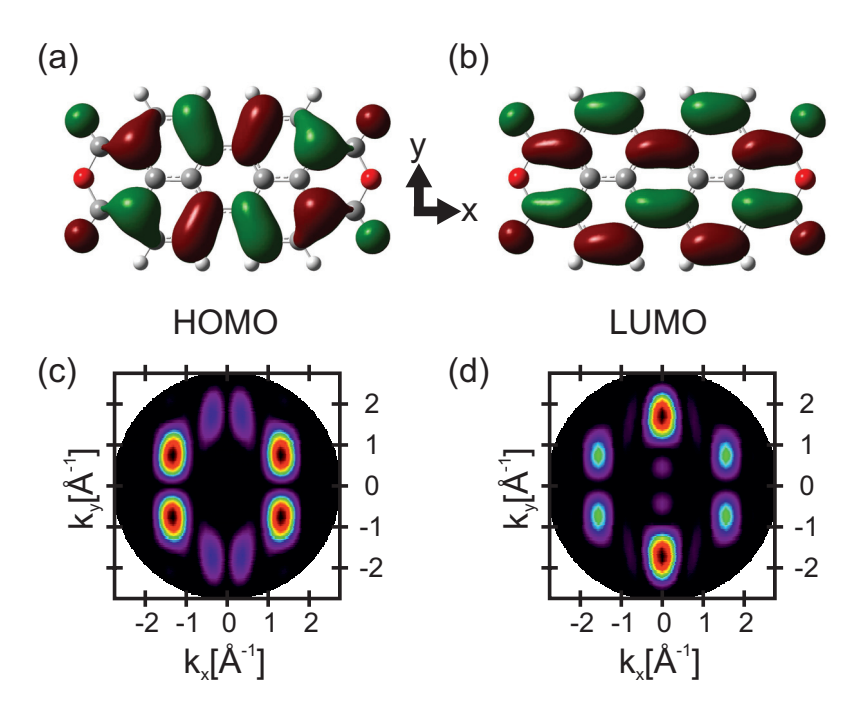


Figure 3.3: Shape of the PTCDA HOMO (a) and LUMO (b) calculated for a free molecule in the gas phase (DFT calculation, B3LYP, basis set: LANL2DZ [FTS⁺]). Similar colors in the orbital surface refer to a similar sign of the orbital wave function. The corresponding momentum maps calculated for the PTCDA HOMO and LUMO are shown in panels (c) and (d) respectively.

wave function exhibits nodal planes, both along (xz-plane) and perpendicular (yz-plane) to the long molecular axis, no intensity can be found in the orbital map for either $k_x = 0$ or $k_y = 0$. The k_x positions of the main features are determined by the periodicity of the nodal planes perpendicular to the long molecular axis, the k_y positions by the periodicity of the nodal planes along the long molecular axis.

For the LUMO, a different shape is observed for the k-space map. This orbital does not show nodal planes perpendicular to the long molecular axis which leads to the appearance of the main emission features at $k_x = 0$. The corresponding emission direction k_y is again based on the periodicity of the nodal planes of the molecular wave function along the long molecular axis (xz-planes).

In order to describe the emission arising from a complete molecular film adsorbed on a surface, the in-plane orientations of the molecules with respect to the substrate have to be taken into account. For the PTCDA monolayer on Ag(111), these can be adapted from the high reso-

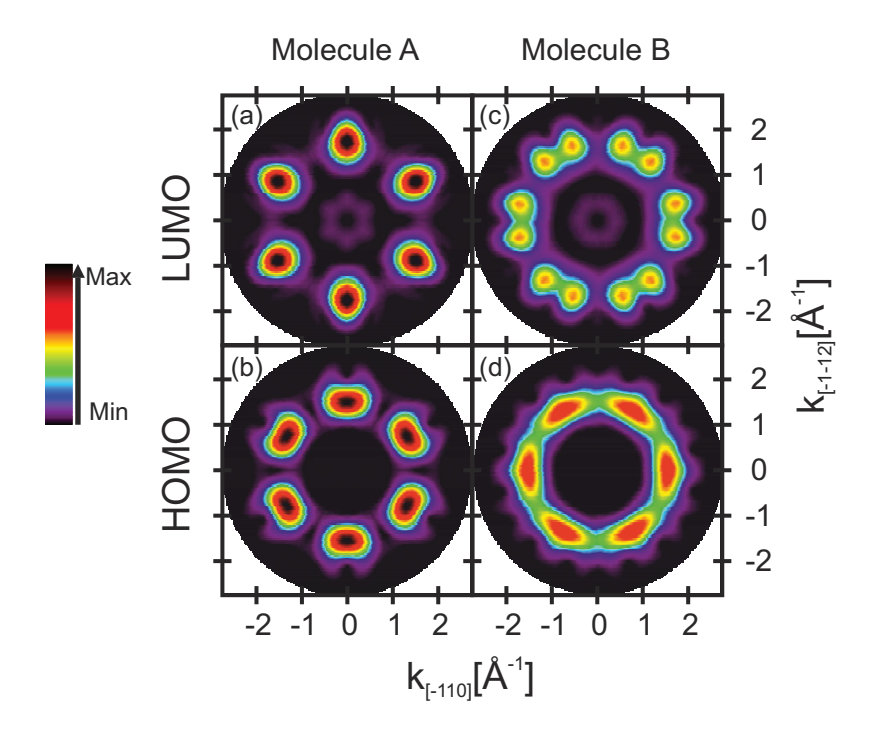


Figure 3.4: Constant binding energy (CBE) maps for the HOMO and LUMO of PTCDA molecules. In all panels the p3m1 symmetry of the substrate surface is considered, which causes a superposition of six different molecular orientations. In (a) and (b) this is performed for molecule A (aligned along [101]), in (c) and (d) for molecule B (77° with respect to [101]) (see also Ref. [SWR+12]).

lution STM data [KTH+06], which have already been introduced in section 3.1.1. Molecule A is directly aligned along the $[\bar{1}01]$ high symmetry direction of the substrate while molecule B is rotated by 77° with respect to molecule A. Considering the six-fold symmetry of the uppermost Ag(111) layer allows to generate the theoretical constant binding energy (CBE) maps for both molecules A and B which are shown in Fig. 3.4 (a-d) for HOMO and LUMO. In panel (a) and (b) the molecular orientation is 0° with respect to the $[\bar{1}01]$ (or equivalent) substrate directions as it is the case for molecule A; in Fig. 3.4(c) and (d) it is 77°, corresponding to the orientation of molecule B. Note that the orientations of some molecules in some domains coincide in the case of molecule A, since it lies parallel to the mirror lines of the structure. For this reason, the LUMO emission pattern shown in Fig. 3.4(a) looks as if only three molecular orientations were averaged. In case of molecule B the misalignment of the molecule with respect to the high symmetry direction becomes clearly visible. It leads to a splitting of the emission maxima by $\pm 17^{\circ}$ as can be seen in panel (c) for the LUMO

state. In case of the HOMO emission (Fig. 3.4(d)) the splitting smears out the intensity to an almost continuous ring.

In Fig. 3.5(a) and (b) calculated CBE maps for the overall emission from the PTCDA monolayer structure are shown. The maps correspond to the sum of the maps for molecules A and B, i.e., Fig. 3.4(a)+(c) for the LUMO and (b)+(d) for the HOMO. Note that this calculation requires the HOMOs (and also the LUMOs) of both molecules are located at the same binding energy. Although this is not strictly fulfilled in the case presented here, a qualitative evaluation is still possible. In the deconvolution procedure presented below this energy discrepancy will be taken into account. Both CBE maps in Fig. 3.5(a) and (b) are dominated by the pattern of molecule A, owing to the higher maximum intensity in these maps caused by the coincidence of several peak positions (see above).

In Fig. 3.5(c) and (d) the corresponding experimental data are shown. The CBE maps represent cuts through the experimental data cubes at binding energies of $E_{\rm b}=0.3\,{\rm eV}$ and 1.6 eV for LUMO and HOMO, respectively. Both maps reveal six distinct photoemission maxima at a well defined distance from the $\bar{\Gamma}$ -point of the surface Brillouin zone and hence match to the predicted maps for the LUMO (panel a) and HOMO (b) very well. The additional sharp and curved photoemission features which are not explained by the simulated molecular emission can be assigned to bands of the silver substrate. This is evident when considering the emission pattern arising from the clean Ag(111) surface which is shown in Fig. 3.5(e)+(f) for the LUMO and HOMO binding energies. The emission signature of the clean Ag(111) surface is very similar to the one reported for the Cu(111) surface [TRH+10].

This result confirms that the peak at the Fermi edge, found in UPS or STS [ZKS⁺06, KTH⁺06], in fact arises from the (former) LUMO state which is shifted below the Fermi energy and (partly) filled due to the interaction of the PTCDA molecule with the surface. This analysis already allows to conclude that the ARPES yield for a molecular adsorbate system, exhibiting six rotational and mirror domains, can be qualitative understood by the concept of the plane wave approximation for the PES final state.

For a more quantitative analysis of the ARPES data of Fig. 3.5(c,d) the tomographic approach can be employed in order to separate the measured ARPES intensity and extract the contributions of the orbitals of the two individual molecules to the density of states. For this reason a procedure very similar to that introduced by Puschnig et al. [PRU+11] is applied which uses the fitting function $F(k_x, k_y, E_b)$ described in equation (3.1) for a least square

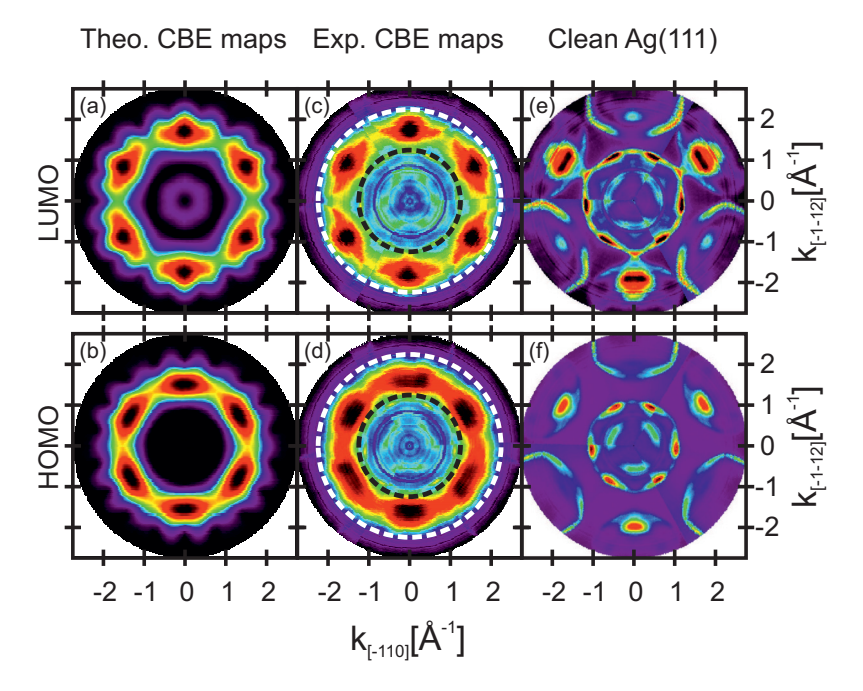


Figure 3.5: Calculated (a,b) and measured (c,d) CBE maps of the LUMO and HOMO level, respectively, for the monolayer structure of PTCDA/Ag(111) (see also Ref. [SWR+12]). Calculated maps consider surface symmetry and different molecular orientations (compare with Fig. 3.4). Experimental maps were recorded for $E_{\rm b}=0.3\,{\rm eV}$ (c) and $E_{\rm b}=1.6\,{\rm eV}$ (d). In panels (e) and (f) the experimental maps of the clean Ag(111) surface recorded at the same binding energies are included as a reference.

fitting of the measured APRES intensity $I(k_x, k_y, E_{\rm b})$.

$$F(k_x, k_y, E_b) = \sum_{i} a_i(E_b) \Phi_i(k_x, k_y) + b(E_b) I_{sub}(k_x, k_y, E_b) + c(E_b)$$
(3.1)

This function consists of a linear combination of all calculated orbital momentum maps $\Phi_i(k_x,k_y)$, that may contribute to the ARPES data, and an additional term $I_{\rm sub}(k_x,k_y,E_{\rm b})$ for the substrate induced background. The latter was obtained experimentally from a clean Ag(111) surface and included in the fitting in order to account for the substrate contribution to the ARPES intensity. Furthermore $c(E_b)$ is an energy dependent offset function.

Based on the linearity of the optimization problem, the adjustment of the fitting parameters $a_i(E_{\rm b}), b(E_{\rm b})$ and $c(E_{\rm b})$ is performed individually for each binding energy. The coefficients $a_i(E_{\rm b})$ represent the actual results. They can be understood as the (energy resolved) con-

tribution of the individual molecular orbital to the photoemission intensity and hence as the density of states projected onto the corresponding molecular orbital (projected density of states, PDOS) [PRU+11]. This is correct as long as the concerned orbitals are far enough from the Fermi level. If this condition is not fulfilled, as in the case of the (former) LUMO state, the fitting result $a_{\text{LUMO}}(E_{\text{b}})$ must be divided by the Fermi distribution function in order to obtain the correct PDOS. For a properly normalized APRES data cube the coefficient $b(E_{\text{b}})$ should reflect the (energy resolved) damping factor of the substrate signal by the organic layer and should consequently reveal a constant curve with a value smaller than 1. For each binding energy E_{b} the fitting was only performed on that part of the experimental data containing the intense molecular features. It has the shape of a ring covering the range $|\mathbf{k}_{||}| = 1.25 \,\text{Å}^{-1} \cdots 2.25 \,\text{Å}^{-1}$ and is marked in Fig. 3.5(c) and (d) by two concentric dashed circles (black and white color is used for improving visibility). For smaller $|\mathbf{k}_{||}|$ only very weak molecular features appear which are superimposed by strong substrate bands. Neglecting that part makes the fit much more stable and avoids artifacts stemming from the substrate bands without compromising the results.

In Fig. 3.6 the results of the orbital tomography analysis are presented for the monolayer film of PTCDA on Ag(111). The PDOS $a_{\rm HOMO}$ and $a_{\rm LUMO}$ for both molecules A and B are shown as a function of binding energy $E_{\rm b}$, in the case of the LUMO after dividing by the Fermi distribution function for an effective temperature of $T_{\rm eff} = 930 \, \rm K$. This is the reason for these curves exceeding the integrated ARPES intensity for the former LUMO in the vicinity of the Fermi energy. The temperature $T_{
m eff}$ is not a real temperature. It also accounts for the broadening of the Fermi distribution function due to the experimental resolution of $\sigma_{\rm res} = 150\,{\rm meV}$. The integrated PES intensity for the entire circular disc is also shown in gray. The latter would be the data obtained in a conventional photoemission experiment and shows no indications for an energy splitting of the orbitals for both molecules, neither for the HOMO nor for the LUMO. However, the result of the deconvolution algorithm reveals that molecule B has higher binding energies for both orbitals. While a relatively small difference of 40 meV was found between the HOMO levels of both molecules, the difference between the LUMO peaks is much larger: 170 meV. These differences in the binding energies of the electronic states of molecules A and B stem from the complex interplay between intermolecular and molecule-substrate interactions. The substrate parameter $b(E_{\rm b})$ as well as the offset $c(E_{\rm b})$ are shown in Fig. 3.6. Both reveal a continuous curve which indicates a proper treatment of the background of the experimental data. While the substrate scaling factor $b(E_b)$ is more or less constant for the HOMO region, it shows for the LUMO a shape comparable to the Fermi distribution function. The latter is caused by an artificial intensity in the substrate data cube $I_{\text{sub}}(k_x, k_y, E_{\text{b}})$ for binding energies above the Fermi level. In order to suppress this signal, the scaling factor $b(E_b)$ decreases significantly when crossing the Fermi energy. The offset $c(E_h)$ shows a peak at almost the same binding energy as the angle integrated

photoemission signal, which is due to an enhanced background in the vicinity of the arising molecular features in the momentum maps.

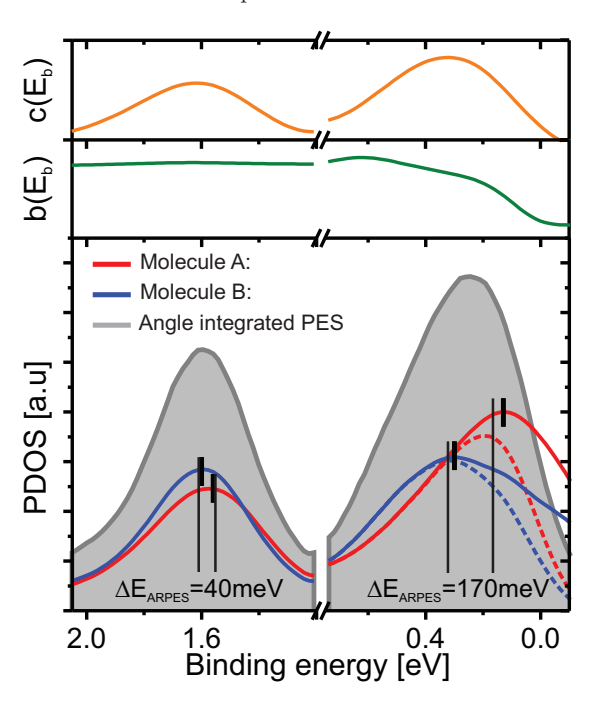


Figure 3.6: Orbital projected density of states (PDOS) curves of the HOMO and LUMO level for both molecules in the PTCDA monolayer structure obtained by the orbital tomography analysis of the ARPES data (see also Ref. [SWR+12]). While the dotted curves for the LUMOs show the fitting parameters a_i , the solid curves are divided by the Fermi distribution function for an effective temperature of 930 K. The gray-shadowed curve represents the ARPES data integrated over the ring in k-space which was used for fitting. Peak positions in the PDOS curves are indicated by vertical markers. Short thick and long thin lines mark the peak positions obtained from ARPES (this work) and STS (Ref. [KTH+06]), respectively. In addition, the substrate parameter $b(E_{\rm b})$ and the offset $c(E_{\rm b})$ are also included.

The results of the tomographic deconvolution are now compared with scanning probe data. Kraft et al. [KTH+06] reported STS measurements that resolve both HOMO and LUMO resonances (they label them "L1" and "L2", respectively) in their spectra for both molecules. They report very similar peak positions and shifts as found in the present study by ARPES and orbital tomography (peak positions are marked in Fig. 3.6 as vertical lines): The difference between molecule A and B for the LUMO resonance is 160 meV (170 meV for the orbital tomography analysis), for the HOMO the values are even identical (40 meV) within experimental errors. Even aspects of the lineshape are in agreement in the case of the LUMO states.

Consequently, the agreement between the STS and ARPES results is excellent. Since both methods are known to be well comparable regarding energy positions of molecular orbitals (in contrast to, e.g., transport gap measurements) [KHT⁺08], this agreement emphasizes the high reliability of the orbital tomography approach, also for adsorbate systems on highly symmetric surfaces with a variety of rotational and corresponding mirror domains.

The different binding energies of the molecular orbitals of PTCDA molecule A and B were already discussed by Rohlfing et al. [RTT07] based on DFT calculations for the freestanding PTCDA monolayer structure. Even when the silver surface is neglected, the positions of both PTCDA molecules in the unit cell are not equivalent. This is caused by the not precisely rectangular unit cell of the PTCDA monolayer structure ($\gamma \approx 89^{\circ}$). This results in different lengths of the hydrogen bonds $O(A)\cdots H(B)$ and $H(A)\cdots O(B)$ between the molecules A and B, which in turn is reflected in higher binding energies for the orbitals of molecule B in the freestanding PTCDA layer [RTT07]. This theoretical prediction matches nicely the PDOS obtained by the orbital tomography. When the substrate is additionally taken into account, the binding energy difference in the electronic states is inverted in the calculations. However, these calculations are less reliable than those for the freestanding film. The experiment does not show such an inversion of energetic peak positions, but higher binding energies for the orbitals of molecule B, similar to the case of the freestanding layer. Hence the energetic positions of the orbitals are more strongly effected by the hydrogen bonds to the neighboring molecules than by the interaction with the surface.

Although a remarkable agreement could be achieved between the STS data and the orbital tomography results, the reliability of the latter method has not been discussed yet. We have tested two different approaches in order to estimate the experimental error bars. While the first one is based on a Monte Carlo simulation of the statistical uncertainty of the experimental ARPES count rates, the second utilizes the linear regression algorithm which is used for the tomographic deconvolution procedure. Therefore, the fitting function introduced in equation (3.1) is rewritten in the form

$$F(k_x, k_y, E_b) = \sum_{i=1}^{p} \alpha_i(E_b) f_i(k_x, k_y).$$
(3.2)

The parameter p describes the number of independent fitting parameters α_i which is 4 in the present case. The fitting parameters α_i are identified as $\alpha_1 = a_A(E_b)$, $\alpha_2 = a_B(E_b)$, $\alpha_3 = b(E_b)$ and $\alpha_4 = c(E_b)$ and present scaling factors for the predefined functions $f_i(k_x, k_y)$. These are identified as the theoretical momentum maps $(f_1 = \Phi_A(k_x, k_y))$ and $f_2 = \Phi_B(k_x, k_y)$, as measured substrate data $(f_3(k_x, k_y)) = I_{sub}(k_x, k_y)$, and as k-independent background $(f_4 = 1)$. The fitting is performed on a discrete, equidistant 2D-grid in k-space with M

grid-points and minimizes

$$\chi^2 = \sum_{k=1}^{M} w_k \left[I(k, E_b) - F(k, E_b) \right]^2.$$
 (3.3)

Note that k is here used as an index numbering all grid points (k_x, k_y) . The weights w_k result from the Poisson-distributed counting statistics, thus w_k is given by the inverse of the corresponding variance which in turn is proportional to the intensity at the k-th data point, $w_k = 1/I_k$. M usually describes the number of available data points used in the fitting algorithm. However, this is not true in case of the orbital tomography technique. The experimental ARPES data are recorded for an equally spaced range of polar and azimuthal angles (ϑ, φ) and then transformed onto an equidistant k-space grid considering the threefold symmetry of the silver fcc(111) surface. This results in a larger number of data points in the intensity cube $I(k_x, k_y, E_b)$ compared to the raw data. As discussed below, this would artificially reduce the uncertainty of the orbital deconvolution. Hence, for a proper error analysis, the theoretical momentum maps $\Phi_A(k_x, k_y)$ and $\Phi_B(k_x, k_y)$ have to be transformed to the spherical coordinate system (ϑ, φ) of the raw data. Alternatively, the entire fitting procedure can be performed within the spherical coordinate system, which proved to give very similar results for the PTCDA monolayer film on Ag(111).

In the first approach for calculating the uncertainties of the fitting parameters $\alpha_i(E_b)$, a Monte-Carlo based error analysis is used. A reference CBE data map is created from the fitting result, i.e., calculated $F(\vartheta, \varphi, E_b)$ values fitting best to the experimental data. This reference momentum map represents the "ideal", noiseless intensity distribution of an ARPES experiment. The experimental noise is now simulated by adding a certain, arbitrary offset to each (ϑ, φ) point of this reference CBE map. This offset is calculated individually for each point in the map using a random number generator according to a normal distribution with standard deviation \sqrt{N} , where N is the count rate of that individual point. For high counting rates this corresponds very well to the expected Poisson distributed noise of the spectral data. The result is a reference CBE map with artificial noise which is now fitted as described above, just as if it were experimental data. The resulting fit parameters $\alpha_i(E_h)$ will deviate from the original result since the reference map was modified by noise based on the experimental count rate. This procedure of calculating and fitting "noisy" data is now repeated many, e.g., 15 times, resulting in 15 different values for each fit parameter. Hence, the uncertainty of the fit parameters can simply be calculated as the statistical error for each of them, i.e., as the standard deviation of the fit parameter's distribution.

This Monte Carlo error analysis for the adsorbate system PTCDA/Ag(111) results in error bars which are only in the range of 2% for all fitting parameters. This small error is due to the fact that the statistical noise does not strongly change the overall shape of the mo-

mentum map which has much more influence on the fitting result than the variation in the intensity of individual data points, as long as the variations are noise-like and not correlated or of systematic nature. The latter could be caused by the use of not ideal fitting pattern f_i , which can only be detected by the residual of the fitting procedure (which is also reflected by χ^2 in equation (3.3)), but not in the uncertainties calculated by the Monte Carlo approach.

Such systematic errors are better treated by our second, alternative approach for calculating the errors in $\alpha_i(E_b)$. Here, we take advantage of the fact that all fitting parameters enter equation (3.3) linearly. This allows to solve the system of equations for each energy slice E_b separately. This system of equations has the form

$$\sum_{j} N_{ij} \alpha_j = v_i. \tag{3.4}$$

For a given energy slice, the matrix N_{ij} and the vector v_j are thus given by summing over all M discrete $\{\vartheta, \varphi\} \equiv \Omega$ points

$$N_{ij} = \sum_{\Omega=1}^{M} w_{\Omega} f_i(\Omega) f_j(\Omega)$$
(3.5)

$$v_i = \sum_{\Omega=1}^{M} w_{\Omega} f_i(\Omega) I(E_b, \Omega), \qquad (3.6)$$

By inverting Eq. (3.4), the desired orbital-projected DOS $a_A(E_b)$ and $a_B(E_b)$, as depicted in Fig. 3.6, as well as the substrate contribution $b(E_b)$ and the background $c(E_b)$ can be obtained. In addition to these results, their respective error bars can be estimated by applying the standard expressions for uncertainty in the model parameters [Wol06]. For the linear fit, the normal matrix N_{ij} is defined as the curvature matrix of χ^2 with respect to the fit parameters α_i ,

$$N_{ij} = \frac{1}{2} \frac{\partial^2(\chi^2)}{\partial \alpha_i \partial \alpha_j},\tag{3.7}$$

is equal to Eq. (3.5). The standard deviations σ and the correlations ρ between the fit parameters are obtained from covariance matrix C_{ij} given by the inverse of the normal matrix multiplied by the sum of least squares χ^2 over the degrees of freedom (M-p)

$$C_{ij} = \frac{\chi^2}{M - p} [N]_{ij}^{-1}. \tag{3.8}$$

Then, the standard deviations of the model parameters α_i are given by the square root of the diagonal terms

$$\sigma_{\alpha_i} = \sqrt{C_{ii}} \tag{3.9}$$

and the correlations between the fit parameters can be analyzed from

$$r_{ij} = \frac{C_{ij}}{\sqrt{C_{ii}C_{jj}}} = \frac{[N]_{ij}^{-1}}{\sqrt{[N]_{ii}^{-1}[N]_{jj}^{-1}}}.$$
(3.10)

Values of r_{ij} are in the range from -1 to +1, where $r_{ij}=0$ indicates uncorrelated model parameters α_i and α_j . The last conversion illustrates that the correlation between the fitting parameters only depends on the theoretical momentum maps used in the fitting procedure. Performing this second approach of the error analysis of the orbital tomography results in relative errors for all fitting parameters of also 2%, and therefore agrees very well with the Monte Carlo approach. The correlation factors are relatively high, $r_{AB}=-0.42$ for the LUMO and $r_{AB}=-0.68$ for the HOMO. However, the reason for rather small errors is here the very large number of grid points M which appears in the denominator of eq. (3.8). Within the ring in k-space, which was used for fitting the ARPES data more than M=6000 data points were measured.

In conclusion, this section did not only explain in detail the ARPES data evaluation by the orbital tomography procedure, it also provides substantial evidence that this method is not limited to low symmetric surfaces. It has proven that the angle resolved photoemission pattern arising from molecular films adsorbed on the more complex fcc(111) surfaces can also be analyzed. This was shown for the example of HOMO and (former) LUMO states of two symmetrically inequivalent PTCDA molecules in the unit cell of its monolayer structure on Ag(111). The resulting projected densities of states revealed an excellent agreement with scanning tunneling spectroscopy results reported earlier [KTH+06]. In addition, the experimental error of the orbital tomography method was estimated by two different approaches. One simulates the experimental uncertainty caused by counting statistics in the ARPES measurement in a Monte Carlo approach, the second is based on the linear regression algorithm used for the tomographic deconvolution. Both approaches yield a relative uncertainty of the method of only $\approx 2\,\%$.

The proof that the orbital tomography is also applicable for p3m1-symmetric surfaces is crucial for the study of hetero-organic systems on the Ag(111) surface. In chapter 4 and 5, this method allows to assign resonances in the UPS spectra to molecular orbitals and hence enables an unambiguous classification of the charge redistribution at the mixed organic-metal interface.

3.2 CuPc/Ag(111)

The CuPc molecule ($C_{32}N_8H_{16}Cu$) is a derivative of the metal free H_2 -phthalocyanine (or tetrabenzoporphyrazine) and consists of an inner pyrrole ring which is terminated symmetrically by four benzene rings [McK98]. The cavity in the center of the molecular core is filled with a copper atom which is chemically bond to the organic body of the molecule. The resulting structure of the CuPc molecule is shown in Fig. 3.7 in a top and side view. Since the size of the copper atom is smaller than the molecular cavity, it can be completely included into the molecular plane. As a consequence, CuPc is planar and does not exhibit a dipole moment perpendicular to the molecular body. The electronic structure of CuPc is dominated by delocalized π -orbitals which expand mainly over the pyrrole and benzene rings.

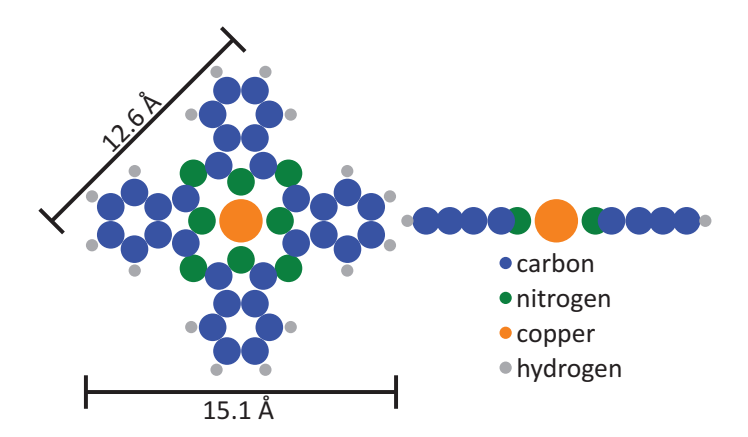


Figure 3.7: Chemical structure of CuPc shown in a top (left) and side view (right) of the molecular body.

In the following, the main aspects of the growth behavior of CuPc on the Ag(111) surface are summarized in section 3.2.1. Furthermore, new experimental photoemission results are presented in section 3.2.2.

3.2.1 A short introduction

The adsorption behavior of CuPc on different noble metal surfaces, and in particular on Ag(111), is very well characterized by various experimental techniques [LWM⁺89, Krö11, KLS⁺09, KSS⁺10, KSK⁺11, SKRK11, Koc09]. This section summarizes the most important findings for CuPc/Ag(111) which are crucial for the discussion of the formation of heteroorganic thin films in the chapters 4,5 and 6.

In contrast to the adsorption of PTCDA/Ag(111) the structural phase diagram of CuPc/Ag(111) reveals a variety of different structures. For coverages below $\Theta_{\text{CuPc}} < 0.75\,\text{ML}$ no ordering of the molecules can be observed. At RT, the molecules diffuse over the surface and form a 2D gas with an average intermolecular distance which decreases continuously with rising coverage. At LT, the molecular motion is reduced and the molecules relax into their favored adsorption site and orientation. This is obvious when considering the LT-STM image in Fig. 3.8(a). Although the lateral positions of the molecules seem to be random, only three distinct orientations of CuPc with respect to the substrate are visible. This leads to the conclusion that the CuPc molecules arrange along silver rows of the substrate at low temperature. Increasing the CuPc coverage up to 0.89 ML results only in a higher density of CuPc in the 2D gas phase at RT. Below $T_{\text{sample}} = 130\,\text{K}$, however, the disordered gas transforms to an ordered commensurate structure with one CuPc molecule per unit cell. The commensurability of the structure proofs that all CuPc molecules condense into the same adsorption site at low temperature.

In the remaining coverage regime between $\Theta_{\text{CuPc}} = 0.89\,\text{ML}$ and $\Theta_{\text{CuPc}} = 1.00\,\text{ML}$, the CuPc molecules form also ordered structures at room temperature. The LEED pattern of the monolayer structure is shown in Fig. 3.8(b). Besides the monolayer structure itself, a variety of ordered point-on-line (p.o.l.) structures are observed in this coverage regime. The unit cell of these lattices shrinks continuously with increasing CuPc coverage which was interpreted as evidence for a repulsive intermolecular interaction between the CuPc molecules [KSS⁺10] (see pannel (c)). A similar behavior was also found for other phthalocyanine molecules on Ag(111) [SHK⁺09, Krö11, KBB⁺12] and can be explained by an optimization of the total interface potential. Adsorbing more phthalocyanine molecules results in an additional adsorption energy gain for the adsorbate system due to the increased number of molecules in contact with the surface, and an energy loss due to the distortion of the adsorbate lattice caused by a less favored adsorption configuration of each individual molecule. As long as this leads to an total energy gain for the metal-organic system, more molecules can be adsorbed on the surface. At $\Theta_{\text{CuPc}} = 1.00\,\text{ML}$, additional molecules would result in such an energetically unfavored situation. Hence, no more molecules are included into the first organic layer.

The adsorption heights of CuPc on Ag(111) and their dependence on coverage and temperature were studied in detail by the XSW-method [KSS+10]. The resulting adsorption geometry for CuPc in the monolayer structure is illustrated in Fig. 3.8(d) by a schematic side view of the molecule. The CuPc molecule adsorbs in a flat geometry on Ag(111) and reveals almost no distortion of the planar molecular body. Only the Cu-atom is located below the molecular plane. The vertical distance of the molecule to the silver surface is smaller than the sum of the van der Waals radii [Bon64] of all molecular components and silver which indicates a chemical interaction between the molecule and the surface. Panel (e) shows how the CuPc

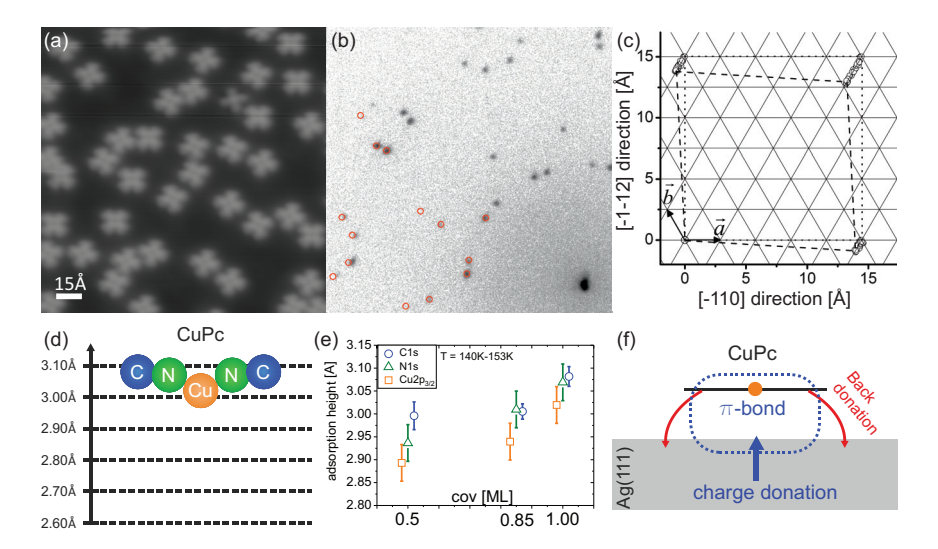


Figure 3.8: (a) LT-STM image of a disordered CuPc sub monolayer film ($U_{\rm Bias}=0.34\,{\rm V},~I=0.02\,{\rm nA},~T_{\rm sample}=5\,{\rm K}$). (b) LEED pattern of the CuPc monolayer film on Ag(111) ($E_{\rm kin}=27.2\,{\rm eV}$). (c) Position of the unit cell corners for all p.o.l. superstructures in the coverage regime between $\Theta_{\rm CuPc}=0.89\,{\rm ML}$ and $\Theta_{\rm CuPc}=1.00\,{\rm ML}$ [Krö11]. (d) Vertical adsorption position of CuPc in the monolayer structure at RT. (e) Adsorption heights of all CuPc components as a function of CuPc coverage [Krö11] for LT films. (f) Schematic model of the interaction channels between CuPc and the Ag(111) surface. Panels (c) and (e) are taken from [Krö11].

adsorption height changes dependent on the coverage. Increasing the CuPc coverage results in a lifting of all atomic species and hence in a reduction of the bonding strength. This behavior can be correlated to the local adsorption geometry of the CuPc molecule. At low CuPc coverage, the molecules are isolated from each other and can adsorb in their favored configuration. Adding more CuPc molecules to the film increases the packing density of the layer and finally leads to a transformation into an ordered structure. In this ordered film the orientation of the CuPc molecules with respect to the substrate is different than in the disordered layer [MEP+07] and the molecular wings are no longer aligned along substrate rows. This sterically induced rotation leads to a reduced overlap of molecular wave functions with substrate states and hence weakens the interaction of the molecule with the substrate.

Putting all findings together to a model for the interaction leads to the schematic picture in Fig. 3.8(f). The low adsorption distance of CuPc on the silver surface indicates a chemical π -bond between the molecule and the silver surface. This bond leads to a charge transfer into the CuPc LUMO level, which is experimentally proven in section 3.2.2. In contrast to the adsorption of PTCDA on Ag(111), no local bond is formed between CuPc and the silver

surface.

In a local picture, this charge donation and back donation can also explain the intermolecular repulsion in the ordered p.o.l.-structures. The molecules compete for the charge in the substrate in order to gain more adsorption energy by filling more charge into their LUMO levels. This competition leads to a maximization of the intermolecular distance between the CuPc molecules in the film which manifests itself in the continuously shrinking unit cells with rising CuPc coverage.

The adsorption of CuPc on Au(111) [SKRK11] shows neither charge transfer into the molecule nor a continuously shrinking unit cell size close to the first closed layer. The comparison between the structure formation of CuPc on Ag(111) [KSS+10] and Au(111) [SKRK11] clearly proves that the repulsive intermolecular interaction is mediated by the charge transfer from the silver surface to the CuPc molecule.

3.2.2 The electronic structure of CuPc/Ag(111): New results

A charge transfer into the LUMO of CuPc upon adsorption on Ag(111) was already reported earlier [KSS+10]. We now studied this system also with the orbital tomography approach. This does not only allow to confirm the assignment of the spectroscopic features found in UPS to molecular orbitals, but also provides information on the in-plane orientation of the molecule on the surface.

The shape of the CuPc HOMO and LUMO is shown in Fig. 3.9(a)+(b) for a free molecule (DFT calculation, B3LYP, basis set: LANL2DZ [FTS⁺]). The HOMO reveals the same fourfold symmetry as the molecule itself. The CuPc LUMO consists of two degenerated states, the square of its wave function exhibits only a twofold symmetry. The wave function of one of the LUMO orbitals is shown in Fig. 3.9(b), the other one is rotated by 90° . The degeneracy of the LUMO states is present in the gas phase and can be lifted by adsorbing CuPc on surfaces [KLS⁺09], an effect that can strongly influence the intermolecular interaction [SKRK11]. The corresponding theoretical momentum maps for a single molecular orientation are shown in Fig. 3.9(c)+(d) and exhibit the same symmetry as the square of the orbital wave functions. The LUMO momentum map does not only show circular emission features but also stripes at high emission angles (high k-space values), which makes this emission pattern distinguishable from the PTCDA LUMO k-space map. This will become important in chapter 4, where the electronic structure of laterally mixed layers of CuPc and PTCDA are discussed.

In order to analyze the angle resolved photoemission pattern arising from the CuPc monolayer structure on Ag(111), the relative orientation of the CuPc molecule in the unit cell has to be considered. An STM study of the CuPc monolayer film at RT revealed that the CuPc molecule is rotated by $5-8^{\circ}$ with respect to the [$\bar{1}01$] (or equivalent) substrate directions [MEP⁺07].

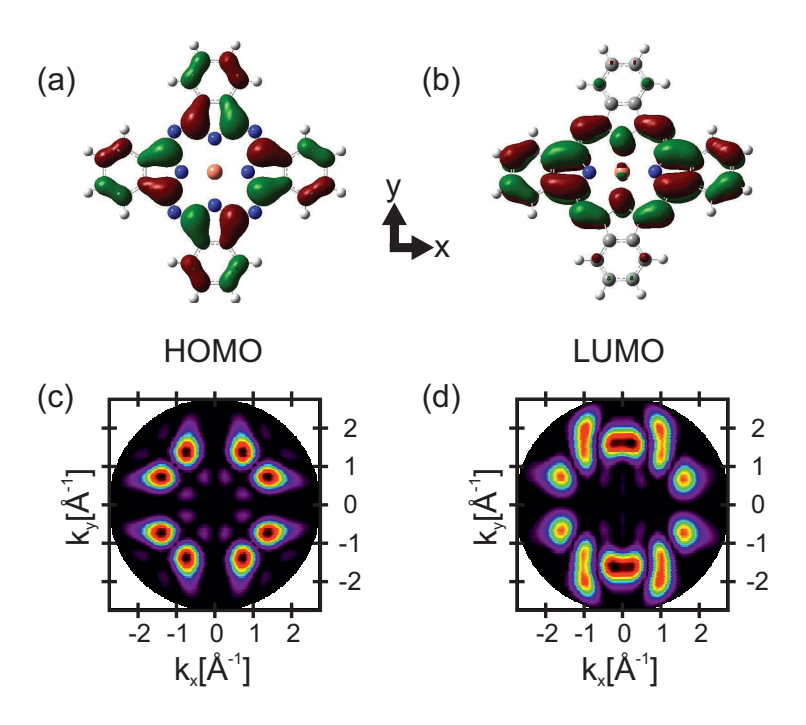


Figure 3.9: Shape of the CuPc HOMO (a) and LUMO (b) level calculated for a free molecule in the gas phase (DFT calculation, B3LYP, basis set: LANL2DZ [FTS⁺]). Similar colors in the orbital surfaces reefer to similar signs of the orbital wave function. The corresponding momentum maps calculated for the CuPc HOMO and LUMO level are shown in panels (c) and (d) respectively.

Taking into account the p3m1 symmetry of the substrate surface and a relative angle of 5° between the [$\bar{1}01$] silver direction and the CuPc molecule results in the momentum maps for the HOMO and LUMO emission shown in Fig. 3.10(a)+(b). The emission pattern of the CuPc HOMO exhibits twelve distinct maxima at a distance of $k_r = 1.55\,\text{Å}^{-1}$ from the $\bar{\Gamma}$ -point of the surface Brillouin zone which are found on an homogeneous circular background. This background arises from the slight misalignment of the molecules with the high symmetry directions of the substrate. In contrast, the LUMO momentum map only reveals six broad maxima which are separated by less intense side lobes at a distance of $k_r = 2.15\,\text{Å}^{-1}$. The latter features arise from the elongated emission maxima in Fig. 3.9(d). Note that the momentum distribution of the LUMO level is based only on one of the degenerated LUMO state. This is reasonable, since lifting of the degeneracy is expected upon adsorption on the surface. The LUMO, which is aligned with the high symmetry direction of the substrate hence interacts more strongly. Therefore, we have selected this orbital for our ARPES analysis.

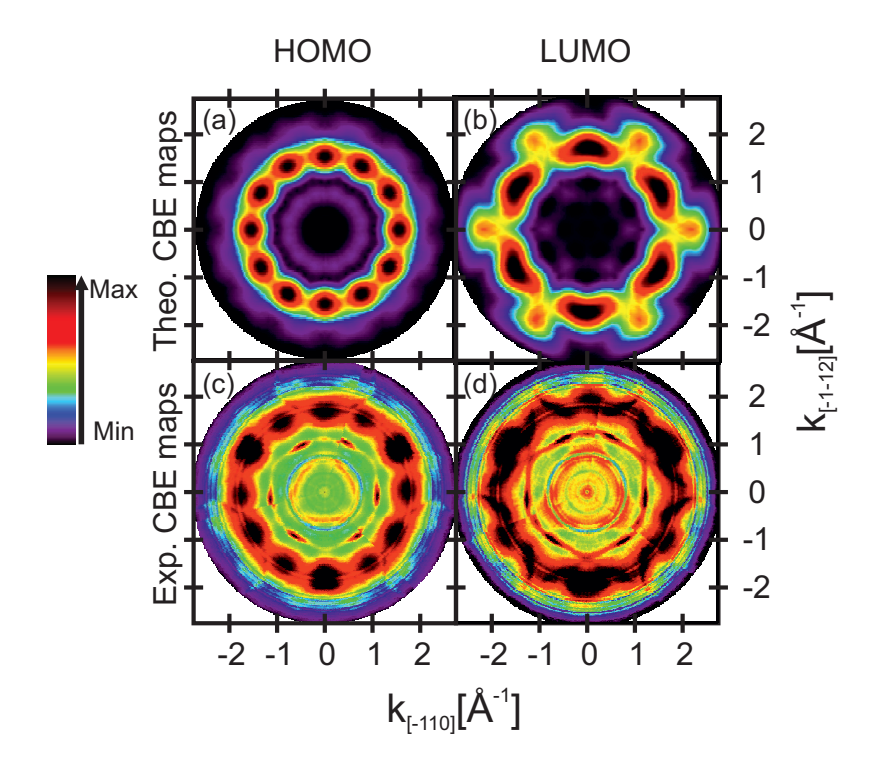


Figure 3.10: Calculated (a,b) and measured (c,d) CBE maps of the HOMO and LUMO level, respectively, for the monolayer structure of CuPc/Ag(111). Calculated maps account for the surface symmetry and the molecular orientations of CuPc reported by STM [MEP+07]. For the LUMO CBE maps, only one of the degenerated LUMO states is considered. Experimental maps were recorded for $E_{\rm b}=1.3\,{\rm eV}$ (c) and $E_{\rm b}=0.2\,{\rm eV}$ (d).

In Fig. 3.10(c)+(d) the corresponding experimental CBE maps are shown for a binding energy of $E_b=1.3\,\mathrm{eV}$ (c) and $E_b=0.2\,\mathrm{eV}$ (d). The momentum distribution at higher binding energy (c) can clearly be assigned to the CuPc HOMO state. The experimental emission pattern does not only exhibit twelve clear emission features like predicted by the modeled CBE map for the HOMO level. It also reveals the homogeneous ring feature underneath the emission spots which confirms that the CuPc molecules are slightly rotated with respect to the high symmetry direction of the Ag(111) surface. The fact that three emission features show a higher intensity compared to the others is caused by a superposition of the molecular PES signature and the substrate signal. The experimental k-space cut at $E_b=0.2\,\mathrm{eV}$ (d) reveals only six clear maxima which are arranged on a circle around the $\bar{\Gamma}$ -point of the surface Brillouin zone. This finding reflects nicely the theoretical momentum distribution of the CuPc LUMO for the molecules in the monolayer structure. The different relative intensities

of the emission maxima in the experimental data (Fig. 3.10(d)) can again be explained by the substrate emission signature at certain directions in k-space. In addition, weaker photoe-mission maxima are found between the substrate bands at a distance of $k_r \approx 2 \,\text{Å}^{-1}$. They can be attributed to the side slopes of the CuPc LUMO map. It can be concluded, that the photoemission resonance close to the Fermi level is caused by the CuPc LUMO state which is populated by the interaction with the silver surface [KSS⁺10]. Furthermore, it should be noted that the experimental emission pattern of the LUMO level matches the theoretical CBE map which is calculated from only one of the degenerated LUMO levels of the CuPc molecule. This indicates, that charge is predominantly transferred from the substrate into one LUMO, namely that one located close to a row of silver atoms. Hence the CuPc LUMO is also asymmetrically populated by the interaction with the Ag(111) surface, quite similar to the case on Cu(111).

The modification of the surface potential Φ upon the adsorption of organic molecules yields crucial information about the charge redistribution at the metal-organic interface. Therefore, the work function of the CuPc/Ag(111) interface was determined from the binding energy position of the secondary electron cutoff in a photoemission experiment. The resulting work functions are summarized in Fig. 3.11 as a function of CuPc coverage. Increasing the amount of CuPc on Ag(111) leads to a continuous decrease of the work function. At $\Theta_{\text{CuPc}} = 1.00\,\text{ML}$, the surface potential barrier is reduced by $\Delta\Phi = (0.50 \pm 0.03)\,\text{eV}$ compared to the bare silver surface and reaches a value of $\Phi = (4.10 \pm 0.02)\,\text{eV}$. In order to understand this behavior the two main effects, contributing to the modification of the work function have to be discussed [RNP+09, RGW+10, FGGM+11]: The push-back or cushion effect which leads to a decrease of the surface potential, and the direction and amount of the charge transfer at the metal-organic interface. An effective charge transfer into the molecule results in a higher surface potential barrier while an effective charge transport into the metal leads to a lower work function of the metal-organic interface.

Since the CuPc molecules do not form ordered islands at low coverages, the molecular density on the surface increases continuously with rising CuPc coverage. In fact, it could be proven that the surface area per molecule is inverse proportional to the coverage of the molecules on the surface [KSS+10]. This is consistent with a maximum intermolecular distance in the 2D gas phase. For the work function, we also found a proportional relation to the inverse coverage. In the inset of Fig. 3.11 the work function Φ is plotted versus the inverse coverage which in turn is proportional to the area per molecule on the surface. This linear relation which we found leads to the conclusion that the changes in the work function can be attributed to the presence of molecules on the surface, even without considering the chemical interaction of the molecules with the surface. Hence, the continuous decrease of the work function is mainly caused by the push-back effect. Based on this finding it can be speculated that the

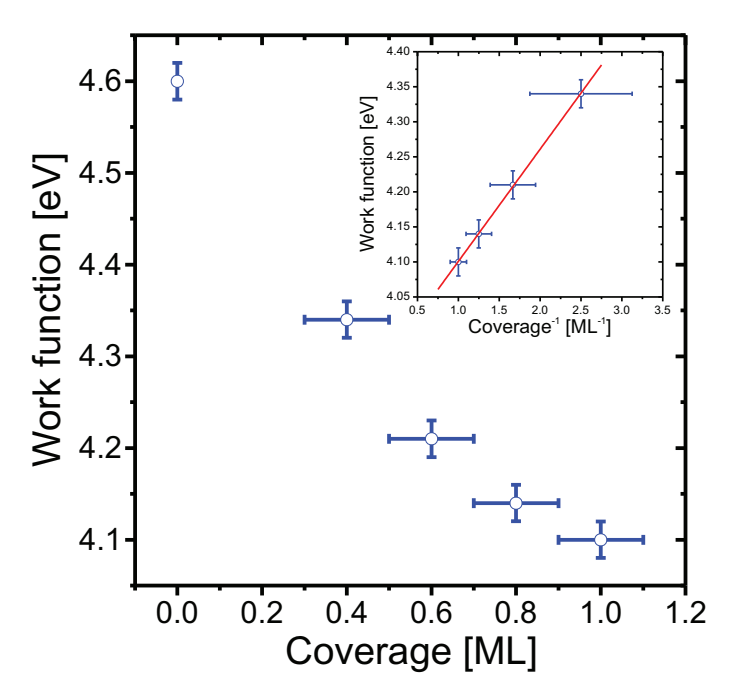


Figure 3.11: Work function Φ of the CuPc/Ag(111) metal-organic interface for different CuPc coverages. In the inset the same data are plotted versus the inverse coverage. The red line represents a linear least square fit to the experimental data.

effective charge transfer into the CuPc molecule is rather weak or even neglectable. This statement is supported by a comparison of CuPc/Ag(111) and the adsorption of PTCDA on the same surface. In the latter system the effective charge transfer of ≈ 0.35 electrons [RTT07] (≈ 0.47 electrons [RNP⁺09]) into each PTCDA molecule results in a surface dipole which can overcompensate the push-back effect of the molecule leading to an overall increase of Φ , an effect which was not observed for CuPc/Ag(111).

4 Lateral intermolecular interaction: CuPc and PTCDA on Ag(111)

The structure formation of the first mono-organic layer in direct contact with the underlying surface is determined by intrinsic property of the interface components and can only be modified by substituting either the surface material or the molecular species itself. This situation becomes much more flexible when hetero-organic thin films consisting of two different types of molecules are considered. These layers yield great potential to selectively tune the shape and size of the adsorbate lattice on a particular surface by changing the relative ratio of adsorbates on the substrate. Furthermore, the altered local environment of the molecules in the mixed film can modify the electronic level alignment of the mixed organic interface compared to mono-organic films. This may lead to new effects that have not yet been observed in mono-organic layers. In order to understand and predict the properties of hetero-organic layers, this chapter focuses on the formation of organic mixed films consisting of the two prototype molecules 3,4,9,10-perylenetetra-carboxylic-dianhydride (PTCDA) and copper-II-phthalocyanine (CuPc) adsorbed on the (111)-oriented surface of a silver single crystal.

The system CuPc and PTCDA on Ag(111) is well suited for this study since the properties of both molecules have been extensively investigated during the last decade. Additionally, the different intermolecular interactions on Ag(111) provide an interesting aspect to the mixed layer formation. While PTCDA reveals an attractive intermolecular interaction on this surface caused by an electrostatic moment on the molecule, CuPc molecules repel each other on Ag(111) [Tau07, KSS+10]. Furthermore, the bonding mechanisms between the molecules and the surface are slightly different for both species [HTS+10, RTT07]. In addition to a π -bond between the carbon backbone and the surface, PTCDA possesses a local bond between the carboxylic oxygen atoms and the underlying silver atoms. The latter results in a site specific bonding of the molecule and hence in the formation of commensurate structures. For CuPc the π -bond causes a competition between the molecules for the acceptance of charge from the substrate and thus results in a repulsive intermolecular interaction between the molecules. This interplay is reflected in a continuously shrinking superstructure unit cell with increasing coverage [SHK+09, KSS+10].

The influence of these different interaction mechanisms on the geometric and electronic prop-

erties of the mixed layer film is the main subject of this chapter.

In the first chapters, the lateral order of the hetero-organic structures, which was studied by high resolution low energy electron diffraction (SPA-LEED) as well as by scanning tunneling microscopy (STM), is discussed depending on the relative coverage of molecules. The alignment of the frontier orbitals in the mixed organic film was accessed by (angle resolved) photoelectron spectroscopy ((AR)PES) as well as scanning tunneling spectroscopy (STS) and is presented. Based on the results of the X-ray standing wave (XSW) technique, the modified interaction strength of the individual molecules with the substrate is introduced. Finally, a model is presented addressing the intermolecular interactions between both molecular species and their influence on the binding strength of the individual molecules with the surface.

4.1 Lateral order: Long range order and local adsorption geometry

The lateral order of mixed films consisting of CuPc and PTCDA on the Ag(111) surface is summarized in Fig. 4.1. Except for very low molecular coverages below 0.2 ML, new long ranged ordered structures are formed, which can be classified according to the relative molecular coverage. The total coverage for all these molecular films is less than or equal to a complete closed layer ($\Theta \leq 1.0\,\mathrm{ML}$). For CuPc coverages (Θ_{CuPc}) smaller than 0.40 ML and PTCDA coverages (Θ_{PTCDA}) larger than 0.50 ML the Mixed Brick Wall (MBW) structure is observed. The lattice of this structure is characterized by a commensurate superstructure containing two PTCDA and one CuPc molecule. Typically, this MBW structure coexists with islands of the bare PTCDA/Ag(111) monolayer structure, which is caused by an excessive supply of PTCDA molecules. Increasing the CuPc coverage up to 0.75 ML and using PTCDA coverages below 0.5 ML, the Mixed One-to-One (M1²1) phase is found. It contains one commensurate and one point-on-line structure with an almost square unit cell and an equal number of CuPc and PTCDA molecules. Finally for $\Theta_{\text{CuPc}} > 0.75\,\text{ML}$ and PTCDA coverages below 0.3 ML, the Mixed Zig-Zag (MZZ) phase is visible. Here, different structures with very large unit cells and two CuPc and one PTCDA molecule are found. Note that all mixed organic films do not reveal any altering of their lattice parameters when changing the sample temperature.

The relative number of molecules found in the mixed structures approximately reflects the coverage of molecules deposited on the surface. This finding indicates that the lateral order in hetero-organic structure can indeed be tuned by changing the relative molecular coverage. Furthermore, it should be mentioned that the formation of ordered structures even for coverages below one monolayer points to an island growth of the molecules and hence to an at-

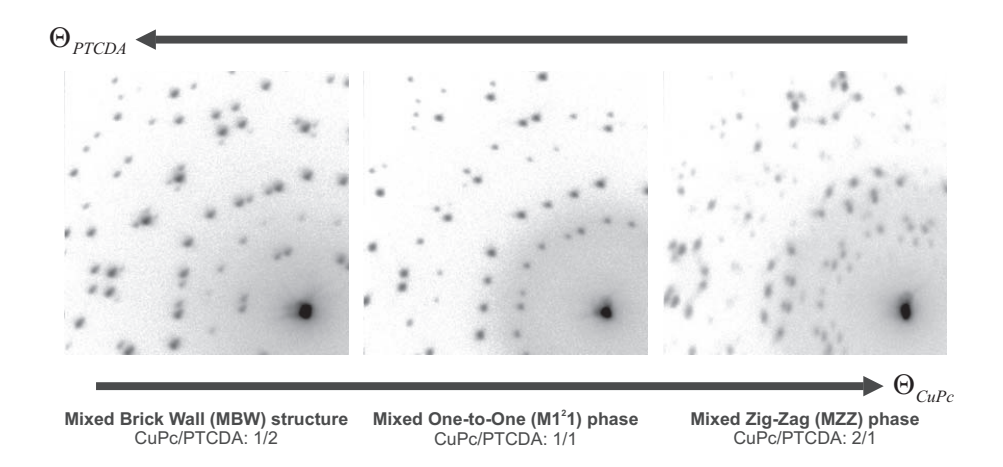


Figure 4.1: Schematic overview of the three different phases existing for different coverages of CuPc and PTCDA on Ag(111). The LEED patterns show the typical diffraction signature of the corresponding phase ($E_{\rm kin}=27.2\,{\rm eV}$).

tractive intermolecular interaction between CuPc and PTCDA. More details on all mentioned mixed organic structures are presented in the subsequent sections.

4.1.1 Modeling the CuPc-PTCDA interaction by pair potential calculations

Before presenting the different mixed structures, the interaction between a single CuPc molecule and a single PTCDA molecule is discussed in the framework of a pair potential approach [KSW+11, Krö11]. More technical details on this method can be found in chapter 2.5. Assuming a flat adsorption geometry of the molecules on the surface, the pair potential energy for all different orientations of CuPc and PTCDA were computed as a function of the lateral distance vector $\vec{r} = (\Delta X, \Delta Y)$ between the center of mass of the molecules. The different orientations Θ_z were achieved by rotating the PTCDA molecule around an axis perpendicular to the molecular plane through the center of mass of the molecule. The rotation angle is given by the angle between the long axis of the PTCDA molecule and the $(\Delta X, 0)$ -direction of the displacement vector. The other rotations around in-plane axes Θ_x and Θ_y as well as the vertical displacement ΔZ between the two molecules were fixed to zero.

In Fig. 4.2, the results of the pair potential calculations for five different orientations Θ_z are shown in form of potential maps. Each point of the map represents the pair potential energy as a function of the displacement vector $(\Delta X, \Delta Y)$ for a fixed relative orientation Θ_z . The color code illustrates the energies of the pair potential calculation with positive energies

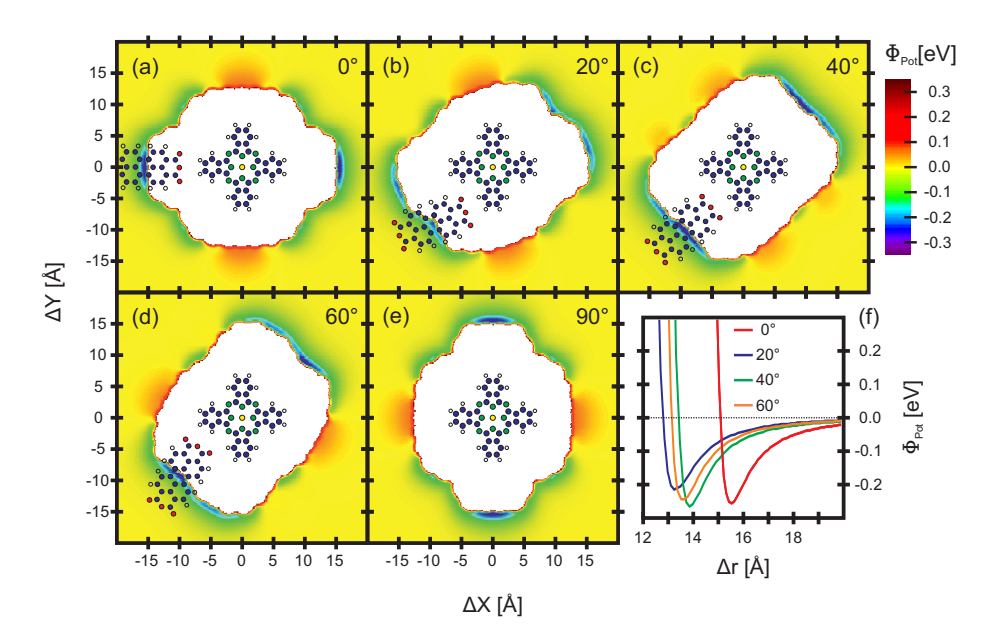


Figure 4.2: (a)-(e): Pair potential maps for different rotational orientations Θ_z between a CuPc and a PTCDA molecule. Red areas indicate regions of intermolecular repulsion and green/blue areas indicate attraction. Panel (f) shows radial line profiles along a line connecting the two molecules for different Θ_z cutting through the prominent potential minima.

depicted in red and negative energies in green and blue. All maps reveal that the interaction between CuPc and PTCDA is dominated by an attractive intermolecular interaction, which appears as large areas of negative potential in the maps. This is caused by an electrostatic attraction between the negatively charged oxygen atoms of the PTCDA molecule and the positive partial charge on the hydrogen atoms of CuPc. Although there are also regions with a repulsion between the molecules, these cover smaller areas in the potential maps. They arise from the electrostatic repulsion between the positively charged hydrogen atoms on both molecules. In conclusion, the interaction between CuPc and PTCDA can be described as mostly attractive.

The attraction between the molecules results in rather sharp and distinct potential minima for all relative orientations. Radial line profiles through the prominent minima for different relative orientations Θ_z are shown in Fig. 4.2 (f). The energy gain in these potential depressions is much larger than the thermal activation energy at room temperature. These potential minima trap PTCDA molecules in the vicinity of CuPc and hence lead to the formation of a mixed structure. The largest energy gain of 270 meV could be found for $\Theta_z=0\,^\circ$ and $\Theta_z=40\,^\circ$. This result for the mixed molecular system lies between the corresponding val-

ues for the interaction between two PTCDA molecules and two CuPc molecules, respectively [KSW⁺11, Krö11]. Note that although the intermolecular interaction between two CuPc molecules is repulsive for almost all intermolecular distances and relative orientations, several sharp potential minimal exist in the corresponding pair potential maps [KSW⁺11, Krö11]. The largest energy gain in those maps is taken as a reference. However, since the optimized distance between CuPc and PTCDA is smaller for $\Theta_z = 40^\circ$ than for 0° , this orientation can achieve a larger energy gain per surface area.

Since the overall interaction between CuPc and PTCDA can be described as attractive, the mixing of CuPc and PTCDA seems to be very likely from this very simple pair potential calculations. This aspect is even enhanced when considering a phase separation between CuPc and PTCDA. CuPc molecules interact by an intermolecular repulsion [KSW+11, SKRK11] leading to an energetic unfavored situation for the molecules. When forming a mixed film with PTCDA, the CuPc molecules can transform the intermolecular repulsion between each other into an attractive interaction with PTCDA. This results in an energy gain for the entire system.

4.1.2 Formation of mixed structures

In this section an overview is given over the formation of mixed structures in the adsorbate layer.

For very low coverages of CuPc and PTCDA ($\Theta < 0.2\,\mathrm{ML}$) no mixing of CuPc and PTCDA could be achieved, even though both types of molecules are present on the same terrace. Changing the sequence of molecular deposition or annealing the sample to 575 K does not result in a mixed structure. However, a real phase separation does not takes place, either. The edges of the PTCDA islands in Fig. 4.3 are decorated with CuPc molecules. This is a first indication for an attractive interaction between the two molecules. It is most probably caused by electrostatic attraction as discussed in the previous chapter 4.1.1. The molecular orientation is indicated for some PTCDA molecules at the island edge by atomic models in Fig. 4.3(b). Comparing the arrangement of CuPc molecules in contact with the edge molecules of the PTCDA island reveals similar orientations as described by the pair potential calculation in Fig. 4.2. The CuPc wings, which are terminated by positively charged hydrogen atoms, point towards the negatively charged oxygen groups of PTCDA. This supports the statement that the initial state of the mixed structure is activated by an electrostatic attraction between the molecules.

Nevertheless, the orientation of CuPc with respect to the substrate lattice is similar for molecules in the direct vicinity of the PTCDA island and molecules on the terraces. All CuPc molecules are aligned with one pair of wings along a row of silver atoms indicated by

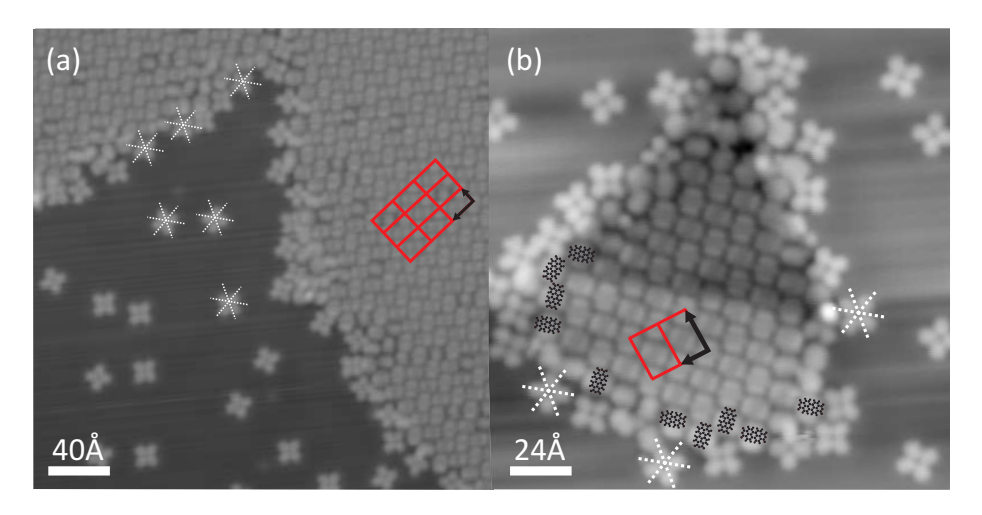


Figure 4.3: STM images of very low coverages of CuPc and PTCDA $\Theta < 0.2\,\mathrm{ML}$ ($U_\mathrm{Bias} = -0.34\,\mathrm{V},\,I = 0.1\,\mathrm{nA}$). The lattice of the PTCDA monolayer structure is indicated in red and the orientation of silver rows of the surface in white dashed lines. For this coverage no mixing of molecules could be achieved.

white dashed lines in Fig. 4.3. This leads to the conclusion that the intermolecular interaction is not strong enough to modify the orientation of the CuPc molecule with the underlying substrate.

For coverages $\Theta > 0.2 \,\mathrm{ML}$, the dynamic process of the mixed layer formation can be investigated in real time with SPA-LEED. This is illustrated in Fig. 4.4. At first, a certain amount of CuPc was deposited on the clean Ag(111) surface. The corresponding LEED images of the CuPc submonolayer films are shown in the left column of Fig. 4.4 for $\Theta_{\text{CuPc}} = 0.25 \,\text{ML}$, $\Theta_{\mathrm{CuPc}} = 0.60\,\mathrm{ML}$ and $\Theta_{\mathrm{CuPc}} = 0.85\,\mathrm{ML}$. The amount of CuPc can be determined from the radius of the diffuse diffraction ring, which reflects the average intermolecular distance of the CuPc molecules [KSS+10]. Subsequently, PTCDA molecules are deposited onto these three pure CuPc films. The LEED pattern corresponding to $50\,\%$ and $100\,\%$ of the final PTCDA covergae are shown in the center and the right column of Fig. 4.4. In all cases, the formation of a mixed structure can be observed. For the lowest CuPc coverage of $0.25\,\mathrm{ML}$ the Mixed Brick Wall structure is formed after depositing half of the total amount of PTCDA. Adding more PTCDA to the layer (LEED pattern right column), the diffuse diffraction signature of the bare CuPc film vanishes completely and additional pure PTCDA island are formed. This is indicated by the appearance of the typical triangles of PTCDA diffraction spots. For higher CuPc coverages ($\Theta_{\text{CuPc}} = 0.60 \,\text{ML}$ and $\Theta_{\text{CuPc}} = 0.85 \,\text{ML}$), the first diffraction spots appear in the lower part of the LEED images in the middle column. Increasing the PTCDA coverage

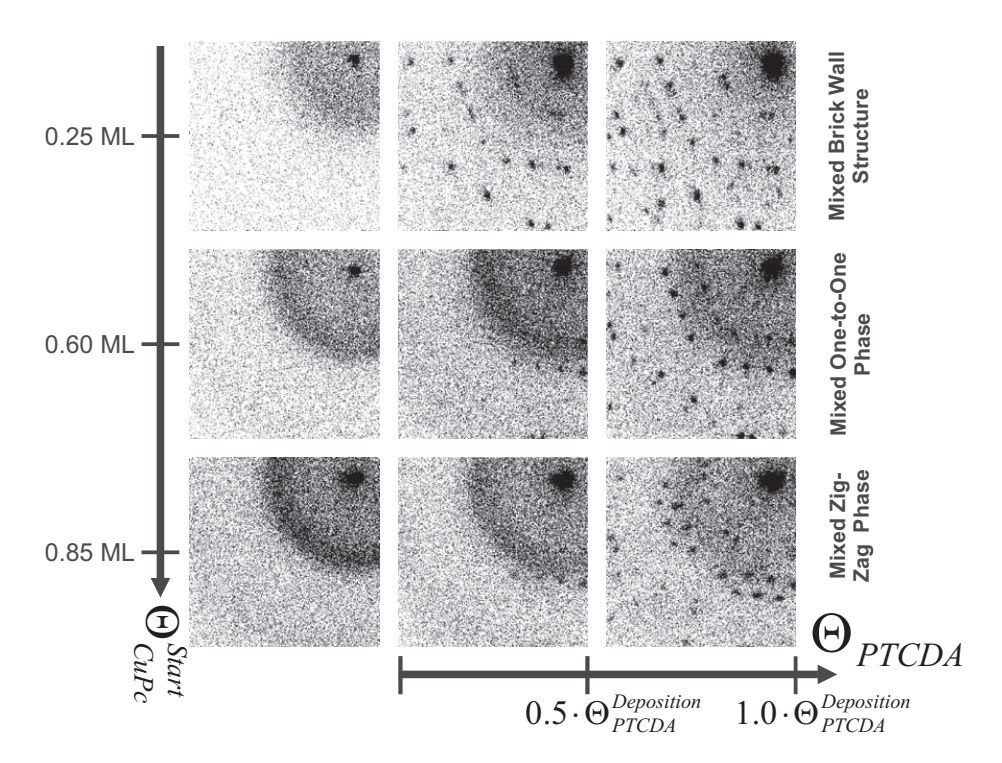


Figure 4.4: SPA-LEED images recorded in-situ during the formation of the mixed organic films ($E_{\rm kin}=27.2\,{\rm eV},\,t_{\rm scan}=52\,{\rm s},\,T_{\rm sample}=300\,{\rm K}$). The left column shows the diffraction data of the initial CuPc layer with increasing coverage from top to bottom. The middle column shows the LEED image after half of the PTCDA coverage is deposited and the right one the final mixed structure. The total coverage of the right column is $\approx 1.0\,{\rm ML}.$

(right column) results in the appearance of higher order diffraction spots of the same LEED pattern, which coincides with a lowering of the diffuse CuPc diffraction intensity. This finding points to the fact that the lateral order of the mixed structure does not change during the PTCDA deposition.

In conclusion, the type of mixed structure which is finally formed depends on the initial amount of CuPc on the surface and consequently on the available free silver surface between the molecules. The size of these areas determines the amount of PTCDA molecules that can adsorb within the first layer and hence can interact with the neighboring CuPc molecules in order to form a mixed island.

The formation of islands indicates an attractive intermolecular interaction. The fact that the hetero-organic structure is formed without sample annealing can be attributed to the high

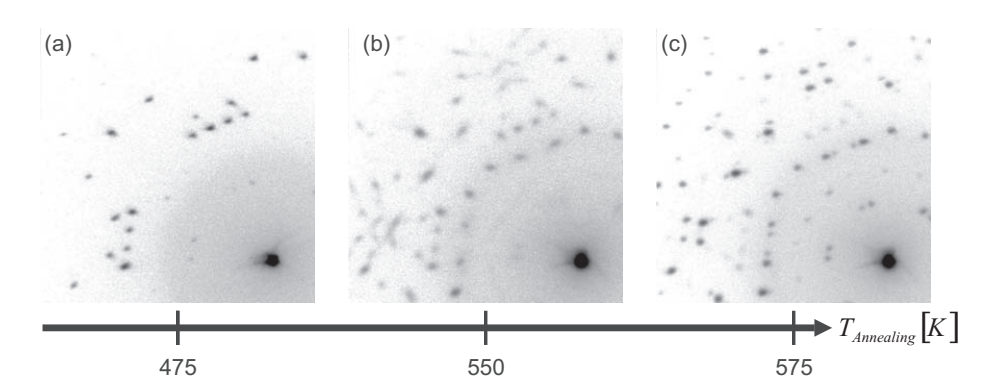


Figure 4.5: Evolution of the LEED pattern demonstrating the mixing process for CuPc deposited on a PTCDA precovered surface ($E_{\rm kin}=27.2\,{\rm eV}$). These films were annealed at the given sample temperature $T_{\rm sample}$ for 20 min.

mobility of CuPc at room temperature. Therefore, no additional activation energy is needed to stimulate the mixing of CuPc and PTCDA.

Changing the deposition sequence, i.e., first PTCDA, then CuPc, results in no direct mixing of CuPc and PTCDA as can be seen in the diffraction pattern in Fig. 4.5(a). It reveals the diffraction signature of a disordered CuPc layer and of ordered PTCDA islands which points to a co-existence of both structures. Even annealing the sample at $T_{\rm sample}=475\,\mathrm{K}$ for $t=20\,\mathrm{min}$ does not create a mixed layer. Increasing the annealing temperature leads, at first, to the appearance of a not well ordered structure indicated by blurred diffraction spots (see Fig. 4.5(b)) which transforms to a well ordered long range structure at 575 K (see Fig. 4.5(c)). At the same time, the diffuse diffraction signature of disordered CuPc molecules disappears. Note that also for this deposition sequence, i.e., first PTCDA, then CuPc, all three mixed phases can be obtained after sample annealing.

In conclusion, an activation energy barrier has to be overcome before a mixed film is formed when PTCDA is deposited first on Ag(111). This is the result of the strong attractive forces between the PTCDA molecules in the close packed PTCDA islands, into which CuPc molecules cannot diffuse at room temperature. The thermal energy increases the mobility of PTCDA at the island edges and and weakens the stability of the islands [HDK12]. As a consequence CuPc can penetrate into the islands and create a mixed film.

The thermally activated mixing also indicates that the mixed layer is the thermodynamic equilibrium state and hence energetically more favorable than two separated phases on one terrace. Therefore, all mixed organic layers were annealed at $T_{\rm sample} = 575 \, \rm K$.

4.1.3 Mixed Brick Wall Structure

The Mixed Brick Wall structure is found for coverages Θ_{CuPc} < 0.4 ML and Θ_{PTCDA} > 0.5 ML, i.e., in the PTCDA-rich regime. A typical LEED pattern of this commensurate structure with two PTCDA and one CuPc molecule is shown in Fig. 4.6(a). In the lower left part, the calculated diffraction spot positions of the superstructure matrix $\begin{pmatrix} 8 & -2 \\ 3 & 7 \end{pmatrix}$ are indicated by blue circles. The corresponding unit cell vectors have a length of $|\vec{A}| = (26.49 \pm 0.10) \,\text{Å}$ and $|\vec{B}| = (17.58 \pm 0.10) \text{ Å}$ with an angle of $\theta_{A,B} = (105.6 \pm 0.4)^{\circ}$. Additional diffraction spots, which cannot be explained by this superstructure matrix, stem from the PTCDA monolayer structure [KUS04]. Apparently, excessive PTCDA molecules start to form mono-organic islands as soon as all CuPc molecules are included in the mixed layer. This indicates that mixed structures with more than two PTCDA molecules per unit cell are not favored. The island growth as well as the formation of a commensurate structure for a large coverage regime are properties of the MBW structure similar to the bare PTCDA monolayer film. This suggests that the mixed film is dominated by the adsorption behavior of the PTCDA molecule. In particular, the site specific interaction of the carboxylic oxygen atoms with the underlying silver should be present in the mixed structure. This should also lead to an alignment of the PTCDA molecules along the silver substrate.

Combing the diffraction results with a local probe technique allows a complete characterization of the unit cell. In the STM image with a submolecular resolution in Fig. 4.6(b), the molecular species in the unit cell can be distinguished easily. While CuPc shows its typical cross like shape the PTCDA molecules feature an elliptic form. A qualitative analysis already reveals that the PTCDA molecules in the MBW structure are not arranged in a herringbone pattern like in the PTCDA monolayer [KTH+06] but form alternating rows with CuPc. A closer look into the unit cell shows that the PTCDA molecules are aligned parallel to each other. Since the orientation of the mixed structure with the silver substrate is known from the diffraction measurement, the orientation of the molecules in the unit cell can be analyzed quantitatively. It turns out, that one pair of CuPc wings is almost aligned with the [$\bar{1}10$]-direction of the substrate ($\theta_{\text{CuPc},[\bar{1}10]} = (-4 \pm 5)^{\circ}$) whereas both PTCDA molecules are rotated 30° with respect to this direction ($\theta_{PTCDA,|\bar{1}10|} = (27 \pm 5)^{\circ}$). The situation is illustrated in Fig. 4.7(a). A substrate grid is also drawn, which indicates that the center of mass of all molecules in the unit cell are located on identical adsorption sites. It turns out that both PTCDA molecules are not aligned along a prominent substrate direction. This leads to the conclusion that both PTCDA molecules are equivalent. However, in this configuration not all carboxylic oxygen atoms can adsorb directly on top of silver atoms and form Ag-O bonds to the substrate.

Although the PTCDA molecule is the prominent species in the MBW structure, its alignment

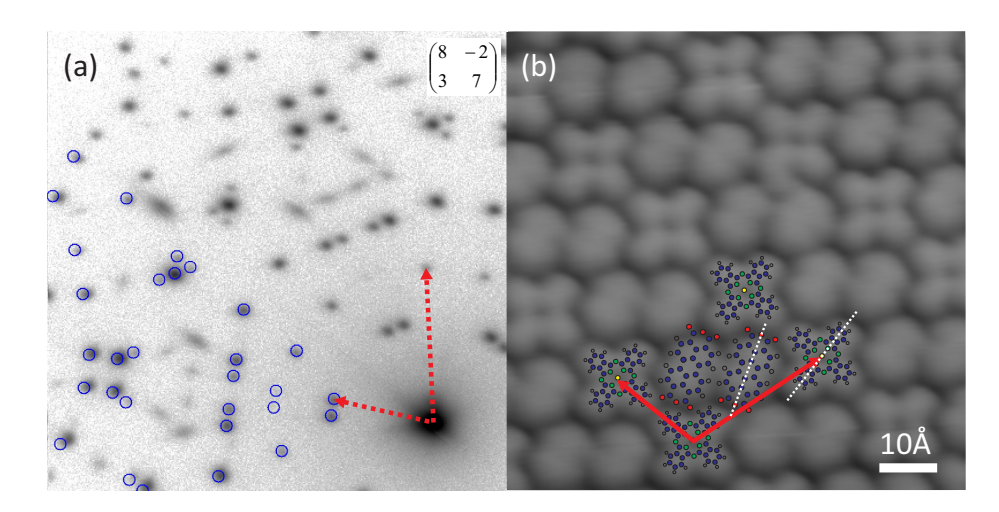


Figure 4.6: (a) Low energy electron diffraction pattern of Mixed Brick Wall structure recorded at $E_{\rm kin}=27.2\,{\rm eV}$. The blue circles in the lower part of the diffraction image model the brick wall structure. The spots not described by blue circles belong to the pure PTCDA monolayer structure. (b) Detailed STM image of the Mixed Brick Wall structure (80 Å × 80 Å, $U_{\rm Bias}=0.2\,{\rm V},\,I=0.01\,{\rm nA}$). The molecules within the unit cell (marked by red arrows) are drawn as ball models whereas the molecular orientation is indicated by white dotted lines.

with the substrate as well as with is neighboring PTCDA molecules is different compared to the pure monolayer structure. However, the formation of a brick wall arrangement of PTCDA molecules in the mixed layer cannot be explained by an electrostatic interaction with CuPc. This statement is the result of a pair potential calculation, in which the lateral position vectors $\vec{r}_i = (\Delta X_i, \Delta Y_i)$ and the rotation angles $\Theta_{z,i}$ of all three basis molecules in the unit cell were optimized [KSW⁺11]. The inner structure of all molecules was fixed according to their gas phase geometry. Further constrains were only the unit cell parameters of the MBW structure and the fact that the unit cell contains two PTCDA molecules and one CuPc molecule located at the same vertical position ($\Delta Z_i = 0$). The CuPc molecules are fixed at the corners of the unit cell. PTCDA molecules are duplicated and translated according to the periodicity in order to ensures that enough neighboring molecules are taken into account.

The structural model in Fig. 4.7(b) illustrates one optimized arrangement of the molecules in the the MBW structure. Although the relaxed molecular orientation of PTCDA fits exactly to the obtained STM data, both PTCDA positions are not equivalent with respect to the Ag(111) substrate. The structure itself is stabilized by the electrostatic attraction between the positively charged hydrogens on PTCDA or CuPc and negatively charged oxygens on PTCDA. The spacing of the atoms in these interacting pairs is in the range of 2.2 Å, close to the distance of a hydrogen bond [Ste02]. Note that a strong repulsion between neighboring

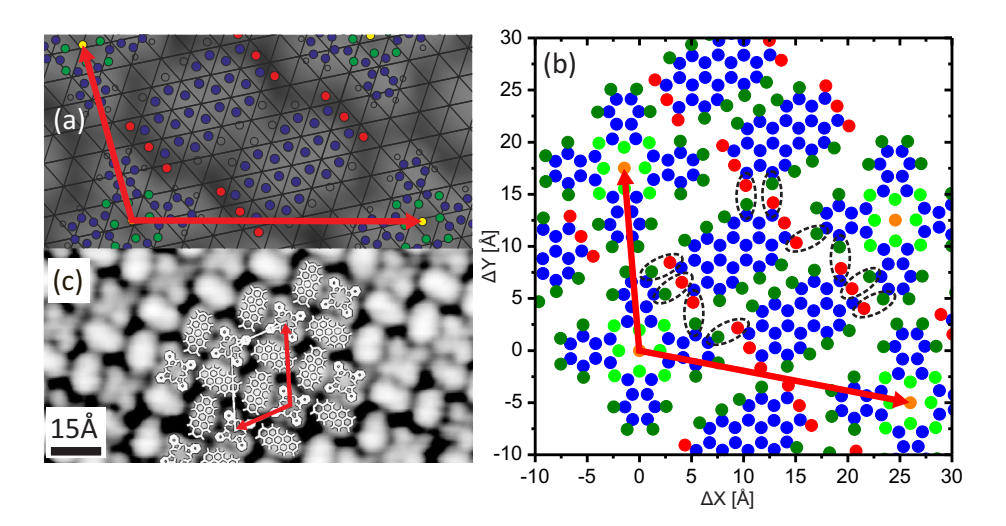


Figure 4.7: (a) Model of the MBW unit cell. The black grid represents the lattice of the Ag(111) surface calculated from the position of the superstructure unit cell vectors. (b) Pair potential optimized structural model for the MBW structure (more details about the calculation can be found in the text). The hydrogen atoms are displayed as dark green circles and the oxygens as red circles. The black ellipses mark the existing O···H interactions. (c) STM image of a similar mixture of one CuPc and two PTCDA molecules on Cu(111) ([BWBM03]). The unit cell is again marked with red arrows and the molecules are represented in a ball and stick model.

PTCDA molecules can be expected for this geometry, since the hydrogen-groups are facing each other (see also pair-potential calculations for PTCDA, Kröger et al. [KSW⁺11]). This drastically reduces the energy gain within the complete unit cell.

Repeating the pair potential calculation for a PTCDA herringbone arrangement in the MBW structure as it is illustrated in Fig. 4.7(c) yields an hypothetic energy gain, which is almost four times larger compared to the brick wall geometry. This suggests that the brick wall orientation is caused by the interaction with the substrate, which is not included in these calculations. The effect of the molecule-substrate interaction on the molecular arrangement in the unit cell becomes clear when considering the so called "Mickey Mouse" phase on Cu(111) [BWBM03]. This structure is the counterpart for a PTCDA-rich mixed phase on Cu(111). Its structure is illustrated in Fig. 4.7(c) and reveals a unit cell almost identical to that of the MBW structure. In the Mickey Mouse phase, the two PTCDA molecules in the unit cell arrange in the energetically more stable herringbone pattern, which is also present in the PTCDA monolayer structure on Cu(111) [WBB+07].

4.1.4 Mixed One-to-One Phase

Upon increasing the CuPc coverage up to $0.75\,\mathrm{ML}$, while keeping $\Theta_{\mathrm{PTCDA}} < 0.5\,\mathrm{ML}$, the Mixed One-to-One (M1²1) phase is formed. In this coverage regime, two main mixed structures with almost square unit cells are observed. Their diffraction pattern together with the corresponding superstructure matrix are displayed in Fig. 4.8(a) and (b). The real space structures with their unit cell vectors are drawn on the grid of the Ag(111) surface in Fig. 4.8(c). For both structures the \vec{B} vectors pointing to the $[\bar{1}\bar{1}2]$ -direction almost coincide. One of them ends exactly on a lattice point of the substrate grid. The other vectors A end either on a substrate lattice point or on a substrate lattice line. This classifies one of these structures as uniaxial point-on-line (p.o.l. M1²1 structure) whereas the other structure is truly commensurate. It turned out that the p.o.l M1²1 structure can be transformed to the commensurate M1²1 structure by sample annealing (40 min at $T_{\text{sample}} = 575 \,\text{K}$) with at least one intermediate structure. This goes along with an expansion of the lattice, since the area of the p.o.l. structure is slightly smaller than the one of the commensurate structure $(F_{v,o,l} = (322 \pm 3) \text{ Å}^2 < (333 \pm 3) \text{ Å}^2 = F_{\text{com}})$. This behavior is very similar to bare CuPc/Ag(111) for which a continuous expansion of the unit cell upon annealing was found and interpreted as an indication for a repulsive intermolecular interaction between CuPc molecules $[KSS^+10]$.

More local information on the molecular assembly of the commensurate M1²1 structure is provided by LT-STM. Interestingly this mixed film is often found in islands on terraces that otherwise are covered with disordered CuPc molecules. The complete edge of the mixed island is decorated by CuPc molecules as can be seen in Fig. 4.9(a). This is the result of the attractive interaction between CuPc and PTCDA.

The molecular arrangement within these islands is very similar to the MBW structure. In Fig. 4.9(b), the molecules belonging to one unit cell are indicated in a ball model. The dotted white line indicates the relative orientation of the molecules. It turns out that the angle between the long axis of PTCDA and one pair of wings of the CuPc molecule is 30° and thus identical to the MBW-film. CuPc aligns with one pair of wings along the substrate. This is similar to the CuPc molecules in the frozen 2D gas phase around the mixed island. However, the CuPc molecules decorating the island edge in Fig. 4.9(a) exhibit a different electronic contrast than the CuPc molecules in the island. The appearance of the edge molecules is equal to the isolated molecules on the silver terrace. This provides evidence for a modified electronic structure of the molecules in the mixed phase, which is mediated by the interaction with all neighboring molecules.

In order to understand the lateral order found in the experiments, both mixed structures are analyzed in the framework of the pair potential approach [KSW⁺11]. The molecular arrange-

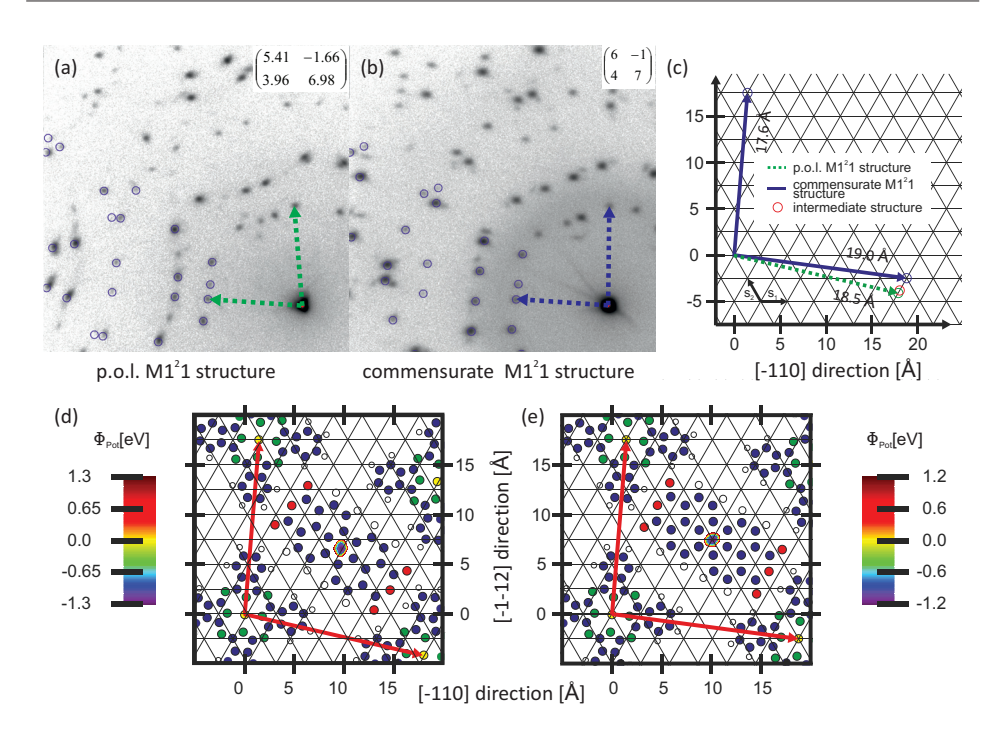


Figure 4.8: Diffraction pattern of the occurring structures in the *Mixed One-to-One* phase. The point-on-line structure on the left side (a) can be transformed to the commensurate structure (b) by sample annealing. For both structures the relative position of the unit cell vectors are drawn on the hexagonal grid of the Ag(111) surface (c). (d)+(e): Pair potential maps for both M1²1 structures. The optimized molecular orientations are indicates by ball models.

ment is optimized with respect to the interaction with eight direct neighbors. Therefore, the unit cell parameters known from LEED are again considered in the calculation. The CuPc molecules are fixed at the corners of the unit cell and the displacement vector $\vec{r} = (\Delta X_i, \Delta Y_i)$ of PTCDA as well as both rotational angles $\Theta_{z,i}$ are relaxed. The geometries with minimal energy are displayed in Fig. 4.8(d)+(e) together with the potential energy maps.

Due to steric conditions, the region for possible PTCDA positions is very small and can be found in the middle of the unit cell. Since both lattices are quite similar, the resulting geometries are also almost identical. The CuPc molecules in both structures are equally orientated and show a tilt angle of 5° with respect to the $[\bar{1}10]$ substrate direction. The PTCDA rotation with respect to the substrate is 30° for the commensurate structure and 40° in the p.o.l. lattice. This agrees very well with the structural model obtained by STM for the commensurate M1²1 structure.

Comparing the pair potential energy of both structures reveals a slightly deeper energy min-

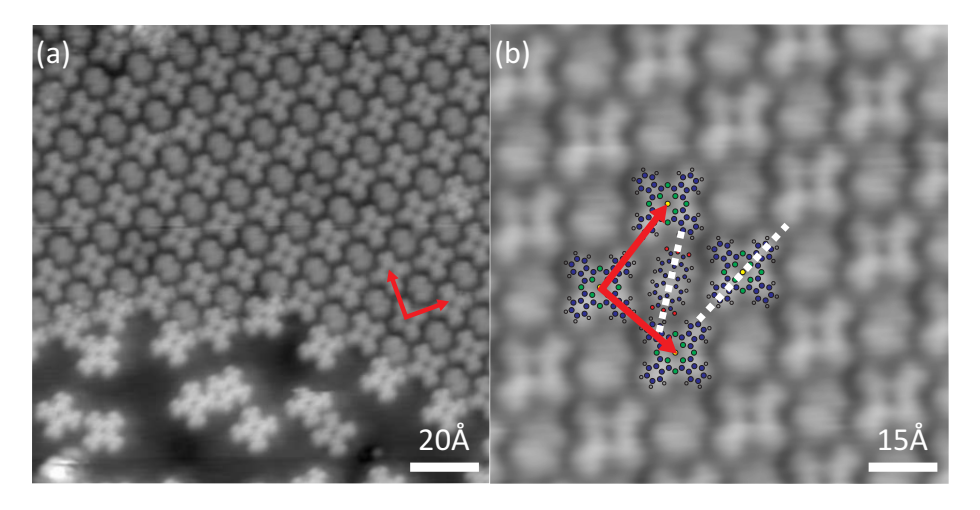


Figure 4.9: STM data for the commensurate M1²1 structure ($U_{\rm Bias} = 0.15\,\rm V$, $I = 0.01\,\rm nA$). (a) Island of the M1²1 structure surrounded by disordered CuPc molecules. The edge of the mixed island is decorated with CuPc molecules. (b) High resolution STM image of the unit cell. The molecules are drawn as ball models, the dotted white lines mark the orientation of the molecules.

imum for the mixed p.o.l. structure. This suggests that the latter structure represents the stable ground state. However, this contradicts the experimental finding that the p.o.l. M1²1 structure can be transformed into the commensurate one. The reason for that could be the interaction with the substrate, which is not considered in this simple pair potential approach.

4.1.5 Mixed Zig-Zag Phase

The structures of the Mixed Zig-Zag (MZZ) phase are visible for CuPc coverages $\Theta_{\rm CuPc} > 0.75\,\rm ML$ and PTCDA coverages below 0.3 ML, i.e., in the CuPc-rich regime. In this coverage regime, a variety of incommensurate structures with roughly the same unit cell size of $F = 520\,\rm \mathring{A}^2$ can be obtained. This value and the deposited amount of both molecules suggests a mixing ratio of two CuPc and one PTCDA in this mixed phase. A detailed analysis of the LEED data indicates that the unit cell size decreases slightly with increasing CuPc coverage. In Fig. 4.10(a) the LEED pattern of the smallest MZZ structure found is shown together with calculated diffraction spots in parts of the image. Almost all additional spots that are not explained by the simulation are caused by multiple scattering of the diffracted electrons at the silver crystal. This can be understood by translating the center of the theoretical pattern from the specular reflection to higher order reflections of the substrate. The resulting pattern

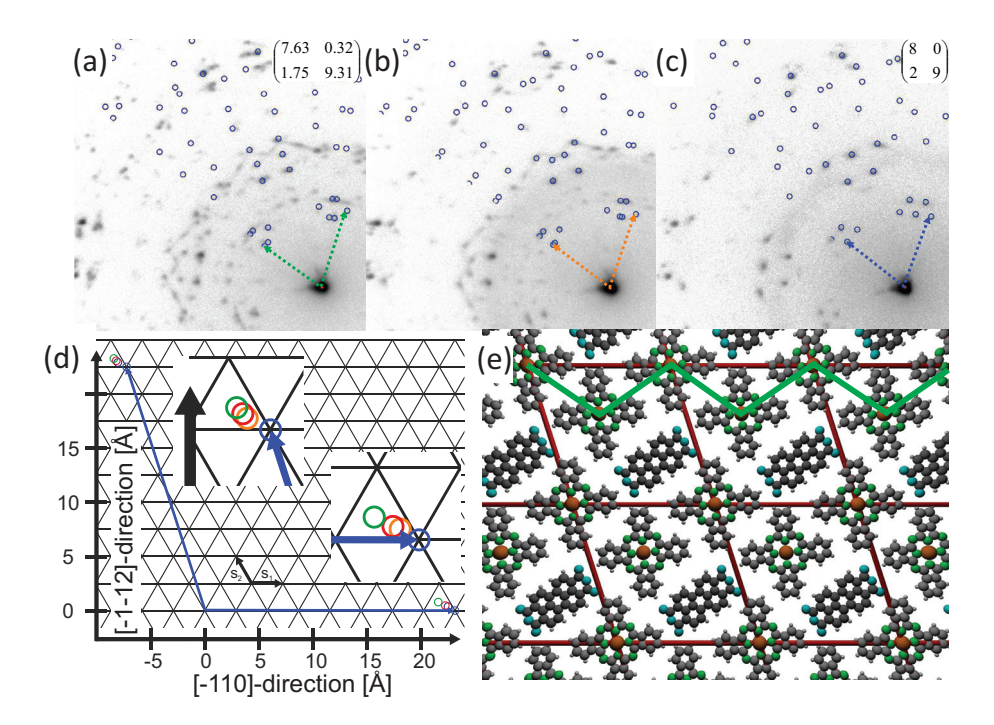


Figure 4.10: (a)+(b): Incommensurate MZZ structures with the smallest (a) and largest (b) unit cell size. (c) Commensurate MZZ structure. (d) Plot of all MZZ structures on the Ag(111) surface lattice. (e) Structural model for the molecular arrangement of the commensurate MZZ structure. The positions and rotational angels are optimized applying a pair potential calculation.

can describe almost all additional diffraction maxima. The same phenomena is observed for all incommensurate lattices in this phase. Note that only for incommensurate structures the multiple electron scattering effect results in additional diffraction maxima. For commensurate superstructures, which were discussed before, the diffraction peak positions of multiple and single scattered electrons coincide.

The diffraction pattern of the smallest MMZ-structure (see Fig. 4.10(a)) can be modified by sample annealing at $575\,\mathrm{K}$ for $20\,\mathrm{min}$. Repeating this annealing procedure several times and monitoring the diffraction pattern after each annealing step reveals a continuous expansion of the mixed structure unit cell. The LEED image of the MMZ-structure with the largest unit cell size is shown in Fig. 4.10(b). The evolution of the adsorbate lattices is illustrated by plotting the unit cell vectors on the Ag(111) grid in Fig. 4.10(d). The heads of the unit cell vectors move on straight lines towards grid points of the silver lattice, which indicates a transformation into a commensurate structure. Although the predicted commensurate lattice was

never found, not even by long sample annealing, it occurred directly after depositing PTCDA on a CuPc covered surface. The corresponding LEED pattern is shown in Fig. 4.10(c).

Even though no STM data is available, we suggest a model for the molecular arrangement in the commensurate MZZ structure, see Fig. 4.10(d). The positions of the molecules as well as their rotation angles are obtained from pair potential calculations as described in section 4.1.3. In the optimized structure, both CuPc molecules are slightly tilted ($\Theta_{z,\text{corner}} = 5.5^{\circ}$, $\Theta_{z,\text{center}} = 3.5^{\circ}$) with respect to the [$\bar{1}10$]-direction of the substrate. This causes the formation of CuPc zig-zag chains which are separated by PTCDA molecules. The rotation angle for the PTCDA molecule is $\Theta_{z,\text{PTCDA}} = 34.5^{\circ}$. This ends up in an angle between CuPc and PTCDA of $\approx 30^{\circ}$ which is very similar to the value found for different mixed phases on Ag(111). This agreement provides evidence for the reliability of the presented model.

Repeating the calculation for all incommensurate MZZ structures reveals that the depth of the pair potential energy minima rises with increasing unit cell size. For the densest molecular packing, even a positive pair potential energy was found suggesting that this structure is not stable. However, since this structure is observed experimentally, it must be stabilized by an interaction that is not covered by the pair potential approach. This can either be the molecule-substrate interaction or an additional intermolecular coupling.

The calculations explain the structural relaxation upon annealing the sample at least partially. Annealing causes a desorption of CuPc molecules from the surface, which increases the available space on the silver surface for the remaining molecules. This allows the structural lattice to expand in order to minimize the pair potential energy.

This behavior is very similar to the structure transformation described for the M1²1 phase or even for the ordered CuPc monolayer structures. In the latter system, this finding was explained by an intermolecular repulsion [KSS⁺10] mediated by the substrate. This causes the molecules to maximize their area per molecule. Since the same trend is observed for the CuPc rich phase, the intermolecular repulsion could be identified as one of the crucial mechanisms for the structure formation.

4.1.6 Conclusion

In this section the formation of hetero-organic thin films consisting of CuPc and PTCDA on Ag(111) was described. Independent of the deposition sequence of the molecules, three different mixing ratios with at most three molecules per unit cell could be achieved: The Mixed Brick Wall structure (2 PTCDA and 1 CuPc), the Mixed One-to-One phase (1 PTCDA and 1 CuPc) and the Mixed Zig-Zag phase (1 PTCDA and 2 CuPc). Although the molecular arrangement is stabilized by $O \cdots H$ interactions, for the PTCDA rich Mixed Brick Wall structure these bonds cannot explain the parallel arrangement of the PTCDA molecules. For

the other coverage regimes, the structures found can be described to some extend by pair potential calculations. The CuPc rich Mixed Zig-Zag phase reveals a series of continuously changing structures which is probably caused by the intermolecular repulsion known for the adsorption of CuPc on Ag(111).

However, some aspects of the molecular assembly are not yet fully understood. In contrast to the pure monolayer structure on Ag(111), the PTCDA molecules in the mixed layers are not orientated along the silver substrate. As a result the formation of a local Ag-O bond between the molecule and the substrate seems no longer possible for all molecules. This points to a decreased interaction strength between PTCDA and Ag(111). Consequently, the influence of the intermolecular interaction on the structure formation should become dominant. However, this is not observed, in particular for the PTCDA rich structure.

In order to understand these issues the electronic structure of the mixed films will be discussed in the following section.

4.2 Electronic structure

The energetic positions of the frontier molecular levels provide information about the interaction mechanism taking place at the metal-organic interface. Especially the charge redistribution can be monitored by the population or depopulation of electronic levels. For these reasons the occupied and unoccupied states close to the Fermi level are investigated with photoelectron spectroscopy and scanning tunneling spectroscopy. Combing these results leads to a comprehensive understanding of the global as well as the local electronic structure of hetero-organic thin films.

4.2.1 Global electronic structure - (AR)UPS

In order to gain a complete understanding of the valence structure, the mixed organic layers are probed with angle integrated as well as angle resolved ultraviolet photoelectron spectroscopy (UPS and ARUPS/ARPES). Combining the latter method with the orbital tomography approach allows to assign the spectral resonances to molecular orbitals. Before turning to this sophisticated data analysis method, conventional UPS data are presented in order to give an overview of the occupied molecular states and their coverage dependency.

UPS studies at different coverages

These UPS spectra were recorded using a hemispherical electron analyzer and a monochromatized UV-source, which provides photons of the He-I $_{\alpha}$ emission line $E_{\hbar\omega}=21.218\,\mathrm{eV}$. The

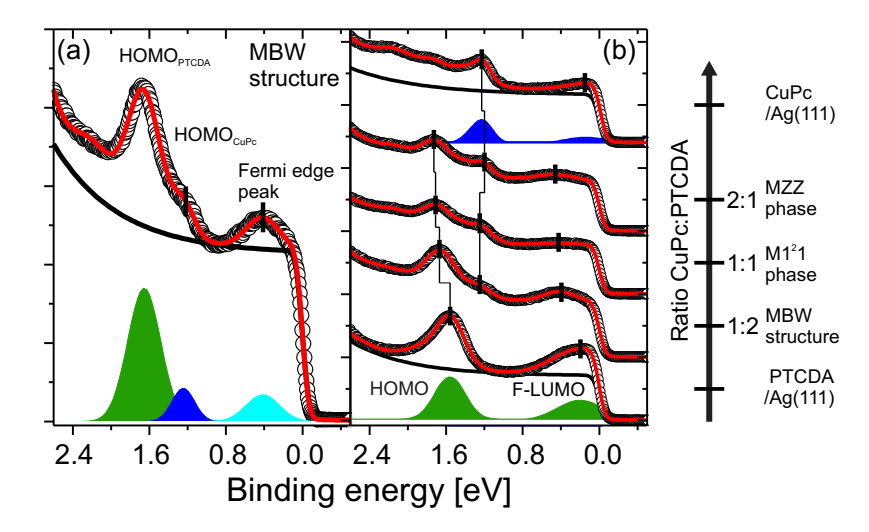


Figure 4.11: Angle integrated UPS spectra of different mixed layer structures ($\hbar\omega=21.218\,\mathrm{eV},\,\theta_\mathrm{Emission}=45\,^\circ$). (a): Spectra of the MBW structure with applied fitting model. (b): UPS spectra of different mixed structures. In addition, the spectra of the pure CuPc and PTCDA monolayer is shown.

emission angle was 45°, the overall energy resolution was better than 30 meV. LEED was used to assign the photoemission data to the corresponding mixed structure. The spectra of three mixed structures containing a different number of molecules per unit cell are shown in Fig. 4.11(b) in the order of ascending PTCDA to CuPc ratio. As a reference, the spectra of the bare monolayer structures are included. The positions of the molecular levels are analyzed by a least square fit to the data, which is shown in Fig. 4.11(b) as red curve. In addition, the complete fitting model for the MBW structure is shown in Fig. 4.11(a). The background of all spectra is modeled by the sum of an exponential background and a Fermi function [Wei05], which is broadened in order to account for the experimental resolution. The resonances in the photoemission spectra themselves are described by independent Gaussian functions.

First,we focus on the spectra of the mono-organic films of PTCDA/Ag(111) and CuPc/Ag(111) (lower- and uppermost curve in Fig. 4.11). Two molecular features can be identified [KSS+10, ZKS+06] (see also chapter 3). The peaks at a binding energy larger than 1 eV are assigned to the Highest Occupied Molecular Orbital (HOMO) of the particular molecule. The second state, which is cut by the Fermi edge, is the Former Lowest Unoccupied Molecular Orbital (F-LUMO), which originates from the LUMO state of the molecule by becoming (partially) filled due to the interaction of the molecule with the surface. For the PTCDA monolayer, the binding energy of the F-LUMO state is found at a slightly higher binding energy compared to the one of CuPc ($E_{\rm LUMO}^{\rm CuPc} = 150 \, {\rm meV}$, $E_{\rm b, LUMO}^{\rm PTCDA} = 200 \, {\rm meV}$). The same trend is observed

for the HOMO levels ($E_{\rm b,HOMO}^{\rm CuPc}=1.23\,{\rm eV},\,E_{\rm b,HOMO}^{\rm PTCDA}=1.56\,{\rm eV}$).

In the spectra of all the mixed organic films, three distinct resonances are present. These features are described by the fitting model presented in Fig. 4.11(a). Two of these states can be assigned to the HOMO levels of CuPc and PTCDA. This is reasonable since the peaks are found at almost the same binding energies as in the mono-organic films. For the MBW structure, which has the lowest CuPc:PTCDA ratio (1:2) of all phases, the HOMO state of the PTCDA is shifted by $110 \, \text{meV}$ to higher binding energies compared to the PTCDA mono-layer structure. This shift increases in the more CuPc-rich phases, up to additional $40 \, \text{meV}$ in the MZZ phase. In contrast, no clear trend was found for the CuPc HOMO state, which was always found in a range of $\pm 30 \, \text{meV}$ around the binding energy of the bare CuPc film.

In agreement to the mono-organic films, all mixed layers exhibit a resonance close to the Fermi level, which is referred to as the Fermi edge peak. For the hetero-organic films, however, this resonance is found at significantly higher binding energies compared to the pure layers. In addition, it is not cut by the Fermi level anymore and an additional shift of 60 meV to higher binding energies is observed when inverting the molecular ratio in the unit cell, i.e., when MZZ- and MBW structure are compared. In contrast to the F-LUMO state of the pure monolayer film, the FWHM of the Fermi edge peak is reduced by a factor of two.

Orbital tomography of the MBW structure

Before discussing the coverage dependency of all states in detail, the origin of the spectral features shall be assured. Therefore ARPES data were recorded for a molecular film, which revealed a coexistence of the MBW structure with islands of the PTCDA monolayer and were analyzed in the framework of the orbital tomography approach. The ARPES experiments were performed at the BESSY II storage ring in Berlin using monochromatic radiation of $\hbar\omega=35\,\mathrm{eV}$. The angular resolved photoelectron distribution was recorded with a toroidal electron analyzer having an acceptance angle of $\pm80^\circ$ and an energy dispersion of 1.0 eV at a pass energy of 10 eV (For more experimental details see chapter 2.2 and 3.1).

In Fig. 4.12(a), constant binding energy (CBE) maps for the binding energy region of the HOMO levels are displayed. The experimental CBE map at $E_{\rm b}=1.40\,{\rm eV}$ exhibits twelve well defined maxima with two different widths which are arranged in an alternating sequence on a circle around the $\bar{\Gamma}$ -point of the surface Brillouin zone. The momentum distribution at $E_{\rm b}=1.65\,{\rm eV}$ reveals only twelve broad emission features, which overlap with each other and create an inhomogeneous ring feature. For a qualitative analysis, these experimental CBE maps are compared to the modeled angular distributions for the CuPc and PTCDA HOMO levels which can be found in panel (c). While the corresponding map of the CuPc

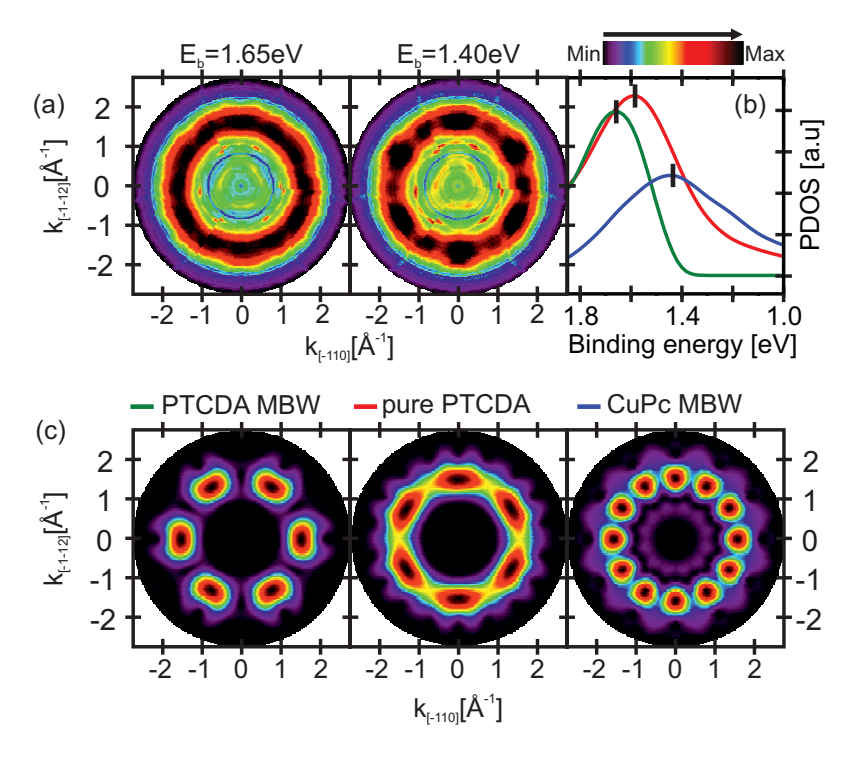


Figure 4.12: (a): Constant binding energy maps of the HOMO region recorded at different binding energies showing the HOMO level of PTCDA and CuPc embedded in different phases. (b): Projected DOS obtained by fitting $I_{\text{HOMO}}(k_x, k_y, E_{\text{b}})$ with the theoretical maps given in panel (c). (c): Theoretical angular momentum maps for all HOMO state involved in the fitting procedure.

HOMO shows twelve sharp maxima, both CBE maps for PTCDA molecules either found in the monolayer structure or in the MBW-film reveal six broad emission features. Hence the experimental CBE map at $E_{\rm b}=1.40\,{\rm eV}$ can be described by a superposition of the CuPc HOMO map and the PTCDA HOMO map calculated for molecules in the pure monolayer structure. Since the six broad emission features of both modeled PTCDA HOMO maps are rotated by 30° with respect to each other, the sum of those maps reflects nicely the experimental CBE map at $E_{\rm b}=1.65\,{\rm eV}$. Consequently the experimental momentum distributions already point to an energetic overlap of the HOMO features.

For a more quantitative understanding, the data cube $I_{\rm HOMO}(k_x,k_y,E_{\rm b})$ is analyzed with the orbital tomography approach [PRU⁺11, SWR⁺12]. The full data cube $I_{\rm HOMO}(k_x,k_y,E_{\rm b})$ is fitted with the theoretical CBE maps shown in Fig. 4.12(c) and the experimental substrate signal. In order to simplify the fitting, the emission from the two inequivalent molecules in

the PTCDA monolayer structure is combined in one momentum map. In agreement with previous studies on the Ag(111) surface [SWR⁺12], the fitting is only performed for a circular ring covering the range $|\mathbf{k}_{||}| = 1.25 \, \mathring{\mathrm{A}}^{-1} \cdots 2.25 \, \mathring{\mathrm{A}}^{-1}$.

The PDOS is shown in panel (b) of Fig. 4.12. It reveals that all three theoretical momentum maps contribute to the HOMO energy region. The PDOS of the PTCDA HOMO state belonging to the monolayer molecules shows the highest intensity for $E_{\rm b}=1.59\,{\rm eV}$. This is in excellent agreement with the result of the pure monolayer sample [SWR+12]. As already discussed for the UPS data in Fig. 4.11(b), the binding energy of the MBW-PTCDA molecules is located at slightly higher binding energies compared to the monolayer film. This prediction is confirmed in the PDOS which yields an binding energy of $E_{\rm b}=1.67\,{\rm eV}$. For CuPc, however, a slightly higher energy position for the HOMO state was obtained by the orbital deconvolution in comparison to the UPS experiments for the MBW structure. ($E_{\rm b,ARPES}=1.40\,{\rm eV}$, $E_{\rm b,UPS}=1.20\,{\rm eV}$). This deviation may be caused by the difficult data evaluation for the HR-UPS data. A precise fit for the CuPc HOMO level is complex due to its high energetic overlap with the PTCDA HOMO level which creates an enhanced uncertainty of the CuPc HOMO position.

In the following we discuss the angular distribution of the Fermi edge peak in order to determine its molecular contributions. Two different constant binding energy maps are shown in Fig. 4.13(a) in the region close to the Fermi level. The momentum distribution recorded at $E_{\rm b}=0.2\,{\rm eV}$ resembles the LUMO emission pattern of the pure PTCDA monolayer structure shown in the right panel of Fig. 4.13(b) very well [SWR⁺12]. The experimental and the theoretical CBE maps show six clear maxima at a distance of 1.75 Å⁻¹ from the $\bar{\Gamma}$ -point of the surface Brillouin zone. The CBE map at $E_{\rm b}=0.44\,{\rm eV}$ shows the angular distribution of the Fermi edge peak of the MBW structure. The theoretical momentum maps for the LUMO levels of CuPc and PTCDA embedded in the MBW structure are calculated for the molecular orientations presented in section 4.1. While the modeled momentum maps for PTCDA and CuPc in Fig. 4.13(b) appear in a sixfold symmetry, the experimental map shows the threefold symmetry of the Ag(111) sample. The dominant features in this momentum distribution are the band structures of the substrate, and a ring of almost constant intensity.

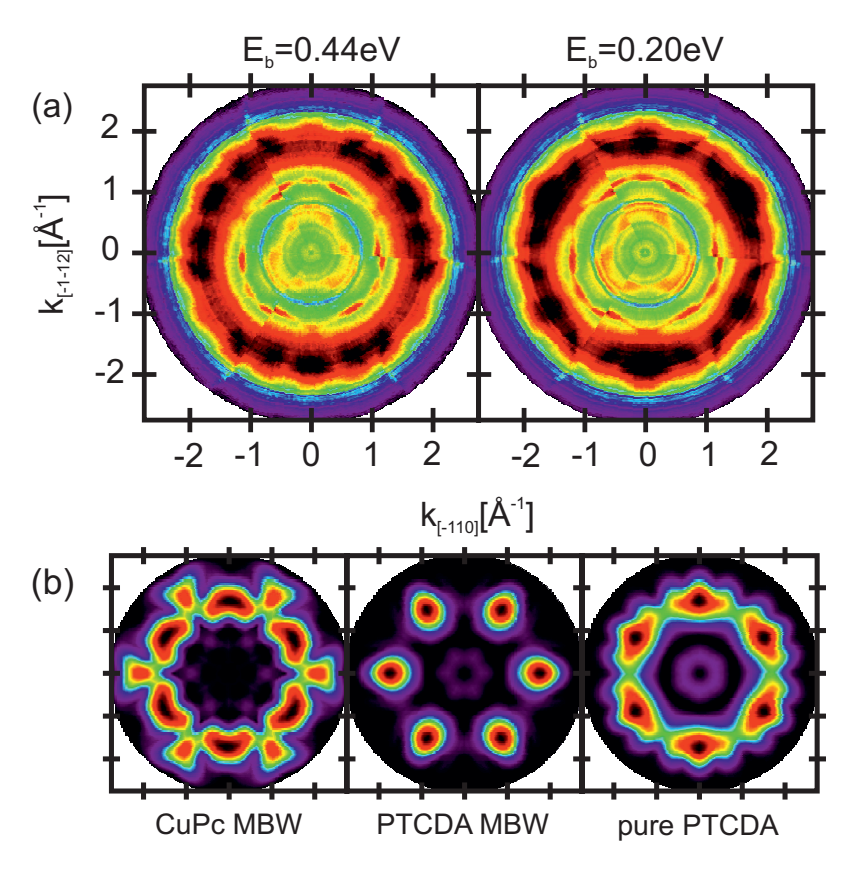


Figure 4.13: (a): Constant binding energy maps (CBE) of the Fermi edge region recorded for different binding energies. The LEED pattern identifies a coexistence of the MBW structure with islands of the PTCDA monolayer structure. (b) Theoretical CBE maps depicting the angular distribution of the LUMO orbital for CuPc and PTCDA included in both structures present on the surface.

In order to identify all orbitals contributing to the photoemission intensity $I(k_x, k_y, E_b)$, the orbital tomography technique [PRU+11, SWR+12] is applied again. The data cube $I_{\text{LUMO}}(k_x, k_y, E_b)$ is fitted with all three theoretical CBE maps shown in Fig. 4.13(b) and the experimental substrate signal. In accordance to the HOMO region, the emission from the two inequivalent molecules in the PTCDA monolayer structure is combined in one momentum map. The resulting binding energy distribution of the projected density of states is shown in Fig. 4.14(a).

The shape and energetic position of the PDOS arising from the F-LUMO state of the PTCDA monolayer molecules (red curve) is in excellent agreement with the results of the pure PTCDA monolayer film (see chapter 3.1.2 and [SWR⁺12]). This result proves that the contributions of

the different phases can be separated by the tomographic approach. The remaining intensity of $I_{\text{LUMO}}(k_x, k_y, E_b)$ yields only one more molecular contribution. While the PDOS of the PTCDA molecules in the MBW structure has its maximum at $E_{\rm b} = 0.44\,{\rm eV}$, the PDOS for CuPc in the same structure is close to zero for all binding energies. This results indicates that the CuPc LUMO is depopulated by the interaction with PTCDA, which is a rather unexpected finding, since for pure CuPc films on Ag(111) the LUMO state gets partially filled due to the molecular interaction with the substrate [KSS⁺10]. Estimating the error bars of the fitting procedure (see chapter 3.1.2 [SWR+12]) yields an uncertainty of 2%. The resulting error bars, which are induced by the statistical spread of the experimental data (Monte Carlo error analysis), seem to be negligible. The same error bars are obtained by the second error analysis method introduced in section 3.1.2, which also consideres possible uncertainties induced by the use of a not ideal fitting function, i.e., an erroneous theoretical CBE map. In addition, all other fitting parameters, like the constant background or the scaling factor of the substrate, show a continuous behavior, which points to an accutrate fitting result. Although the PDOS appears to be a rather solid result, this interpretation will be cross-checked by further analyzing the ARPES data using different types of line profiles.

One suited feature to discriminate the theoretical momentum distributions for CuPc and PTCDA can be found in Fig. 4.13(b) at an angle of 60° with respect to the [$\bar{1}10$]-direction. Both emission maps show well defined maxima at different distances from the $\bar{\Gamma}$ -point as depicted by the radial line profiles in Fig. 4.14(b). In green, blue and red the corresponding cuts through the calculated CBE maps are shown. Their direction is indicated by white dashed lines in the maps of Fig. 4.14(a). While the green curve for the MBW-PTCDA LUMO as well as the red curve for the pure PTCDA structure show clear peaks at $k_{R,\text{PTCDA}} = \pm 1.75 \,\text{Å}^{-1}$ the CuPc feature is found at a distance of $k_{R,\text{CuPc}} = \pm 2.05 \,\text{Å}^{-1}$ (blue curve). The cut through the experimental data at $E_{\rm b} = 0.44 \, {\rm eV}$ shows a well defined maximum at $k_{R,{\rm exp}} = \pm 1.75 \, {\rm \AA}^{-1}$, and a small shoulder at slightly lower k-values. While the position and even the width of this peak reflects the shape of the MBW-PTCDA LUMO line profile, no shoulder or peak could be detected at the position predicted for the CuPc LUMO. The shoulder at lower k-values is caused by the emission from molecules belonging to the pure PTCDA monolayer structure (red curve). This supports the conclusion that the Fermi edge peak of the organic mixed film is only derived from the PTCDA LUMO level but not from the CuPc LUMO. A second radial line profile taken at a binding energy of $E_{\rm b} = 0.20\,{\rm eV}$ (Fig. 4.14(c)) leads to the same conclusion. At this binding energy, the CuPc LUMO would be expected in the case that the population of the CuPc LUMO does not change by the interaction with PTCDA. However, this radial line profile is also dominated by features belonging to the PTCDA LUMO emission. Consequently, no trace of an occupied CuPc LUMO level is found for any energies close to the Fermi level.

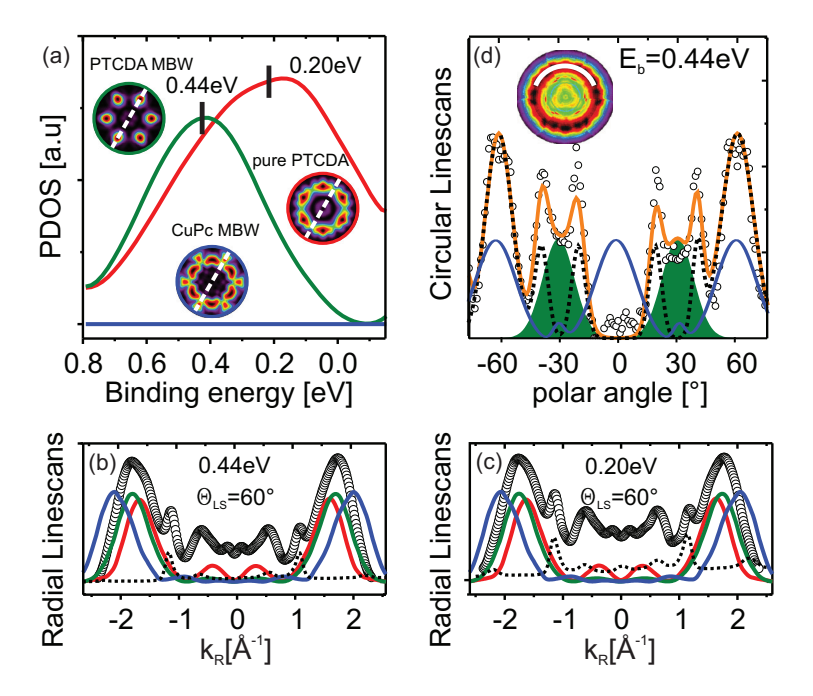


Figure 4.14: (a): Projected DOS for the LUMO energy region $(I_{\rm LUMO}(k_x,k_y,E_{\rm b}))$. The color code described in (a) holds for all other panels in this figure. (b)+(c): Radial line profiles cutting through the experimental CBE map at an angle of 60 ° with respect to [110]-direction. For comparison the same line profiles for the theoretical maps and the substrate (dotted line) are shown. The cutting direction for the theoretical maps is indicated in the inset of (a). (d): Circular line profile for $E_{\rm b}=0.44\,{\rm eV}~(r_{k,{\rm cirlce}}=1.75\,{\rm \AA}^{-1})$. The insets indicates the cutting direction through the data. The dotted black lines represent the contribution of the substrate. The red curve shows the fit of the substrate and the molecular contribution to the experimental data.

Finally, a circular intensity profile, cutting the momentum map at $E_{\rm b}=0.44\,{\rm eV}$ at a fixed distance of $k_R=\pm 1.75\,{\rm \AA}^{-1}$ from the $\bar{\Gamma}$ -point, is created and shown in Fig. 4.14(d) (data points). The position of the circular cut in the map is illustrated in the inset. All features in the intensity profile can be explained either by the contribution of the substrate shown as dotted black line or by the emission from the PTCDA LUMO state shown as green peaks. The orange curve represents the least square fit of a superposition of these two contributions to the experimental intensity. The small residual intensity for $0\,^{\circ}$, which is not captured by the model, can be attributed to the intensity of the PTCDA monolayer emission. In addition, the corresponding circular cut through the theoretical CuPc LUMO map is included as blue curve in Fig. 4.14(d). It is obvious that this curve is not suited to improve the quality of the

fit (orange curve). This finding also suggests the absence of any CuPc LUMO contribution to the Fermi edge peak.

In conclusion, all previous experimental results strongly suggest that the Fermi edge peak can be assigned to the PTCDA LUMO level. No signature of the CuPc LUMO is detected for the occupied states indicating a depopulation of this level caused by the formation of the mixed film.

Orbital tomography of the M1²1 structure

A similar data set was obtained for the p.o.l. M1²1 structure. Since the ARPES results for HOMO energy region of this structure match the findings for the MBW structure almost perfectly, we show only the results for the region close to the Fermi level. A CBE map recorded for this layer at $E_b = 0.47 \,\mathrm{eV}$ is shown in Fig. 4.15(a). Aside from the substrate features, which have a threefold symmetry, the maxima of this experimental map can be described by the emission arising from the MBW-PTCDA LUMO level (see Fig. 4.13(b)). This is reasonable since it was revealed by STM in section 4.1 that the molecular orientations in the MBW structure and the commensurate M1²1 structure are identical. Due to steric conditions, the orientation of the molecules in the corresponding p.o.l. structure has to be similar. Pair potential calculations discussed in section 4.1.4 suggest a similar alignment for CuPc and a small tilt of 10° for PTCDA compared to the commensurate structure. Such small tilt angles do not change the shape of the theoretical momentum maps strongly and hence do not affect the conclusions of the ARPES data. In addition, the recorded momentum distribution exhibits weak intensity at k-space positions typical for the LUMO states of PTCDA monolayer molecules or CuPc molecules within the mixed layer. The appearance of the first, which indicates the existence of PTCDA islands, is not surprising since this mixed film was prepared by annealing a stacked bilayer film of CuPc on PTCDA [SSK+12] which could lead to the observed coexistence of a mixed structure with islands of the pure PTCDA monolayer structure.

Apart from this qualitative analysis of the ARPES data, the orbital tomography method was also applied. Based on the high agreement of the molecular alignment in the MBW structure and the $\rm M1^21$ phase, all three theoretical momentum maps presented in Fig. 4.13(b) are used in the fitting routine.

The PDOS of the LUMO levels, which is shown in Fig. 4.15(b), is not as conclusive as the one for the MBW structure. The fitting result for the M1²1-PTCDA molecules yields the expected sharp maximum at a binding energy of $E_{\rm b}=0.47\,{\rm eV}$ (green curve). In contrast to the results of the MBW structure, a small contribution of the CuPc LUMO is detected for the M1²1 structure. However, the origin of this density of states is not unambiguously

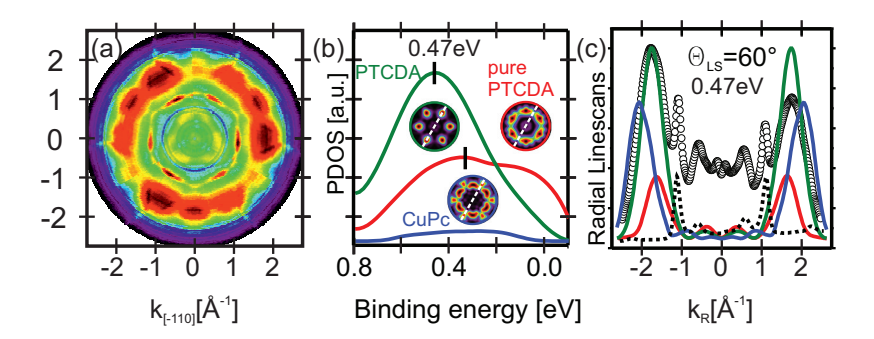


Figure 4.15: ARPES data for the M1²1 structure. (a): Constant binding energy map (CBE) of the Fermi edge region recorded at $E_{\rm b}=0.47\,{\rm eV}$. (b): Projected DOS obtained by fitting the data cube $I_{\rm LUMO}(k_x,k_y,E_{\rm b})$ with the three theoretical maps shown in Fig. 4.13(b). (c): Radial line profile cutting through the experimental CBE map for $E_{\rm b}=0.47\,{\rm eV}$ at an angle of 60° with respect to $k_{[\bar{1}10]}$. For comparison the same line profiles for the theoretical maps (colored lines) and the clean substrate (dotted line) are shown. The cutting direction for the theoretical maps is indicated in the inset of panel (b).

clear. The shape of this signal is very broad and its integral intensity is more than one order of magnitude smaller than the one stemming from the PTCDA molecules in the same structure. Consequently, the number of CuPc molecules contributing to this signal does not reflect the relative number CuPc and PTCDA molecules in the M1²1 structure. Hence, the CuPc signal is either caused by a not complete depopulation of the CuPc LUMO level in the mixed layer or by a minority of CuPc molecules that are not located in the mixed film. The latter seems more likely when considering that CuPc molecules decorate the M1²1 structure islands, which was revealed by STM data in section 4.1.4. It was also shown by STM that these edge molecules are electronically different compared to the molecules within the mixed film. Their STM contrast is similar to isolated molecules in the pure CuPc phase. Since UPS demonstrated a partially occupied LUMO level for isolated CuPc molecules on Ag(111), the edge molecules surrounding the mixed islands might explain the not vanishing PDOS for the CuPc molecules in the M1²1 structure.

The PDOS for the PTCDA monolayer molecules (red curve) shows a different shape compared to the spectra of a perfectly ordered PTCDA monolayer film ([SWR⁺12] and chapter 3.1). The highest PDOS of this orbital emission is found at higher binding energies ($E_{\rm b}=0.31\,{\rm eV}$) compared to the monolayer structure ($E_{\rm b}=0.25\,{\rm eV}$). This is surprising when considering the orbital tomography results for PTCDA monolayer islands, which coexisted with the-MBW structure. There the contribution of the PTCDA monolayer molecules to the APRES intensity was perfectly separated from the other molecular signals in section 4.2.1. This different findings might be explained by the sample preparation. While the MBW structure was di-

rectly prepared by first depositing CuPc on Ag(111) and subsequently PTCDA, the M1²1 structure was obtained by annealing a stacked bilayer film of CuPc on PTCDA [SSK⁺12]. Unfortunately, the experimental setup did not allow a precise temperature control during the annealing process. Therefore, it is likely that a perfectly ordered mixed structure is not formed on the complete silver surface. The remaining parts of the surface might be covered with small PTCDA islands which are decorated by CuPc molecules (see section 4.1.2). The interaction between CuPc and PTCDA at the island edges might result in a different electronic signature for PTCDA molecules in direct vicinity of CuPc compared to the molecules in the pure monolayer film. In addition, the LUMO level of those CuPc molecules is probably still occupied in analogy to the CuPc molecules decorating the M1²1 structure. Consequently, this argument might explain the not vanishing density of states of the CuPc LUMO as well as the modified shape of the PTCDA LUMO signature for molecules in the monolayer islands.

In analogy to the data treatment of the MBW structure, radial line profiles which cut through the same features were performed. These profiles are shown in Fig. 4.15(c) for $E_{\rm b}=0.47\,{\rm eV}$. In agreement with the results for the MBW structure, the peak in the experimental intensity profiles coincides with the one for the modeled CBE map of the PTCDA molecule in the mixed structure. Also for the M1²1 structure, neither a peak nor a shoulder could be identified at $k_{R,{\rm CuPc}}=\pm2.05\,{\rm \mathring{A}}^{-1}$. This again indicates a vanishing contribution of the CuPc LUMO level to the Fermi edge binding energy region.

In conclusion, for both mixed layer structures investigated with ARPES, the Fermi edge peak at $E_{\rm b}\approx 0.44\,{\rm eV}$ could be assigned to the LUMO level of the PTCDA molecules within the mixed structures. No signature of the CuPc LUMO state could be identified in the valence band region close to the Fermi level. This leads to the conclusion that the CuPc LUMO, which should be populated by the interaction with the silver surface, is depopulated when forming a mixed structure with PTCDA.

Work function and molecular level alignment

Since the work function Φ is sensitive to charge redistributions at the interface, its changes upon the formation of a mixed layer is investigated with photoelectron spectroscopy. In the left panel of Fig. 4.16, the work function of three different mixed structures is shown together with the reference data for the pure monolayer films (green dots). The data are again shown in ascending order of the PTCDA to CuPc ratio. In addition, the work functions of the pure CuPc submonolayer films before the formation of the mixed organic layers are displayed as blue dots. Differences in these values stem from the different CuPc coverages since the system CuPc/Ag(111) shows a continuously decreasing work function with increasing coverage.

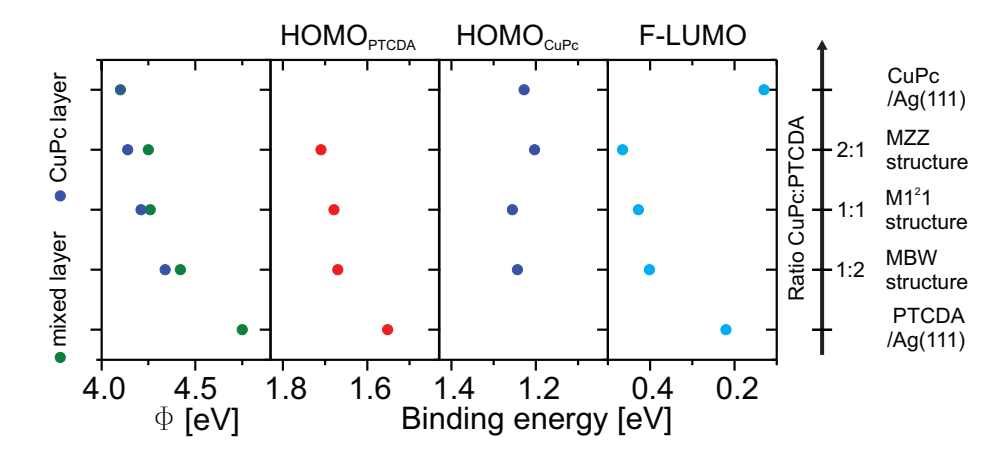


Figure 4.16: Work function Φ and binding energy positions of the molecular features for three mixed structures with different ratio of CuPc to PTCDA. In the panel depicting the work function changes, the green circles mark the work function of the mixed film and the blue circles the one for the pure CuPc film before the mixing process. The error of the experimental data is reflected by the size of the circles.

This has been discussed in section 3.2.2. The work function of the mixed films decreases stepwise starting from $\Phi = 4.75\,\mathrm{eV}$ for the pure PTCDA monolayer structure to $\Phi = 4.10\,\mathrm{eV}$ for the closed CuPc film. This corresponds to the increasing ratio of CuPc to PTCDA in the mixed structures. Furthermore, the formation of a hetero-structure increases the surface potential of the CuPc film. This becomes evident when comparing the work function before (blue circles) and after (green circles) the formation of the mixed layer. Since both molecules do not feature an intrinsic dipole moment perpendicular to the molecular plane, the changes of work function must be caused by charge redistribution at the mixed organic metal interface. It has been discussed in literature [RNP+09, RGW+10, FGGM+11] that the work function modification upon the adsorption of planar organic molecules on noble metal surfaces is dominated by two effects: the push-back or cushion effect and the charge transfer between molecule and substrate. The latter results in the formation of an interface dipole. The orientation of the dipole depends on the balance between the push-back effect decreasing the interface potential and the direction and the amount of the charge redistribution at the interface. It has been reported in chapter 3.2.2, that the work function of CuPc layers on Ag(111) decreases continuously with the coverage of the molecules. Since the coverage is inversely proportional to the area per molecule on the surface, the work function is only decreased by the presence of the molecules on the surface without considering the chemical interaction. Therefore, the work function change is mainly attributed to the push-back effect. For the PTCDA monolayer on Ag(111) an effective charge transfer into the molecule of 0.31 electrons was calculated [RNP+09]. This charge exchange leads to a surface dipole,

which overcompensates the push-back effect and results in an increase of the work function of $\Delta\Phi = 0.15\,\mathrm{eV}$. This modification is rather small in comparison to the value of $\Delta\Phi = -0.46\,\mathrm{eV}$ found for the monolayer CuPc/Ag(111).

For the mixed films, however, both effects are superimposed. In analogy to the bare films, the CuPc molecules in the mixed structure decrease the work function due to the push-back effect. In contrast, the charge transfer into the PTCDA molecule, which is enhanced by the formation of a mixed layer, creates a surface dipole oriented with its positive end towards the surface [RNP+09]. This dipole increases the work function of the mixed system. However, the influence of CuPc on the modification of the overall surface potential barrier is much larger than the one of PTCDA. Consequently, the work function of the mixed layer depends mainly on the CuPc coverage.

The other panels in Fig. 4.16 illustrate the binding energy positions of all molecular orbitals visible in the mixed and mono-organic interfaces, as obtained from the UPS data. All states arising from the PTCDA molecule show the same trend. Compared to the pure PTCDA monolayer structure, the LUMO and HOMO state of PTCDA in the MBW structure reveal a large shift to higher binding energies. This shift is larger for the LUMO. Increasing the CuPc:PTCDA ratio both states shift to even higher binding energies. While the first larger shift upon forming a hetero-organic layer can be attributed to the additional charge transfer into the PTCDA molecule, the smaller shifts between different mixed structures must be caused by the different environment of the PTCDA molecule [WSS+13]. In contrast, the CuPc HOMO state does not shift significantly when forming a mixed layer. It also seems to be rather insensitive to different mixing ratios. In addition, its binding energy differs from the one found for other systems with unoccupied CuPc LUMO states like CuPc/PTC-DA/Ag(111) [SSK+12] or CuPc/Au(111) [SKRK11]. The CuPc HOMO binding energy for those surfaces was found to be below $E_{\rm b} = 0.9\,{\rm eV}.$ This points to an interaction channel between the molecules, which has not yet been discussed in literature. In order to unmask the origin of electronic level alignment, the local density of states are investigated by scanning tunneling spectroscopy.

4.2.2 Local electronic structure - STS

After the previous discussion of the occupied frontier orbitals based on photoelectron spectroscopy, a local view of these state is now presented, which was obtained by scanning tunneling spectroscopy (STS). In Fig. 4.17 dI/dV spectra, recorded at different positions in the unit cell, are shown for the MBW structure as well as for the M1²1 structure. These spectra represent the local density of states (LDOS) at different positions on the surface. At first, we discuss the occupied states of the MBW structure (Fig. 4.17(a)). An almost flat line without obvious peaks is found for all CuPc spectra (blue, green and black curve) up to an energy

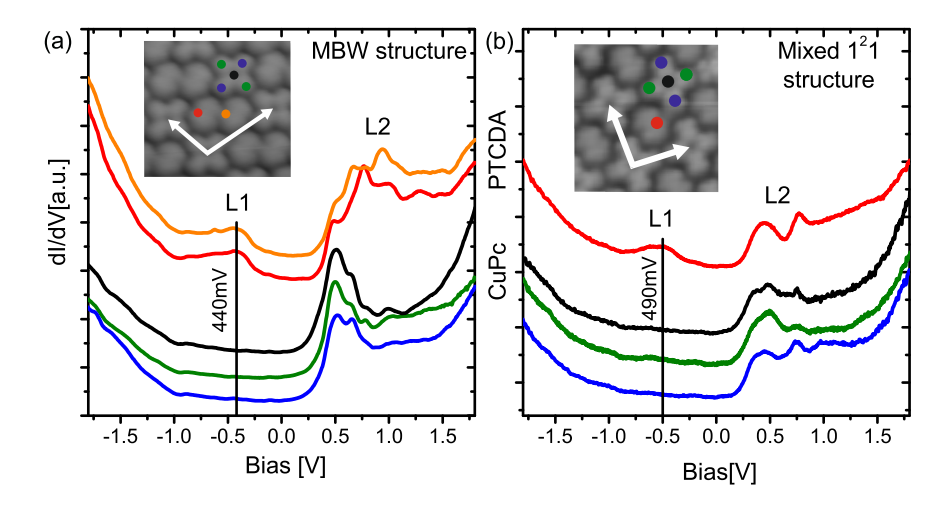


Figure 4.17: Averaged scanning tunneling dI/dV spectra recorded at different positions in the unit cell. ($T=10\,\mathrm{K}$, modulation $\nu=780\,\mathrm{Hz}$, $5\,\mathrm{mV}$) (a): MBW structure ($I=0.1\,\mathrm{nA}$), (b): M1²1 structure ($I=0.03\,\mathrm{nA}$). The colored dots on the STM image in the inset of (a) and (b) mark the positions where the spectra of the same color code was taken.

of $-1.0\,\mathrm{V}$. In contrast, both dI/dV curves belonging to the two PTCDA molecules (red and orange curves) in the unit cell exhibit a defined broad maximum (L1) at a bias voltage of $-0.44\,\mathrm{V}^1$. It can obviously be assigned to the PTCDA LUMO state due to its STM contrast [KTH+06]. Both observations support the conclusion made by photoelectron spectroscopy in the previous chapter. The LUMO state of PTCDA is shifted to higher binding energies upon forming a mixed layer, and no significant contribution of the CuPc LUMO to the density of states close to the Fermi level could be identified. The absence of a spectroscopic CuPc LUMO signature in STS supports the PES results. However, since it is known that strongly hybridized states often show no fingerprint in the dI/dV spectra, the STS results do not allow an unambiguous conclusion. The HOMO state is also not visible in the STS spectra due to a lack of sensitivity to this state by a not modified tip [KTH+06].

In the regime of unoccupied states, all spectra of the MBW structure show an intensity step at $\approx 400\,\mathrm{mV}$ followed by a nearly constant level and a complex peak structure. Basic quantum mechanics shows that a step in the DOS is a sign for a delocalized 2D gas like state. Since this step is present in all spectra with an onset at almost the same bias voltage this delocalized state seems to be expanded over all molecules in the unit cell.

¹This value is obtained by a least square fit. The local density of states is modeled by a Gaussian profile and the increasing background by an exponential function.

The appearance of a delocalized state in the bias regime of the unoccupied molecular orbitals has already been observed for pure PTCDA adsorbed on Ag(111) [TSLT06, KTH+06] in form of the so called *interface state* (IS). This interface state is derived from the surface state, which is depopulated by the adsorption of PTCDA [SSM+08, MZS+11]. According to DFT calculations, it contains significant contributions of the LUMO+1 and LUMO+2 levels of the PTCDA molecule [DP10]. In case of CuPc adsorption on Ag(111), the surface state is depopulated which suggests an involvement of the surface state in the CuPc-Ag interaction [Koc09]. In the case of the mixed organic films, the question could be raised whether the interface state is not only a depopulated and shifted surface state but also exhibits a mixture of unoccupied molecular orbitals of both molecules as in the case of PTCDA/Ag(111) [DP10, ZNEC12]. This would result in an electronic coupling of the molecules in the mixed film via this interface state. Such a connection between the electronic structure of all molecules in the mixed layer could explain the depopulation of the CuPc LUMO and a stronger filling of the PTCDA F-LUMO state.

In order to determine the precise position E_{IS} of the delocalized state, a step function was fitted to the data.

$$f(V) = a \cdot \left(1 - erf\left(\frac{E_{IS} - V}{\sigma \cdot \sqrt{2}}\right)\right)$$
 (4.1)

The energy position of the interface state for the PTCDA molecules in the monolayer structure was determined to be $E_{IS} = (570 \pm 30) \,\mathrm{meV}$ at 90 K [MZS⁺11]. This is considerably higher in energy than $E_{IS}^{\mathrm{MBW}} = (375 \pm 30) \,\mathrm{meV}$ obtained for the MBW structure. These different energies of the interface state could be ascribed to a different interaction of the molecules with the substrate as it was found for NTCDA and PTCDA on Ag(111) [MZS⁺11]. The interface state for NTCDA/Ag(111) in the relaxed commensurate monolayer structure is found at an energy that is 200 meV lower compared to PTCDA on Ag(111). This coincides with a larger adsorption height for NTCDA (h_{NTCDA} , $h_{\mathrm{Backbone}} = (3.00 \pm 0.02) \, \mathring{\mathrm{A}}$) compared to PTCDA (h_{PTCDA} , $h_{\mathrm{Backbone}} = (2.86 \pm 0.01) \, \mathring{\mathrm{A}}$) [SHS⁺07, HTS⁺10]. The situation for the PTCDA molecules in the MBW structure is comparable as will be shown in chapter 4.3: Their perylene backbone is lifted to the same height as the average carbon height of NTCDA/Ag(111), which can explain the lower E_{LS}^{MBW} .

The occupied states of the dI/dV spectra for the M1²1 structure in Fig. 4.17(b) reflect the photoemission results. While the PTCDA LUMO level is shifted slightly to higher binding energies, no signature of the CuPc LUMO is detected. In analogy to the MBW-film, an intensity step is observed for the unoccupied states. A further decrease of the IS to $E_{IS}^{\rm M1^21}=(275\pm30)\,\mathrm{meV}$ is observed for this phase, which has a smaller number of PTCDA molecules in the unit cell compared to the MBW structure. Since this shift occurs by changing the structure of the mixed film and hence the ratio of CuPc to PTCDA, it can be attributed to a different local environment of the molecules. The same trend was observed for all occupied

PTCDA orbitals by photoelectron spectroscopy.

4.2.3 Conclusion

Occupied and unoccupied frontier orbitals were studied in the this chapter by photoelectron spectroscopy and scanning tunneling spectroscopy. All results point to a significant modification of the molecular valence structure by the formation of mixed films. While the PTCDA LUMO is found at higher binding energies compared to the pure PTCDA monolayer structure, no sign of the CuPc LUMO is evident in the energy region close to the Fermi level. This points to an enhanced charge transfer into the PTCDA LUMO and a depopulation of the CuPc LUMO. In the CuPc rich structures (MZZ phase), the PTCDA LUMO level is located at even higher binding energy than in the PTCDA-rich MBW structure. This is attributed to a different molecular environment and a different number of O···H bonds between the molecules [WSS+13]. However, the binding energy of the CuPc HOMO is not effected. For energies above the Fermi level, a delocalized interface state was observed which revealed the same energy for all molecules in one structure. This suggests that this state is expanding over all molecules in the layer and might enable the coupling of the molecular orbital structure. The energy position of the interface state also depends on the local environment as indicated by different results for the MBW and M1²1 structure.

4.3 Vertical adsorption geometry: The Mixed Brick Wall structure

The vertical adsorption geometry and in particular the adsorption height of a molecule on a substrate provides crucial information about the interaction mechanism at the interface. For isolated molecules this bonding distance is only determined by the interaction with the underlying surface. In an ordered organic layer, it can be modified by the interaction with neighboring molecules. In order to study the influence of the mixed layer formation on the bonding strength of each molecule, their adsorption heights are investigated with the X-ray standing wave technique. Comparing the modified adsorption geometry to the mono-organic reference data provides insight into the interaction mechanisms in the hetero-organic film. We selected the Mixed Brick Wall structure for this experiment. It was prepared by annealing a vertically stacked CuPc/PTCDA film on Ag(111) [SSK+12] leading to the formation of a mixed layer. The desorption process was controlled by monitoring the thermal desorption signal. The lateral order of this film was identified by LEED and the ratio of molecules (two PTCDA and one CuPc) was confirmed by the integrated core level signal. During the experiment, the sample temperature was kept constant at $T = 50 \,\mathrm{K}$ and the data acquisition time on one spot on the surface was less than 20 min. Within that time, no radiation damage was observed for this sample.

The following subsection first describes the treatment of the photoemission core level data in order to extract partial yield curves for all chemically different species of both molecules. After that, the resulting adsorption heights are discussed in detail.

4.3.1 Core level models

In order to determine the adsorption heights of both molecules in the mixed film, the core level emission signals from nitrogen N1s, copper Cu2p, oxygen O1s and carbon C1s are recorded. While Cu2p and N1s can only be assigned to CuPc, the O1s emission stems only from the PTCDA molecule. In contrast, the C1s yield contains contributions from both molecules. Exemplary core level spectra of all atomic species are shown in Fig. 4.18. The background of all spectra can be described by a Shirley function [Shi72], takes into account the inelastic scattered photoelectrons. This type of background, which is more common for bulk core level states, originates from the detection angle of almost 90° with respect to the surface normal. This emission direction increases the surface sensitivity of the photoemission experiment and hence attenuates features of the silver substrate. A Ag3d plasmon, which forms a complex background in the energy region of the N1s state, had to be considered by an expensive background in earlier data sets [KSS+10, MMM+10].

The resonances of the N1s and Cu2p state contain only one chemical species and are well described by Voigt functions with 30 % Lorentzian contribution. The shape of the other core level spectra is much more complex. A doublet splitting is found for the oxygen O1s spectra which is caused by the two chemically different oxygen species in PTCDA. The component at lower binding energy stems from the carboxylic oxygens (peak 6), the other from the anhydride oxygens (peak 7). However, the two peaks in the oxygen spectrum depicted in Fig. 4.18 do not only contain the main lines of the corresponding species but also a complex satellite structure. This is obvious since the integrated peak intensity does not reflect the stoichiometric ratio of two carboxylic oxygens to one anhydride oxygen. Furthermore, the O1s spectroscopic line shape is significantly different compared to the adsorption of PTCDA/Ag(111). Consequently, it is impossible to directly apply the fitting model suggested by Hauschild et. al. [HTS+10] for a separation of the oxygen species. In particular, the satellite structure of the carboxylic oxygen seems to be different leading to a less pronounced dip between both main lines. The best fitting quality for the O1s core level spectrum of the MBW structure is achieved with the fitting model shown in Fig. 4.18. The energy difference between the carboxylic (green solid curve) and the anhydride (blue solid curve) oxygen main lines is adopted from the Hauschild model [HTS+10] and the energy gap between the satellite peaks and the corresponding main line is reduced compared to the O1s model for PTCDA/Ag(111). The tail of the spectrum at high binding energies is modeled by a separate peak, which contains inelastically scattered electrons of both chemical species.

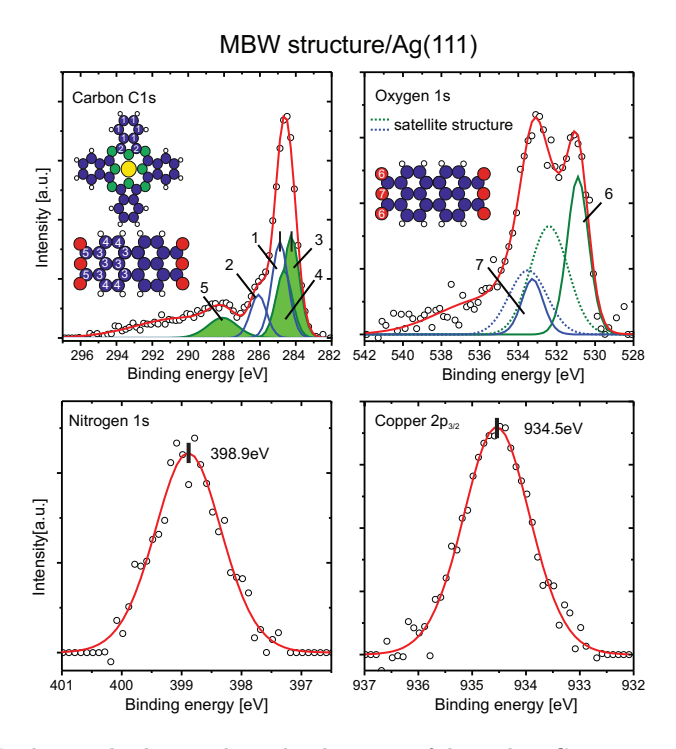


Figure 4.18: Background subtracted core level spectra of the carbon C1s, nitrogen N1s, oxygen O1s, and copper Cu2p emission arising from the molecules in the MBW structure. The spectra are obtained at an energy 4 eV below the Bragg energy. For C1s and O1s, the chemically different species are separated by the shown model. The Gaussian curve of the energy loss tail at high binding energies is not shown in those models.

The satellite structure of this presented model is similar to the fitting model reported for the metastable LT-phase of PTCDA on Ag(111) [HTS+10]. In this case, a significant overlap of the carboxylic satellite with the anhydrite main line was described. An explanation for this changed satellite structure is a different interaction of the molecule with the underlying metal in the different structures. This results in modified charge transfer satellites, which are visible in the core level spectra [Häm10].

For each component of the O1s fitting model, the peak parameters are summarized in table 4.1. The stoichiometric ratio between the carboxylic oxygens and the anhydride oxygen (2:1) is reflected in the relative intensity of the superpositions of main line and corresponding satellite emission. In order to create the partial yield curves for both oxygen species, the en-

O1s species	$E_{\rm b}[{ m eV}]$	FWHM [eV]	Intensity [%]
Carboxylic Oxygen Main line	530.8	1.3	23
Carboxylic Oxygen Satellite	530.8 + 1.5	2.3	28
Anhydride Oxygen Main Line	530.8 + 2.4	1.3	9
Anhydride Oxygen Satellite	530.8 + 2.6	2.3	16
Energy Loss Satellite	535.6	5.8	24

Table 4.1: Summary of the binding energy position $E_{\rm b}$, the FWHM, and the relative area (intensity) of the fitting model contributions used to deconvolute the contribution of the carboxylic and the anhydride oxygen belonging to the PTCDA molecule.

ergy positions and the FHWM of all peaks are fixed to the values in table 4.1. Furthermore, the relative intensity of the satellite features to their corresponding main line is fixed. The presented fitting model results in the highest coherent fraction F^H for the XSW analysis, which indicates a successful separation of both oxygen contributions.

The correlation between the highest coherent fractions and the best separation of two contributions to one core level spectrum can be understood in a simple example. In order to clarify this, we assume two chemically different species which are located at different adsorption heights. An ideal core level model, which would perfectly separate both contributions, would yield certain values for the coherent fractions for both species in the XSW analysis. Each other core level model, which does not perfectly separate both contributions, results in yield curves, which contain information about both adsorption heights. Hence, the XSW analysis would result in lower coherent fractions for these yield curves, since the vertical order is reduced by the contributions of the other adsorption heights. For large adsorption height differences for both species, this effect becomes more pronounced.

In order to separate the contribution of PTCDA and CuPc to the carbon C1s spectrum shown in Fig. 4.18, all chemical species within the PTCDA and the CuPc molecule have to be considered.

The C1s core level signature for PTCDA was studied in detail both for the thick film and the monolayer structure on Ag(111) [SZJ⁺04, ZKS⁺06]. Four different carbon species could be identified. While three of these chemically different PTCDA carbon species form the main line with an asymmetric peak structure, the carbon atoms directly connected to the oxygen atoms are shifted $\approx 4\,\mathrm{eV}$ to higher binding energies. Based on this information, the PTCDA contribution to the C1s signal of the MBW structure can be described by the green curve in Fig. 4.18. In order to simplify the fitting model, the asymmetric main line is modeled by only two Gaussian profiles (3) and (4). The peak of the C-O carbon species (5) is located at 3.7 eV higher binding energies than the main line. This energy difference is smaller compared to a thick PTCDA film ($\Delta E_{\rm b}^{\rm C-O} = 4.05\,\mathrm{eV}$). Since a similar shift was also observed when

C1s species	$E_{\rm b}[{ m eV}]$	FWHM [eV]	Intensity [%]
CuPc C-C (1)	284.9	1.2	21
CuPc C-N (2)	284.9 + 1.2	1.2	9
PTCDA C-C (incl. C-C-O) (3)	284.3	1.2	22
PTCDA C-H (4)	284.3 + 0.4	1.2	14
PTCDA C-O (5)	284.3 + 3.8	1.7	8
Energy Loss Satellite	290.5	5.6	24

Table 4.2: Summary of the binding energy position $E_{\rm b}$, the FWHM, and the relative area of the fitting model used to separate the contribution of CuPc and PTCDA to the carbon C1s core level signature.

comparing a multilayer and a monolayer structure of PTCDA on Ag(111), it points to a different interaction of the molecules with their surrounding environment. The C-C main line of PTCDA is found at 0.3 eV higher binding energies compared to the monolayer structure [Häm10], which indicates a different polarizability of the molecule. This could also be an indication for the different charge transfer into the PTCDA molecule.

For a correct separation of the PTCDA partial yield, the relative peak areas of all PTCDA components is constrained to their stoichiometric ratio.

For CuPc, the carbons located at the pyrrole ring (2) can be distinguished from those of the benzene rings (1) due to the more positively charged environment [ECS+07]. Fixing the relative peak areas to the ratio reported for gas phase photoemission data [ECS+07] results in the blue curves in Fig. 4.18 which depicts the CuPc contribution to the mixed C1s spectra. The relative shift of the C-N carbon (2) with respect to the CuPc main line (1) is fixed to $\Delta E_{\rm b}^{\text{C-N, MBW}} = 1.2\,\mathrm{eV}$, a value that was also reported for the monolayer adsorption of SnPc/Ag(111) [HSS+09]. This constrain allows to determine the binding energy of the CuPc main line to $E_{\rm b}^{\text{C-C,MBW}} = 284.9\,\mathrm{eV}$. This value agrees well with the peak position for the pure CuPc monolayer structure.

All details of the fitting model applied to separate the contributions of CuPc and PTCDA to the carbon core level emission are summarized in table 4.2. This fitting model also revealed the highest coherent fraction F^H in the XSW analysis, which again indicates an appropriate separation of the chemical species. The FWHM of all lines are constrained to the same value except the C-O peak of PTCDA. For the XSW analysis, the relative ratios of the integrated intensities of all peaks belonging to CuPc and to PTCDA as well as all energetic peak positions are fixed resulting in only one fitting parameter for each molecule. This was necessary since otherwise no significant results could be obtained. The resulting coherent position P^H consequently represents an average adsorption height of the molecular carbon body.

4.3.2 Adsorption heights

Based on the core level models introduced in the previous chapter 4.3.1, the core level spectra are fitted and analyzed. In Fig. 4.19, exemplary photoemission yield curves for single XSW scans are shown together with a typical reflectivity profile of the Ag(111) crystal. In order to determine the XSW fitting parameters, i.e., the coherent position P^H and fraction F^H , a least square fit of the yield curves was performed using the dedicated XSW-analysis program Torricelli by Giuseppe Mercurio [Mer12]. The resulting fitting curve and the coherent positions and fractions of these single XSW scans are included in Fig. 4.19.

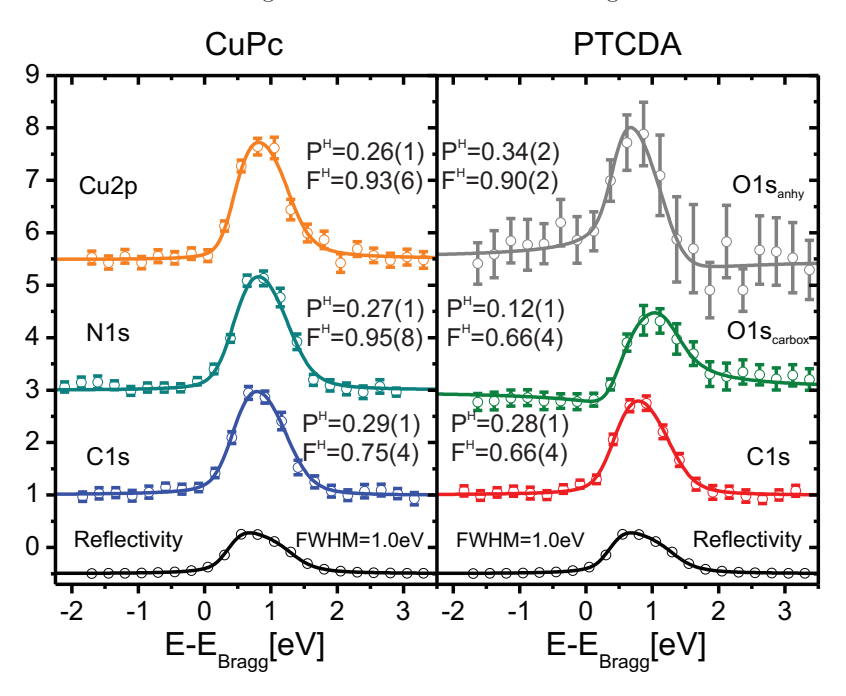


Figure 4.19: Yield curves of a single XSW scan for all chemically different species found for the mixed brick wall structure. The yield curves were created by fitting the core level data according to the models discussed in chapter 4.3.1. The solid lines represent fits to the yield curves performed with *Torricelli* [Mer12]. The numbers given for the each species represent the fitting result this particular single XSW scan.

The uncertainty of a single XSW scan can be estimated in two steps. First, the error bars of the photoemission yield curve are calculated by the Monte Carlo error analysis included in CasaXPS [Mer12, Fai11]. In this way, the statistical error of the experimental data and its impact on the core level fitting result is taken into account. In the XSW-analysis, these errors are considered in the fitting procedure of the yield curve implemented in *Torriceli* and

hence are also propagated onto the uncertainties of the coherent position and fraction.

For a complete XSW data set, usually several single XSW scans are performed for each species. The error of each species can be estimated by the spreading of the coherent positions P^H and fractions F^H and can hence be calculated by the standard deviation of all fitting results. In Fig. 4.20(a), these fitting results are displayed in the so called Argand diagram, in which the coherent position P^H is plotted as a polar angle and the coherent fraction F^H as the radial component. For the Cu2p (orange circles) and the anhydride oxygen species (gray circles), the scattering of the data is larger compared to all other species. The reason for this is the small number of copper atoms, which results in a rather poor signal to noise ratio of the Cu2p core level signal and hence in a larger statistical spread of the fitting parameters. The scattering of the anhydride oxygen data is caused by its high energetic overlap with the core level signal carboxylic oxygen species. The photoemission signal of the anhydride oxygen emission is found on a background, which is formed by the carboxylic oxygen emission. Consequently, the uncertainty of the integrated carboxylic intensity introduces an additional error on the background in the energy region of the anhydride core level features. This effect and the statistical variation of the anhydride signal itself sum up to larger uncertainties of the integrated O1s_{anhy} signal. These larger errors consequently increase the uncertainties of the XSW results.

In this way, the uncertainty of the adsorption height of the anhydride oxygen atoms and of the other species was determined to $d_{\text{anhy}}^H = \pm 0.05 \,\text{Å}$ and $d^H = \pm 0.02 \,\text{Å}$, respectively.

chemical species	P^H	F^H	$d_{\mathrm{MBW}}^{H}\left[\mathrm{\mathring{A}} ight]$	$d_{ ext{PTCDA,ML}}^{H} \left[ext{Å} ight]$	$d_{\mathrm{CuPc},\mathrm{ML}}^{H}\left[\mathrm{\mathring{A}} ight]$
C1s _{sum}	0.280 ± 0.004	0.73 ± 0.01	3.01 ± 0.01	-	-
C1s _{CuPc}	0.293 ± 0.007	0.77 ± 0.03	3.04 ± 0.02	-	3.08 ± 0.02
C1s _{PTCDA}	0.277 ± 0.007	0.71 ± 0.04	3.00 ± 0.02	2.86 ± 0.01	-
O1s _{sum}	0.173 ± 0.005	0.55 ± 0.05	2.76 ± 0.02	2.86 ± 0.02	-
O1s _{carbox}	0.120 ± 0.007	0.63 ± 0.04	2.63 ± 0.02	2.66 ± 0.03	-
O1s _{anhy}	0.320 ± 0.020	0.80 ± 0.10	3.10 ± 0.05	2.98 ± 0.08	-
O1s _{anhy,VA}	0.290 ± 0.030	0.62 ± 0.15	3.03 ± 0.09	2.98 ± 0.08	-
N1s _{CuPc}	0.270 ± 0.007	0.95 ± 0.05	2.98 ± 0.02	-	3.07 ± 0.04
Cu2p _{CuPc}	0.261 ± 0.010	0.98 ± 0.10	2.97 ± 0.02	-	3.02 ± 0.04

Table 4.3: Summary of the XSW results for the MBW structure averaged over all single XSW scans. The literature results for the pure PTCDA [HTS+10] as well as for the CuPc monolayer structure [KSS+10] on Ag(111) are included for comparison. The results for C1s_{sum} and O1s_{sum} are obtained by analyzing the total photoelectron yield of the corresponding atomic species. For the anhydride oxygen species, the $P_{\rm VA}^H$ and $F_{\rm VA}^H$ were calculated from the fitting results of the total oxygen yield and the carboxylic partial yield under consideration of the stoichiometric ratio of carboxylic to anhydride oxygen atoms.

A complete summary of all XSW-fitting results, i.e., the average coherent positions, fractions, and the resulting adsorption heights, can be found in table 4.3. For comparison, the corresponding adsorption height of the molecules in their pure monolayer structures are also included.

For the carbon and oxygen species, the partial electron yield of the separated components and the total electron yield were analyzed (see table 4.3). This allows to inspect the reliability of the separation of the included species.

For the carbon species in CuPc and PTCDA, almost identical adsorption heights are obtained by the partial yield analysis (see table 4.3). This finding is supported by the high coherent fraction F_{sum}^H of the total C1s electron yield, which is comparable to the corresponding value of PTCDA or CuPc in a mono-organic monolayer film on Ag(111) [HTS⁺10, KSS⁺10]. In analogy to the latter films, this indicates a high vertical order of all carbon atoms in the mixed organic film and hence points also to a similar adsorption height for PTCDA and CuPc. Consequently, the obtained adsorption heights for the partial carbon yields of CuPc and PTCDA are reliable.

The coherent fraction F_{sum}^H of the total O1s electron yield is significantly lower compared to the corresponding value for the carbon atoms and hence points to the appearance of several adsorption heights. This is in agreement with the pure PTCDA monolayer film, in which different adsorption heights have been reported for the carboxylic and anhydride oxygen atoms [HTS+10]. The XSW fitting results of the total O1s yield can be calculated from the sum of the fitting results of the oxygen partial yields when considering the stoichiometric ratio of both oxygen species. In the same way, the coherent fraction F_{VA}^H and position P_{VA}^H of the anhydride oxygen species can be calculated from the fitting results of the total oxygen yield and the carboxylic partial yield. The fitting parameters are labeled with the index VA in table 4.3. Within the experimental uncertainties, these calculated XSW parameters match the fitting results of the anhydride oxygen partial yield and also point to a reliable separation of the carboxylic and anhydride oxygen species.

In agreement with the findings for the CuPc monolayer structure, the CuPc molecules in the MBW structure reveal an almost flat adsorption geometry. This statement is based on the similar adsorption heights of all molecular species, but also on their high coherent fractions. The decrease of the coherent fraction F^H from copper via nitrogen to carbon is just a tribute to the increasing number of atoms of the corresponding species. However, the nitrogen atoms are found at a slightly smaller adsorption height than the carbon wings, which was already reported for H_2Pc and CuPc on Ag(111) [Krö11, KBB⁺12]. Fig. 4.21 illustrates the vertical adsorption geometry. The CuPc molecules in the mixed layer are shown in color, those from the monolayer structure in gray. For the latter, an average adsorption distance

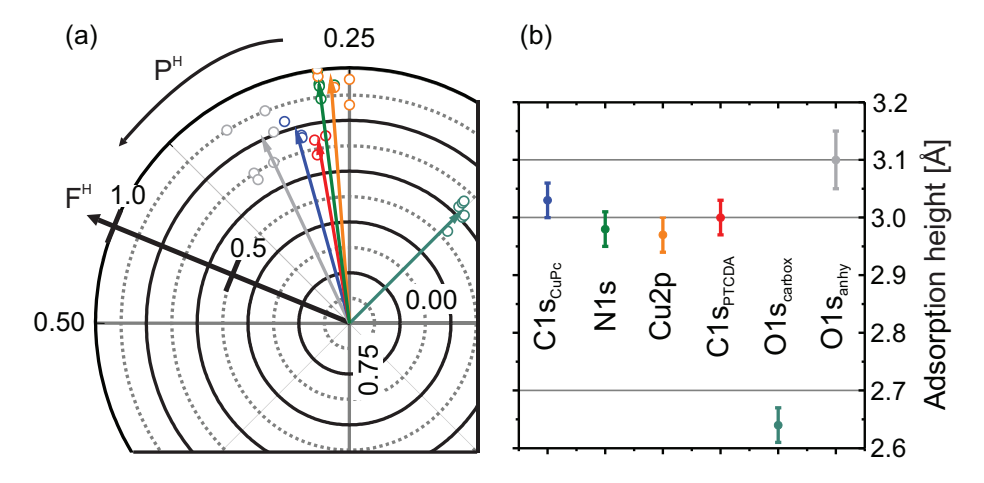


Figure 4.20: (a) Argand representation of the fitting results for all individual XSW scans. The arrows indicate the coherent position P^H and fraction F^H averaged over all single XSW scans of one atomic species. (b) Adsorption height of the atomic species included in CuPc and PTCDA. The color code holds also for the Argand diagram shown in (a).

of $\bar{d}_{\text{CuPc}} = 3.05\,\text{Å}$ was reported [KSS⁺10]. This value is smaller than the sum of the corresponding van der Waals radii suggesting an overlap of the molecular wave functions with substrate states. Consequently, this finding indicates a chemical interaction between the molecule and the substrate [KSS⁺10, Krö11]. In the MBW structure CuPc was found at an even lower height of 3.01 Å, which suggests a stronger binding to the surface. This value is similar to the one for the disordered submonolayer coverage of CuPc/Ag(111) at low temperatures [KSS⁺10, Krö11]. In this phase, the molecules align along the silver rows of the substrate, similar to the case of CuPc in the MBW structure. Obviously, this alignment leads to a reduced adsorption height, which can be explained by higher overlap of molecular and substrate wave functions, compared to the monolayer structure. In the ordered monolayer structure of CuPc on Ag(111), the orientation of the molecules is different, which also changes the adsorption height [KSS⁺10].

However, the average adsorption height of CuPc in the MBW structure clearly indicates a chemical interaction with the substrate. This is not in agreement with the absence of an occupied CuPc LUMO in the electronic valence regime. Obviously, geometric structure (adsorption height) and electronic structure are decoupled in this case. This effect can only stem from the presence of (and interaction with) PTCDA in the MBW structure.

The PTCDA molecules in the mixed layer are significantly distorted compared to the flat molecule in the gas phase. This already points to a chemical interaction between the molecule

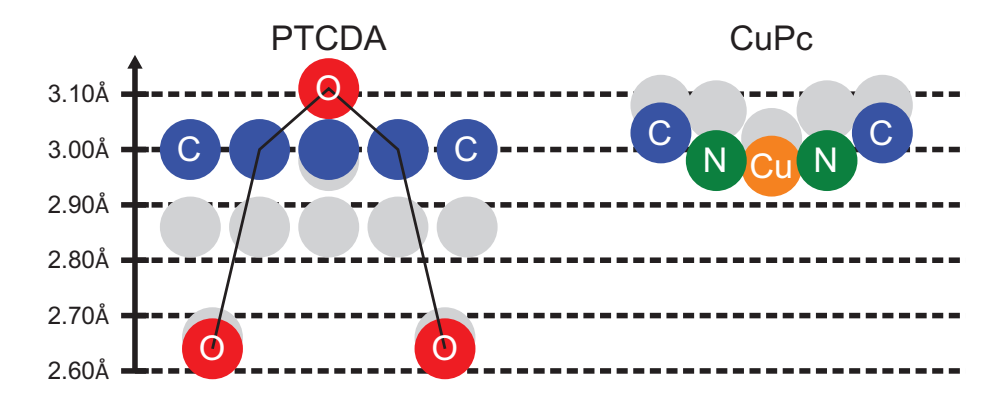


Figure 4.21: Model of the vertical adsorption geometry of CuPc and PTCDA in the MBW structure. PTCDA is shown in the typical front view and CuPc in a schematic side view. The colored circles mark the adsorption heights of the molecules in the mixed layer whereas the gray ones indicate the vertical position for the pure CuPc and PTCDA monolayer structure [HTS+10, KSS+10].

and the substrate. The carboxylic oxygen atoms are found at a smaller adsorption distance than the carbon backbone of the molecule, whereas, the anhydride oxygen atoms are located above the backbone. This vertical geometry is qualitatively known from the monolayer structure and the disordered LT-phase ("precursor phase") of PTCDA on Ag(111) [HTS⁺10]. It is attributed to different interaction channels between the silver surface and the molecule. The carboxylic oxygen atoms are bent towards the surface and form a local Ag-O bond [HKC⁺05, RTT07, KHT⁺08]. The height of the perylene backbone, however, reflects the interaction strength of the delocalized π -bond, which forms between the molecule and the surface [HBL⁺07, GSS⁺07].

In order to highlight the differences between the PTCDA molecules in the mixed and the pure monolayer film both vertical adsorption geometries are illustrated in Fig. 4.21, again in color for the MBW structure and in gray for the pure monolayer film. The vertical position of the carboxylic oxygen is almost the same for PTCDA in both structures, i.e., the Ag-O bond is not influenced by the interaction between PTCDA and CuPc. This is surprising since the PTCDA molecules in the mixed layer are no longer aligned along the atomic rows of the substrate. Consequently, not all oxygen atoms of PTCDA can adsorb on top of silver atoms as it is the case in the pure phase. On the other hand, this bond can also be modified by the interaction between neighboring molecules. The attractive O···H interaction between two PTCDA molecules in the herringbone monolayer structure can result in a lifting force on the carboxylic oxygen atoms. These lateral bonds can also be formed to the hydrogen terminated CuPc molecule and might explain the unchanged adsorption height of the carboxylic oxygens. In contrast, the carbon backbone of the PTCDA molecule in the mixed layer is clearly lifted

 $0.14\,\text{Å}$ due to the interaction with CuPc. The increased adsorption height of the perylene core, where the LUMO level of PTCDA is located, indicates a weakening of the π -bond with the surface. This should be reflected in a depopulation of the LUMO state [DGS⁺08, Krö11]. However, even an additional population of this molecular level is observed (see section 4.2.1), which suggests an even stronger interaction with the surface. This contradictory experimental findings will be further discussed in the next chapter 4.4.

4.3.3 Conclusion

We have investigated the vertical adsorption geometry using the X-ray standing wave-technique. All core level signals of the chemical species involved could be separated, even for the complicated case of the C1s spectrum with five different components. Therefore, the average carbon contribution of PTCDA and CuPc could be separated.

The resulting vertical adsorption height of CuPc in the MBW structure is slightly lower than in the ordered monolayer structure on Ag(111) suggesting a stronger interaction with the surface. For PTCDA, the carboxylic oxygens, which form a local Ag-O bond to the surface, are found at the same height as in the bare monolayer structure. In contrast, the perylene backbone of the molecule is lifted leading to the assumption that the π -bond between the molecule and the substrate is weakened. However, the lower adsorption height of CuPc as well as the lifted the carbon backbone of PTCDA do not agree with the electronic structure found for this mixed system. In the valence region, no signature of the CuPc LUMO state was found and an additional charge transfer into the PTCDA LUMO was detected. Both contradictory findings will be discussed in detail in the next chapter 4.4.

4.4 Influence of the lateral intermolecular interaction on the adsorption behavior

Up to now, the different experimental findings, like the lateral or vertical geometry as well as the electronic structure, have always been analyzed in order to reveal the adsorption properties of the individual molecules in the mixed organic film. Comparing these findings to the molecules in the pure monolayer films allowed to characterize their modifications upon the formation of a mixed film. This resulted in contradictory conclusions for the electronic structure and the adsorption height of the individual molecules in the mixed film, which are discussed in the following.

For mono-organic films like $\operatorname{CuPc/Ag}(111)$ [KSS⁺10] or PTCDA/Ag(111) [Tau07], the charge

transfer into the molecular LUMO level, and hence the strength of the molecule-substrate interaction [DGS⁺08, Krö11], is always reflected in the average adsorption height of the molecules, i.e., a reduced adsorption height results in an enhanced population of the LUMO state [HBL⁺07, GSS⁺07, KSK⁺11]. This concept established for mono-organic systems cannot explain the findings in the mixed organic film. While the PTCDA LUMO is further populated due to the interaction with CuPc, its carbon backbone is lifted. The CuPc LUMO, which is partially occupied in the pure monolayer film on Ag(111), is completely depopulated in the mixed structure. Its adsorption height, however, is even lower than in the monolayer structure.

These conflicting results suggest that, for the individual molecules in the mixed film, the charge transfer into the molecule is not coupled to its vertical adsorption height anymore. Consequently, the binding energy position of electronic valence states of the molecules are no longer reflected in their bonding distance to the surface. The modified population of the molecular orbitals has to be induced by the intermolecular interaction with the neighboring molecules. Such an interaction can also explain the unusual brick wall pattern for the PTCDA molecules in the MBW structure. In fact, the unoccupied molecular states of the mixed layered system reveal a delocalized interface state, which expands over all molecules in the mixed structure (see chapter 4.2.2). This interface state is a hybrid state caused by the depopulation of the surface state and contains an admixture of the lowest unoccupied PTCDA and CuPc states, as can be seen from the analogy to the pure PTCDA layer [TSLT06, KTH+06, RTT07, SSM+08, DP10, MZS+11]. Based on this conclusion, the electronic structure of both molecules in the mixed structure cannot be interpreted separately anymore. They are coupled via the hybrid state with the substrate leading to the formation of a common band structure. This common electronic interface state might also cause the lifting of the PTCDA backbone to almost the same height as the carbon rings of CuPc in order to create a similar overlap of the π -conjugated orbitals with the substrate.

Such an electronic coupling of both molecules can explain the charge redistribution between CuPc and PTCDA when reconsidering the interaction channels between the individual molecules and the substrate. In general, the interaction with the substrate is explained by charge transfer from the molecule into the substrate ("donation") and from the surface into the molecule ("back-donation"). The latter causes the population of the molecular LUMO state [AS09, SHK+09]. For PTCDA, the measured adsorption height of the carboxylic oxygen atoms suggests that the charge donation into the substrate is not strongly changed by the formation of the mixed layer [HTS+10]. The same is true for CuPc since the organic body of the molecule is in roughly the same distance from the silver surface compared to bare CuPc layers. The charge transfer back into the molecule leads to the occupation of the energetically lowest orbital available. In case of individual molecules, this is just the LUMO.

In the case of different types of molecules as in the MBW structure, which reveal a coupling of their electronic states, that obviously is the PTCDA LUMO, which appears energetically below the CuPc LUMO. This conclusion appears to be reasonable since for the pure adsorbate systems the binding energy of the PTCDA LUMO is higher than the one of the CuPc LUMO state [ZKS+06, DGS+08, KSS+10]. Whether the enhanced charge transfer into the PTCDA molecule directly originates from the silver substrate or is mediated via the CuPc molecule cannot be answered without quantum chemical calculations. Very recently, the first results from such calculations became available and are briefly discussed in the outlook.

A charge redistribution between two organic molecules on a noble metal surface has up to now only been reported for typical charge transfer complexes like tetrathiafulvalene (TTF) and tetracyanoquinodimethane (TCNQ) adsorbed on a Au(111) surface [GLFTF⁺08]. For this mixed organic system, a defined charge transfer of one electron from the TTF HOMO state to the TCNQ LUMO level was observed for a flat adsorption of both molecules on gold. A charge transfer directly from one molecule to the other is also known for TTF-TCNQ mixed bulk crystals. However, the charge redistribution for this system is fundamentally different to the situation reported here for the CuPc-PTCDA mixed system. Our results suggest that both molecules transfer charge to the substrate followed by a back donation into only one molecular orbital. Consequently, the chemical interaction with the substrate is crucial for the charge exchange. This is not the case for the TTF-TCNQ complex since the charge exchange does also occur in molecular crystals. Furthermore, two unequal interface states are observed for TTF-TCNQ on Au(111). Each of these unoccupied states is confined to one molecular species and results from a different interaction of both molecules with the surface. Their energetic position is also not identical. All these aspects represent differences between the TTF-TCNQ and the CuPc-PTCDA/Ag(111) system. In our case, the interface state is delocalized and expands over both molecules. It is more likely a result of the complex interaction of the unoccupied orbitals of both molecules with the silver surface state.

4.5 Conclusion

In this chapter, the geometric and the electronic properties of laterally mixed films of CuPc and PTCDA adsorbed on Ag(111) were discussed, based on various experimental findings.

The lateral order in these mixed films was examined with high resolution low energy electron diffraction (SPA-LEED) and scanning tunneling microscopy (STM). Three different mixed phases were found by mixing different coverages of CuPc and PTCDA in the submonolayer regime. In the PTCDA-rich regime, the commensurate Mixed Brick Wall (MBW) structure

with two PTCDA and one CuPc molecule occurs. The structures of the Mixed One-to-One $(M1^21)$ phase reveal an equal number of both molecular species and the CuPc-rich Mixed Zig-Zag phase contains a variety of continuously changing unit cells with two CuPc and one PTCDA per unit cell.

Although the superstructure lattices of these three phases are completely different, the molecular orientations in all structures are very similar. The CuPc molecules align with on pair of wings along or close to atomic rows of the silver substrate while PTCDA is rotated $\approx 30^{\circ}$ with respect to that. This relative orientation of the molecules in all mixed structures allows the formation of $O \cdot \cdot \cdot H$ bonds with neighboring molecules.

The occupied and unoccupied electronic valence structure of the mixed organic films was accessed by angle resolved photoelectron spectroscopy (ARPES) and scanning tunneling spectroscopy (STS). For all three mixed phases, the same modifications of the valance structure were found upon forming a mixed layer. The PTCDA LUMO is located at higher binding energies than in the monolayer structure, which suggests an enhanced population of the PTCDA LUMO. On the other hand, no sign of the CuPc LUMO is evident in the energy region close to the Fermi level. Consequently, the latter state is depopulated by the interaction with PTCDA. This is obvious since the CuPc LUMO is partially occupied in the pure CuPc films on Ag(111).

For energies above the Fermi level, a delocalized interface state was discovered, which expands over all molecules of the mixed film. This state is a hybrid state, which is derived from the depopulated surface state of Ag(111) and contains an admixture of unoccupied CuPc and PTCDA states.

The adsorption height of CuPc and PTCDA in the mixed film is studied with the X-ray standing wave technique. For PTCDA, the carbon backbone is lifted compared to the monolayer film while the carboxylic oxygen atoms are found at the same adsorption height in the pure and mixed phase. CuPc is located at a slightly lower adsorption height compared to the monolayer film and matches the height of the PTCDA backbone in the mixed film. These modifications of the molecular adsorption heights indicate a stronger bonding of CuPc to the silver surface while the PTCDA π -bond is weakened compared to the mono-organic films. However, this interpretation contradicts the energetic positions of the molecular orbitals found in ARPES.

The conflicting results of the electronic valence structure and the adsorption height of the individual molecules in the mixed organic film suggest that the charge transfer into the molecules is no longer coupled to their adsorption height. Instead, the electronic orbital structure of all molecules in the mixed film are coupled via an unoccupied interface state. Consequently, the charge transfer from the substrate into this common electronic structure only leads to a

population of the energetically lowest molecular orbital. In the CuPc-PTCDA mixed films, this state is the PTCDA LUMO.

4.6 Outlook

The investigation of the hetero-organic films revealed significant differences in the adsorption behavior of the individual molecules in the mixed organic layer compared to the pure adsorbate systems. Especially, the very interesting relation between geometric structure (adsorption height) and electronic structure (shift of the charge transfer from CuPc to PTCDA) is a highly interesting experimental observation, which requires additional studies of the MBW structure before the adsorption behavior is fully understood.

We explained these phenomena by a coupling of the molecular levels via the interface state, which expands over all molecules in the unit cell. Since this state was identified by conventional tunneling spectroscopy, the dispersive character of this state is unknown. With two photon photoelectron spectroscopy, the dispersion of this state and its effective band mass can be determined. Furthermore, density functional theory (DFT) calculations could unmask the metal and molecular states contributing to the interface state and hence assists in the understanding of this delocalized state. Quantum chemical calculations would also provide substantial insight into the charge transport channels occurring in this system and hence could contribute to a more general understanding of metal-mixed organic interfaces.

Very recently, first results from such calculations became available for the MBW structure. Peter Puschnig and coworkers [LP12] used density functional theory to calculate the projected density of states (PDOS) of the individual molecules in the MBW structure. In agreement with our spectroscopic results (see chapter 4.2), they found a completely populated PTCDA LUMO with highest PDOS at $E-E_F\approx 0.4\,\mathrm{eV}$ and a depopulated CuPc LUMO. As a reference for the pure CuPc and PTCDA phases on Ag(111), they removed either the CuPc or the PTCDA molecules from the MBW unit cell and repeated the calculations. This results in the PDOS of the mono-organic systems, which also revealed LUMO binding energy positions very close to the experimentally obtained values, i.e., both LUMO levels are partially occupied. Consequently, these first DFT calculations could reproduce the modification of the electronic structure of the molecules in the MBW structure.

Although the lateral structures of the CuPc-PTCDA mixed layers have been investigated in detail, the mixing process itself has only been mentioned briefly. There are only few methods that can provide time resolution in order to study kinetic processes in real time. Suited tools are photoelectron emission microscopy (PEEM) and low energy electron microscopy (LEEM). First results, obtained recently, show that the formation of mixed islands during

the organic film growth can be observed [HK]. Temperature dependent experiments can contribute to a better understanding of the energy barriers of the mixing process.

Apart from additional projects with the materials CuPc and PTCDA on Ag(111), a variety of different prototype molecules and surfaces show great potential for interesting studies. Since the interaction between CuPc and PTCDA and the surface plays a crucial role for the electronic properties of the hetero-organic system, a variation of the substrate could result in a more fundamental understanding of the mixed interfaces. Turning from the medium reactive silver surface to the inert gold substrate, the molecule-substrate interaction is significantly weakened. Consequently, the growth properties of these films should be dominated by intermolecular interactions. On the other hand, by using Cu(111) stead of Ag(111) substrates the molecule-substrate interaction could be enhanced.

Furthermore, changing the adsorbate molecules opens a wide field of new opportunities. Substituting PTCDA by the smaller perylene derivate NTCDA could lead to different lateral structures with smaller unit cell sizes. In addition, the electronic structure of NTC-DA/Ag(111) reveals a many-body resonance in the ARPES signature very close to the Fermi level [SKZ+10]. A similar feature was also reported for CuPc/Ag(111) at low temperatures [KSS+10]. This sharp state is attributed to a Kondo-resonance and hence results from an effective spin moment on the molecule. If both molecules in the mixed film exhibit an effective spin moment, this could lead to a spin-spin interaction in the organic film, which provides an additional interaction channel between the molecules.

5 Vertical intermolecular interaction: CuPc on PTCDA on Ag(111)

The investigation of organic-organic interfaces is on the one hand motivated by their important role in organic electronic devices, on the other hand by the fundamental interest in intermolecular interaction mechanisms between different types of molecules. Here we consider in particular the interaction along their stacking direction in the hetero-organic film. This information is complementary to the results obtained for the laterally mixed organic films discussed in chapter 4. For the latter system, the molecule-substrate interaction as well as the substrate mediated intermolecular interaction has a crucial impact on the structure formation of those mixed films. In contrast, the organic-organic interfaces are expected to be decoupled from the substrate and the intermolecular interactions between the layers are mainly induced by the molecular π -electron systems. Consequently, a combination of the findings obtained for both mixed organic systems can lead to a comprehensive understanding of the various interaction channels between different organic molecules.

Although up to now only a few studies focused on hetero-organic interface [HMSK00, SSHT $^+$ 01, MLF05, CHC $^+$ 08, HGS $^+$ 10], it is commonly believed, that the interaction strength between different organic materials is generally dominated by weak van der Waals forces. This idea arises from the analogy of these interfaces to organic bulk crystals which are often stabilized by the π - π -interactions between molecular layers. All experimental results support this idea so far. Häming et al. [HGS $^+$ 10] reported a photoelectron spectroscopy study of the SnPc/PTCDA interface on Ag(111) which revealed that the line shape of all SnPc core level features is identical to the ones for SnPc bulk films. This finding indicates a van der Waals interaction between SnPc and PTCDA. Based on a pair potential approach, Mannsfeld et al. [MLF05] even suggested a general point-on-line registry between two organic lattices at hetero-organic interfaces which also points to a weak vertical intermolecular interplay.

We contribute to these studies by inspecting the CuPc/PTCDA interface on Ag(111) with a variety of different experimental techniques. Especially the determination of the vertical adsorption geometry of this stacked layer can quantify the interaction strength present at the interface. But we also found surprising consequences for the lateral structure formation, as will be discussed below.

The prototype molecules 3,4,9,10-perylenetetra-carboxylic-dianhydride (PTCDA) is most suited for our study since the first closed monolayer on Ag(111) can be prepared by a controlled thermal desorption from a thick PTCDA film. This quality ensures a high reproducibility of the prepared template layer. On top of this layer, thin films of copper-II-phthalocyanine (CuPc) are grown in order to create a hetero-organic interface. The choice of these prototype molecules is justified by the fact that their individual growth properties are well known on this particular surface. Hence, a modification of the adsorption properties of PTCDA/Ag(111), which is induced by the adsorption of CuPc can be identified. This fact allows not only to study the formation of the organic-organic interface but also to reveal modifications of the organic-metal contact induced by CuPc.

Experimental results are presented in the subsequent chapter. The structure formation of the first CuPc layer on PTCDA is presented for various CuPc coverages. In addition, the electronic level alignment of all occupied frontier orbitals is accessed with (angle resolved) photoelectron spectroscopy which yields the first information about the vertical intermolectular interaction strength. The latter is directly studied by the X-ray standing wave method which determines the binding distances at the organic-organic as well as at the metal-organic interface. Combining all experimental results allows to create a model explaining the interaction strength as well as the electronic level alignment at the hetero-organic interface. Note that we already published results of the CuPc/PTCDA hetero-organic bilayer system in Ref. [SSK $^+$ 12], which are also presented in this chapter.

5.1 Lateral order: Long range order and local adsorption geometry

The lateral structure formation of the first layer CuPc on one closed PTCDA monolayer film on Ag(111) is summarized by the high resolution low energy electron diffraction patterns in Fig. 5.1 [SSK+12]. The well known diffraction spots of the PTCDA monolayer structure [KUS04] are visible in all images and marked by red circles. This indicates that the lateral order within the PTCDA film is not lifted by the adsorption of CuPc. Besides the signature of PTCDA, new diffraction features, which can be assigned to CuPc, arise at room temperature. At first, between 0.3 ML and 0.5 ML, only a diffuse, disk-like diffraction intensity is found around the (0,0) reflection which indicates a lack of any long-range order in the CuPc film (Fig. 5.1(a)). The diffuse diffraction intensity condenses into a sharp homogeneous ring when adding more CuPc molecules to the film (Fig. 5.1(b)). The radius of this ring, which corresponds to the average distance between the CuPc molecules on PTCDA, increases continuously with rising coverage and indicates a shrinking intermolecular distance [KSS+10, SKRK11]. When the first CuPc layer is almost closed the molecular order changes.

The diffuse diffraction ring is transformed into sharp diffraction spots which appear in addition to the PTCDA monolayer pattern (Fig. 5.1(c)). This indicates a transition from a disordered layer to one long range ordered film. Similar to the case of CuPc/Ag(111) [KSS+10], this transformation is caused by a steric hindering of the molecular diffusion for high coverages which leads to a trapping of the molecules in minima of the interface potential. This ordered bilayer system CuPc/PTCDA/Ag(111) is in the following referred to as Stacked-Bilayer (SB) structure.

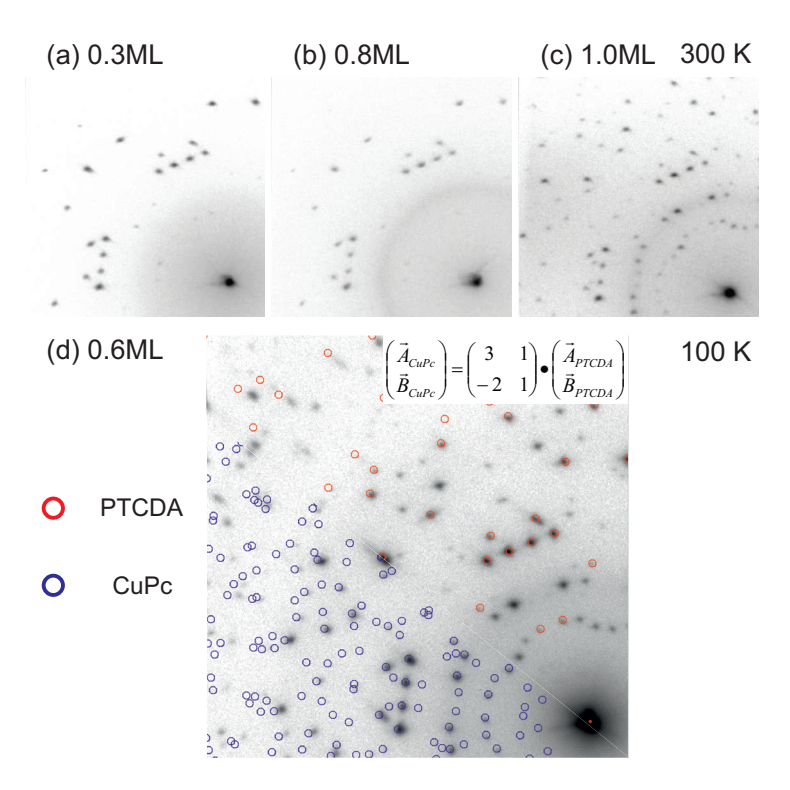


Figure 5.1: High resolution LEED images ($E_{\rm kin}=27.2\,{\rm eV}$) for different CuPc coverages adsorbed on a closed layer PTCDA/ Ag(111) [SSK+12]. Images (a-c) are recorded at RT, image (d) at 100 K. Red and blue circles mark calculated positions of diffraction spots from the PTCDA monolayer structure and the CuPc/PTCDA Stacked-Bilayer structure, respectively. The figure is taken from [SSK+12].

For coverages larger than 0.40 ML, a phase transition to the same ordered structure occurs upon cooling the sample below $T_{\rm sample} < 160\,\rm K$. Here, reducing the thermal energy at the interface leads to condensation of CuPc molecules in energetically favored adsorption sites and results in an ordered structure. Since the lateral order vanishes again when heating the

sample to RT, the energy gain per molecule in the ordered SB structure has to be smaller than the thermal energy at room temperature $\Delta E_{\rm pot} < 25\,{\rm meV}$. However, since reducing the sample temperature or closing the layer results in the SB structure, it represents the global minimum of the total interface potential.

In general, the lateral order of CuPc adsorbed on PTCDA reveals a similar behavior as it is known for its adsorption on the clean Ag(111) [KSS+10] or Au(111) surface [SKRK11]. At RT, no island formation is observed which is the result of a weak or even repulsive interaction between the CuPc molecules. Condensation into ordered islands takes place when reducing the sample temperature. This is a hint for a not vanishing interaction with the underlying layer, i.e., with the PTCDA monolayer or even directly with the silver surface below.

All diffraction spots of the SB structure can be explained by one structural model. A simulated diffraction pattern of this CuPc unit cell is superimposed on the experimental LEED image in the lower left part of Fig. 5.1(d) (blue circles). The diffraction features of the PTCDA monolayer structure are marked with red circles in the upper right part of the image. All PTCDA spots can also be assigned to the SB structure. Consequently, the lattice of the CuPc layer shows a commensurate registry with the PTCDA grid and hence also with the silver surface. This is reflected by the superstructure matrix of the SB structure, which only exhibits integer numbers ¹:

$$\begin{pmatrix} \vec{A} \\ \vec{B} \end{pmatrix}_{\text{SB}} = \begin{pmatrix} 3 & 1 \\ -2 & 1 \end{pmatrix} \cdot \begin{pmatrix} \vec{A} \\ \vec{B} \end{pmatrix}_{\text{PTCDA}} = \begin{pmatrix} 3 & 16 \\ -12 & -9 \end{pmatrix} \cdot \begin{pmatrix} \vec{A} \\ \vec{B} \end{pmatrix}_{\text{Ag}}$$
 (5.1)

This result is rather surprising. A commensurate registry between two grids is usually an indication for a relatively strong interaction between the adsorbate layer and the underlying template. The appearance of this commensurate structure at an organic-organic interface is up to now a unique finding and stands in contrast to the structure formation usually reported in literature [MLF05, CHC+08, SSHT+01, HCC+09]. Even the same interface (CuPc/PTCDA) reveals a completely different behavior on highly ordered pyrolytic graphite (HOPG). Periodic displacement lines in the CuPc grid reflect the lattice mismatch between the CuPc and PTCDA film [CHC+08].

For CuPc/PTCDA/Ag(111), the commensurate registry of both organic grids results in an unusual shape of the CuPc unit cell. Instead of the square unit cell found usually, which resembles the fourfold symmetry of CuPc, an oblique unit cell with the dimensions $|\vec{A}_{\rm SB}| = (42.6 \pm 0.1) \,\text{Å}$, $|\vec{B}_{\rm SB}| = (31.3 \pm 0.1) \,\text{Å}$ and $\gamma = (116.3 \pm 0.4)^{\circ}$ is obtained. Since the PTCDA monolayer structure exhibits a rectangular grid and CuPc molecules usually form

¹The unit cell vectors of the PTCDA cell $(\vec{A}, \vec{B})_{\text{PTCDA}}$ correspond to the PTCDA superstructure cell (3 5 | 6 1) which describes one of the mirror domains of the more commonly used matrix (7 1 | 2 5).

square lattices [CHC⁺08, KSS⁺10, SKRK11], the commensurability is not the result of an arbitrary match between two lattices. It is rather an indication for a significant interaction across the hetero-organic junction which dominates the structure formation of the second molecular layer.

The molecular arrangement within the SB structure has been revealed with low temperature scanning tunneling microscopy. In Fig. 5.2(a) a CuPc island can be seen on a closed PTCDA layer with submolecular resolution. The bare PTCDA film in the lower part of the image shows the well known herringbone structure. This image already confirms that CuPc grows homogeneous on top of PTCDA. The lattice of the SB film is marked in blue, the PTCDA monolayer structure in red. Translating the PTCDA unit cell onto the SB film approves the commensurate registry of the latter and the unit cell dimensions found in SPA-LEED. A closer look into the unit cell is shown in Fig. 5.2(b). Six inequivalent molecules are identified per unit cell and highlighted with ball and stick models. Even though all CuPc molecules show their typical cross like shape, not all molecular wings reveal the same STM contrast. This is caused by an electronic effect rather than a different height. In Fig. 5.2(c)the positions of the underlying PTCDA molecules are marked as dotted ellipses, which illustrates that bright CuPc wings are located directly above a PTCDA molecule, whereas dark wings are found above a gap of the PTCDA layer. This result clearly states that the different contrasts in the STM image are caused by an electronic coupling between the molecules in the first and second layer.

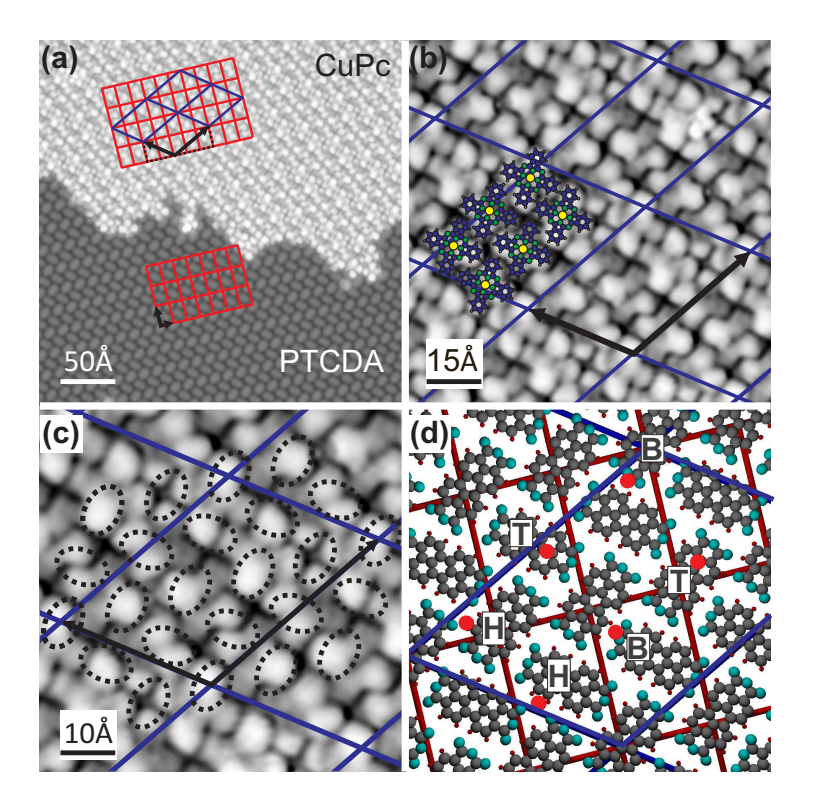


Figure 5.2: (a-c): STM images of the SB phase at T=10 K (0.75 V, 18 pA) [SSK+12]. (a) A CuPc island (bright contrast) has condensed on a closed PTCDA monolayer on Ag(111). PTCDA and CuPc lattices are indicated by red and blue lines, respectively. (b) Close-up of the CuPc island. Six CuPc molecules (one unit cell) are shown as ball-and-stick models. (c) Dotted ellipses indicate the positions of PTCDA molecules under the CuPc layer. Bright STM contrast is found where CuPc wings lie above the PTCDA core. (d) Model of the PTCDA ML-structure. Adsorption sites of CuPc molecules are marked by red circles, the size of which indicate statistical errors. This figure is taken from [SSK+12].

A closer look on the molecular arrangement shows that all six CuPc molecules in the unit cell are equivalent apart from their different electronic contrast. They are equally oriented with an angle of $(45\pm2)^\circ$ relative to the $[\bar{1}10]$ -direction of the silver substrate. When the STM contrast differences are neglected, they form a square lattice with a spacing of $\approx 14\,\text{Å}$, which reflects the size as well as the fourfold symmetry of the CuPc molecule. These structural parameters are comparable to densely packed CuPc layers on various metal surfaces [CHC⁺08, KSS⁺10, SKRK11]. Consequently, the STM contrast difference between those molecules has to be caused by their specific adsorption configurations. Indeed, three distinct

adsorption sites, each occupied twice per unit cell, are found for the six CuPc molecules. The exact adsorption positions are highlighted with red circles in Fig. 5.2(d), their size corresponds to the statistical distribution for this specific adsorption site. The center of the CuPc molecule is either located on top of the PTCDA backbone (PTCDA-top-site, labeled "T" in Fig. 5.2d), above the ditch between two (bridge-site, "B") or between three PTCDA molecules (hollow-site, "H"). Due to the lattice mismatch between the rectangular PTCDA/Ag(111) structure and the fourfold symmetry of CuPc, it is impossible for all molecules to adsorb on identical sites. This also inhibits the formation of an even denser layer. Consequently, the observed CuPc structure represents the best compromise between adsorbing as many CuPc molecules as possible (forming the densest packing possible) and obtaining the energetically best adsorption sites. For this reason the adsorption energy gain at these three adsorption sites must be rather large. Otherwise, more molecules would be adsorbed on the surface leading to the formation of a more densely packed point-on-line or even incommensurate lattice. This again supports the statement of an unusual strong interaction at the CuPc/PTCDA hetero-organic interface.

Another hint for the influence of the PTCDA layer on the SB structure is found when studying the CuPc growth behavior beyond the first closed layer. The diffraction pattern of $1.4\,\mathrm{ML}$ CuPc is shown in Fig. 5.3(a). Adding CuPc molecules to the ordered SB structure at room temperature leads to a change in the diffraction signature. In order to highlight the slightly modified diffraction pattern of the CuPc layer with higher coverage, characteristic k-space regions are enlarged and displayed next to the LEED image. The same k-space regions of a LEED image of the SB structure are presented in panel (c). Additional spots appear between the second (red boxes) and fourth order (green boxes) diffraction spots of the SB structure in Fig. 5.3(a), which indicates a coexistence of two structures in the electron diffraction pattern. The new diffraction maxima can be modeled by a single lattice with the superstructure matrix $\begin{pmatrix} 1.24 & 5.42 \\ -5.54 & -1.70 \end{pmatrix}$. The positions of the calculated diffraction spots are marked with blue circles in the lower left part of Fig. 5.3(a). In contrast to the large unit cell of the SB film, the lateral order of the 2nd CuPc layer can be described by a square grid with a spacing of $|A_{2nd}| = |B_{2nd}| = 14.2 \text{ Å}$. These lattice parameters describe the intrinsic fourfold symmetry and size of CuPc and reflect the structural results for CuPc molecules adsorbed on weakly interacting surfaces [SKRK11, HLM+10]. The appearance of a smaller unit cell, which only reflects the periodicity of the molecular density, suggests that all CuPc molecules in the 2nd CuPc layer are truly equivalent. The lattice corresponds to the six local adsorption sites of the CuPc molecules in the SB film introduced in Fig. 5.2(d). Connecting the red circles in the latter figure, which mark the different adsorptions sites, reveals a square lattice, which almost matches the CuPc 2nd layer grid. Consequently, the molecular order in the second CuPc layer on PTCDA is locally very similar to the first layer. The different adsorption sites in the SB film are attributed to differences in the electronic structure due to the interaction of

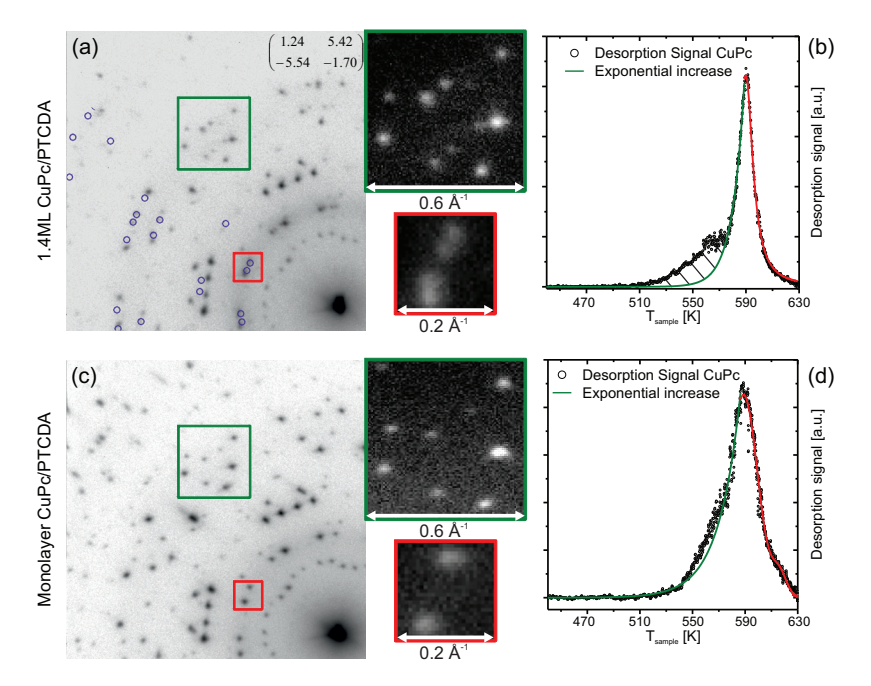


Figure 5.3: (a)+(c): High resolution LEED images ($E_{\rm kin}=27.2\,{\rm eV}$) for the 1.4 ML and 1.0 ML CuPc on PTCDA. The insets enlarge k-space regions which reveal a slightly changed diffraction signature upon increasing the coverage. (b)+(d): CuPc thermal desorption signal of the corresponding layer. The green curve represents an exponential fit to the data in the relative temperature range of $T=455\,{\rm K}$ to $465\,{\rm K}$ and $T=570\,{\rm K}$ to $585\,{\rm K}$.

CuPc with the underlaying PTCDA. Obviously, the interaction at the CuPc/CuPc interface is much weaker than at the CuPc/PTCDA interface.

The study of the CuPc/CuPc interface on PTCDA does not only provide further information about the subsequent CuPc layer growth, but also enables a CuPc coverage calibration. Fig. 5.3(b)+(d) show the thermal desorption signature of the CuPc molecules which was monitored with a quadrupole mass spectrometer (QMS) during sample annealing . An aperture smaller than the crystal surface was placed between the sample and the QMS in order to suppress artificial desorption signals arising from the sample holder. It should be noted, that the sample temperature $T_{\rm sample}$ could only be increased manually and the temperature was not precisely calibrated resulting in a possible temperature offset of up to $\Delta T_{\rm sampe} = \pm 40\,{\rm K}$. However, the quality of the data is still appropriate for a semi-quantitative analysis.

The desorption spectrum of the SB film in Fig. 5.3(d) reveals only one almost symmetric peak which implies that all molecules of the film are in the same adsorption state and hence

in the same layer. Consequently, this desorption feature is assigned to CuPc molecules in direct contact with PTCDA. For the 2nd CuPc layer an additional broad shoulder at lower desorption temperature is observed. This suggests two different adsorption energies for this film and supports the previous conclusion that the additional diffraction spots of the corresponding film in Fig. 5.3(a) are caused by CuPc molecules in the 2nd CuPc layer (3rd organic layer). Based on this information, we used the LEED pattern shown in Fig. 5.3(c) to define $\Theta_{\text{CuPc}} = 1.0 \,\text{ML}$ since it only exhibits a negligible intensity of molecules in higher CuPc layers. During sample preparation, the molecular flux was monitored with the QMS. Normalizing the integrated molecular flux of each sample preparation to the one of the defined monolayer structure allows to estimate the coverage of each submonolayer film. Compared to the growth of CuPc directly on Ag(111), ≈ 1.3 times more material is needed to achieve the same CuPc coverage on PTCDA. This indicates a reduced sticking coefficient of CuPc on PTCDA. For the 2nd CuPc layer, the coverage is estimated by the relative intensity ratio of the 2nd and 1st CuPc layer desorption feature. The intensity of the 2nd CuPc layer desorption signal is accessed by modeling the exponential increase of the desorption peak for the first CuPc layer, resulting in the green curve in Fig. 5.3(b)+(d). The exceeding measured intensity stems from the 2nd CuPc layer (dashed area in Fig. 5.3).

We can conclude the following findings: The structure of one closed PTCDA layer on Ag(111) is not lifted by the additional adsorption of CuPc. The growth behavior of CuPc on PTCDA is quite similar to that on Ag(111) or Au(111). At RT, the CuPc molecules do not form ordered structures, but form a 2D gas with an average intermolecular distance dependent on the coverage. Closing the first CuPc layer on PTCDA or decreasing the sample temperature below 160 K results in a phase transition from that disordered CuPc film to an ordered commensurate superstructure. This so called Stacked-Bilayer structure contains six CuPc molecules in the second layer and 10 PTCDA molecules in the first organic layer per unit cell. All six CuPc molecules in the SB film are equally oriented with $(45 \pm 2)^{\circ}$ relative to the [110] direction of the silver substrate and form a squared lattice with a spacing of ≈ 14 Å if differences in their electronic structure (revealed by their STM contrast) are neglected. The molecules occupy three distinct adsorption sites on PTCDA: "on top" of the PTCDA backbone, above a ditch between two (bridge) or three (hollow) PTCDA molecules.

Increasing the CuPc coverage to more than one layer results in the formation of a CuPc bilayer film. The diffraction signature of this structure reveals a squared lattice with one molecule per unit cell for the 2nd CuPc layer.

5.2 Electronic structure

The interaction strength between organic molecules and their underlying substrate is usually reflected by the molecular level alignment at the interface and a charge transfer across the interface. Since the commensurate registry between the CuPc and PTCDA lattices at the hetero-organic interface provides evidence for a relatively strong intermolecular interaction, the energetic positions of the frontier orbitals were studied by (angle resolved) UPS. In Fig. 5.4(a), valence spectra for different submonolayer coverages of CuPc on PTCDA/Ag(111) are displayed for two different emission angles, normal emission and 45° emission. These data have been recorded at room temperature using a monochromatized UV-source (He I α emission) and a Scienta R4000 electron analyzer.

The spectra of the bare PTCDA monolayer film, lowermost curve in Fig. 5.4(a), exhibits two molecular contributions for both emission angles, which can be assigned to the HOMO and F-LUMO level of PTCDA [KTH+06, ZKS+06, SWR+12]. The latter is populated by charge transfer into the molecular orbital due to the interaction with the substrate. The different intensities of the molecular features are based on the characteristic photoemission angular dependence of the individual orbitals [PRU+11, SWR+12].

Upon adsorption of CuPc on top of the PTCDA layer two new peaks appear in the spectra, the HOMO and HOMO-1 states of CuPc. Their intensity increases with increasing CuPc coverage as can be seen from the different spectra in Fig. 5.4(a). For the topmost one, a fitting model for all molecular resonances is shown. While most molecular orbitals can be described by a single Gaussian peak, the spectral feature at a binding energy of $E_{\rm b} = 0.88\,{\rm eV}$ reveals an asymmetric line shape. For this reason, this spectral line can be assigned to the CuPc HOMO level [ECS+07]. This typical line shape is due to a vibronic progression of the molecular level and is modeled by two additional Gaussians [ECS+07].

At a coverage of $0.2\,\mathrm{ML}$ (all coverages refer to CuPc in the following) the CuPc HOMO is found at a binding energy of $E_\mathrm{b} = 0.88\,\mathrm{eV}$, but shifts significantly (by $40\,\mathrm{meV}$) to higher binding energies at higher coverage ($0.9\,\mathrm{ML}$). It is well visible for both emission angles, whereas the HOMO-1 state can only be seen clearly under off-normal emission. It appears as a shoulder of the PTCDA HOMO-peak at $E_\mathrm{b} = 1.90\,\mathrm{eV}$, but becomes better visible at higher coverage due to a shift of $+80\,\mathrm{meV}$.

The binding energy of the PTCDA HOMO is not affected by the adsorption of CuPc. Its intensity decreases with increasing CuPc film thickness which is caused by scattering of photoelectrons in the CuPc layer. In Fig. 5.4(b), the PTCDA HOMO intensity, normalized to the one of the pure PTCDA monolayer film, is shown for different CuPc coverages. The attenuation of the photoemission signal by an overlayer of thickness Θ can be described in

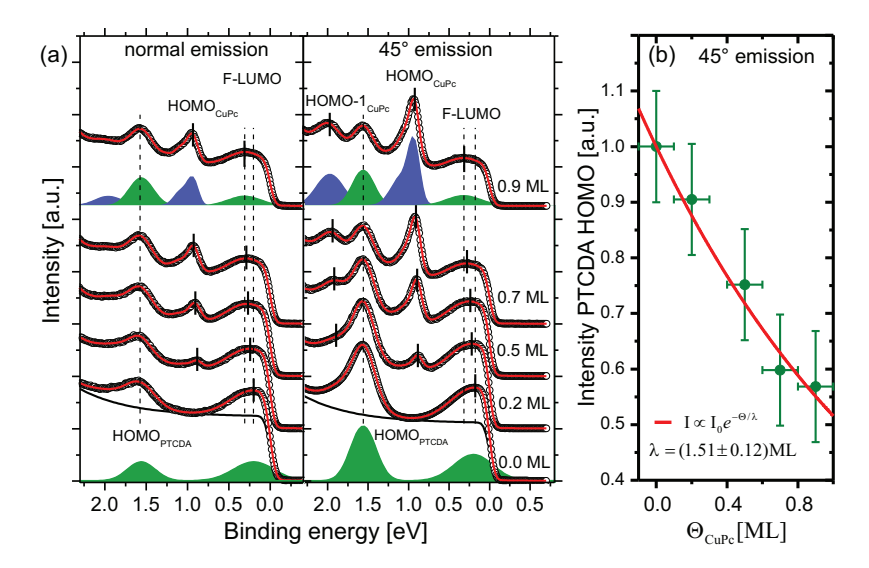


Figure 5.4: (a):UPS data of CuPc/PTCDA/Ag(111) for different CuPc-coverages at RT (black circles, $\hbar\omega=21.218\,\mathrm{eV}$). Red curves represent least square fits to the data. For the lower- and uppermost curves the fitting model consisting of up to four independent peaks is shown, PTCDA and CuPc states are displayed in green and blue, respectively. For fitting the background we used a Fermi function which was broadened in order to account for the instrumental resolution, plus an exponential component (black curve). (b) Intensity of the PTCDA HOMO level as function of CuPc coverage. The red curve illustrates the exponential fitting curve. Panel (a) of this figure is taken from [SSK+12].

the most simple way by the "Lambert-Beer" law:

$$I = I_0 e^{-\Theta/\lambda} \tag{5.2}$$

 I_0 is the intensity of the film underneath the overlayer. The attenuation length λ depends on the kinetic energy of the photoelectrons and the emission angle. An exponential fit to the HOMO intensities in Fig. 5.4(b) allows to determine an attenuation length $\lambda = (1.51 \pm 0.12)\,\mathrm{ML}$ which is similar to the corresponding value reported recently for the adsorption of PTCDA/Ag(111) [GFSR11]. This result becomes important when discussing the revered system PTCDA/CuPc on Ag(111) in chapter 6.

The more important change in the spectra caused by the adsorption of CuPc is a shift of the F-LUMO state close to the Fermi level. As illustrated by vertical dashed lines in Fig. 5.4, this state shifts continuously from $E_{\rm b}=0.20\,{\rm eV}$ to $E_{\rm b}=0.32\,{\rm eV}$, i.e., by as much as 120 meV. This is significant with respect to both instrumental resolution (30 meV) and width of the peak

(between 0.45 eV and 0.55 eV, depending on coverage). It indicates an additional filling of the PTCDA F-LUMO induced by the adsorption of CuPc molecules, i.e., an increase of the charge transfer between substrate and adsorbate (and/or between both organic layers). However it is not yet clear, whether the state close to the Fermi level is only the PTCDA F-LUMO level which shifts to higher binding energies or if this state contains an additional contribution arising from CuPc. In order to answer this question, angle resolved photoelectron spectroscopy data were obtained and analyzed with the orbital tomography approach [PRU+11, SWR+12].

The ARPES data were obtained at the BESSY II synchrotron ($\hbar\omega = 35\,\mathrm{eV}$) and the complete angular distribution of the emitted photoelectrons was recorded by a toroidal analyzer (see chapter 2.2 and 3.1.2). For a film of 0.7 ML CuPc on PTCDA, three constant binding energy (CBE) maps are displayed in Fig. 5.5(a). The binding energies of these maps correspond to the energy positions of the main features identified in the UPS spectra in Fig. 5.4.

The peak at $E_{\rm b}=0.92\,{\rm eV}$ is attributed to the CuPc HOMO. The corresponding CBE map is dominated by a homogeneous ring, which is consistent with the molecular disorder in the CuPc submonolayer film. A continuous circular intensity distribution is caused by a *rotational* disorder of the molecules. Hence this finding confirms the SPA-LEED results, which additionally indicates a translational disorder.

The other two momentum distributions in Fig. 5.5(a) exhibit a defined peak structure in their azimuthal distribution and are hence at least to some extent caused by the ordered PTCDA monolayer. In agreement to the results for the pure PTCDA monolayer film [SWR⁺12], both momentum distribution patterns reveal six defined maxima at a well defined distance from the $\bar{\Gamma}$ -point of the surface Brillouin zone. However, while the PTCDA HOMO map $(E_{\rm b}=1.58\,{\rm eV})$ shows the expected sixfold symmetry, the molecular intensity distribution arising from the LUMO level $(E_{\rm b}=0.27\,{\rm eV})$ only has a threefold symmetry. Although the molecular features of the LUMO level with high photoelectron intensity are found at the same positions in k-space as a substrate band structure, the substrate bands alone can not explain the excessive intensity of those features. The contribution of substrate features to the photoemission intensity has already been reduced significantly by the adsorption of one closed PTCDA layer and should consequently decrease further with rising molecular coverage. As a consequence, this variation in intensity is most probably caused by scattering at the CuPc layer as will be discussed later.

The projected density of states (PDOS) of all involved molecular orbitals can be obtained separately by the orbital tomography approach. This allows to clarify the contribution of all molecules and the substrate to the ARPES data. In analogy to the study of PTCDA on Ag(111) (see chapter 3.1.2), only a circular ring covering the range $|\mathbf{k}_{\parallel}| = 1.25 \,\text{Å}^{-1} \cdots 2.25 \,\text{Å}^{-1}$ is taken into account. For the data cube $I_{\text{HOMO}}(k_x, k_y, E_{\text{b}})$, which was recorded in the energy range of the HOMO levels, only two theoretical momentum maps (CuPc and PTCDA HOMO)

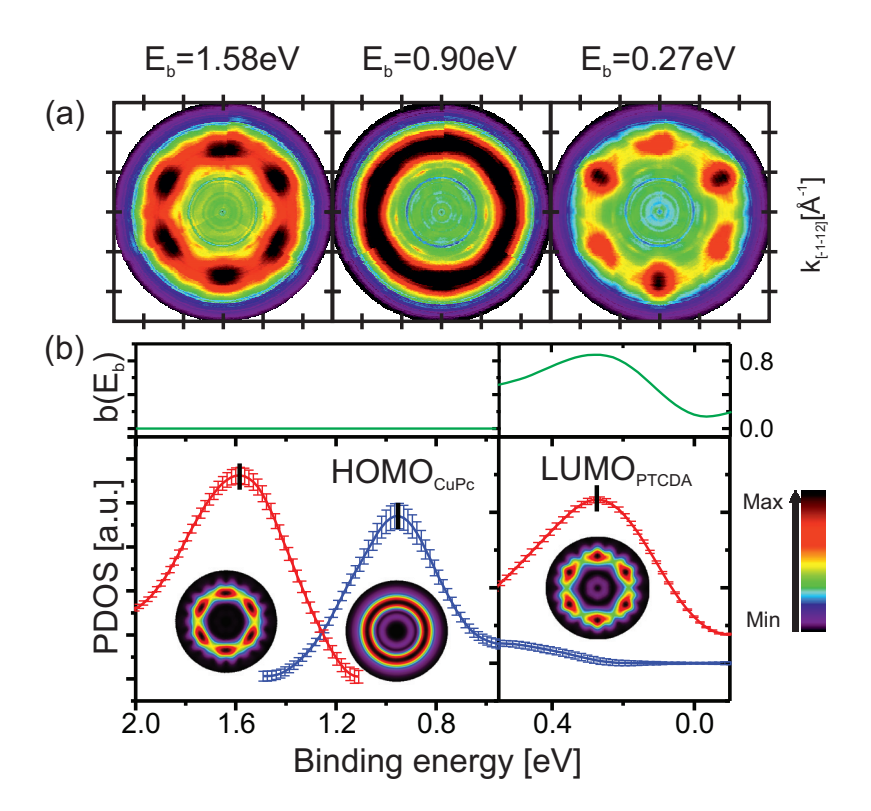


Figure 5.5: (a) Constant binding energy maps for three different binding energies of $\approx 0.7\,\mathrm{ML}$ CuPc on PTCDA. The ARPES data were obtained using synchrotron radiation of $\hbar\omega=35\,\mathrm{eV}$ and recorded with a toroidal analyzer. (b) Projected density of states (PDOS) and substrate contribution $b(E_\mathrm{b})$ obtained by the orbital tomography analysis of the ARPES data. The theoretical momentum maps used for the fitting procedure are depicted below the corresponding curves in (b).

are considered. This is, on the one hand, the momentum map calculated from the HOMOs of the two inequivalent PTCDA molecules and on the other hand, the map for the CuPc HOMO (middle inset of Fig. 5.5(b)). The latter corresponds to a homogeneous ring since the CuPc molecules are randomly orientated. Since no emission features of the substrate are visible in the selected k-space ring, the contribution of the substrate is constrained to zero. The resulting PDOS is shown in the left panel of Fig. 5.5(b) together with error bars estimating the uncertainty of the orbital deconvolution procedure [SWR⁺12]. The energetic positions of the PDOS resonances reflect almost perfectly the results of the UPS study presented in Fig. 5.4. While the CuPc HOMO shows highest density at $E_{\rm b}=0.90\,{\rm eV}$ the corresponding PTCDA level is observed at $E_{\rm b}=1.58\,{\rm eV}$. In addition, a small shoulder is found at the higher binding energy side of the CuPc HOMO which is caused by the well known vibronic progression of

this state $[ECS^+07]$.

The composition of the state just below the Fermi level is even more interesting. Also here, two inequivalent PTCDA and all randomly oriented CuPc molecules have to be considered for calculating the LUMO momentum maps (see above). However, in contrast to the HOMO energy region, the contribution of the substrate cannot be neglected here. The threefold symmetry of the experimental maps in Fig. 5.5(a) shows this clearly, since it cannot be reproduced by the momentum maps of the molecules. This leads to the PDOS displayed in the right panel of Fig. 5.5(b), which is dominated by the emission of the PTCDA LUMO. In fact, only a small signal of the CuPc LUMO is detectable at higher binding energies which could also be attributed to the low energy tail of the CuPc HOMO peak. This fitting result is not unexpected since the geometric shape of the 2D map in Fig. 5.5(a) reflects nicely the theoretical prediction for the PTCDA LUMO state.

However, the pronounced threefold symmetry of the experimental data can only be attributed to the substrate signal which is less damped than for PTCDA/Ag(111). The substrate scaling factor $b(E_b)$, which has also been optimized in the tomography procedure, is shown in Fig. 5.5 (green curve) and reveals a surprising behavior. Instead of the expected almost flat curve, it shows a clear peak at roughly the same binding energy as the PDOS of the PTCDA LUMO. This indicates that the substrate emission is enhanced at the k-space positions of the PTCDA LUMO resonance which was not observed for the pure PTCDA monolayer film [SWR⁺12]. Consequently this effect must be caused by the adsorption of CuPc. Repeating the orbital tomography fitting procedure without considering the substrate contribution results in almost the identical density of states for both molecular orbitals but with a clearly structured residual. This residual does not only reveal a clear threefold symmetry, but also maxima in k-space, which are known both for the substrate bands and the PTCDA LUMO emission. This supports the statement, that the threefold symmetry of the experimental LUMO map is caused by the emission from the substrate. Although this finding must be caused by the adsorption of CuPc, the mechanism behind this effect is not clear yet.

However, regardless of this effect, it can be concluded, that the spectroscopic feature right below the Fermi energy is caused by the PTCDA LUMO level only and does not contain any CuPc contribution. This proves that the PTCDA F-LUMO state is becoming gradually populated by the adsorption of CuPc.

The modifications of all relevant molecular energy levels with changing coverage are summarized in Fig. 5.6. The level alignment is qualitatively different from previously studied organic-organic interfaces [HMSK00, HGS⁺10], since the adsorption of the molecules in the 2nd layer modifies the binding energies of the orbitals for molecules in the first layer. Consequently, the interface between CuPc and PTCDA can not be discussed without considering the influence of the silver surface.

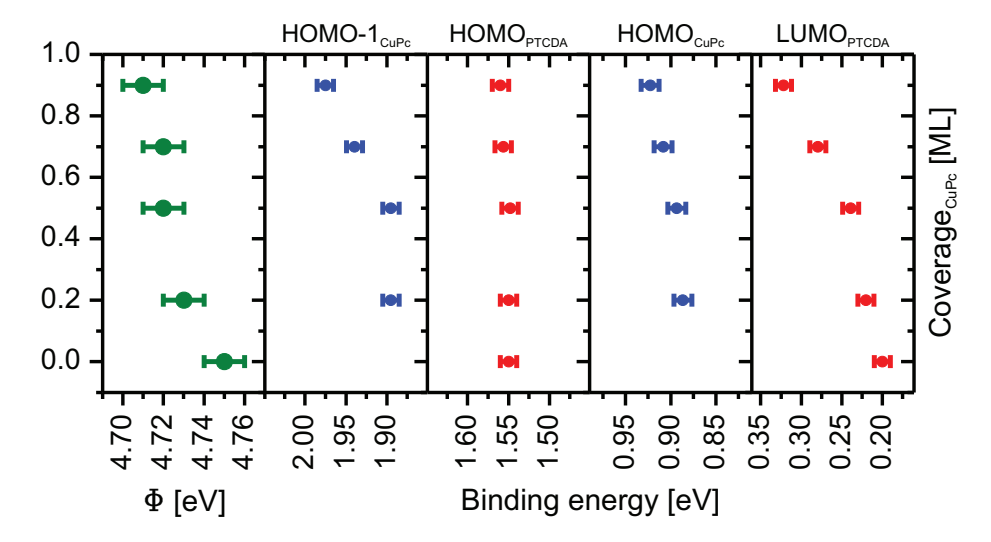


Figure 5.6: Work function Φ and binding energy positions of all molecular features identified for the hetero-organic interface CuPc/PTCDA on Ag(111) as a function of the CuPc coverage. All data have been obtained at RT using a photoemission setup with an energy resolution better than 30 meV.

The adsorption of CuPc leads to a continuous filling of the PTCDA LUMO with rising coverage and an according shift of the energy level. In contrast, the energetic position of the PTCDA HOMO state is hardly influenced, so that the HOMO-LUMO gap of the molecule in direct contact with the Ag(111) surface is reduced. This finding suggests a stronger binding of PTCDA to the silver surface induced by the adsorption of CuPc [KHT⁺08] and differs from the SnPc/PTCDA bilayer on Ag(111), for which no changes of the line shape or the energetic positions of the PTCDA valence levels were detected upon adsorption of SnPc. Accordingly, the interaction strength at the organic-organic interface layer was considered to be physisorptive [HGS⁺10].

When looking at the HOMO to HOMO-1 gap of CuPc on PTCDA/Ag(111), an increase of 40 meV to 1.05 eV can be noticed when increasing the CuPc coverage to almost 1.0 ML. This matches the corresponding gap for a 2 ML CuPc film on CuPc/Ag(111) ($E_{\rm Gap}=1.06\,{\rm eV}$ [Krö11]) and hence indicates a similar decoupling for both molecular systems from the silver substrate.

The work function Φ is also shown in Fig. 5.6. It decreases continuously with increasing CuPc coverage. In order to explain is finding, two effects have to be considered. The formation of a CuPc film on PTCDA enhances the charge transfer into the PTCDA LUMO

and hence modifies the charge redistribution at the metal-organic interface. This results in a larger interface dipole at the silver-PTCDA interface, which on the one hand should leads to a larger work function [RNP+09]. On the other hand, the effective charge in the PTCDA LUMO level polarizes the CuPc molecules and induces a dipole layer in the CuPc film. According to Häming et al. [HGS+10], this dipole layer reduces the work function of the whole metal-organic system to a value smaller than the one of the PTCDA monolayer film. This effect overcompensates the larger interface dipole at the PTCDA/Ag interface. Hence, more CuPc molecules on PTCDA results in more and more dipoles in the second layer which can stepwise reduce the work function of the overall system.

Up to now, the modifications of the valence levels have only been discussed at room temperature. With increasing CuPc coverage, the arrangement of the CuPc molecules changes from lateral disorder to a commensurate superstructure, which coincides with an additional filling of the PTCDA LUMO level. The same lateral phase transition can also be achieved by reducing the temperature of a submonolayer CuPc film below $T_{\rm sample} < 160\,\mathrm{K}$. The corresponding effect on the orbital alignment is shown in the UPS spectra in Fig. 5.7, which have been recorded above (a) and below (b) the transition temperature. Even though the number of molecular features is not changed by the structural phase transition, the PTCDA resonances are slightly modified. In order to understand these changes, the morphology of the film has to be considered. The phase transition corresponds to a change from a PTCDA layer homogeneously covered by a diluted CuPc film to the case of compact CuPc islands on the PTCDA film coexisting with PTCDA regions not covered by CuPc. This goes along with a photoemission spectrum at LT, which is a superposition of the pure PTCDA monolayer signature and the spectral fingerprint of PTCDA molecules covered with CuPc.

In order to identify the binding energy positions of both PTCDA species in the LT-phase, the fitting model shown in Fig. 5.7(b) is employed. The Gaussian curves describing the emission of the uncovered PTCDA areas are displayed in brown. Their energetic positions and their FWHM are fixed at the values determined earlier for the pure PTCDA monolayer sample. The relative intensity of the PTCDA peaks of the CuPc uncovered and covered areas are constrained by considering the CuPc coverage and the damping factor for the UPS signal for PTCDA molecules covered with CuPc. The damping factor was calculated by the Lambert-Beer law using the attenuation length $\lambda = (1.51 \pm 0.12)\,\mathrm{ML}$ which was determined earlier in this section.

The resulting peaks for PTCDA molecules covered with CuPc are displayed as green curves in Fig. 5.7(b). The PTCDA LUMO level in the mixed film is shifted by 200 meV to higher binding energies compared to the PTCDA monolayer film. This shift is even larger than the largest shift of the corresponding state at RT. In contrast to the RT data, the PTCDA HOMO also reveals a slight increase in binding energy of 50 meV. Due to the large energetic

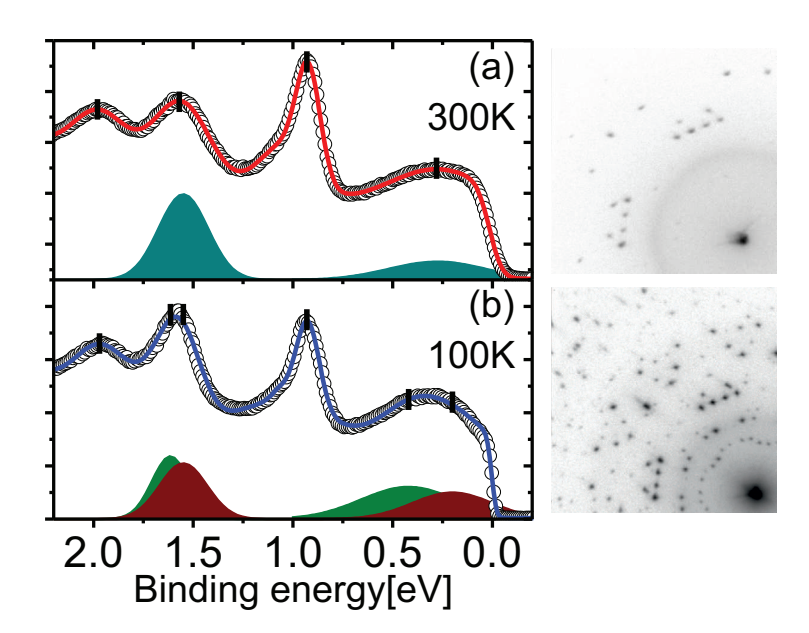


Figure 5.7: UPS spectra of 0.6 ML CuPc on PTCDA at room (a) and at liquid nitrogen (b) temperatures, recorded with an emission angle of 45°. The Gaussian curves modeling the PTCDA peaks are displayed below the spectral data (for the color coding see text). The lateral order of the films is indicated by the corresponding SPA-LEED images.

overlap of the PTCDA HOMO levels, it is hard to estimate the absolute uncertainty of this fitting result. Therefore we cannot predict whether the shift of the PTCDA HOMO level which we obtained by our fitting model, is significant with respect to the uncertainty of the fitting procedure. In addition, no spectrum for a pure PTCDA monolayer film was available for a LT film. Therefore, it is not unambiguously clear, whether our assumptions regarding the energetic positions and the FWHM of the "pure" PTCDA peaks are correct. For the PTCDA LUMO level a larger splitting is observed which is more reliable. It even exceeds the energetic shift of the corresponding state at room temperatures. Here, we can also not exclude, that the LUMO state of the pure PTCDA monolayer film reveals a slight energetic shift at LT.

Although the accuracy of our fitting model is not too high it is still evident, that the PTCDA LUMO underneath the CuPc film is also populated due to the phase transition at low temperature. This provides evidence, that independent from the sample temperature, only the CuPc density on PTCDA influences the interaction of PTCDA with the silver surface. Hence, the population of the PTCDA LUMO level depends on the density of the CuPc film in the 2nd layer.

At low sample temperature, the height of the PTCDA HOMO peak increases compared to room temperature. At LT, the fitting model reveals that the FWHM for the HOMO peak of PTCDA molecules covered with CuPc (green curve) is reduced by a factor of 0.65 compared to the value of the corresponding peak at RT. Based on the sample morphology and the damping factor for the PTCDA HOMO level, we estimated that the sum of the peak areas (intensities) for both PTCDA species at LT is almost similar to the peak area of the PTCDA HOMO at RT. Consequently, the increased height of the HOMO peak can be attributed to a more narrow line shape of the HOMO peak at LT and not to a modified intensity of the molecular features due to the sample morphology.

In contrast, no change of the line shape or the energetic position is observed for both CuPc levels. Since a shift of the CuPc states is observed upon increasing the CuPc density at RT, this may point to a different modification of the intermolecular interaction strength for both temperatures. For the adsorption of CuPc directly on the silver surface, a correlation between a binding energy shift of the HOMO level and a modified adsorption height of the molecule on the Ag(111) surface was reported [KSS+10]. This might suggest for the mixed interface, that the intermolecular distance between CuPc and PTCDA is modified at RT when increasing the CuPc coverage, but stays unchanged when reducing the temperature. This situation would agree with the results for CuPc/Ag(111), since no change of its vertical adsorption geometry was observed for the temperature induced phase transition [KSS+10] for the latter system. The adsorption heights, which directly reflect the strength of the different interaction channels quantitatively, are studied in the next section 5.3 using the X-ray standing wave-technique.

In conclusion, the occupied electronic valence structure of the CuPc/PTCDA interface on Ag(111) was studied with (angle resolved) photoelectron spectroscopy ((AR)UPS). Within the first CuPc layer, two new CuPc related molecular orbitals appear in the valence regime, the CuPc HOMO at $E_{\rm b}=0.88\,{\rm eV}$ and the CuPc HOMO-1 at $E_{\rm b}=1.90\,{\rm eV}$. Most remarkable, the PTCDA LUMO state exhibits a shift of 120 meV towards higher binding energies which indicates a strong influence of CuPc on the chemical interaction of the PTCDA/Ag(111) interface. The orbital tomography method excluded any CuPc contribution to the shifting PTCDA LUMO level. A similar shift of the PTCDA LUMO level occurs upon decreasing the sample temperature and transforming the disordered CuPc film into islands of CuPc adsorbed on PTCDA. Both findings suggest an enhancement of the charge transfer into the PTCDA LUMO upon increasing the CuPc layer density on the PTCDA monolayer film.

5.3 Vertical adsorption geometry

The adsorption heights of all atomic species in the CuPc/PTCDA bilayer film on Ag(111) were investigated using the XSW-method. This technique allows to measure the heights of both molecules independently, and hence provides access to two different bonding strength: the one between both organic layers and the one between the PTCDA layer and the silver substrate. The latter is of course influenced by the CuPc adsorption. This effect can be judged by a comparison with the corresponding heights of the PTCDA monolayer structure on Ag(111).

The additional charge transfer into the PTCDA LUMO observed by photoemission, should be reflected in a reduced bonding distance between PTCDA and the silver surface compared to the pure PTCDA monolayer film. This additional population of the PTCDA LUMO scales with the CuPc density on PTCDA. It is highest when the CuPc coverage is increased at RT, or when the sample temperature is reduced below 160 K.

We have investigated both effects by measuring the vertical adsorption geometry of 0.60 ML CuPc film on PTCDA at room temperature and at $T=50\,\mathrm{K}$. In addition the molecular adsorption heights of an almost closed CuPc film on PTCDA ($\Theta=0.95\,\mathrm{ML}$) was studied at RT. The obtained results allow a comprehensive characterization of the mixed organic bilayer system.

5.3.1 Core level models

The partial electron yield of each different chemical species in the hetero-organic CuPc/PTCDA film is obtained from the integrated intensity of the corresponding core level signal. Exemplary core level spectra are shown in Fig. 5.8 and 5.9. In order to account for inelastically scattered photoelectrons, a Shirley function [Shi72] was subtracted from all photoemission spectra in analogy to the photoemission data treatment in chapter 4.3.1. The core level signature of the nitrogen N1s and copper Cu2p emission which only arises from CuPc are shown in Fig. 5.8(a)+(b) for two different CuPc coverages. For the higher CuPc coverage (HC), the nitrogen core level spectrum reveals an additional peak structure at higher binding energies of $E_{\rm b}=399.2\,{\rm eV}$ which was not observed for $\Theta_{\rm CuPc}=0.60\,{\rm ML}$ (LC). A similar side lobe was observed in all Cu2p spectra at $E_{\rm b}=395.7\,{\rm eV}$ for both coverages. This additional feature leads to an asymmetric line shape of the main peak which was also observed for the CuPc monolayer film on Au(111) and Cu(111) [KSK+11]. The partial yield curves for nitrogen and copper are obtained by the intensity of the main peak in the core level signature shown as green curve in Fig. 5.8(a)+(b).

The oxygen O1s core level spectrum is displayed in Fig. 5.8(c). The line shape of this O1s

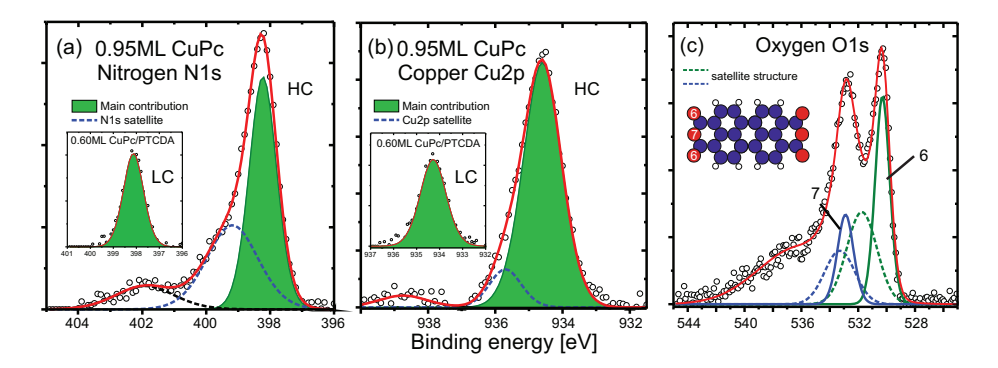


Figure 5.8: Background subtracted core level spectra of nitrogen N1s (a), copper Cu2p (b) and oxygen O1s (c) emission arising from the CuPc/PTCDA bilayer with a CuPc coverage of $\Theta_{\text{CuPc}} = 0.95\,\text{ML}$ at RT. The insets of panel (a) and (b) depict the line shape for a lower CuPc coverage of $\Theta_{\text{CuPc}} = 0.60\,\text{ML}$. The red line is the best fit using a fitting model consisting of one Gaussian profile for the main peak (green area or in case of (c) green and blue solid lines) and at least one more peak for satellites (dotted lines). For the oxygen emission the model for the energy loss tail at higher binding energies is not displayed.

emission is similar to the O1s signature reported for the pure PTCDA monolayer film on Ag(111) [HTS⁺10]. In contrast to the findings for the Mixed Brick Wall structure (see chapter 4.3.1), the O1s spectrum of the PTCDA molecules below CuPc exhibits a clear minimum between the two main lines of the two carboxylic and anhydride oxygen components. This indicates that the satellite structure of the O1s emission of the CuPc/PTCDA bilayer film is similar to the PTCDA monolayer structure and does not reflect the situation for the laterally mixed layers.

The best fitting quality for the O1s core level spectrum was achieved with the fitting model shown in Fig. 5.8(c). The energy difference between the carboxylic and anhydride oxygen main line was adapted from the O1s fitting model for the PTCDA monolayer film on Ag(111) [HTS+10]. Further more, the stoichiometry between both oxygen species was considered. All other parameters are varied in the fitting process and resulted in the values which are listed in table 5.1. The high binding energy tail of the spectrum is modeled by a separated Gaussian, which contains inelastically scattered electrons of both species. Using this O1s fitting model for fitting XSW data yielded highest coherent fractions for both oxygen species which indicates a reliable separation of the both contributions.

This model for separating both oxygen species is quite similar to the fitting model for the disordered PTCDA LT-phase [HTS⁺10]. Especially the energetic positions of the satellite peaks are almost the same in both core level models, but differ from the model used for the

O1s species	$E_{\rm b}[{ m eV}]$	FWHM [eV]	Intensity [%]
Carboxylic Oxygen Main Line	530.3	1.3	22
Carboxylic Oxygen Satellite	530.3 + 1.5	2.5	20
Anhydride Oxygen Main Line	530.3 + 2.6	1.3	11
Anhydride Oxygen Satellite	530.3 + 3.0	2.5	10
Energy Loss Satellite	535.8	6.5	37

Table 5.1: Summary of binding energies $E_{\rm b}$, the FWHM, and the relative area of the contributions used in the fitting model for the O1s emission.

monolayer structure. This could be a first hint for an increased interaction strength between PTCDA and the surface similar to the observation for the PTCDA LT-structure.

This model was then used for fitting the XSW data, i.e., the XPS spectra for each photon energy were fitted separately. The energetic peak positions as well as the intensity ratios between the main line and the corresponding satellite are fixed to the values given in table 5.1. In addition, no variation of the FWHM is allowed for any peak. Hence, the intensities of both main peaks and the one of the energy loss peak are the only free parameters in the core level fitting procedure.

The separation of the CuPc and PTCDA contributions to the carbon C1s spectrum is rather challenging. It was achieved by an iterative improvement of the fitting model in order to maximize the coherent fractions of the CuPc and PTCDA carbon yields. In contrast to the XSW study of the Mixed Brick Wall structure in chapter 4.3.1, the coherent fraction of the integrated carbon signal (obtained in the XSW analysis of the C1s integrated signal) is very low ($F^H = 0.23$) for both CuPc coverages. This indicates that CuPc and PTCDA are located at very different adsorption heights. Consequently a clear separation of the C1s signal from PTCDA and CuPc is important, the fitting model therefore is crucial for the fitting results. The C1s fitting model for $0.60\,\mathrm{ML}$ CuPc on PTCDA is shown in Fig. 5.9(b). The CuPc contribution can be described by two peaks (blue curves) which arise from chemically different carbon species marked in Fig. 5.9(b). The energy difference between those peaks is constrained to the value determined for molecules in the gas phase [ECS⁺07]. The intensity of the carbon main line (1) is 3.25 times larger than for the C-N peak (2), and hence does not exactly reflect the stoichiometry in the CuPc molecule (3:1).

In agreement with the laterally mixed films in chapter 4.3.1, the PTCDA C1s emission is modeled by three Gaussian peaks which are depicted as green curves in Fig. 5.9(b). The relative intensities of these peaks could not be constrained to the stoichiometry in the PTCDA molecule, but had to be slightly varied in order to achieve a better separation of the CuPc and PTCDA contributions to the C1s spectrum. The number of free fitting parameters was reduced by constraining the energy difference between the C-C lines of PTCDA and CuPc to

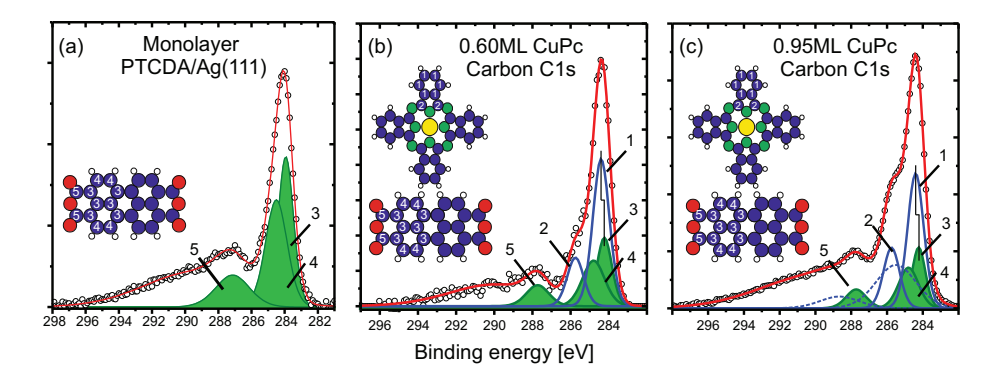


Figure 5.9: Background subtracted C1s core level spectra for different coverages of CuPc on PTCDA/Ag(111). The Voigt profiles in the photoemission spectra represent the fitting models used to separate the chemical components of CuPc (blue lines) and PTCDA (green peaks). Details of the fitting model are summarized in table 5.2. For clarity, the profile of the energy loss tail at higher binding energies is not displayed for all spectra.

 $\Delta E_{\rm b}^{\rm C-C} = -0.17\,{\rm eV}$. This shift was determined by Sauer et al. [SS12] for the same heteroorganic system using high resolution core level spectroscopy.

All optimized parameters of the fitting model are summarized in table 5.2. The intensities of the PTCDA main lines (3) and (4) are identical and do not reflect the stoichiometry of the corresponding carbon atoms of 3:2 in the PTCDA molecule. In Fig. 5.9(a), this PTCDA core level model obtained for the mixed interface is used to fit a C1s spectrum for a pure PTCDA monolayer film. It is obvious, that the line shape of the pure PTCDA monolayer emission is well reproduced by our fitting model. Consequently, our PTCDA core level model is suited to describe the PTCDA C1s core level signature although the relative peak ratios of the single components do not reflect the stoichiometry of the molecule. Note that all other fitting models which we tested, resulted in lower coherent fractions F^H for the carbon species in CuPc and PTCDA. This indicates that our fitting model yields the best separation of the CuPc and PTCDA contributions to the C1s core level emission.

The C1s spectrum for 0.95 ML CuPc on PTCDA is shown in Fig. 5.9(c) which reveals a significant difference in the C1s line shape compared to the lower CuPc coverage. While the intensity of the carbon main line (1) is only slightly higher, at the position of the the C-N component (2) the intensity is clearly higher. This leads to a more pronounced shoulder at the higher binding energy side of the mixed carbon main peak. However, this observation is caused by an additional satellite structure of the CuPc components. A similar new satellite peak has also been observed for the N1s core level emissions of CuPc in Fig. 5.8(a). For that

C1s species	$E_{\rm b}[{ m eV}]$	FWHM [eV]	I _{LC} [%]	I _{HC} [%]
CuPc C-C (1)	284.4	1.0	26	22
CuPc C-N (2)	284.4 + 1.4	1.0	8	9
CuPc C-C Satellite (1)	284.4 + 1.1	2.6	-	16
CuPc C-N Satellite (2)	284.4 + 4.3	2.6	-	4
PTCDA C-C (incl. C-C-O) (3)	284.4 - 0.17	1.1	16	8
PTCDA C-H (4)	284.4 + 0.40	1.5	16	8
PTCDA C-O (5)	284.4 + 3.3	1.7	8	4
Energy Loss Satellite	290.0	6.0	26	29

Table 5.2: Summary of binding energies $E_{\rm b}$, the FWHM, and the relative area of the contributions of CuPc and PTCDA to the carbon C1s core level spectrum. For a $\Theta_{\rm CuPc} = 0.95\,\rm ML$ (HC) additional satellite structures arising from CuPc are observed which were not evident for $\Theta_{\rm CuPc} = 0.60\,\rm ML$ (LC).

reason, we have introduced one additional satellite peak which is assigned to the CuPc C-C component. A compatible extra feature in the energy range of the C-N peak appearing at high CuPc coverage is also known for C1s core level spectra of the pure monolayer film on different noble metal surfaces [KSS+10, KSK+11] recorded at high photon energy ($\hbar\omega > 2.6\,\mathrm{keV}$). Consequently, the appearance of this additional intensity is not an indication for a bad film quality or CuPc molecules located in an extra (3rd) organic layer on top of the CuPc/PTCDA film. A second satellite peak for the carbon atoms located at the CuPc pyrrole ring (2) is included in the fitting model in Fig. 5.9(c). This feature was also identified by Sauer et al. [SS12].

Note that the CuPc C-C (1) satellite structure was not observed in the high resolution core level spectroscopy [SS12]. Therefore it might be caused by the Recoil effect of photoelectron spectroscopy. This effect occurs only at high photon energies and leads to the appearance of new satellite features which are caused by the momentum transfer to the carbon atoms in the photo ionization process [TKS+08]. Since the C-N satellite (2) can also be observed at low photon energies ($\hbar\omega=335\,\mathrm{eV}$), it might be caused by a different excitation mechanism and hence reveals a different energy difference to its main line than the C-C satellite peak (1). The XSW yield curves for the CuPc and PTCDA carbon contributions are obtained by fitting the core level spectra for all photon energies of the XSW scan. Therefore, the intensity ratio of all spectral peaks belonging to one molecule are fixed to that ratio found in the fitting model of the core level data (see table 5.2). In addition, all energetic positions and FWHM are also constrained to the values found in the fitting model. In agreement with chapter 4.3.1, this results in two separated yield curves for PTCDA and CuPc, which contain information about the average adsorption heights for both molecules in the mixed organic film.

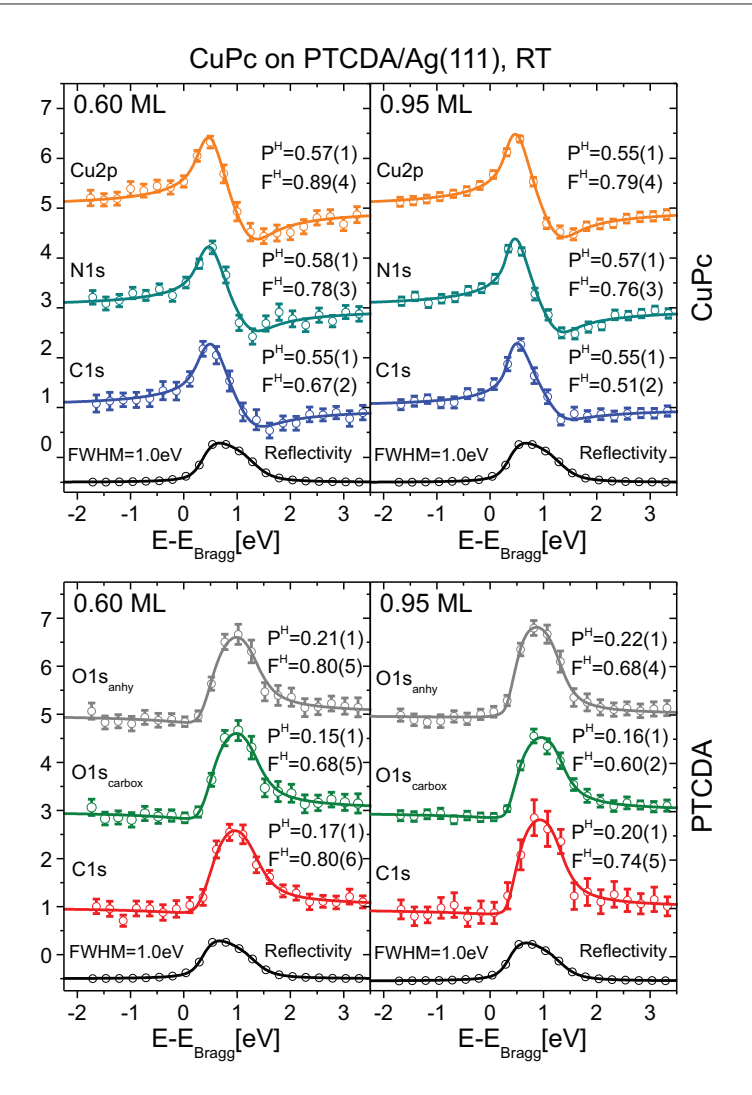


Figure 5.10: Partial yield curves of single XSW scans for all chemically different species in the hetero-organic CuPc/PTCDA bilayer film for two different CuPc coverages (left: $\Theta_{\text{CuPc}} = 0.60\,\text{ML}$, right: $\Theta_{\text{CuPc}} = 0.95\,\text{ML}$). The lowermost curves represent typical reflectivity profiles of the sample. Solid lines represent the curves fitted to the data using Torricelli [Mer12]. Fitting results (coherent position P^H and fraction F^H) are given for each single XSW scan. The error bars of the yield curves are calculated by a Monte Carlo error analysis included in CasaXPS [Fai11].

5.3.2 Vertical adsorption geometry at different coverages

Based on the fitting models for the core level spectra presented in section 5.3.1, the partial yield curves are obtained for two room temperature films with different CuPc coverages. For each species of both hetero-organic layers, single XSW scans are shown in Fig. 5.10 to demonstrate the quality of the obtained data. The error bars of the photoemission yield curves are based on a Monte Carlo error analysis implemented in CasaXPS [Mer12, Fai11]. The yield data itself were evaluated using the XSW analysis software Torricelli [Mer12] and the coherent fractions F^H and positions P^H given in Fig. 5.10 represent the fitting results for each particular XSW scan. The uncertainties of these fitting parameters are calculated by error propagation based on the error bars of the photoemission yield curve.

In Fig. 5.11(a)+(b), all coherent positions and fractions obtained for the individual XSW scans are displayed in the Argand diagram as data points (colored circles). Colored arrows mark the positions of the averaged experimental results which are also summarized in table 5.3. The Argand diagram nicely illustrates, that CuPc and PTCDA are located at different adsorption heights since all arrows representing the species of one molecule are found close to each other, but well separated from those of the other molecule. The height of PTCDA ($\approx 2.8 \,\text{Å}$) agrees well with a chemical interaction between the molecule and the surface [SHS+07, HTS+10, KSS+10]. In order to convert the coherent position P^H for CuPc into an adsorption height, we have to consider that the coherent position P^H represents the adsorption height modulo the bulk lattice spacing. This allows two possible adsorption heights for CuPc, namely $\approx 3.7 \,\text{Å}$ and $\approx 6.1 \,\text{Å}$. Since it is known from STM, that CuPc is located in the 2nd organic layer, only the latter value is reasonable. All adsorption heights, calculated from the coherent positions, are plotted in Fig. 5.11(c). As a reference, the heights for the pure PTCDA monolayer film ($\Theta_{\text{CuPc}} = 0 \,\text{ML}$) are also included [HTS+10].

In agreement to the previous XSW study for the MBW structure, the experimental errors for the adsorption heights are determined by the standard deviation of the fitting results. We obtained uncertainties of $\Delta d^H = \pm 0.02\,\text{Å}$ for the adsorption height of all species except for the copper species in the low CuPc coverage film. For the latter species, the rather poor signal to noise ratio in the core level signal causes a larger spreading of the XSW results and hence a larger uncertainty for the adsorption heights of $\Delta d^H = \pm 0.04\,\text{Å}$.

The position of the carbon atoms is crucial for investigating the adsorption height of organic molecules, since this species is dominant and defines the height of the entire molecule. It also accumulates the wave functions of the π -conjugated molecular orbitals which are essential for the interaction mechanism. Hence, a precise height determination of the carbon atoms is important, but very difficult in this case since the carbon core level spectrum reveals a superposition of both molecular contributions. Beside the careful development of the C1s

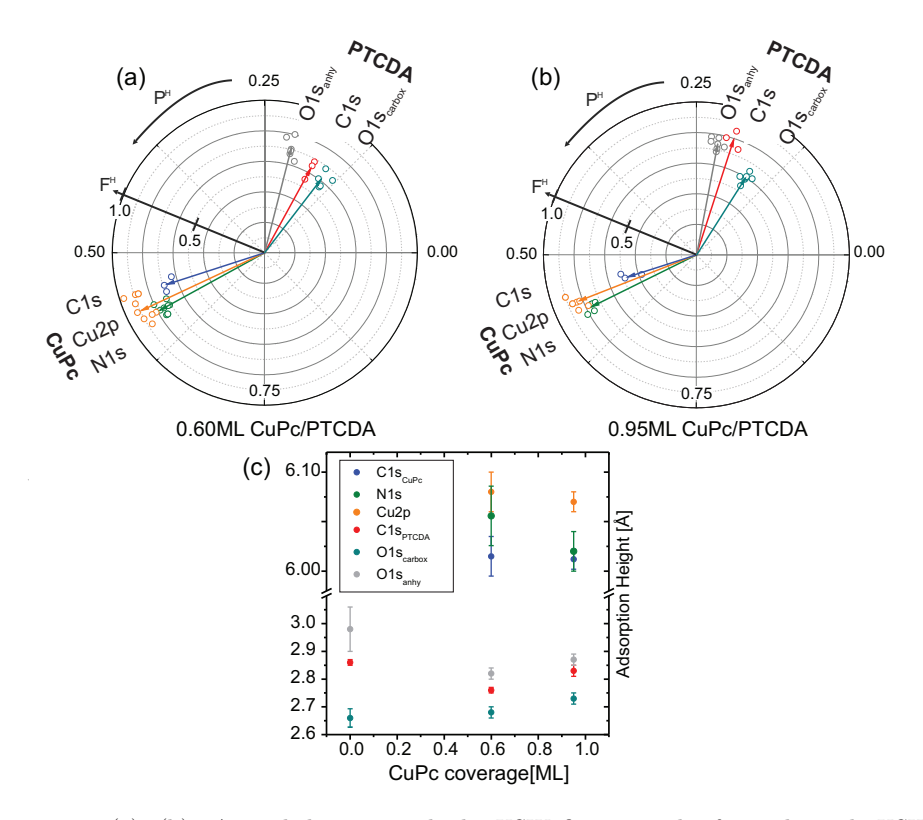


Figure 5.11: (a)+(b): Argand diagram with the XSW fitting results for each single XSW scan. ((a) $\Theta_{\text{CuPc}} = 0.60\,\text{ML}$ and (b) $\Theta_{\text{CuPc}} = 0.95\,\text{ML}$). The arrows indicate the averaged results for the coherent position P^H and fraction F^H . The resulting adsorption heights of all atomic species of the CuPc/PTCDA bilayer are displayed in panel (c) including the reference data of the pure PTCDA monolayer film [HTS⁺10].

core level model described above, there are more indications for the precision and reliability of the C1s XSW results: For CuPc and PTCDA the vertical carbon positions are close to or lie in between the adsorption heights of the other species for the same molecule. Also the coherent fractions of the different carbon species lie in the same range as the ones for the other atomic species. Both findings indicate that the molecules are not strongly bent or disordered. In particular, for molecules adsorbed in two different layers, a high coherent fraction is a strong indication for a correct separation of the molecular carbon contributions. There is only one coherent fraction slightly lower than the others, namely that for the CuPc C1s in the high coverage phase: $F^H=0.50$. This might indicate a slight disorder in this rather densely packed film. However, these data were also the most difficult ones to analyze due to the satellite structure in the core level signal.

	$P_{0\mathrm{ML}}^{H}$	$F_{0\mathrm{ML}}^{H}$	$P_{0.60\mathrm{ML}}^{H}$	$F_{0.60 { m ML}}^{H}$	$P_{0.95\mathrm{ML}}^{H}$	$F_{0.95ML}^{H}$
	1 OML	1 0ML	1 0.60ML	1 0.60ML	1 0.95ML	1 0.95ML
C1s _{sum}	-	-	0.337 ± 0.011	0.23 ± 0.01	0.423 ± 0.005	0.25 ± 0.02
$C1s_{CuPc}$	-	-	0.550 ± 0.010	0.67 ± 0.03	0.544 ± 0.011	0.50 ± 0.11
C1s _{PTCDA}	0.214 ± 0.004	0.54	0.170 ± 0.010	0.63 ± 0.03	0.195 ± 0.009	0.77 ± 0.07
$O1s_{sum}$	0.212 ± 0.010	0.52	0.173 ± 0.013	0.62 ± 0.01	0.180 ± 0.010	0.62 ± 0.02
O1s _{carbox}	0.128 ± 0.012	0.47	0.142 ± 0.008	0.61 ± 0.05	0.160 ± 0.006	0.59 ± 0.03
O1s _{anhy}	0.263 ± 0.032	0.79	0.210 ± 0.010	0.71 ± 0.06	0.221 ± 0.007	0.73 ± 0.03
N1s _{CuPc}	-	-	0.581 ± 0.008	0.75 ± 0.03	0.574 ± 0.005	0.76 ± 0.03
Cu2p _{CuPc}	-	-	0.566 ± 0.015	0.89 ± 0.04	0.561 ± 0.007	0.85 ± 0.04

Table 5.3: Summary of the XSW results for both CuPc coverages on PTCDA averaged over all XSW scans. Results from literature for the pure PTCDA [HTS $^+$ 10] on Ag(111) are included for comparison. The results for C1s_{sum} and O1s_{sum} are obtained by analyzing the total photoelectron yield of the corresponding atomic species.

Similar to the adsorption on various noble metal surfaces [KSS⁺10, KSK⁺11], the CuPc molecules are lying almost flat on PTCDA. The bending of the molecule is smaller than 0.1 Å for both coverages. In contrast, the PTCDA molecules are distorted as in the case of the pure monolayer structure on Ag(111). The carboxylic oxygen atoms bend towards the silver surface while the anhydride oxygen is found above the carbon backbone. This indicates, that the bending of the PTCDA molecule is not lifted by the adsorption of CuPc. Both observations are illustrated in a vertical adsorption model displayed in Fig. 5.12. As a reference the adsorption geometry of the pure PTCDA monolayer structure is shown in gray.

We first focus on the lower CuPc coverage ($\Theta_{\text{CuPc}} = 0.60\,\text{ML}$). The modification of the adsorption height of the PTCDA molecule upon adsorption of CuPc is obvious. The carbon backbone and the anhydride oxygen atoms are located at smaller distances to the silver surface compared to the monolayer film. The carboxylic oxygen atoms are slightly lifted from the surface. In conclusion, the distortion of the PTCDA molecule in the mixed organic film is reduced. The adsorption position of the PTCDA backbone leads to a larger overlap of the LUMO wave functions with the substrate. This suggests a stronger interaction of the PTCDA molecule with the silver surface, which is in good agreement with the additional charge transfer into the molecule that has been observed by (AR)UPS ([SSK+12] and section 5.2). Results regarding the geometric and electronic structure (XSW and UPS) are perfectly consistent in this aspect.

Furthermore, the difference in the vertical position of PTCDA and CuPc can be employed to characterize the intermolecular interaction at the hetero-organic interface. We normalized the distances between the PTCDA backbone and the components of CuPc to the sum of the van der Waals radii of the involved atomic species [Bon64] (see table 5.4). This allows to

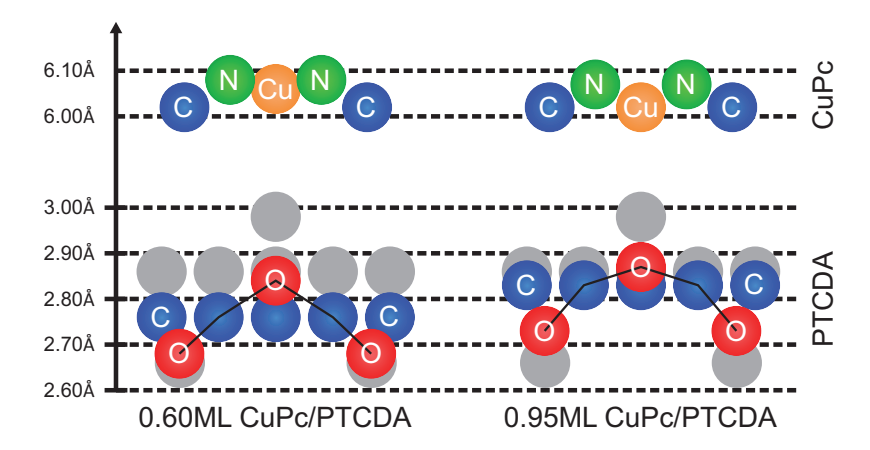


Figure 5.12: Model of the vertical adsorption geometry of the CuPc/PTCDA bilayer film for $\Theta_{\text{CuPc}} = 0.60\,\text{ML}$ and $\Theta_{\text{CuPc}} = 0.95\,\text{ML}$ at room temperature. PTCDA is depicted in its typical front view while for CuPc the heights are shown only schematically. Colored circles mark the adsorption heights of the molecules in the mixed film, gray circles the vertical positions of the pure PTCDA monolayer film [HTS+10].

estimate the molecular overlap. While for the nitrogen and copper atoms the distance from the PTCDA backbone is equal or larger than the sum of the van der Waals radii, a small overlap is evident for the CuPc carbon atoms. This overlap is caused by the larger van der Waals radius of carbon compared to the other atoms, and also by a slight bending of the CuPc carbon atoms towards the PTCDA molecule. The CuPc height is also compared to the position of the anhydride oxygen atoms which are located above the PTCDA backbone. Since the van der Waals radius of the oxygen atoms is clearly smaller than the one for carbon, the molecular overlap is even reduced compared to the PTCDA backbone.

Based on the normalized CuPc-PTCDA distances, it can be concluded that the interaction between CuPc and PTCDA is mainly dominated by van der Waals forces between the molecules. However, such a weak interaction cannot explain the strong influence of CuPc on the adsorption height of PTCDA.

We now turn to a discussion of the higher CuPc coverage of $\Theta_{\text{CuPc}} = 0.95 \,\text{ML}$. No significant change of the vertical positions of all CuPc species can be observed. While a marginal decrease of the nitrogen and copper adsorption height is detected, the position of the carbon atoms is unchanged. The vertical positions of the PTCDA atoms, however, are altered by the increase of the CuPc coverage. After the PTCDA backbone has been moved towards the silver surface by CuPc adsorption at low coverage, it is now again lifted to almost the same position as in the monolayer film. This behavior suggests a reduced interaction strength of

	$\Theta_{\mathrm{CuPc}}\mathrm{ML}$	d^{H} [Å]	$\Delta d_{\mathrm{PTCDA,BB}}^{H} [\%]$	$\Delta d_{\mathrm{PTCDA,anhy}}^{H} \left[\%\right]$
$Carbon_{CuPc}$	0.60	6.02 ± 0.02	92 ± 2	97 ± 2
Nitrogen _{CuPc}	0.60	6.09 ± 0.02	100 ± 2	107 ± 2
$Copper_{CuPc}$	0.60	6.06 ± 0.04	104 ± 2	111 ± 2
Carbon _{PTCDA}	0.60	2.76 ± 0.02	-	-
Oxygen _{carbox}	0.60	2.68 ± 0.02	-	-
Oxygen _{anhy}	0.60	2.84 ± 0.02	-	-
$Carbon_{CuPc}$	0.95	6.00 ± 0.02	89 ± 2	96 ± 2
Nitrogen _{CuPc}	0.95	6.07 ± 0.02	97 ± 2	105 ± 2
$Copper_{CuPc}$	0.95	6.02 ± 0.02	100 ± 2	108 ± 2
Carbon _{PTCDA}	0.95	2.83 ± 0.02	-	-
Oxygen _{carbox}	0.95	2.73 ± 0.02	-	-
Oxygen _{anhy}	0.95	2.87 ± 0.02	-	-

Table 5.4: Summary of the adsorption heights obtained for two different CuPc coverages on PTCDA. The spacial overlap between the molecules is characterized by the distance of the CuPc atomic species to the PTCDA carbon backbone $\Delta d_{\rm PTCDA,BB}^H$ and to the PTCDA anhydride oxygen atoms $\Delta d_{\rm PTCDA,anhy}^H$, respectively. These distances are normalized to the sum of the corresponding van der Waals radii ($r_C = 1.77$ Å, $r_N = 1.55$ Å, $r_{Cu} = 1.40$ Å, $r_O = 1.50$ Å) [Bon64].

the PTCDA molecule with the underlying surface and hence should be reflected in a reduced charge transfer into the PTCDA LUMO level. However, exactly the opposite is observed by photoelectron spectroscopy, the PTCDA LUMO is continuously filled when increasing the CuPc coverage up to the first closed layer (see chapter 5.2). The carboxylic oxygen atoms are further released form the surface which also indicates a weakening of the local Ag-O bond between PTCDA and the silver substrate.

This finding can maybe be understood in terms of the hydrogen bonding in the PTCDA layer. For the pure adsorbate system PTCDA/Ag(111) it has been shown that the adsorption height of the carboxylic oxygens increases when $O \cdots H$ bonds are formed with neighboring molecules $[HTS^+10]$. The observed population of the LUMO level provides additional charge on the molecule, which leads to a rearrangement of the charge within the PTCDA molecule. This could result in more positively polarized hydrogen atoms which would enhance the $O \cdots H$ bonding strength between two PTCDA molecules arranged in a herringbone structure. This would consequently pull the oxygen atoms away from the surface. In a DFT calculation of the free PTCDA molecule, we could show that a larger positive charge is located on the hydrogen atoms, when an additional charge of 2e is placed on the molecule (DFT calculation details: B2LYP, basis set: LANL2DZ $[FTS^+]$). This strongly simplified calculation supports the explanation suggested here for the lifting of the carboxylic oxygen atoms from the surface.

Since the adsorption height of CuPc is not changed when increasing the CuPc coverage,

the lifting of the PTCDA from the surface results in a reduced vertical distance between the molecules at the interface. The normalized molecular distances in table 5.4 are noticeably smaller for the high CuPc coverage compared to the low coverage, which indicates a stronger interaction between PTCDA and CuPc. A similar normalized distance was introduced in order to quantify the interaction strength of CuPc on various noble metal surfaces [KSK+11]. Comparing these values from literature to our results indicates a similar overlap for CuPc/PTCDA and CuPc/Ag(111). This finding suggests a noticeable overlap of the molecular wave functions of CuPc and PTCDA and might point to an intermolecular interaction beyond pure van der Waals forces.

In order to characterize the interaction strength at the CuPc/PTCDA interface further, the distances between the organic layers are also compared with stacking distances in molecular crystals. The layer spacing in such crystals is mainly influenced by the van der Waals interaction and electrostatic forces between the π -conjugated molecules. While for the PTCDA crystal an interlayer distance of 3.21 Å was determined by X-ray diffraction [FZ94], the corresponding value for the β -phase of the CuPc crystal is 3.37 Å [McK98]. The latter distance is only slightly smaller than the sum of two carbon van der Waals radii. The interlayer distance in the PTCDA crystal is clearly smaller that in the CuPc crystal. This is most probably due to the quadrupole moment of PTCDA, which mediates an additional Coulomb attraction between the molecules in the bulk crystal. The value for the PTCDA crystal, however, yields a normalized distance of $\Delta d_{\rm PTCDA,MC} = 91\,\%$, which is inbetween the corresponding CuPc-PTCDA distances obtained for $\Theta_{\rm CuPc} = 0.60\,\rm ML$ and $\Theta_{\rm CuPc} = 0.95\,\rm ML$. Hence, the interaction strength at the hetero-organic CuPc/PTCDA interface is not significantly stronger than in molecular crystals, which suggests a mainly electrostatic and van der Waals driven interaction between the molecular layers at the mixed organic interface.

5.3.3 Vertical adsorption geometry at different temperatures

In this chapter, the XSW results of the temperature induced phase transition from a disordered CuPc film at room temperature into the ordered Stacked-Bilayer structure at low temperature are discussed. In order to avoid a interference of coverage and temperature dependent effects, the same film of $\Theta_{\text{CuPc}} = 0.60\,\text{ML}$, which has been discussed in the previous section 5.3.2, was also studied at 50 K. The same data analysis procedure as for the corresponding RT data set was used. The resulting coherent positions P^H and fractions F^H are shown in the Argand diagram in Fig. 5.13 (b). Exemplary partial yield curves of all chemical species are also shown in panel (a) of the same figure.

In agreement with the findings for the RT film, the largest experimental uncertainty of the

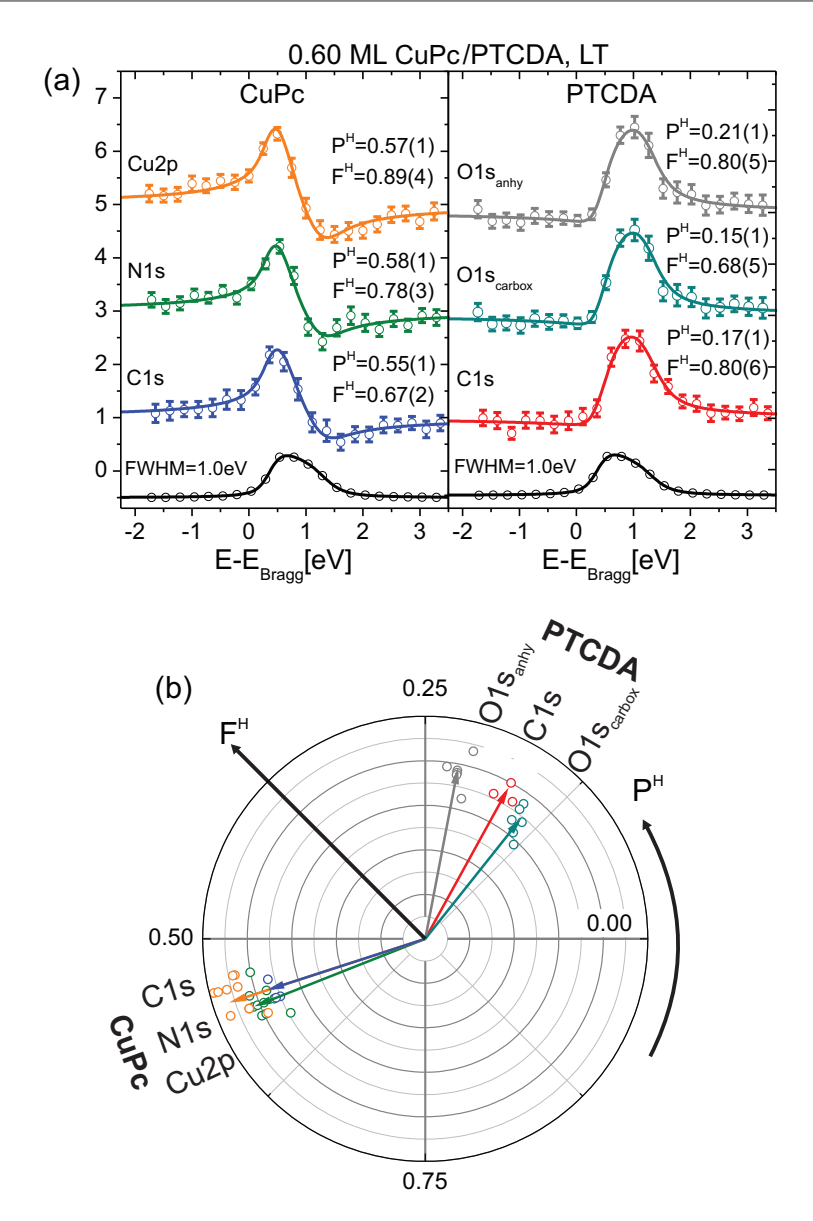


Figure 5.13: (a): Partial yield curves of single XSW scans for all species in the SB film at LT (0.60 ML CuPc, 50 K). Solid lines represent the curves fitted to the data with Torricelli [Mer12]. Fitting results are given for each single XSW scan. The error bars of the yield curves are calculated by a Monte Carlo error analysis. (b): Argand diagram of the XSW fitting results for each single XSW scan. The arrows indicate the averaged results for the coherent position P^H and fraction F^H . The color code is identical in (a) and (b).

adsorption height is found for the nitrogen and copper atoms. The obtained coherent fractions F^H for all species are also comparable to the ones of RT-film. The averaged fitting parameters for all CuPc components can directly be transferred into adsorption heights, which are presented in table 5.5. However, for the signals arising from the PTCDA layer the situation is more complex.

In section 5.1 is was reported, that CuPc molecules condense into ordered islands on the PTCDA film when decreasing the sample temperature to values below $T < 160\,\mathrm{K}$. The PTCDA layer is no longer homogeneously covered with CuPc but also exhibits areas with uncovered PTCDA monolayer structure. This scenario has consequences for the interpretation of the partial PTCDA yield obtained for different sample temperatures. This is illustrated in a simple model in Fig. 5.14(a) and (b) where CuPc molecules are shown as blue ellipses and PTCDA molecules are displayed as red and orange rectangles, respectively. At room temperature (a), all PTCDA molecules are equally covered with CuPc and hence are all part of the same structure. The analysis of the partial yield of all PTCDA species directly results in the vertical adsorption geometry of the layer. However, at low temperature (b), only a certain fraction of PTCDA molecules, marked in red, lie underneath CuPc, while the rest of the PTCDA film (orange) is uncovered and forms the pure monolayer structure. Hence, the partial yield curves contain contributions of two types of PTCDA molecules, those in the pure PTCDA monolayer and those in the mixed SB film. In order to access the actual adsorption height of PTCDA in the hetero-organic interface at LT (red line in Fig. 5.14(b)), the contribution of the pure PTCDA monolayer (orange line in Fig. 5.14(b)) has to be identified and subtracted from the averaged values of the complete PTCDA film. The attenuation of the photoemission signal of the PTCDA molecules in the SB film by the CuPc molecules also plays a role and has to be considered.

The attenuation factor D_f can be determined from the experimental results for the room temperature film of $\Theta_{\text{CuPc}} = 0.60\,\text{ML}$, for which CuPc homogeneously covers all PTCDA molecules. In Fig. 5.14(c), the vectors $\mathbf{Z}_{\text{CuPc/PTCDA}}$ of the CuPc and PTCDA carbon partial yield results are shown in a Argand diagram, together with the vector of the total carbon yield \mathbf{Z}_{TY} in green. The latter can be computed from the partial carbon yield vectors, if their lengths are scaled according to their contributions to the molecular film [Woo98]. Adjusting their lengths to their relative coverage (in terms of carbon atoms per surface area) results in the gray vectors. However, their linear combination, shown as orange vector \mathbf{Z}_{sum} , does not match the measured total yield vector \mathbf{Z}_{TY} . Instead, it is found at a too low coherent position due to an overestimated PTCDA contribution. The PTCDA signal has to be reduced by a factor of $D_f = (80 \pm 10)\,\%$ in order to achieve a coincidence between the sum vector and the total carbon yield. Hence, the PTCDA contribution to the total electron yield is decreased by 20 % due to the CuPc molecules in the 2nd layer.

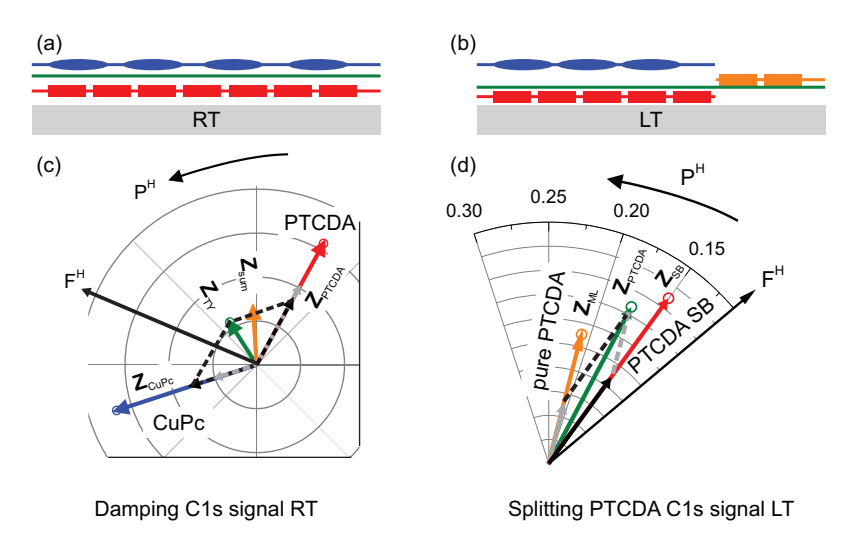


Figure 5.14: Vertical adsorption model illustrating the temperature induced phase transition from RT (a) to LT (b). The PTCDA molecules are shown as red and orange rectangles respectively and CuPc as blue ellipses. (c): Argand diagram of the total and partial carbon yield results for 0.60 ML CuPc/PTCDA at RT. The black arrows represent the vector sum which is used to estimate the damping factor for PTCDA below CuPc. (d): Argand diagram for the LT phase, illustrating the splitting of the PTCDA carbon yield into the vectors of the pure PTCDA monolayer and the PTCDA molecules in the SB structure.

Knowing the damping factor D_f , we can now determine the adsorption height of the PTCDA molecules in the SB film at LT. For the carbon species, the vector analysis is illustrated in the Argand diagram in Fig. 5.14(d). The total PTCDA yield vector $\mathbf{Z}_{\text{PTCDA}}$ is shown in green, the one for the pure PTCDA monolayer molecules \mathbf{Z}_{ML} [HTS⁺10] in orange. Since no XSW data for an ordered LT PTCDA monolayer film is available, \mathbf{Z}_{ML} had to be based on the adsorption height of PTCDA at RT. Again the relative contribution of the PTCDA molecules in the SB phase (n_{SB}) and in the pure PTCDA monolayer structure (n_{ML}) had to be estimated. The CuPc coverage $\Theta_{\text{CuPc}} = \Theta_{\text{SB}} = (0.6 \pm 0.1) \,\text{ML}$ and the damping factor $D_f = (80 \pm 10) \,\%$, provides sufficient information to calculate these factors $n_{\text{SB/ML}}$. The vector of the pure PTCDA monolayer molecules is scaled with n_{ML} which results in the gray vector in Fig. 5.14(d). Substracting this vector from the total yield vector $\mathbf{Z}_{\text{PTCDA}}$ ends up in the solid black vector $n_{\text{SB}} \cdot \mathbf{Z}_{\text{SB}}$. This vector has to be rescaled with $n_{\text{SB/ML}}$ in order to determine the coherent fraction $F_{\text{SB,cor}}^H$ and position $P_{\text{SB,cor}}^H$ of the PTCDA carbon atoms in the SB film at LT.

	$P_{ m LT}^H$	$F_{ m LT}^H$	$d_{\mathrm{LT}}^{H}\left[\mathrm{\mathring{A}} ight]$	$P_{\mathrm{SB,cor}}^{H}$	$F_{\mathrm{SB,cor}}^{H}$	$d_{\mathrm{SB,cor}}^{H}$ [Å]
$C1s_{sum}$	0.370 ± 0.010	0.27 ± 0.02	3.21 ± 0.01	-	-	-
$C1s_{CuPc}$	0.550 ± 0.010	0.72 ± 0.04	6.00 ± 0.02	-	-	-
C1s _{PTCDA}	0.170 ± 0.008	0.70 ± 0.02	2.75 ± 0.02	0.15 ± 0.02	0.87 ± 0.15	2.70 ± 0.05
$O1s_{sum}$	0.170 ± 0.008	0.67 ± 0.07	2.75 ± 0.02	-	-	-
$O1s_{carbox}$	0.143 ± 0.008	0.67 ± 0.07	2.69 ± 0.02	0.15 ± 0.02	0.86 ± 0.15	2.70 ± 0.05
O1s _{anhy}	0.218 ± 0.008	0.76 ± 0.07	2.86 ± 0.02	0.19 ± 0.02	0.77 ± 0.15	2.80 ± 0.05
$N1s_{CuPc}$	0.560 ± 0.011	0.90 ± 0.07	6.01 ± 0.03	-	-	-
$Cu2p_{CuPc}$	0.550 ± 0.014	0.80 ± 0.03	5.98 ± 0.04	-	-	-

Table 5.5: Summary of the XSW results for the low temperature SB film of $\Theta_{\text{CuPc}} = 0.60\,\text{ML}$ CuPc on PTCDA. The values labeled with LT are directly obtained by fitting the partial or total yield curve of the corresponding species. For the PTCDA molecules these results had to be corrected for a contribution of the pure PTCDA monolayer structure by a vector analysis in the Argand diagram (see text). These values are labeled with "SB,cor".

This procedure allows to calculate the corrected coherent positions $P_{\mathrm{SB,cor}}^H$ and fractions $F_{\mathrm{SB,cor}}^H$ for all PTCDA species. The resulting values are summarized in table 5.5 together with the corresponding adsorption heights $d_{\mathrm{SB,cor}}^H$. The uncertainties of those values are larger compared to the ones directly obtained from analyzing the partial yield curves. This is mainly attributed to the fact that several values determined experimentally were used for this correction procedure, which themselves also contain an experimental uncertainty. The largest contribution stems from the the damping factor D_f .

On the right side of Fig. 5.15, the vertical positions for all atomic species in the SB film at LT are illustrated in a vertical adsorption geometry model. As a reference, the vertical adsorption model of the same hetero-organic bilayer film studied at RT (see section 5.3.2) is included on the left side of the same figure. In gray, the adsorption heights for a RT-film with a CuPc coverage of $0.95\,\mathrm{M}$ are shown.

At LT, the CuPc molecules are located closer to the silver surface than in the corresponding disordered RT-film. This is noticeable when comparing the heights of the nitrogen and the copper species in both layers. In contrast, the carbon wings of the molecule appear at the same vertical position for both temperatures, which results in a smaller molecular bending of the CuPc molecules in the ordered LT structure. A slightly reduced adsorption height of nitrogen and copper has also been reported in section 5.3.2 for the higher CuPc coverage on PTCDA at RT. This allows the conclusion that the vertical position of CuPc in the LT-film is mainly influenced by the enhanced molecular density on PTCDA due to the island formation and not directly by the reduced sample temperature.

The molecular distortion of PTCDA, known for the pure monolayer [HTS⁺10], is almost

completely lifted in the SB structure at LT. While the PTCDA backbone moves closer to the silver surface, the carboxylic oxygen atoms are found at a larger adsorption distance resulting in a coincidence of the adsorption heights of both PTCDA species. In agreement with the finding for the pure monolayer structure [HTS⁺10], the anhydride oxygen atom is still located above the molecular body. The different adsorption heights for both oxygen species, however, suggest that the distortion of the molecule is not completely lifted. Therefore we can speculate, that the PTCDA carbon backbone is still located between both oxygen species. This is not unlikely when considering the rather large error bars of the PTCDA adsorption heights.

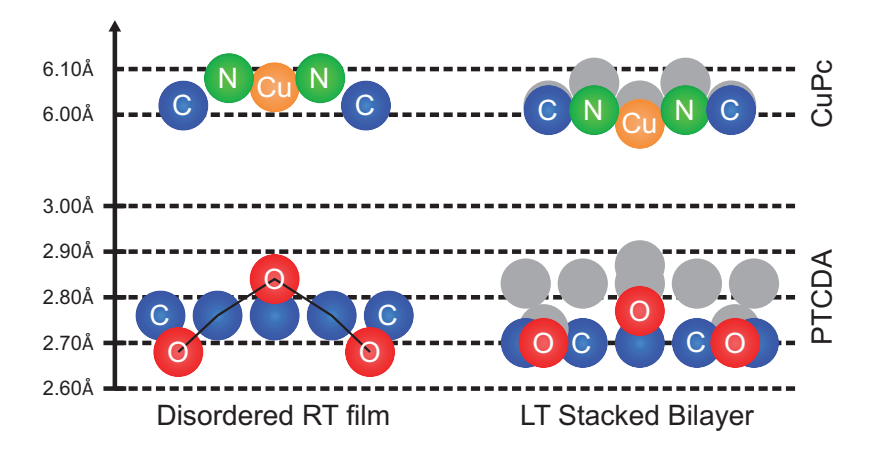


Figure 5.15: Model of the vertical adsorption geometry of $\Theta_{\text{CuPc}} = 0.60\,\text{ML}$ CuPc at different temperatures. PTCDA is depicted in its typical front view, CuPc in a schematic view of the molecule. Colored circles mark the adsorption heights of the molecules in the mixed film, gray circles in a film with 0.95 ML CuPc on PTCDA at RT (see section 5.3.2).

The changes of the vertical distance between CuPc and PTCDA upon cooling are different for the chemical species. On the one hand, the vertical distance between the carbon atoms of both molecules increases by $\approx 0.1\,\text{Å}$ to $\Delta d^H = (3.30\pm0.07)\,\text{Å}$, while on the other hand the distance between all other CuPc species and the PTCDA backbone is unchanged. This is quantified in table 5.6, which summarizes the adsorption heights of all species in the CuPc/PTCDA bilayer film for both temperatures. However, these differences are all smaller than the large experimental uncertainties caused by the large error bars of the PTCDA adsorption heights in the LT-SB film. Therefore, we can only conclude, that within the experimental accuracy the CuPc-PTCDA distance is not modified upon decreasing the sample temperature. Furthermore, we propose, that the adsorption height of the carbon backbone is reduced by the same amount as the copper and nitrogen atoms of CuPc when reducing the sample temperature.

	$d_{\mathrm{LT}}^{H}\left[\mathrm{\mathring{A}} ight]$	$d_{\mathrm{RT}}^{H}\left[\mathrm{\mathring{A}}\right]$	$\Delta d_{\mathrm{PTCDA,LT}}^{H} [\%]$	$\Delta d_{ ext{PTCDA,RT}}^{H} [\%]$
$Carbon_{CuPc}$	6.00 ± 0.02	6.02 ± 0.02	97 ± 7	92 ± 2
Nitrogen _{CuPc}	6.01 ± 0.03	6.09 ± 0.02	100 ± 7	100 ± 2
$Copper_{CuPc}$	5.98 ± 0.04	6.06 ± 0.04	103 ± 7	104 ± 2
Carbon _{PTCDA}	2.70 ± 0.07	2.76 ± 0.02	-	-
Oxygen _{carbox}	2.70 ± 0.07	2.68 ± 0.02	-	-
Oxygen _{anhy}	2.77 ± 0.07	2.84 ± 0.02	-	-

Table 5.6: Summary of the adsorption heights for $\Theta_{\mathrm{CuPc}} = 0.60\,\mathrm{ML}$ obtained at RT and LT $(T_{\mathrm{sample}} = 50\,\mathrm{K})$. The spatial overlap between the molecules is characterized by the distance of the CuPc species to the heights of the PTCDA carbon backbone $\Delta d_{\mathrm{PTCDA}}^H$. These distances are normalized to the sum of the corresponding van der Waals radii $(r_C = 1.77\,\mathrm{\mathring{A}},\,r_N = 1.55\,\mathrm{\mathring{A}},\,r_{Cu} = 1.40\,\mathrm{\mathring{A}},\,r_O = 1.50\,\mathrm{\mathring{A}})$ [Bon64].

The changes in of the vertical adsorption geometry obtained for the temperature induced phase transition reflect the observed changes in the corresponding UPS data presented in Fig. 5.7. These spectra reveal an additional shift of the PTCDA LUMO level upon cooling, which coincides nicely with the lower adsorption height of the PTCDA backbone at LT. The unchanged distance between CuPc and PTCDA can also explain that there is no shift of CuPc orbitals during the phase transition into the ordered SB structure. The latter finding is also characteristic for the adsorption of CuPc directly on the Ag(111) surface [KSS+10]. For this system a similar phase transition upon decreasing the sample temperature was reported which did neither lead to a modified adsorption height for the molecule nor to a shift in the frontier CuPc orbitals.

Although the lateral structure of the LT-SB structure and the high-coverage RT-SB film are identical, the vertical adsorption geometry of the molecules is significantly different. As illustrated in Fig. 5.15 and discussed in section 5.3.2, the PTCDA backbone of the CuPc rich RT bilayer film is located at a clearly higher adsorption position. This suggests a smaller overlap of molecular orbitals with the substrate states compared to the LT-phase and consequently a reduced charge transfer into the molecule. However, the PTCDA LUMO level is found at roughly the same binding energy position in both films.

5.3.4 Conclusion

We investigated the vertical adsorption geometry of several hetero-organic bilayer films of CuPc and PTCDA with the X-ray standing wave technique. The photoelectron core level signals were measured in order to obtain the partial yield for all different atomic species. The two different oxygen species in PTCDA, the carboxylic and the anhydride oxygen, could be differentiated in the XSW analysis easily. For the C1s emission, the situation is much more complicated, since five different species from both molecules are found at very similar binding

energies. However, we succeeded in separating the core level emission from both molecules. In agreement with the STM results shown in section 5.1, the CuPc molecules adsorb flat lying directly on the PTCDA monolayer film. At room temperature, the vertical distance between the CuPc and the PTCDA layer is reduced from $(3.26\pm0.03)\,\text{Å}$ to $(3.17\pm0.03)\,\text{Å}$ when increasing the CuPc coverage from 0.60 ML to 0.95 ML. This is mainly caused by a change in the vertical position of the PTCDA molecule. The CuPc molecule is found at a height of $\approx 6.02\,\text{Å}$ in both films. At low CuPc coverage, the adsorption height of the PTCDA backbone is slightly smaller (0.10 Å) compared the pure monolayer film. Adding more CuPc molecules lifts the PTCDA backbone again by 0.07 Å. While the anhydride oxygen atoms follow the movement of the PTCDA backbone, the adsorption height of the carboxylic oxygen atoms is increased with rising CuPc coverage. However, the higher distance between the PTCDA backbone and the silver surface does not explain the enhanced charge transfer into the PTCDA molecule when increasing the CuPc coverage. This aspect could not be fully understood and needs to be further investigated.

Upon decreasing the sample temperature of the $0.60\,\mathrm{ML}$ film, the CuPc molecules condense in islands on the PTCDA layer which leads to a simultaneous reduction of the vertical position of CuPc and PTCDA. The intermolecular distance between both molecules is not changed by temperature. This results in a smaller distance between PTCDA and the Ag(111) surface. The PTCDA backbone as well as the anhydride oxygen atoms are located $0.06\,\mathrm{\mathring{A}}$ closer to the silver surface, which reflects the energetic shift of the PTCDA LUMO level when reducing the temperature of the adsorbate system.

5.4 Modification of the PTCDA/Ag(111) interaction by the adsorption of CuPc

In the following section 5.4 the vertical adsorption behavior presented so far is correlated to the lateral order as well as to the electronic level alignment at the hetero-organic bilayer film. A strong modification of the PTCDA/Ag(111) interface was found, caused by the adsorption of CuPc. This is evident by both, an additional charge transfer into the PTCDA LUMO level and a changed adsorption height of the PTCDA molecule. These changes also depend on the CuPc coverage. A direct chemical interaction between CuPc and PTCDA is unlikely, since the PTCDA-CuPc distance is comparable to the interlayer spacing in a PTCDA van der Waals crystal (see section 5.3.2).

Our findings can be explained by a screening effect induced by the adsorption of CuPc on PTCDA [FTFP08, SWTT09]. Placing charge in the LUMO level of a neutral molecule leads to a Coulomb repulsion between this new charge and the electronic system of the molecule.

As a result, the total energy gain of the molecular system caused by the charge transfer, decreases by the on-site Hubbard energy U which accounts for the additional Coulomb repulsion. For a free molecule in the gas phase this energy U also modifies the binding energies of the molecular orbitals leading to an expansion of the HOMO-LUMO energy gap.

For the same molecule adsorbed in a molecular film on a metal surface, an image charge is created in the metal and the additional charge on the molecule can polarize the surrounding molecules. Both effects screen the charge on the molecule partly and consequently reduce the on-site Hubbard energy U [MS79, HTS97, BK97, FTFP08]. This results in a lower total interface potential for the adsorbate system.

This general consideration also applies to the hetero-organic system CuPc on PTCDA/Ag(111). The interaction between PTCDA and the Ag(111) surface results in an effective charge transfer of 0.31 electrons into each PTCDA molecule in the pure monolayer structure [RNP⁺09], which leads to an on-site Hubbard energy U per molecule. The energy gain in the adsorbate system is also reduced by the repulsive Coulomb interaction between the effective charges on neighboring molecules, which is in the range of $V = 140 \, \mathrm{meV}$ for two PTCDA molecules with an intermolecular distance of 10 Å. For a favorable adsorption situation the adsorption energy gain of the metal-organic system has to be larger than the energy costs due to the repulsive electrostatic interaction energies U and V. This limits the amount of charge which is transfered into the organic layer.

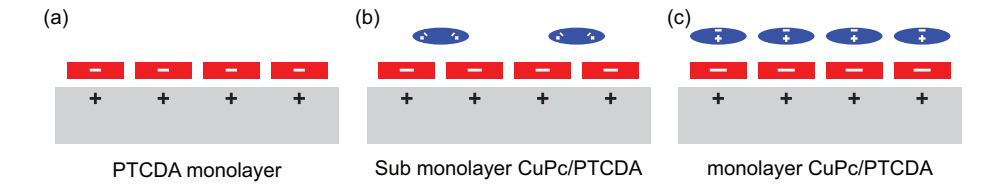


Figure 5.16: Schematic model for the screening mechanism in organic films. (a) The effective charge in the PTCDA LUMO level creates and image charge in the metal in order to reduce the on-site U and the intermolecular repulsion V. (b)+(c) CuPc molecules on PTCDA are polarized and contribute to the screening of the charged PTCDA molecule. The polarizability of the CuPc layer depends on the molecular density and hence the CuPc coverage.

If we now add CuPc molecules on the PTCDA monolayer film, we also introduce a new screening effect for the charge in the PTCDA layer. The CuPc molecules are polarized by the charge in the PTCDA LUMO which reduces the on-site energy U as well as the intermolecular repulsion energy V. This creates a new equilibrium between the adsorption energy gain due to charge redistribution at the interface and the energy loss caused by U and V. As a consequence, additional charge transfer into the PTCDA molecule can become energetically

favorable again. The amount of transfered electrons into the molecular orbital depends on the screening strength of the CuPc molecules in the second layer. According to literature [BK97, FTFP08], the reduction of the on-site Hubbard energy caused by molecular screening can be expressed by

$$U = U_0 - \frac{N \cdot q^2 \cdot \alpha}{2R^4}.\tag{5.3}$$

In this equation N describes the coordination number, q the additional charge, α the polarizability of one molecule and R the intermolecular distance.

This screening term is proportional to $\frac{1}{R^4}$, which explains that molecules in the neighboring layer contribute more effectively to the shielding than those in the same layer. In our case lateral distance are 10-15 Å, vertical distances are ≈ 3 Å. Hence, only molecules in the CuPc layer are considered when discussing molecular screening effects for PTCDA molecules.

We now consider the growth behavior of the CuPc film on PTCDA in this context. CuPc does not form ordered islands at low coverages but a diluted homogeneous 2D gas. Hence, the coordination number N raises proportional to the molecular density with coverage and consequently also the polarizability of the CuPc film $(N \cdot \alpha)$. Fig. 5.16(b) and (c) illustrates the increase of coverage and polarization of the CuPc molecules (blue). The increasing number of CuPc molecules per PTCDA molecules results also in a more effective screening of the additional charge in the PTCDA LUMO level. This screening, in turn, enables an additional charge transfer into the PTCDA LUMO and hence explains the LUMO shift seen in UPS. The same argument also explains the additional filling of the PTCDA LUMO level, upon cooling, which results in the lateral phase transition to the ordered SB structure. During the phase transition, the CuPc molecules condense to islands with a higher CuPc density compared to the disordered RT-phase. This also improves the effective polarizability of the bilayer film and explains the spectroscopic observation.

Besides the additional charge transfer into the PTCDA LUMO level, which was discussed in this chapter so far, the vertical adsorption geometry of PTCDA at room temperature is also modified by changing the CuPc coverage (see section 5.3.2). For the low CuPc coverage of 0.60 ML, the PTCDA backbone is located at a smaller adsorption height than in the pure monolayer structure. This was interpreted as a stronger interaction of PTCDA with the silver surface, which is also reflected by the additional charge transfer into the PTCDA LUMO observed in UPS. Increasing the amount of CuPc on PTCDA however, results in a lifting of the PTCDA backbone to almost the same height as known for the PTCDA monolayer structure. The interaction strength of PTCDA to the silver substrate seems to be reduced again, which contradicts the simultaneous shift of the PTCDA LUMO to higher binding energies. It also conflicts with the established concept, that the binding energy position of the molecular valance states reflect the molecule-substrate interaction [DGS⁺08, KSK⁺11].

However, the larger adsorption height of PTCDA in the CuPc rich mixed bilayer film results in a smaller distance between the organic layers which points to an enhanced CuPc-PTCDA interaction. This may be the result of an electrostatic attraction between the negative charge in the PTCDA LUMO state and the induced positive charge in the CuPc molecule. The smaller distance between the organic layers is energetically favored since it leads to an additional energy gain due to the Coulomb attraction between the molecules. On the other hand, equation (5.3) indicates that the smaller interlayer distance makes the screening by the CuPc layer again more effective, which allows even more charge redistribution at the metal organic interface.

It has to be stated that the reason for the lifting of the PTCDA molecules for higher CuPc coverages is not completely clear. The reduction of the distance between the organic films can be the driving force, but it could also be realized by lowing the height of the CuPc molecules. Nevertheless, the hetero-organic system seems to gain energy by reducing the overlap of the PTCDA wave functions with the substrate. The larger distance between PTCDA and the metal surface should also reduce the charge redistribution inside the metal due to a weakening of the image charge. It can be speculated that this is favorable, since it reduces the interaction between the image charges. At this point, the necessity for input from quantum chemical calculations becomes obvious.

5.5 Thermally induced molecular exchange at the hetero-organic interface

In section 5.3.2 it was discussed that the interlayer distance at the CuPc/PTCDA interface is in the same range as the layer spacing in the PTCDA crystal [FZ94]. It can be concluded that the interaction strength at this organic-organic boundary is much weaker than at the PTCDA-silver interface. One can therefore expect, that it is possible to desorbed CuPc from the PTCDA/Ag(111) system without destroying the PTCDA monolayer structure, as it is the case for bi- and multilayer PTCDA films [ZKS+06].

However, we found that the LEED pattern obtained after annealing the mixed bilayer samples at $T_{\rm sample} = 570\,\mathrm{K}$ did never show the pattern of the pure PTCDA monolayer structure. For a CuPc coverage of $\Theta_{\rm CuPc} = 0.50\,\mathrm{ML}$, the LEED patterns before and after annealing are shown in Fig. 5.17(a)+(c). The diffraction signature of the CuPc/PTCDA bilayer film in panel (a) reveals all diffraction features of this structure, as described in section 5.1: Ordered spots arise from the PTCDA monolayer structure, the diffuse diffraction intensity surrounding the specular reflection from the disordered CuPc layer on PTCDA. During the annealing process,

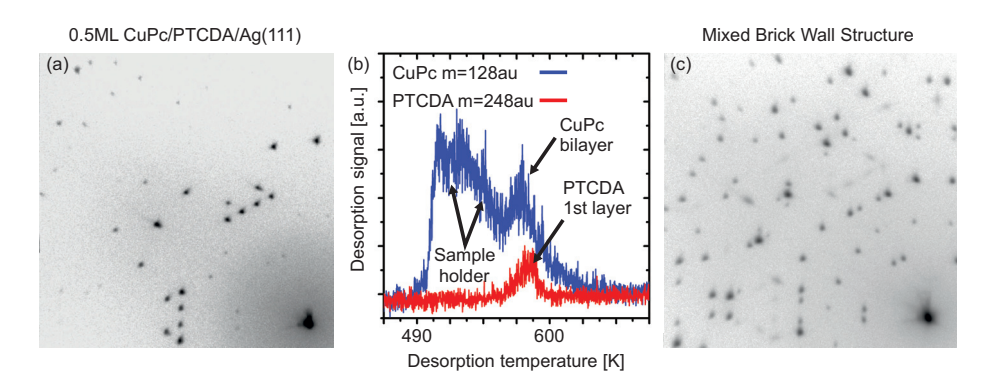


Figure 5.17: (a) Low energy electron diffraction pattern of $\Theta_{\text{CuPc}} = 0.50\,\text{ML}$ CuPc on PTCDA recorded at RT. (b) Desorption signal of CuPc (blue line) and PTCDA (red line) monitored during the desorption process of CuPc from the hetero-organic bilayer. (c) Diffraction pattern after annealing at 600 K. The diffraction spots can be attributed to the laterally mixed MBW structure which has been presented in section 4.1.3. All diffraction data was recorded at $E_{\text{kin}} = 27.2\,\text{eV}$.

the desorbing molecular fragments ($m=128\,\mathrm{au}$ for CuPc and $m=248\,\mathrm{au}$ for PTCDA) were monitored with a quadrupole mass spectrometer as a function of the sample temperature. The resulting desorption spectrum is shown in Fig. 5.17(b)². The desorption signal of CuPc shown in blue exhibits a steep raise at 490 K, followed by a complex peak structure. While the first three peaks in this spectrum can be assigned to molecules desorbing from the sample holder, the maximum at the highest sample temperature is caused by the desorption of molecules from the hetero-organic film (labeled "CuPc bilayer"). At roughly the same temperature, an increase in the PTCDA desorption signal shown in red is observed. This clearly proves that during the desorption of CuPc also PTCDA molecules desorb from the organic film. It can be excluded that this PTCDA signal arises from other parts of the sample holder than the sample surface, since the PTCDA monolayer itself was prepared by annealing a PTCDA multilayer film at the PTCDA bilayer desorption temperature. At that temperature, all PTCDA molecules which could create an artificial desorption signal have already been removed.

The structures which are formed by the annealing process can be identified as laterally mixed organic films containing CuPc and PTCDA. This is obvious when comparing the diffraction pattern of the annealed hetero-organic CuPc/PTCDA bilayer films with the LEED images of directly prepared mixed organic films introduced in section 4.1. For the particular case

 $^{^2}$ The sample temperature was manually increased with a temperature rate of $\approx 1\,\frac{K}{s}$. Therefore, the desorption spectrum contains only qualitative information of the desorption process. Since the thermocouple was not properly calibrated to the absolute temperature, an offset in the given temperature in the range of up to $\pm 40\,K$ is possible. In addition, no aperture was used in order to suppress artificial desorption features arising from different parts of the sample holder.

of $\Theta_{\text{CuPc}} = 0.50\,\text{ML}$ CuPc on PTCDA, presented in Fig. 5.17, the diffraction pattern of the annealed bilayer film in panel (c) clearly arises from the Mixed Brick Wall structure. This information does not only reveal that PTCDA can be desorbed from the silver surface, it furthermore proves that CuPc molecules substitute PTCDA molecules in order to create a laterally mixed organic film. The mixing ratio of CuPc and PTCDA in the first layer after annealing depends on the CuPc coverage on PTCDA at the organic-organic interface. Below 0.60 ML CuPc on PTCDA the Mixed Brick Wall structure with one CuPc and two PTCDA molecules per unit cell is obtained. For higher CuPc coverages between 0.60 ML and 1.3 ML, different structures of the Mixed One-to-One phase with one CuPc and one PTCDA are observed. The electronic properties of all these mixed layers created by annealing a heteroorganic bilayer film are identical to directly prepared laterally mixed structures. This finding consequently introduces a new method for preparing laterally mixed organic structures.

The desorption of PTCDA from the silver surface and the formation of laterally mixed films allows two main conclusions. First, the adsorption of CuPc on PTCDA modifies the bonding strength of the first layer molecules in a way that they can be desorbed from the surface. This is in agreement with in the vertical adsorption geometry presented in section 5.3.2. The carboxylic oxygen atoms are lifted from the silver surface upon adsorption of CuPc which reduces the local Ag-O interaction. The strength of this local bond may be the reason which hinders the desorption of PTCDA from silver. Other molecules which only form a π -bond with the Ag(111) surface, like CuPc, can be desorbed from this surface without destroying the molecule [KSS⁺10]. It can be speculated, that the weakening of the PTCDA-Ag(111) bond by a second organic layer is a general effect. It is unknown (and very difficult to verify) if this also occurs in bilayer or multilayer PTCDA films. It could easily be, that upon annealing a bilayer PTCDA film, also 1st layer PTCDA molecules are desorbed, but replaced by 2nd layer PTCDA molecules. This would be the same effect as observed here for CuPc/PTC-DA/Ag(111), it just cannot be verified easily since 1st and 2nd layer PTCDA molecules are identical.

Secondly, the development of mixed layers upon annealing an organic-organic interface suggests, that the laterally mixed films are energetically more favored than the pure CuPc or PTCDA monolayer structure. Even for a 10 ML thick CuPc film on PTCDA, no complete replacement of the PTCDA molecules from the surface could be achieved [Bru12]. However, since thermal activation is necessary to create the ordered mixed layer, an energetic barrier must exist for the exchange process of the molecules.

For the reversed situation, when PTCDA is deposited on a closed layer of CuPc, and sub-sequently annealed, the formation of ordered mixed films was also observed. However, the adsorption behavior for PTCDA on CuPc is completely different than for the reversed system which makes a direct comparison of the molecular exchange process upon annealing rather difficult. This will be discussed in chapter 6.

Similar exchanges of organic layers have been observed recently for various organic-organic interfaces on noble metal surfaces [Sch11, SLQ $^+$ 11]. For the boundary between pentacene (PEN) and para-sexiphenyl (p-6P) grown on the Cu(110) surface, a complete layer inversion was reported [SLQ $^+$ 11]. It was explained by a thermally induced diffusion of the PEN molecules through the p-6P film to the Cu(110) substrate which coincides with a expulsion of the p-6P monolayer structure. Since the replacement between both molecules is not reversible the authors concluded, that the p-6P/PEN/Cu(110) interface is energetically favored against the initial adsorption state.

When the CuPc molecule is substituted by Tin-phthalocyanine (SnPc) i.e., annealing a SnPc/PTCDA/Ag(111) film, a complete layer inversion was observed if the SnPc coverage was larger than 2.0 ML [Sch11, SK]. Schöll et al. [Sch11] explained this complete exchange of the PTCDA and the SnPc layer by a smaller on-site Hubbard repulsion U for SnPc compared to PTCDA (see discussion in chapter 5.4). Hence, the adsorption energy gain in the SnPc monolayer is larger compared to the PTCDA monolayer. Consequently, the formation of a SnPc monolayer is energetically favored when a sufficient amount of SnPc is present in the hetero-organic film.

A similar statement can explain the formation of mixed organic layers containing CuPc and PTCDA. In these laterally mixed films the CuPc LUMO is depopulated by the interaction with PTCDA (see section 4.2.1). Therefore, no Coulomb repulsion energy U_{CuPc} reduces the adsorption energy of CuPc. The additional charge transfer into the PTCDA molecule can be efficiently screened by the neutral CuPc molecules. For this reason, mixed organic layers might be energetically more favored on Ag(111) than mono-organic monolayer structures since for the latter systems, all molecules reveal a not vanishing on-site repulsion energy U. Although first ideas have been formulated which might explain the exchange reaction at organic-organic interfaces, the kinetic process of the molecular diffusion in these systems is still not well understood. In order to obtain a more detailed understanding of the exchange reactions of organic molecules on noble metal surfaces, "real time" studies which monitor the structural changes as a function of annealing temperature are mandatory.

5.6 Conclusion

In this chapter geometric and electronic properties of hetero-organic CuPc/PTCDA bilayer films on Ag(111) were discussed, based on various experimental findings.

The lateral order of the CuPc films on PTCDA was examined with high resolution low energy electron diffraction (SPA-LEED) and scanning tunneling microscopy (STM). For all molecular films, no lifting of the lateral order of the PTCDA layer upon adsorption of CuPc was observed. The CuPc molecules just adsorb on top of the PTCDA layer. At room temperature,

the CuPc molecules do not form long range ordered structures in the submonolayer regime. They arrange in a homogeneous diluted 2D gas with an average intermolecular distance that decreases continuously with rising coverage. Closing the first CuPc layer on PTCDA, or decreasing the sample temperature below 160 K, results in a phase transition from the disordered CuPc film to an ordered commensurate superstructure. This ordered structure, which is referred to as Stacked-Bilayer structure, contains six CuPc molecules adsorbed on ten PTCDA molecules in the first layer.

All six CuPc molecules in the SB film are equally oriented with $(45 \pm 2)^{\circ}$ relative to the [110] direction of the silver substrate. In addition they are arranged in a square lattice with a spacing of $\approx 14\,\text{Å}$ and reveal three distinct adsorption sites on PTCDA: on the PTCDA backbone, above a ditch between two, and a gap between three PTCDA molecules.

The occupied electronic valence structure was investigated with (angle resolved) UV photoelectron spectroscopy ((AR)UPS). The study of different CuPc submonolayer coverages on PTCDA revealed the appearance of two new states, arising upon adsorption of CuPc. While the CuPc HOMO could be identified at a binding energy of $E_{\rm b}=0.88\,{\rm eV}$, the CuPc HOMO-1 was found at $E_{\rm b}=1.90\,{\rm eV}$. Most remarkable, the PTCDA LUMO state shifts 120 meV to higher binding energy within the adsorption of a full layer of CuPc on PTCDA which indicates a strong influence of CuPc on the chemical interaction of PTCDA with the Ag(111) surface. A similar shift of the PTCDA LUMO level occurs upon decreasing the sample temperature and transforming the disordered CuPc film to the ordered SB structure. Both findings suggest an additional charge transfer into the PTCDA LUMO level with increasing CuPc layer density on PTCDA.

In order to estimate the interaction strength at the CuPc/PTCDA interface as well as to characterize the modification of the PTCDA monolayer upon forming the hetero-organic bilayer film, the vertical adsorption geometry was studies with the X-ray standing wave (XSW) method. At room temperature, two samples with CuPc coverages of 0.60 ML and 0.95 ML have been investigated. Both samples exhibit a distance between the organic layers of $\Delta d = 3.2 \,\text{Å}$ which is in good agreement to the interlayer spacing for a PTCDA molecular crystal. This result indicates a mainly electrostatic and van der Waals interaction between the organic CuPc and PTCDA layers. However, the chemical bond between the PTCDA monolayer molecules and the silver surface is strongly modified by the on top adsorption of CuPc. For $\Theta_{\text{CuPc}} = 0.60 \,\text{ML}$, the PTCDA backbone is located closer to the surface compared to the pure monolayer structure, which is in agreement to the charge transfer into the PTCDA LUMO level found in UPS. However, increasing the CuPc coverage further lifts the PTCDA backbone again to almost the initial position in the pure monolayer. This goes along with a further filling of the corresponding LUMO state. While the anhydride oxygen atom follows the displacement of the backbone, the carboxylic oxygen atoms are continuously lifted from

the surface with rising CuPc coverage.

The additional population of the PTCDA LUMO level can be explained by a screening effect induced by the adsorption of CuPc. According to the Hubbard model, a charge transfer into a molecule results in an on-site Hubbard energy U, which lowers the energy gain of the adsorbate system. This energy loss U can be reduced by the surrounding CuPc molecules, which screen the additional charge in the PTCDA LUMO [MS79, HTS97, BK97, FTFP08]. As a consequence, the adsorption energy balance is influenced by the additional screening and it becomes energetically favorable to transfer additional charge into the PTCDA molecule. The vertical position of the PTCDA molecule is modified in order to maximize its overlap with the silver surface as well as to create an optimized screening of the accepted charge by the CuPc layer.

Finally, the desorption behavior of CuPc from the CuPc/PTCDA bilayer films was monitored with a quadrupole mass spectrometer and the resulting structures were identified by LEED. Surprisingly, besides CuPc, also PTCDA molecules desorb from the stacked organic film when annealing the sample at temperatures above 570 K. After annealing, the molecular order could be assigned to laterally mixed films containing CuPc and PTCDA molecules of different ratios. These findings prove, that, on the one hand, the PTCDA interaction with the silver surface is modified in order to enable a desorption of PTCDA from the surface. On the other hand, since no pure PTCDA or CuPc monolayer structure is observed after annealing, the mixed organic films is energetically more favored than the mono-organic layers.

6 Molecular exchange at a hetero-organic bilayer: PTCDA on CuPc on Ag(111)

After the structure formation of CuPc on one closed layer PTCDA on Ag(111) has been discussed in chapter 5, this chapter deals with the reversed system: PTCDA on CuPc/Ag(111). This is interesting not only to complete the series of all different mixed organic interfaces containing CuPc and PTCDA on Ag(111), but also to study the influence of the metal-organic interface on the properties of the organic-organic interface. In particular, the lateral intermolecular interactions between the molecules in the first organic layer have a crucial influence on the stability of the ordered template and consequently also on the mixed organic interface created on top.

In the previous chapter 5, we revealed that CuPc molecules adsorbed on a closed layer of PTCDA at room temperature do not lift the lateral order of the metal-organic interface. However, supplying enough thermal energy to the hetero-organic film leads to a diffusion of CuPc molecules to the silver surface and hence to an exchange of PTCDA and CuPc. Highly ordered mixed films containing CuPc and PTCDA are formed (see chapter 4) which indicates that the mixed organic films are more stable than the mono-organic pure PTCDA or CuPc monolayer structure. This conclusion should now be reviewed by reversing the molecular order on the silver surface.

In analogy to the previous chapters, we study the vertically stacked system PTCDA/CuPc on Ag(111) with SPA-LEED, UPS and XSW. The experimental results of the geometric and electronic structure allow us to analyze the structure formation and to characterize the interaction mechanisms in this hetero-organic system. Certainly, these results are also compared to the different mixed organic systems discussed in chapters 4 and 5.

6.1 Lateral order: Long range order

The lateral order of the system PTCDA/CuPc was investigated with SPA-LEED at different PTCDA coverages. The CuPc monolayer films have been prepared by thermal desorption from a CuPc bilayer film, the success of the sample preparation is confirmed each time by

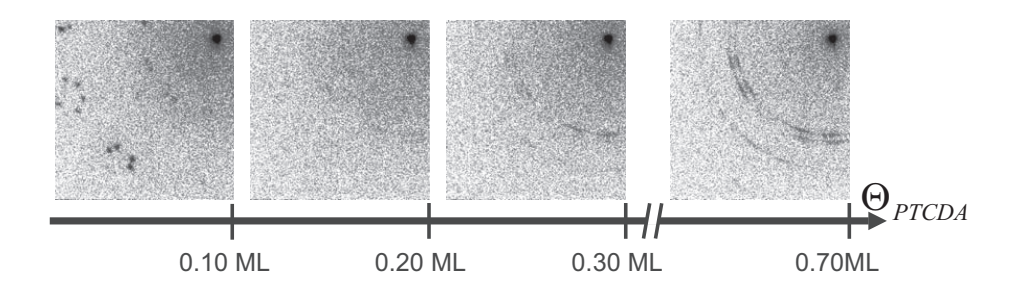


Figure 6.1: SPA-LEED images recorded in real time during the deposition of 0.70 ML of PTCDA on the monolayer structure CuPc/Ag(111) ($E_{\rm kin}=27.2\,{\rm eV},\,t_{\rm scan}=52\,{\rm s},\,T_{\rm sample}=300\,{\rm K}$).

LEED [KSS⁺10]. Subsequently the PTCDA molecules were deposited on the closed CuPc layer at room temperature and the formation of the hetero-organic film is monitored in real time by very short SPA-LEED scans. LEED images recorded during PTCDA film growth are shown in Fig. 6.1 for various coverages. The diffraction spots of the CuPc monolayer structure, which are still visible in the first LEED image in Fig. 6.1 ($\Theta_{\text{PTCDA}} < 0.10\,\text{ML}$), vanish during the PTCDA deposition. They are replaced by new diffraction features which become more defined with increasing PTCDA coverage.

The disappearance of the CuPc monolayer spots indicates that the lateral order of the film is lifted by the adsorption of PTCDA. Increasing the PTCDA coverage further leads to some reordering of the organic mixed film to a new structure. These findings are completely different for the reversed hetero-organic system CuPc on PTCDA/Ag(111) [SSK⁺12]. In order to identify the differences between both stacked hetero-organic bilayer films, the LEED pattern of the system PTCDA/CuPc has to be understood.

The diffraction pattern of the new PTCDA/CuPc structure is shown in more detail in Fig. 6.2(a). All diffraction features are elongated in azimuthal direction but rather narrow in radial direction. This suggests a rotational disorder in the mixed organic film. The positions of all streaky diffraction features of the hetero-organic film are quite similar to the ones for a pure PTCDA monolayer film on Ag(111) [KUS04]. They can be modeled by the superstructure matrix $(\frac{7.84}{1.85}, \frac{1.25}{5.00})$. In the lower left part of pannel (a), the corresponding diffraction maxima are included as blue circles. The unit cell vectors of this rectangular structure have a length of $|\vec{A}| = (20.1 \pm 0.1)$ Å and $|\vec{B}| = (12.7 \pm 0.1)$ Å, respectively. These values are confirmed by one dimensional intensity profiles shown in Fig. 6.2(b) which reveal a cut through the first order diffraction maxima. The angle between the unit cell vectors is determined to be $\theta_{A,B} = (90.0 \pm 0.4)^{\circ}$ and the unit cell is rotated by $\theta_{\vec{A},[\bar{1}10]} = (9.0 \pm 0.4)^{\circ}$ with respect to the $|\bar{1}10|$ -direction of the substrate. In order to describe the azimuthal intensity distribution of

the diffraction streaks, the orientation of the adsorbate lattice has to be continuously modified from $\theta_{\vec{A},[\bar{1}10]} = 6.5^{\circ}$ to $\theta_{\vec{A},[\bar{1}10]} = 11.5^{\circ}$ while the other lattice parameters are kept constant. This results in a continuous rotation of the calculated superstructure diffraction pattern in Fig. 6.2(a) with respect to the substrate spots. Hence, the lateral order of the PTCDA/CuPc interface on Ag(111) is characterized by a well defined unit cell which reveals a continuous angle range of orientations with the silver substrate.

In Fig. 6.2(c), three selected orientations of the mixed organic unit cell are plotted on a silver lattice. While the light gray and black unit cell vectors illustrate the lattice parameters for a maximum ($\theta_{\vec{A},[\bar{1}10]}=11.5^{\circ}$) and minimum ($\theta_{\vec{A},[\bar{1}10]}=6.5^{\circ}$) rotation of the grid with respect to the substrate, the dark gray vectors correspond to the lattice of the calculated diffraction spots in panel (a). It is obvious that no distinct registry exists between the adsorbate lattice and the silver surface. This points to a rather weak influence of the substrate on the molecular order in the hetero-organic adsorbate system and thus to a dominant role of the intermolecular interactions on the lateral structure.

The rectangular shape and the size of the unit cell shown in Fig. 6.2(c) clearly reflect the lattice parameter of the PTCDA monolayer structure on the Ag(111) surface [KUS04, KTH⁺06]. This finding suggests that the PTCDA molecules do not adsorb on top of the CuPc film but immediately diffuse through the CuPc layer to the silver surface. Probably, PTCDA molecules penetrate randomly into the CuPc template layer already at very small PTCDA coverages which destroys the lateral order of the CuPc film. Increasing the PTCDA density than leads to a clustering of PTCDA molecules and to the formation of an ordered structure. However, the structure formation is disturbed by the presence of CuPc. As a consequence, no uniform orientation of the PTCDA adsorbate lattice and the silver grid can be formed, which causes the rotational disorder discussed before. CuPc molecules probably separate the PTCDA domains, which have different orientations to the substrate. Those which are replaced by PTCDA move up to the second organic layer.

In conclusion, the SPA-LEED results reveal a lifting of the lateral order of the CuPc template layer upon the adsorption of PTCDA at RT and very low PTCDA coverage. At higher PTCDA coverage, the diffraction signature of an ordered structure is visible, which exhibits a rotational disorder with respect to the substrate grid. The lattice parameters of this structure agree with the grid of the PTCDA monolayer structure on Ag(111). This is explained by a penetration of PTCDA into the CuPc layer and a corresponding displacement of CuPc into the 2nd layer. The PTCDA molecules cluster on the silver surface and form ordered domains, which are separated by CuPc molecules. The different orientations of the PTCDA lattice in these domains is caused by the stress induced by the remaining CuPc molecules in the first layer.

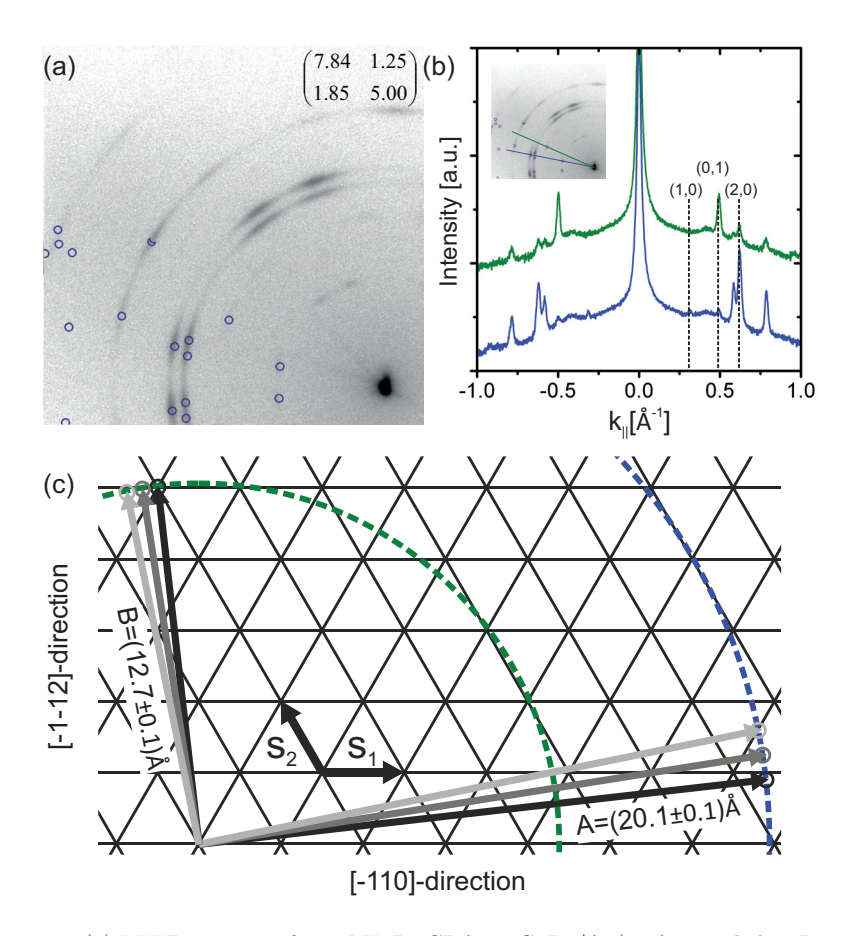


Figure 6.2: (a) LEED pattern of 0.70 ML PTCDA on CuPc/Ag(111) recorded at RT ($E_{\rm kin}=27.2\,{\rm eV}$). In the lower left part of the diffraction image, calculated diffraction spots are shown as blue circles. The corresponding superstructure matrix is also given in panel (a). (b) Radial intensity profiles recorded along the scan directions indicated in the inset of panel (b). (c) Three selected orientations of the PTCDA/CuPc unit cell vectors on the Ag(111) surface grid. The light gray and black unit cell vectors illustrate the maximum and minimum rotation of the unit cell with respect to the substrate. The superstructure matrix in panel (a) corresponds to the unit cell shown in dark gray.

Although this model can nicely explain the modification of the CuPc diffraction signature upon adsorption of PTCDA, more experimental evidence is mandatory to prove the statement that PTCDA indeed diffuses into the CuPc template layer.

6.2 Electronic structure

We have studied the molecular level alignment of PTCDA/CuPc bilayer films on Ag(111) with angle integrated UPS. In Fig. 6.3(a), valence spectra for different coverages of PTCDA on CuPc are displayed. The PTCDA coverage is estimated by the deposition time and molecular flux which was calibrated beforehand. These data have been recorded at room temperature using a monochromatized UV-source (He I α emission) and a Scienta R4000 electron analyzer. In addition, the work function of each PTCDA coverage is shown in Fig. 6.3(b). It is determined by the onset of the secondary electron cutoff recorded in normal emission geometry.

The spectrum of the pure CuPc monolayer structure in Fig. 6.3(a) (0.0 ML) exhibits two molecular features, which can be assigned to the HOMO and LUMO state of CuPc [KSS+10]. The latter state is partially populated by the interaction of CuPc with the silver substrate. Upon adsorption of 0.4 ML PTCDA on the CuPc film, a new molecular orbital appears at a binding energy of $E_{\rm b}=1.65\,{\rm eV}$ which can be attributed to the PTCDA HOMO state. In addition, the CuPc LUMO level is replaced by an almost completely filled state which is located at a clearly higher binding energy of $E_{\rm b}=0.45\,{\rm eV}$. A shift of the partially occupied LUMO, as it was observed for CuPc on PTCDA/Ag(111), is unlikely since this shift occurs rather quickly at small PTCDA coverage (< 0.4 ML). This finding indicates an enhanced charge transfer into the mixed organic film due to the adsorption of PTCDA which probably fills a new, previously unoccupied molecular state. This is supported by the increase in the work function upon the adsorption of PTCDA on CuPc. The surface potential barrier rises by $\Delta\Phi=330\,{\rm meV}$ which indicates an increased interface dipole at the metal-organic interface and hence an accumulation of charge in the organic layer. The binding energy of the CuPc HOMO is not affected by the adsorption of PTCDA.

Since no ARPES data are available, the unknown state at $E_{\rm b}=0.45\,{\rm eV}$ has to be assigned to a molecular orbital by comparison with other mixed organic systems.

Based on the SPA-LEED results, we have suggested that both CuPc and PTCDA are present at the silver surface and that CuPc decorates these PTCDA islands. Consequently, the UPS spectra should show a superposition of the CuPc and PTCDA LUMO signature of the monorganic films. This is, however, not observed. Instead, the UPS spectra for the system PTCDA/CuPc reveal the same number of resonances at similar binding energies as the spec-

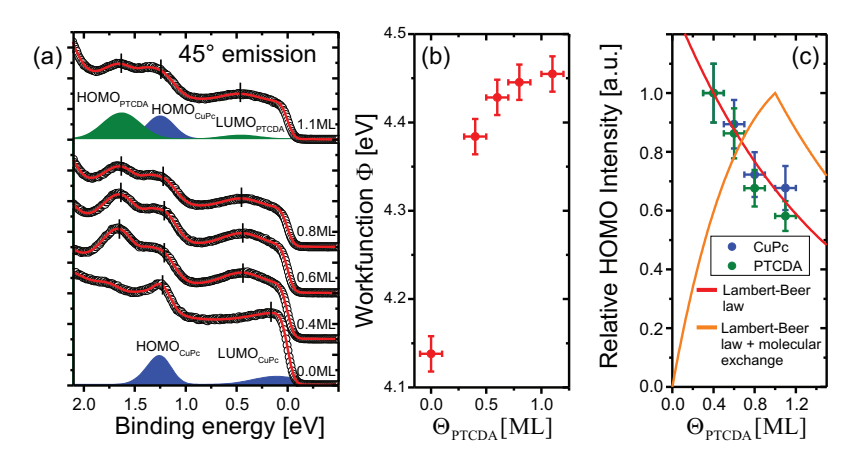


Figure 6.3: UPS data (a) of PTCDA/CuPc/Ag(111) for different PTCDA-coverages at RT (black circles, $\hbar\omega=21.218\,\mathrm{eV}$, photoelectron acceptance angle 30°). Red curves represent least square fits to the data. For the lower- and uppermost curves the fitting models consisting of up to three independent peaks are shown. The corresponding work functions are shown in panel (b). (c) Intensity of the CuPc and PTCDA HOMO level normalized to the corresponding signal at $\Theta_{\text{PTCDA}}=0.4\,\mathrm{ML}$ as a function of PTCDA coverage. The red curve describes the exponential attenuation of a constant first layer UPS signal, the orange curve the one of a linearly increasing signal.

tra of the laterally mixed films (see section 4.2.1). Hence, it can be speculated that the UPS feature at $E_{\rm b}=0.45\,{\rm eV}$ is caused by the population of the PTCDA LUMO for molecules in the first layer. In analogy to the mixed films, these PTCDA molecules should be located in direct vicinity of CuPc. Since no indication for an ordered mixed structure was found in LEED, the CuPc and PTCDA molecules might form a disordered mixed phase in the interspace between ordered PTCDA domains. Such a disordered mixed phase was recently reported for the co-adsorption of CuPc and PTCDA on Cu(111) [CSS⁺12]. In these disordered films, small PTCDA clusters of ≈ 3 PTCDA molecules are surrounded by ≈ 6 CuPc molecules.

The existence of a disordered CuPc-PTCDA mixed phase in between the PTCDA domains could explain the electronic and geometric structure of the hetero-organic system PTC-DA/CuPc. However, it is not clear, whether the electronic structure of this disordered mixed phase, i.e., the charge transfer into the PTCDA LUMO, is caused by an electronic coupling via a hybrid state, like in the ordered mixed structures.

For higher PTCDA coverage up to 1.1 ML, no significant shifts of the molecular features occur in the UPS data and only a marginal increase of the work function Φ can be detected. The intensities of the CuPc and PTCDA HOMO levels change with increasing PTCDA cov-

erage. Their intensities, normalized to their signal at $\Theta_{PTCDA} = 0.4 \,\mathrm{ML}$, are plotted in Fig. 6.3(c) as a function of PTCDA coverage. Although the PTCDA coverage is increased, the normalized peak intensity of the PTCDA HOMO decreases continuously, similar to the CuPc HOMO intensity. This behavior is similar to the damping of the PTCDA HOMO signal for the adsorption of CuPc on PTCDA (see chapter 5) and can be described by an exponential decay ("Lambert-Beer" law) [GFSR11]:

$$I = I_0 e^{-\Theta/\lambda}. (6.1)$$

This model describes the attenuation of the photoelectron intensity I_0 by an overlayer of thickness Θ . In Fig. 6.3(c), the theoretical decay of the photoelectron intensity of the first organic layer is plotted for an attenuation length $\lambda = 1.51\,\mathrm{ML}$ (red curve). Note that this attenuation length λ is not the result of a fit to the data, but was determined for the reference system CuPc/PTCDA on Ag(111) (see chapter 5).

The agreement between this model curve and the decay of the PTCDA HOMO intensity suggests that a certain amount of PTCDA penetrates into the CuPc layer and exchanges CuPc molecules. The CuPc molecules in the second layer hence cause the damping of the PTCDA signal. However, not all PTCDA molecules can be located in the first organic layer. This is indicated by the orange curve in Fig. 6.3(c), for which it is assumed that all PTCDA molecules available at a coverage Θ move in the first layer, i.e., $I_0 \propto \Theta$ until the first layer is completely filled up with PTCDA. Since PTCDA exchanges CuPc, the same coverage Θ of CuPc molecules is located in the second layer. The resulting HOMO intensity (orange curve) therefore increases not linearly, but is increasingly damped until all CuPc molecules in the first layer are exchanged by PTCDA. Afterwards, PTCDA molecules also adsorb on the first PTCDA layer and contribute to the damping of the signal arising from PTCDA in the 1st layer. Since the shape of this orange curve does not describe the experimental data we can exclude that all PTCDA molecules penetrate into the CuPc film. A part of the PTCDA molecules remains in the second layer. Since we only observe a decrease of the PTCDA HOMO intensity for coverages larger than 0.4 ML, we can even estimate that the amount of PTCDA molecules moving in the first layer is smaller than 0.4 ML.

Although we assume that CuPc is exchanged by PTCDA and hence present in the first and second organic layer, we only find one CuPc HOMO peak in the UPS spectra. This is different for a CuPc bilayer film on Ag(111) for which a splitting of $\approx 300\,\mathrm{meV}$ was reported for the CuPc HOMO state. The CuPc molecules in the second layer are decoupled from the metal substrate and the energetic position of their HOMO state is determined by its ionization potential IP. On a metal surface, the ionization potential can be calculated by the sum of the work function and the binding energy of the corresponding state. For the CuPc bilayer film, this results in IP = 5.6 eV. Note that the same IP is also obtained for the

system CuPc/PTCDA/Ag (111) (see chapter 5). Based on this value and the work function of PTCDA/CuPc on Ag(111) (see Fig. 6.3(b)), the HOMO should be located at $E_{\rm b}=1.2\,{\rm eV}$ for CuPc molecules in the second layer. This binding energy coincides with the corresponding value for CuPc molecules in the first organic layer and hence explains the absence of a separated second layer CuPc HOMO feature.

In conclusion, the molecular level alignment of the CuPc/Ag(111) template layer is strongly modified by the adsorption of PTCDA. Besides the appearance of the PTCDA HOMO state, the partially occupied CuPc LUMO is replaced by a new state located 300 meV higher in binding energy. Since all UPS-spectra for PTCDA/CuPc are very similar to the ones of the mixed organic films, it is concluded that the new state is the PTCDA LUMO level which is filled due to the lateral interaction with CuPc. The PTCDA molecules have to be in direct contact with the silver surface and with CuPc molecules. Hence, we suggest that both molecules form a disordered mixed phase similar to CuPc and PTCDA on Cu(111) [CSS+12]. The continuous decreasing PTCDA HOMO intensity with rising PTCDA coverage indicates, that not all PTCDA molecules can be located in the first organic layer. A certain amount of PTCDA has to adsorb in the second layer.

6.3 Vertical adsorption geometry

The previous results in sections 6.1 and 6.2 suggest that the PTCDA molecules do not adsorb on the closed CuPc monolayer but penetrate into the CuPc layer. We propose that PTCDA clusters in small domains, which are surrounded by a disordered mixed film of CuPc and PTCDA. In order to test this adsorption scenario, the vertical adsorption geometry of CuPc and PTCDA is studied with the X-ray standing wave technique.

A sample of 0.50 ML PTCDA on a CuPc monolayer film has been studied with the XSW method at 50 K. The sample preparation was controlled by LEED. Also here, core level spectra of carbon, oxygen, nitrogen, and copper were recorded.

After a short discussion of all atomic core level signals from the mixed organic layer, the obtained XSW results are discussed in section 6.3.2.

6.3.1 Core level models

As far as possible, the core level spectra have been modeled in the way described in the previous sections 4.3 and 5.3. Here, we only discuss differences which had to be introduced in the C1s and O1s emission lines. The core level model applied to separate the carboxylic and anhydride oxygens is shown in the right panel of Fig. 6.4, all fitting parameters are summarized in table 6.1. A model quite similar to the one used for the vertically stacked

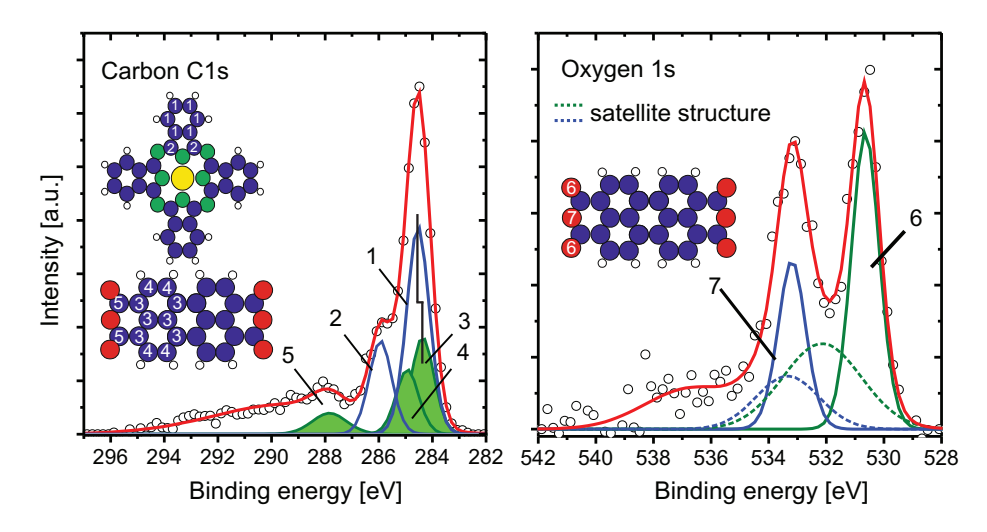


Figure 6.4: Background subtracted core level spectra of the carbon C1s, and oxygen O1s emission arising from the molecules in the PTCDA/CuPc structure on Ag(111). The spectra are obtained at an energy 4 eV below the Bragg energy. All components of the models used for fitting the data are shown as colored lines, except the Gaussian of the energy loss tail at high binding energies.

system CuPc/PTCDA (see section 5.3.1) resulted in the best fitting quality. This already indicates that PTCDA is in direct contact with the silver surface. The energy positions of the satellite structure and their relative intensity to their main line is modified in order to fit the more pronounced dip between the main peaks of the spectrum. All modifications of the fitting model are constrained to the condition that the emission from both oxygen species reflects the stoichiometry of the molecule. The exact fitting parameters are optimized by maximizing the resulting coherent fraction F^H for both separated components. In order to obtain the oxygen partial yield curves, the energetic positions as well as the FWHM and the relative intensity of the main line and its satellite structure are fixed to the values given in table 6.1.

For the C1s core levels, the situation is much more complex. In our adsorption model, we propose at least three inequivalent contributions to the C1s signal: CuPc and PTCDA molecules in the first layer and at least CuPc molecules in the second layer. Although it cannot be excluded that also PTCDA molecules are located in the second layer, their amount should be rather low due to the low PTCDA coverage of 0.5 ML. In a first attempt, the C1s emission was analyzed with the fitting model of the MBW structure. Although the binding energies of the frontier molecular orbitals for the PTCDA/CuPc and the MBW structure are almost identical, the C1s core level data could not be fitted very well. A much better fitting quality

O1s species	$E_{\rm b}[{ m eV}]$	FWHM [eV]	Intensity [%]
Carboxylic Oxygen Main Line (6)	530.6	1.2	31
Carboxylic Oxygen Satellite	530.6 + 1.5	3.2	24
Anhydride Oxygen Main Line (7)	530.6 + 2.6	1.2	17
Anhydride Oxygen Satellite	530.6 + 2.7	3.2	12
Energy Loss Satellite	536.6	6.5	16
C1s species	$E_{\rm b}[{ m eV}]$	FWHM [eV]	Intensity [%]
CuPc C-C (1)	284.5	1.0	30
CuPc C-N (2)	284.5 + 1.4	1.0	14
PTCDA C-C (incl. C-C-O) (3)	284.5 - 0.17	1.1	14
PTCDA C-H (4)	284.5 + 0.4	1.1	9
PTCDA C-O (5)	284.5 + 3.3	1.5	5
Energy Loss Satellite	289.5	6.3	28

Table 6.1: Summary of the binding energy position $E_{\rm b}$, the FWHM and the relative area of the fitting model employed in order to deconvolute the contributions of the O1s and C1s core level spectra.

was achieved with the model for 0.60 ML CuPc on PTCDA/Ag(111) (see section 5.3.1). A further optimization of the relative intensities of this fitting model leads to the fitting parameters which are summarized in table 6.1. In order to obtain the carbon partial yield curves, again the energetic positions, FWHM as well as relative peak intensities of all species within one molecule are fixed to those values in table 6.1. With these constraints, only average coherent positions and fractions can be obtained for the carbon atoms of PTCDA and of CuPc. The signals from identical molecules in the first and second layer cannot be separated. This will be discussed further in the following.

6.3.2 Adsorption heights

A yield curve from a single XSW scan is shown in Fig. 6.5 for each chemical species of the hetero-organic PTCDA/CuPc structure. The data and the experimental error are treated in the same way as described before. Relatively small error bars indicate a high quality of the data set. Fitting results for all single XSW scans are plotted on the Argand diagram in Fig. 6.6. The XSW results of the CuPc components N1s and Cu2p as well as of the PTCDA carboxylic oxygen species reveal a narrow distribution around their arithmetic means, which are included as colored arrows. The experimental errors of these fitting parameters are determined by the standard deviation and result in $\Delta d^H = \pm 0.02$ Å for the adsorption height. For the anhydride oxygen, a larger error of $\Delta d^H_{\rm O1sanhy} = \pm 0.04$ Å was found for the same reasons as described before (see chapter 4.3 and 5.3.2).

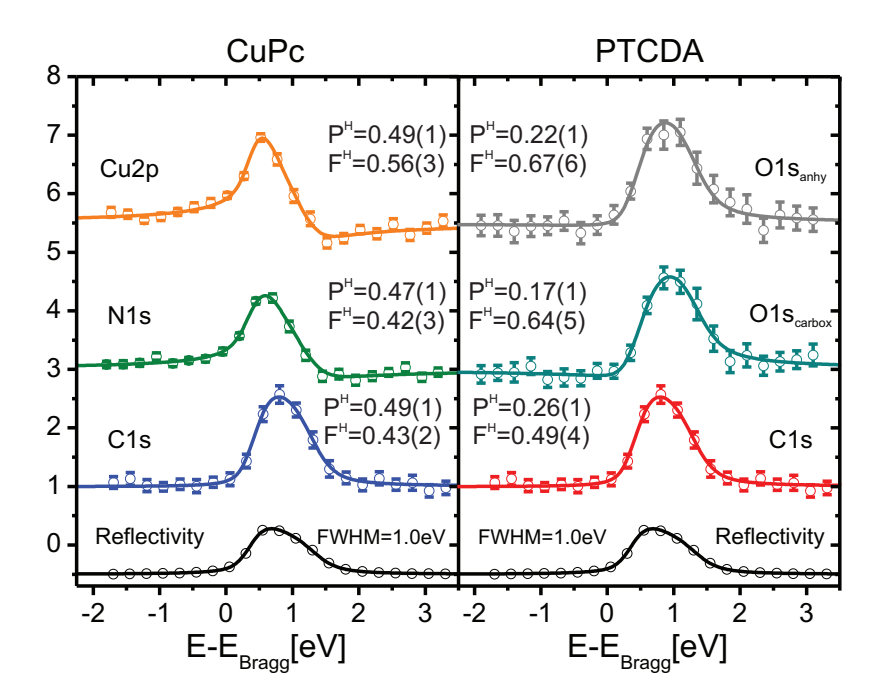


Figure 6.5: Yield curves of a single XSW scan for all chemically different species found for the PTCDA/CuPc bilayer film on Ag(111). The yield curves were obtained by fitting the core level data according to the models discussed in chapter 6.3.1. The solid lines represent fits to the yield curves performed with *Torricelli* [Mer12]. The numbers given for each species represent the fitting result of this particular single XSW scan.

In table 6.2 the averaged coherent fractions F^H and positions P^H for all chemical species are summarized together with the resulting adsorption heights. As reference, the adsorption heights of the pure CuPc and PTCDA monolayer films are also included [KSS⁺10, HTS⁺10]. The coherent positions P^H of all PTCDA species are not identical. Both carboxylic as well as the anhydride oxygen atoms are located below the carbon backbone of the molecule. This indicates a bending of the molecule which is so strong that it can only be caused by the interaction with a metal surface. This proves that PTCDA molecules move to the first adsorbate layer. The coherent fractions of the oxygen species are comparable to the corresponding values of a PTCDA monolayer film [HTS⁺10]. It shall be mentioned that the carbon yield of PTCDA might still contain a small contribution from CuPc carbon atoms due to an imperfect core level model, which can explain its rather low coherent fraction.

The coherent positions P^H of all CuPc species can not be transferred directly into reasonable adsorption heights. It was also found that all coherent fractions are considerably smaller

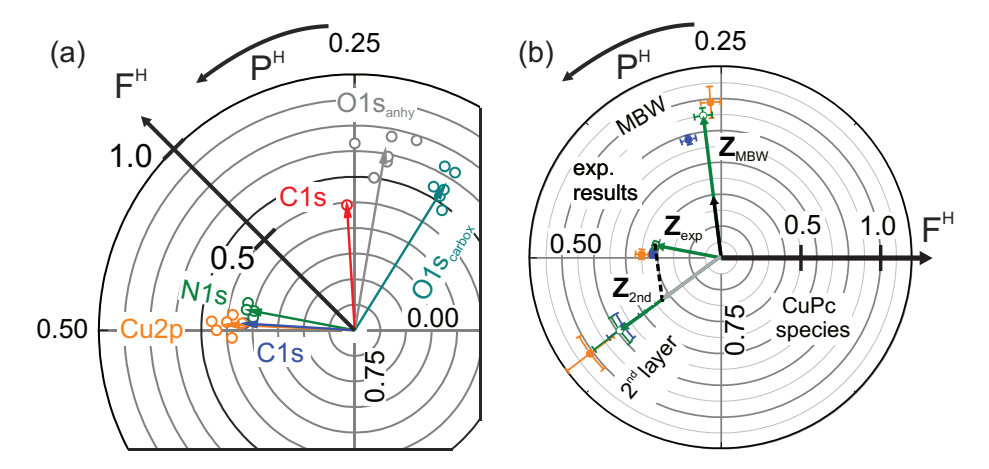


Figure 6.6: (a) Argand diagram showing the XSW results for all single XSW scans for the adsorption of 0.50 ML PTCDA on one monolayer $\mathrm{CuPc/Ag(111)}$ at 50 K. The arrows indicate the averaged results for the coherent position P^H and fraction F^H . (b) Fourier-component analysis for the XSW results of CuPc . The vector sum is exemplary shown for the nitrogen species. It is assumed that the first layer CuPc molecules of the PTCDA/CuPc structure exhibit the same adsorption height as in the MBW structure (see section 4.3.2). The position of the 2nd layer CuPc molecules can then be calculated, see text. The color code for the different CuPc species is identical in both panels.

than those of all other XSW studies of hetero-organic systems discussed so far. This indicates either the existence of a very wide distribution of heights, e.g., caused by a strong tilt of the molecule, or of several distinct adsorption heights. The latter is more likely since all experimental results discussed previously point to an exchange of CuPc and PTCDA and hence to the occurrence of two distinct vertical positions for CuPc. This statement can be proven by the Fourier component analysis of the CuPc correlated fitting results. The analysis can be performed in the Argand diagram since there the Fourier components are represented by polar vectors which just have to be summed up to obtain the experimental results.

However, one of the components, either the adsorption height of CuPc in the first or in the second organic layer, has to be estimated. This is more straight forward for the molecules in the first layer since the height of CuPc in the MBW structure can be used as a reference (see section 4.3.2). This allows to access the adsorption position of the CuPc molecules in the second layer from the measured CuPc adsorption height. The Fourier analysis is illustrated in the Argand diagram in Fig. 6.6(b). The XSW results for all CuPc species both in the Mixed Brick Wall structure (see section 4.3.2) and in the PTCDA/CuPc structure are shown.

	P^H	F^H	$d_{\mathrm{PonC}}^{H}\left[\mathrm{\AA} ight]$	$d_{ ext{PTCDA,ML}}^{H} \left[ext{Å} ight]$	$d_{\mathrm{CuPc,ML}}^{H} \left[\mathrm{\mathring{A}} \right]$
$C1s_{sum}$	0.38 ± 0.01	0.33 ± 0.02	3.24 ± 0.01	-	-
C1s _{CuPc}	0.49 ± 0.01	0.43 ± 0.02	3.50 ± 0.02	-	3.08 ± 0.02
$C1s_{PTCDA}$	0.26 ± 0.01	0.49 ± 0.04	2.96 ± 0.02	2.86 ± 0.01	-
$O1s_{sum}$	0.182 ± 0.013	0.63 ± 0.09	2.78 ± 0.03	2.86 ± 0.02	-
O1s _{carbox}	0.162 ± 0.008	0.66 ± 0.06	2.73 ± 0.02	2.66 ± 0.03	-
O1s _{anhy}	0.223 ± 0.016	0.71 ± 0.07	2.88 ± 0.04	2.98 ± 0.08	-
$N1s_{CuPc}$	0.470 ± 0.007	0.42 ± 0.02	3.45 ± 0.02	-	3.07 ± 0.04
$Cu2p_{CuPc}$	0.493 ± 0.010	0.50 ± 0.04	3.51 ± 0.02	-	3.02 ± 0.04

Table 6.2: Summary of the XSW results for 0.50 ML PTCDA on CuPc at $T_{\rm sample} = 50\,{\rm K}$ averaged over all single XSW scans. The literature results for the pure PTCDA [HTS⁺10] as well as for the CuPc monolayer structure [KSS⁺10] on Ag(111) are included for comparison. The results for C1s_{sum} and O1s_{sum} are obtained by analyzing the total photoelectron yield of the corresponding atomic species.

	P_{MBW}^{H}	$F_{ m MBW}^H$	P_{2nd}^{H}	$F_{\rm 2nd}^H$	$d_{\mathrm{2nd}}^{H}\left[\mathrm{\AA} ight]$
$C1s_{CuPc}$	0.29 ± 0.01	0.77 ± 0.02	0.60 ± 0.02	0.75 ± 0.12	6.11 ± 0.05
$N1s_{CuPc}$	0.27 ± 0.01	0.95 ± 0.05	0.60 ± 0.02	0.78 ± 0.20	6.11 ± 0.05
$Cu2p_{CuPc}$	0.26 ± 0.01	0.98 ± 0.10	0.60 ± 0.02	1.02 ± 0.18	6.11 ± 0.05

Table 6.3: Summary of the coherent fraction $F_{\rm 2nd}^H$ and position $P_{\rm 2nd}^H$ of the CuPc molecules in the second layer of the PTCDA/CuPc structure. All values are obtained by a vector analysis illustrated in the Argand diagram in Fig. 6.6.

For the nitrogen species, the vector analysis is shown in more detail. The vector of the second layer CuPc molecules \mathbf{Z}_{2nd} can be calculated by subtracting the vector \mathbf{Z}_{MBW} of the MBW molecules from the vector of the experimental results \mathbf{Z}_{exp} . Therefore \mathbf{Z}_{MBW} has to be scaled according to its contribution to \mathbf{Z}_{exp} . This scaling factor has to consider the relative coverage of CuPc in the first layer which is equal to the PTCDA coverage of $(0.50\pm0.1)\,\mathrm{ML}$. The latter assumes that all PTCDA molecules are located in the first layer. In addition, the reduced transmission of the first layer photoemission signal has to be taken into account by the damping factor $D_f = (80\pm10)\,\%$ determiend in section 5.3.3. Both facts decrease the length of \mathbf{Z}_{MBW} by a factor of 0.4 (black vector). This vector is now subtracted from \mathbf{Z}_{exp} which results in the gray vector. While the direction of this vector already reflects the coherent position P^H of the nitrogen atoms in the second layer, its length only reveals its relative contribution to the averaged nitrogen signal. The coherent fraction and hence \mathbf{Z}_{2nd} is obtained by rescaling the vector length by the inverse of its contribition to \mathbf{Z}_{exp} .

In analogy, the vertical positions of all CuPc components in the second organic layer can be obtained which are summarized in table 6.3. For all CuPc species, a coherent position of

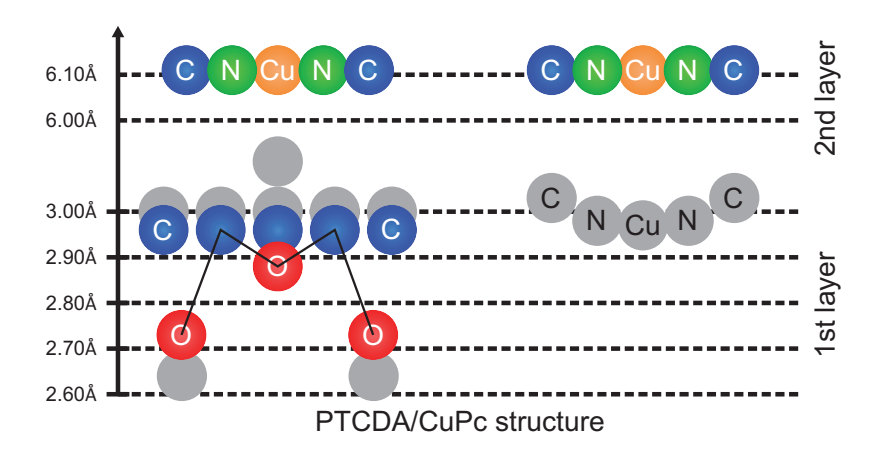


Figure 6.7: Model of the vertical adsorption geometry of CuPc and PTCDA in the PTC-DA/CuPc film on Ag(111). PTCDA is shown in the typical front view and CuPc in a schematic side view. The colored circles mark the experimentally obtained adsorption heights of the molecules in the mixed interface. The gray circles indicate the vertical positions of the PTCDA and CuPc molecules in the laterally mixed MBW structure (see section 4.3.2).

 $P_{\text{CuPc,2nd}}^H = (0.60 \pm 0.02)$ is found. The corresponding adsorption height of $d^H = (6.11 \pm 0.05)$ Å matches the value of CuPc adsorbed on PTCDA and hence confirms that CuPc molecules are located in the second layer. The uncertainty of the vector analysis is estimated by repeating the analysis for 800 different combinations of D_f , \mathbf{Z}_{MBW} and $\Theta_{\text{CuPc}}^{\text{1st}}$ within their experimental error bars and calculating the standard deviation of this distribution.

The adsorption heights of all CuPc and PTCDA species are shown in a vertical adsorption model in Fig. 6.7. The measured adsorption heights are shown in color, the ones for molecules in the MBW structure in gray.

The CuPc molecules in the second layer are located at an adsorption height of $d^H = (6.11 \pm 0.05)$ Å, which is almost identical to the adsorption height of CuPc on PTCDA/Ag(111). This supports our adsorption scenario in which we suggest an exchange of CuPc and PTCDA molecules and a subsequent diffusion of CuPc into the second organic layer. The vertical distance between CuPc and the PTCDA backbone is $\Delta d = (3.15 \pm 0.05)$ Å and hence agrees well with the expected lattice spacing in organic molecular crystals [FZ94, McK98].

The situation for PTCDA is not as clear as for CuPc. The PTCDA molecules reveal a distortion that is quite unusual for their adsorption on the Ag(111) surface [HTS⁺10]. Both oxygen species are located below the carbon backbone, which has not been observed yet for PTCDA molecules on the Ag(111) surface, neither in the pure [HTS⁺10, SSK⁺12] nor in the

mixed phases (see section 4.3.2 and 5.3). The adsorption heights of both oxygen species are very similar to the results for 0.95 ML CuPc on PTCDA. Consequently, the unusual distortion of PTCDA might be caused by an artifact, namely a too large vertical position of the carbon backbone. This could be caused by a second contribution to the PTCDA carbon yield which could not be separated. The reason for such a second contribution to the PTCDA carbon yield is not unambiguously clear. A contribution from PTCDA molecules in the second layer could be one reason. In the Argand diagram, the total carbon yield vector would then be shifted to higher cohered positions. Consequently, the adsorption height appears larger for molecules in the first layer as long as the second contribution is not subtracted.

Based on our UPS study, we also proposed that PTCDA molecules can be found in the second layer. Although this scenario cannot be ruled out, it is rather unlikely since it should also affect the adsorption height of the oxygen species similarly, i.e., their position would also be lower. Consequently, it can not explain the distortion of PTCDA. On the other hand, the low coherent fraction for the PTCDA carbons could suggest a not properly performed separation of the CuPc and PTCDA contributions. In this case, the PTCDA yield also contains a contribution from CuPc molecules in the second layer, which artificially increases the adsorption height of the PTCDA backbone.

In any case, it seems very likely, that the PTCDA carbon atoms are located between both oxygen species. This would result in an vertical adsorption configuration similar to the one for 0.95 ML CuPc on PTCDA.

The height of the carbolic oxygen atoms is larger than in the MBW or the pure PTCDA monolayer structure. This could be explained by the rotational disorder in the PTCDA/CuPc film, which does not allow a distinct adsorption site or rotation for PTCDA molecules on silver. Hence, the oxygen atoms are located not only above atoms of the silver surface but reveal a wider distribution of adsorption sites. Since no uniform Ag-O bond can be formed between the molecule and the surface in this case, it results in a lifting of the carboxylic oxygen atoms.

In general we propose, that the vertical adsorption configuration of the molecules in the PTCDA/CuPc structure is similar to the adsorption of CuPc on PTCDA. This agrees well with our structural model. PTCDA penetrates into the CuPc film which leads to the appearance of CuPc molecules in the second layer on top of PTCDA. Also the existence of disordered mixed phases in the first layer does not necessarily contradict to the obtained adsorption height of PTCDA. For the ordered mixed structure, we proposed a decoupling of the adsorption height and the charge transfer into the molecule. The adsorption height of PTCDA in the disordered mixed phase could also be modified by CuPc in the second layer without disturbing the charge redistribution in the first layer.

In conclusion, we studied the vertical adsorption geometry of 0.50 ML PTCDA on a closed

monolayer CuPc/Ag(111) with the X-ray standing wave technique. The molecular distortion of PTCDA clearly indicates a direct adsorption of the molecule on the silver surface. The oxygen atoms are located at adsorption heights similar to the adsorption of CuPc on PTCDA, the carbon backbone is found above both oxygen species. We argued that this might be due to an artifact, namely a contribution of carbon atoms in the second layer to the PTCDA carbon yield and proposed an adsorption geometry for PTCDA similar to the system CuPc on PTCDA.

For all CuPc species, low coherent fractions indicated the existence of several adsorption heights. A vector analysis in the Argand diagram proved that all CuPc yield curves contain contributions from CuPc molecules in the first and second layer. All these findings support our structural model in which PTCDA penetrates into the CuPc film resulting in an exchange of CuPc and PTCDA. The excess of CuPc molecules is located in the second layer.

6.4 The metal-organic interface: The basis for the hetero-organic growth

The different results obtained for the adsorption of CuPc on PTCDA (chapter 5) and PTCDA on CuPc allows to determine the influence of the template layer on the subsequent structure formation in the mixed organic film.

As we have reported above, PTCDA does not adsorb on CuPc at RT, but penetrates into the CuPc film and forms a disordered mixed film with CuPc, which is electronically similar to the ordered mixed structures on Ag(111). Therefore, a certain amount of CuPc molecules is exchanged by PTCDA and moves to the 2nd layer.

These findings indicate that the exchange of CuPc molecules by PTCDA on the Ag(111) surface results in a lower total interface potential than the adsorption of PTCDA on CuPc. The repulsive intermolecular interaction between CuPc molecules and their usually high mobility at RT leads to a low stability of the lateral order in the monolayer film. Hence, PTCDA can easily penetrate into the CuPc layer due to its probably larger adsorption energy on Ag(111) compared to CuPc and replace the latter molecules. In this way, the intermolecular repulsion between neighboring CuPc molecules is also transfered into an attractive interaction between CuPc and PTCDA. Both effects result in an energy gain for the total interface potential and can hence explain the adsorption behavior of PTCDA on CuPc.

The adsorption behavior for the reversed system, CuPc on PTCDA, is completely different. The CuPc molecules adsorb in the second layer on the closed PTCDA monolayer structure independent from the CuPc coverage. At RT, the electrostatic moment of the PTCDA

molecules results in an intermolecular attraction which causes a high stability of the PTCDA monolayer islands [KUS04, MGS⁺06]. Since the adsorption energy gain of CuPc is not large enough to crack the PTCDA islands, CuPc cannot penetrate into the PTCDA layer and adsorbs in the second layer.

At elevated sample temperatures of $\approx 575\,\mathrm{K}$, however, CuPc penetrates into the PTCDA monolayer structure and replaces PTCDA at the metal-organic interface in order to create a perfectly ordered mixed organic film. At these temperatures, the mobility of the PTCDA molecules is enhanced which might lead to a reduced stability of the PTCDA islands. Note that for submonolayer films of PTCDA/Ag(111), the ordered PTCDA islands even dissolve at elevated sample temperatures [HDK12]. This might also weaken the interaction strength between PTCDA and silver since no local Ag-O can be formed easily for diffusing PTCDA molecules. Hence, a higher mobility and a probably reduced interaction strength of PTCDA and Ag(111) enable CuPc to penetrate into the PTCDA film.

In conclusion, the intermolecular and the molecule-substrate interactions in the template layer determine the structure formation of organic-organic interfaces. For a strong lateral attraction between the molecules which stabilizes the lateral order in the first layer, a heteroorganic bilayer is formed at RT. But if the adsorption energy of the second molecules on the metal surface is large enough to crack the template layer, they can penetrate into this film and form a mixed structure. The stability of the first layer is reduced by increasing the sample temperature which also results in the formation of a mixed film.

6.5 Conclusion

In this chapter, the adsorption behavior of PTCDA on one closed CuPc layer was reported based on a variety of different experimental results.

The lateral order of the mixed organic film was studied with SPA-LEED. It was found that the CuPc monolayer structure is destroyed by the adsorption of PTCDA. The PTCDA molecules penetrate into the template layer and initially (already at $\approx 0.1\,\mathrm{ML}$) break the periodicity of the long range ordered CuPc film. This results in the disappearance of the CuPc LEED pattern. At higher coverage, a diffraction signature of an ordered lattice with a rotational disorder occurs. This disorder manifests itself in streaky diffraction features in azimuthal directions in the LEED pattern. They correspond to a lateral rotation of the superstructure unit cell in the range of a few degrees around their center position. The lattice parameters of this structure are very similar to the PTCDA monolayer grid on Ag(111).

The frontier orbitals were investigated with UPS. For PTCDA coverages up to 1.1 ML, the spectroscopic fingerprint of the PTCDA/CuPc structure is almost identical to the one of the mixed organic films introduced in chapter 4. This indicates that PTCDA molecules are in direct contact with the silver surface and form a disordered mixed phase with CuPc in the gap between the ordered PTCDA domains. The binding energy of the PTCDA LUMO level points to an additional charge transfer into the molecule, similar to the mixed CuPc and PTCDA films. The PTCDA HOMO signal is continuously decreased with rising PTCDA coverage. We believe, this suggests that not all PTCDA molecule penetrate into the CuPc film, but also adsorb in the second layer.

The vertical adsorption positions of CuPc and PTCDA were accessed by XSW. These data confirm that (almost) all PTCDA molecules move to the first layer. The oxygen atoms are located at adsorption heights similar to the adsorption of CuPc on PTCDA, the carbon backbone is found above. It was argued that this is probably caused by an artifact, namely a contribution of CuPc carbon atoms which could not be separated. Hence, we suggest that the PTCDA adsorption height is similar to the system CuPc on PTCDA/Ag(111). For CuPc, two adsorption heights were found, one in the first and one in the second layer. Both results agree again with our structural model that PTCDA moves to the silver surface and that CuPc and PTCDA molecules are exchanged.

Finally, we have compared the different adsorption behaviors of the hetero-organic system CuPc on PTCDA/Ag(111) (chapter 5) and the reversed system PTCDA on CuPc/Ag(111). The stability of the lateral order in the template layer and the adsorption energy of the molecules on the surface determines the subsequent organic-organic film growth. The repulsion between the CuPc molecules leads to a low stability of the monolayer structure. Therefore, PTCDA can easily penetrate into the CuPc monolayer film and exchange CuPc molecules since their adsorption energy on Ag(111) is lower than the one of PTCDA. In contrast, the molecules in the PTCDA monolayer film are more strongly connected to each other by an intermolecular attraction. Hence, CuPc can only penetrate into the PTCDA monolayer structure after thermal activation of the molecular exchange process. At RT, CuPc adsorbs on the closed PTCDA layer on Ag(111).

6.6 Outlook

The investigation of the hetero-organic systems CuPc on PTCDA/Ag(111) and the reversed system PTCDA on CuPc/Ag(111) revealed interesting experimental results. Especially for the first system, we proposed several models in order to explain these findings. However,

there are still many highly interesting observations which require additional experimental and theoretical studies before these effects can be fully understood.

For the adsorption of CuPc on PTCDA, a strong modification of the interaction between PTCDA and the silver surface was observed. This was reflected by an enhanced charge transfer into the PTCDA molecule and in a smaller adsorption height of the PTCDA backbone. We proposed that an additional charge transfer into PTCDA becomes energetically favored since the CuPc molecules screen the charges located on PTCDA more effectively. This results in an enhanced interaction between PTCDA and the silver surface. Density functional theory could provide a more sophisticated view into the interaction mechanisms of the CuPc/PTCDA bilayer films on Ag(111). Such calculations should be able to reveal whether the changed adsorption properties of PTCDA are induced by an interaction between CuPc and PTCDA or by an direct interaction of CuPc with the silver surface.

Very recently, Egbert Zojer and coworkers [ERAS+13] used a new van der Waals functional [RLZ+12] in DFT in order to calculate the molecular adsorption heights and the density of states of the molecules in the CuPc/PTCDA bilayer structure on Ag(111). Although they reported a small lowering of the PTCDA adsorption height for a very low CuPc coverage, they could not detect an additional charge transfer into PTCDA. Hence, they concluded that the vertical PTCDA height is changed by a van der Waals interaction between CuPc and the silver surface. These calculations were performed for a smaller unit cell with only one CuPc molecule per four PTCDA molecules and therefore with a much smaller CuPc density. This might be the reason for the fact that these calculations could not yet reproduce the experimental findings for the CuPc/PTCDA bilayer film on Ag(111).

We reported that PTCDA does not adsorbs on CuPc at RT, but penetrates into the CuPc film which leads to an exchange of PTCDA and CuPc. For the reverse system, CuPc/PTCDA, this molecular exchange occurs only after thermal activation. A suited tool to study this effect in real time is photoemission electron microscopy (PEEM) or low energy electron microscopy (LEEM). Temperature dependent LEEM/PEEM experiments (also at LT) can provide information about the energy barriers which play a role for the molecular exchange. It is an interesting question if a reduced mobility of the molecules at LT prevents the intermixing of the molecules and hence leads to the formation of a "real" hetero-organic interface for the system PTCDA on CuPc/Ag(111).

Since the interactions between the first organic layer and the substrate seem to play an important role for the formation of the hetero-organic junction, they can be tuned either by changing the substrate or the molecules. First results were obtained for exchanging PTCDA by 1,4,5,8-naphthalene-tetracarboxylic acid dianhydride (NTCDA) [SSK13], i.e. for the ad-

sorption of CuPc on NTCDA. This molecule is very similar to PTCDA, but has a naphthalene instead of a perylene core and forms two different ordered monolayer structures on Ag(111): the commensurate "relaxed monolayer structure" and the incommensurate, more densely packed "compressed monolayer structure" [KSK⁺08]. On the more densely packed compressed monolayer, CuPc does not lift the lateral order of the NTCDA monolayer film. However, on the more open relaxed monolayer structure, the adsorption of CuPc results in the formation of a laterally mixed film at RT, which can also be obtained when depositing submonolayer coverages of CuPc and NTCDA directly on Ag(111). These first results on this related system also suggest, that CuPc can diffuse into a more open organic layer (as the relaxed NTCDA structure) in order to optimize the total interface potential, but adsorbs on top of the densely packed NTCDA film.

Finally, we propose to investigate the adsorption of CuPc on an ordered mixed layer consisting of CuPc and PTCDA on Ag(111) in future. These studies could help to understand the properties of the PTCDA/CuPc structure. For this film, we proposed the formation of a disordered mixed structure in the first layer which results in the appearance of CuPc molecules in the second layer. Secondly, this model system allows to study the structure formation at hetero-organic bilayer films and how they depend on the lateral order of the first template layer. The latter can be tuned by the relative coverage of CuPc and PTCDA in the first layer. All mixed systems revealed a strong modification of the electronic structure of the individual molecules. Therefore the electronic properties of the molecules in the first layer might again be modified upon adsorption of CuPc.

7 Summary and conclusion

This work presents a systematic study of the structure formation in different hetero-organic systems containing CuPc and PTCDA molecules which are adsorbed on the Ag(111) surface.

Complementary experimental methods were used in order to characterize the mixed organic films. The lateral structure was studied by SPA-LEED and STM, the adsorption height of the individual molecules by XSW. The electronic structure was investigated by (AR)UPS and orbital tomography as well as by STS. The orbital tomography, a new method which allows to identify the emitting molecular orbitals by their angle resolved photoemission pattern, was so far only applied to low symmetric surfaces. A first result obtained in this work is, that this method can also be applied to highly symmetric fcc(111)-surfaces. This was demonstrated by studying the well known electronic structure of the two inequivalent PTCDA molecules in the monolayer structure on Ag(111) [SWR+12]. Although this system exhibits twelve different molecular orientations due to three rotational domains, each having one mirror domain, the angle resolved emission yield for the LUMO and HOMO revealed a well defined peak structure which could be understood qualitatively in the framework of the orbital tomography approach. The projected density of states for both molecules was obtained by a fitting algorithm of the ARPES data and revealed an excellent agreement with the DOS reported earlier by STS [KTH+06].

In chapter 4, we focused on the adsorption properties of laterally mixed CuPc and PTCDA films adsorbed directly on the Ag(111) surface. The relative coverage of the molecules determines the composition of the ordered mixed organic structures which can be divided into three different phases: the Mixed Brick Wall (MBW) structure in the PTCDA-rich regime, the CuPc-rich Mixed Zig-Zag (MZZ) structure and the Mixed One-to-One (M1²1) structure with a balanced mixture between the molecules. This finding proves, that the structure of mixed organic films can indeed be tailored by changing the relative molecular coverage on the surface. The molecular arrangement in all structures is quite similar, which could be attributed to the $O \cdots H$ bonds between CuPc and PTCDA that are formed in all these mixed phases.

For all three phases, a similar modification of the electronic valence structure was found: The PTCDA LUMO was located at higher binding energy than in the monolayer film and no sign

of the CuPc LUMO state was visible below the Fermi level. This indicates an effective charge transfer from CuPc to PTCDA which results in the depopulation of the CuPc LUMO and an enhanced filling of the PTCDA LUMO. In addition, a delocalized interface state, expanding over all molecules in the mixed film, was discovered. We propose that this state is derived from the depopulated surface state of the Ag(111) surface which hybridizes with unoccupied molecular orbitals and mediates the effective charge transfer between the molecules.

A very surprising and interesting finding is that the vertical bonding distance of the individual molecules to the silver surface is no longer correlated with their electronic structure. Although the PTCDA LUMO is completely populated, the molecular backbone is lifted away from the silver surface (compared to the pure PTCDA/Ag(111) monolayer structure) and the depopulation of the CuPc LUMO coincides with a marginal lowering of the CuPc-Ag distance. Therefore we proposed, that the adsorption height of the individual molecules is no longer coupled to the charge transfer into the molecules. Instead a common electronic structure forms in the mixed film, probably involving the interface state, which leads to the population of the energetically lowest level, which in our case is the PTCDA LUMO.

The hetero-organic CuPc/PTCDA bilayer films on the Ag(111) surface were discussed in chapter 5. It was found that CuPc molecules adsorb in the second layer on PTCDA and do not destroy the lateral order of the PTCDA monolayer film. At RT, the arrangement of CuPc on PTCDA is very similar to that directly on Ag(111): CuPc forms a homogeneous 2D gas with an average intermolecular distance, which decreases continuously with rising coverage. Closing the first CuPc layer on PTCDA or reducing the sample temperature below 160 K results in a phase transition from the disordered CuPc film to an ordered commensurate structure, the so called Stacked-Bilayer (SB) structure.

The organic layers in the hetero-organic interface are separated by $\Delta d \approx 3.2\,\text{Å}$, which is in good agreement to the lattice spacing for a PTCDA molecular crystal. Hence we concluded, that the interaction across the organic-organic interface is mainly dominated by electrostatic and van der Waals forces. More remarkably, the chemical bond between the PTCDA molecules and the silver surface is strongly modified upon CuPc adsorption. This is reflected by a reduced adsorption height of the PTCDA carbon backbone for low coverages (0.60 ML) compared with the pure monolayer structure. Closing the first CuPc layer on PTCDA, however, results again in a lifting of the PTCDA backbone to almost the same height as in the monolayer structure.

Furthermore, our UPS study revealed, that the PTCDA LUMO level shifts 120 meV to higher binding energies within the adsorption of the first CuPc layer on PTCDA. This indicates an enhanced charge transfer into the PTCDA molecule and hence points to a changed interaction strength between PTCDA and the silver surface.

The additional population of the PTCDA LUMO and the modified interaction at the PTC-DA/Ag(111) interface was explained by a screening effect induced by the adsorption of CuPc.

This creates a new equilibrium for the charge redistribution at the PTCDA/Ag interface which results in an enhanced charge transfer into PTCDA.

The reversed system, PTCDA on a monolayer CuPc/Ag(111) forms no smooth organic-organic interface. Instead, a certain amount of PTCDA molecules penetrates into the CuPc layer and destroys the lateral order of the CuPc film. Our XSW results indicate, that CuPc molecules are exchanged by PTCDA and move to the second organic layer in order to reduce the stress in the first organic layer. Since the electronic fingerprint of the resulting PTCDA/CuPc structure is almost identical to the laterally mixed films, we propose that the remaining CuPc molecules form a mixed phase with PTCDA which, according to LEED results, is disordered. Most likely it is located in between clusters of a rotationally disordered PTCDA structure.

We believe that the molecular exchange is caused by the lack of attractive interaction between the CuPc molecules in the first layer and by the higher gain in adsorption energy for PTCDA molecules compared to CuPc when directly adsorbed on Ag(111). For the reversed system, CuPc on PTCDA/Ag(111), a molecular exchange was only observed after thermal activation.

Altogether, our study of hetero-organic systems revealed several unexpected findings which cannot be explained by the established adsorption models for the individual molecules in the mixed film. The intermolecular interactions between these different types of molecules result in novel effects in the hetero-organic structures, which were not yet observed in mono-organic adsorbate systems. Consequently our study shows clearly, that a hetero-organic film is "more than the sum of its parts".

Sample preparation

In order to gain consistent results all samples were prepared in the same way.

The sample surface of the (111)-oriented Ag single crystal was cleaned by repeated cycles of Ar ion bombardment ($\pm 55\,^{\circ}$ incident angle of the ion beam, $2\times 30\,\mathrm{min}$, $I_{sample}=4\mu\mathrm{A}$) and subsequent annealing with temperatures of 723 K for approx. 30 minutes. Evaluating the transfer width of the specular reflection obtained with the SPA-LEED instrument, the mean width of the Ag(111) terraces was determined to be larger than 600 Å.

The organic layers were prepared by organic molecular beam epitaxy (OMBE) using a dedicated evaporator. For all preparations the sample was kept at room temperature. The CuPc and PTCDA molecules were deposited one after another onto the Ag(111) surface. During the growth process, the molecular flux was monitored by measuring molecular fragments with a QMS ($m=128\,\mathrm{au}$ for CuPc and $m=248\,\mathrm{au}$ for PTCDA). We used constant deposition rates of $\approx 0.10\,\mathrm{\frac{ML}{min}}$. The coverage was determined by the integrated QMS signal which was normalized to the one of the corresponding monolayer coverage.

After deposition of the organic molecules, all laterally mixed films were annealed at $T=575\,\mathrm{K}$ for 20 min. In contrast, the hetero-organic bilayer films were not annealed after sample preparation.

Bibliography

- [AS09] A. Abbasi and R. Scholz, Ab Initio Calculation of the Dispersion Interaction between a Polyaromatic Molecule and a Noble Metal Substrate: PTCDA on Ag(110), J. Chem. Phys. C 113 (2009), 19897–19904.
- [Bar61] J. Bardeen, Tunnelling from a many-particle point of view, Phys. Rev. Lett. 6 (1961), 57–59.
- [Bay08] Patrick Bayersforfer, SPA-LEED-Studie zur Adsorption von metallfreien Phthalocyaninen auf Ag(111) im Bereich kleiner Bedeckungen, Diplomarbeit, 2008.
- [BC64] B.W. Batterman and H. Cole, Dynamical Diffraction of X Rays by Perfect Crystals, Rev. Mod. Phys. **36** (1964), 681–717.
- [BCK05] J. V. Barth, G. Costantini, and K. Kern, Engineering atomic and molecular nanostrucutres at surfaces, Nature 437 (2005), 671.
- [BK97] K.D. Boni and V.V. Kresin, Electric-Dipole Polarizabilities Of Atoms, Molecules, And Clusters, World Scientific, 1997.
- [BKF⁺09] S. Berkebile, G. Koller, A.J. Fleming, P. Puschnig, C. Ambrosch-Draxl, K. Emtsev, T. Seyller, J. Riley, and M.G. Ramsey, The electronic structure of pentacene revisited, J. Electron Spectrosc. Relat. Phenom. 174 (2009), 22 27.
- [Bon64] A. Bondi, Van der Waals Volumes + Radii, J. Phys. Chem. 68 (1964), 441.
- [BRGW82] G. Binnig, H. Rohrer, Ch. Gerber, and E. Weibel, Tunneling through a controllable vacuum gap, Appl. Phys. Lett. 40 (1982), 178–180.
- [Bru12] Florian Bruchner, Elektronische Struktur von homo- und hetermolekularen Adsorbatsystemen an Ag(111) Oberflächen, Diplomarbeit, 2012.
- [BTH+05] L. Broekman, A. Tadich, E. Huwald, J. Riley, R. Leckey, T. Seyller, K. Emtsev, and L. Ley, First results from a second generation toroidal electron spectrometer,
 J. Electron Spectrosc. Relat. Phenom. 144-147 (2005), 1001 1004.

- [BWBM03] C. Bobisch, T. Wagner, A. Bannani, and R. Möller, Ordered binary monolayer composed of two organic molecules: Copper-phthalocyanine and 3,4,9,10perylene-tetra-carboxylic-dianhydride on Cu(111), J. Chem. Phys. 119 (2003), 9804–9808.
- [CHC⁺08] W. Chen, H. Huang, S. Chen, X. Y. Gao, and A.T.S. Wee, Low-Temperature Scanning Tunneling Microscopy and Near-Edge X-ray Absorption Fine Structure Investigations of Molecular Orientation of Copper(II) Phthalocyanine Thin Films at Organic Heterojunction Interfaces, J. Phys. Chem. C 112 (2008), 5036–5042.
- [Che93] C.J. Chen, Introduction to Scanning Probe Microscopy, Academic Press, San Diego, 1993.
- [CSS+12] M.C. Cottin, J. Schaffert, A. Sonntag, H. Karacuban, R. Möller, and C.A. Bobisch, Supramolecular architecture of organic molecules: PTCDA and CuPc on a Cu(111) substrate, Appl. Surf. Sci. 258 (2012), 2196 2200.
- [DGS+08] S. Duhm, A. Gerlach, I. Salzmann, B. Braeker, R.L. Johnson, F. Schreiber, and N. Koch, PTCDA on Au(111), Ag(111) and Cu(111): Correlation of interface charge transfer to bonding distance, Org. Electron. 9 (2008), 111 – 118.
- [DP10] M.S. Dyer and M. Persson, The nature of the observed free-electron-like state in a PTCDA monolayer on Ag(111), New J. Phys. 12 (2010), 063014.
- [ECS+07] F. Evangelista, V. Carravetta, G. Stefani, B. Jansik, M. Alagia, S. Stranges, and A. Ruocco, Electronic structure of copper phthalocyanine: An experimental and theoretical study of occupied and unoccupied levels, J. Chem. Phys. 126 (2007), 124709.
- [Ein05] A. Einstein, Über einen die Erzeugung on Verwendung des Lichtes betreffenden heuristischen Gesichtspunkt, Ann. Physik **332** (1905), 132–148.
- [ERAS+13] D. Egger, V.G. Ruiz, W.A. Al-Saidi, T. Bucko, A. Tkatchenko, and E. Zojer, Understanding structure and bonding of multilayered metal-organic nanostructures, J. Phys. Chem. C 117 (2013), 3055.
- $[Fai11] \hspace{1cm} \textbf{N. Fairley, } \textit{Peak Fitting Statistics.}$
- [FE74] P.J. Feibelman and D.E. Eastman, Photoemission spectroscopy Correspondence between quantum theory and experimental phenomenology, Phys. Rev. B 10 (1974), 4932–4947.

- [FGGM+11] J. Fraxedas, S. Garcia-Gil, S. Monturet, N. Lorente, I. Fernandez-Torrente, K. J. Franke, J. I. Pascual, A. Vollmer, R.-P. Blum, N. Koch, and P. Ordejon, Modulation of Surface Charge Transfer through Competing Long-Range Repulsive versus Short-Range Attractive Interactions, J. Phys. Chem. C 115 (2011), 18640–18648.
- [For97] S.R. Forrest, Ultrathin organic films grown by organic molecular beam deposition and related techniques, Chem. Rev. 97 (1997), 1793–1896.
- [FTFP08] I. Fernandez Torrente, K.J. Franke, and J.I. Pascual, Spectroscopy of C₆₀ single molecules: the role of screening on energy level alignment, J. Phys.: Condensed Matter 20 (2008), 184001.
- $[FTS^+]$ M. J. Frisch, G. W. Trucks, H. B. Schlegel, G. E. Scuseria, M. A. Robb, J. R. Cheeseman, J. A. Montgomery, Jr., T. Vreven, K. N. Kudin, J. C. Burant, J. M. Millam, S. S. Iyengar, J. Tomasi, V. Barone, B. Mennucci, M. Cossi, G. Scalmani, N. Rega, G. A. Petersson, H. Nakatsuji, M. Hada, M. Ehara, K. Toyota, R. Fukuda, J. Hasegawa, M. Ishida, T. Nakajima, Y. Honda, O. Kitao, H. Nakai, M. Klene, X. Li, J. E. Knox, H. P. Hratchian, J. B. Cross, V. Bakken, C. Adamo, J. Jaramillo, R. Gomperts, R. E. Stratmann, O. Yazyev, A. J. Austin, R. Cammi, C. Pomelli, J. W. Ochterski, P. Y. Ayala, K. Morokuma, G. A. Voth, P. Salvador, J. J. Dannenberg, V. G. Zakrzewski, S. Dapprich, A. D. Daniels, M. C. Strain, O. Farkas, D. K. Malick, A. D. Rabuck, K. Raghavachari, J. B. Foresman, J. V. Ortiz, Q. Cui, A. G. Baboul, S. Clifford, J. Cioslowski, B. B. Stefanov, G. Liu, A. Liashenko, P. Piskorz, I. Komaromi, R. L. Martin, D. J. Fox, T. Keith, M. A. Al-Laham, C. Y. Peng, A. Nanayakkara, M. Challacombe, P. M. W. Gill, B. Johnson, W. Chen, M. W. Wong, C. Gonzalez, and J. A. Pople, Gaussian 03, Revision C.02, Gaussian, Inc., Wallingford, CT, 2004.
- [FZ94] S. R. Forrest and Y. Zhang, Ultrahigh-vacuum quasiepitaxial growth of model van der Waals thin films. I. Theory, Phys. Rev. B 49 (1994), 11297–11308.
- [GFSR11] T. Graber, F. Forster, A. Schöll, and F. Reinert, Experimental determination of the attenuation length of electrons in organic molecular solids: The example of PTCDA, Surf. Sci. 605 (2011), 878 – 882.
- [GG10] H.-J. Gao and Li. Gao, Scanning tunneling microscopy of functional nanostructures on solid surfaces: Manipulation, self-assembly, and applications, Prog. Surf. Sci. 85 (2010), 28 – 91.
- [GHD⁺11] A. Gerlach, T. Hosokai, S. Duhm, S. Kera, O. T. Hofmann, E. Zojer, J. Zegenhagen, and F. Schreiber, Orientational Ordering of Nonplanar Phthalocyanines

- on Cu(111): Strength and Orientation of the Electric Dipole Moment, Phys. Rev. Lett. 106 (2011), 156102.
- [GLFTF+08] N. Gonzalez-Lakunza, I. Fernandez-Torrente, K.J. Franke, N. Lorente, A. Arnau, and J.I. Pascual, Formation of Dispersive Hybrid Bands at an Organic-Metal Interface, Phys. Rev. Lett. 100 (2008), 156805.
- [GSS+07] A. Gerlach, S. Sellner, F. Schreiber, N. Koch, and J. Zegenhagen, Substrate-dependent bonding distances of PTCDA: A comparative X-ray standing-wave study on Cu(111) and Aq(111), Phys. Rev. B 75 (2007), 045401.
- [Hal88] W. Hallwachs, Über den Einfluss des Lichtes auf elektrostatisch geladene Körper, Ann. Physik 269 (1888), 269–301.
- [HBL⁺07] S.K.M. Henze, Bauer.O., T.-L. Lee, M. Sokolowski, and F.S. Tautz, *Vertical bonding distances of PTCDA on Au(111) and Ag(111): Relation to the bonding type*, Surf. Sci. **601** (2007), 1566 1573.
- [HCC⁺09] H. Huang, W. Chen, S. Chen, D.C. Qi, X.Y. Gao, and A.T.S. Wee, *Molecular orientation of CuPc thin films on C*₆0/Ag(111), Appl. Phys. Lett. **94** (2009).
- [HDK12] C. Henneke, T. Duden, and C. Kumpf, Photoemission electron microsopy data, unpublished, 2012.
- [Her87] H. Hertz, Über einen Einfluss des ultravioletten Lichtes auf die elektrische Entladung, Ann. Physik **267** (1887), 983–1000.
- [Hüf03] S. Hüfner, Photoelectron Spectroscopy Principles and Applications, Springer, 2003.
- [HGS+10] M. Häming, M. Greif, C. Sauer, A. Schöll, and F. Reinert, Electronic structure of ultrathin heteromolecular organic-metal interfaces: SnPc/PTCDA/Ag(111) and SnPc/Ag(111), Phys. Rev. B 82 (2010), 235432.
- [HK] C. Henneke and C. Kumpf, to be published.
- [HKC⁺05] A. Hauschild, K. Karki, B.C.C. Cowie, M. Rohlfing, F.S. Tautz, and M. Sokolowski, *Molecular Distortions and Chemical Bonding of a Large* π -Conjugated Molecule on a Metal Surface, Phys. Rev. Lett. **94** (2005), 036106.
- [HLC⁺12] T.H. Han, Y. Lee, M.-R. Choi, S.H. Woo, S.-H. Bae, B.H. Hee, J.H. Ahn, and T.W. Lee, Extremely efficient flecible organic light-emitting diodes with midfied graphene anode, Nature Photonics 6 (2012), 105–110.

- [HLM+10] Y.L. Huang, H. Li, J. Ma, H. Huang, W. Chen, and A.T.S. Wee, Scanning Tunneling Microscopy Investigation of Self-Assembled CuPc/F16CuPc Binary Superstructures on Graphite, Langmuir 26 (2010), 3329–3334.
- [Häm10] Marc Häming, Electronic Many-Bondy Effects in organic Thin Films and Interfaces, Ph.D. thesis, Universität Würzburg, 2010.
- [HMSK00] I.G. Hill, D. Milliron, J. Schwartz, and A. Kahn, Organic semiconductor interfaces: electronic structure and transport properties, Appl.d Surf. Sci. 166 (2000), 354 362.
- [HSS+09] M. Häming, C. Scheuermann, A. Schöll, F. Reinert, and E. Umbach, Coverage dependent organic-metal interaction studied by high-resolution core level spectroscopy: SnPc (sub)monolayers on Ag(111), J. Electron Spectrosc. Relat. Phenom. 174 (2009), 59 64, Advanced Spectroscopies of Molecular Materials for Electronics.
- [HTS97] R. Hesper, L.H. Tjeng, and G.A. Sawatzky, Strongly reduced band gap in a correlated insulator in close proximity to a metal, Europhys. Lett. 40 (1997), 177–182.
- [HTS+10] A. Hauschild, R. Temirov, S. Soubatch, O. Bauer, A. Schöll, B.C.C. Cowie, T.-L. Lee, F. S. Tautz, and M. Sokolowski, Normal-Incidence X-ray standing-wave determination of the adsorption geometry of PTCDA on Ag(111): Comparison of the ordered room-temperature and disordered low-temperature phases, Phys. Rev. B 81 (2010), 125432.
- [HvH99] M. Horn-von Hoegen, Growth of semiconductor layers studied by spot profile analysing low energy electron diffraction, Zeitschrift für Kristallographie 214 (1999), 591–629.
- [JSY82] F. Jona, J.A. Strozier, and W.S. Yang, Low-energy electron diffraction for surface structure analysis, Rep. Prog. Phys. 45 (1982), 527.
- [KBB+12] I. Kröger, P. Bayersdorfer, Stadtmüller B., C. Kleimann, G. Mercurio, F. Reinert, and C. Kumpf, Submonolayer growth of H₂-Phthalocyanine on Ag(111), Phys. Rev. B 86 (2012), 195412.
- [KDR+02] B. Krause, A. C. Dürr, K. Ritley, F. Schreiber, H. Dosch, and D. Smilgies, Structure and growth morphology of an archetypal system for organic epitaxy: PTCDA on Ag(111), Phys. Rev. B 66 (2002), 235404.
- [KHT+08] L. Kilian, A. Hauschild, R. Temirov, S. Soubatch, A. Schöll, A. Bendounan, F. Reinert, T.-L. Lee, F. S. Tautz, M. Sokolowski, and E. Umbach, Role of Intermolecular Interactions on the Electronic and Geometric Structure of a

- Large π -Conjugated Molecule Adsorbed on a Metal Surface, Phys. Rev. Lett. **100** (2008), 136103.
- [KLS+09] H. Karacuban, M. Lange, J. Schaffert, O. Weingart, Th. Wagner, and R. Möller, Substrate-induced symmetry reduction of CuPc on Cu(111): An LT-STM study, Surf. Sci. 603 (2009), L39–L43.
- [Koc09] Mario Kochler, Hochauflösende Photoelektronenspektroskopie and dünnen CuPc-Filmen auf Edelmetall(111)-Oberflächne, Diplomarbeit, 2009.
- [Krö11] Ingo Kröger, Adsorption von Phthalocyaninen auf Edelmetalloberflächen, Ph.D. thesis, Universität Würzburg, 2011.
- [KSK+08] L. Kilian, U. Stahl, I. Kossev, M. Sokolowski, R. Fink, and E. Umbach, The commensurate-to-incommensurate phase transition of an organic monolayer: A high resolution LEED analysis of the superstructures of NTCDA on Ag(111), Surf. Sci. 602 (2008), 2427 – 2434.
- [KSK+11] I. Kröger, B. Stadtmüller, C. Kleimann, P. Rajput, and C. Kumpf, Normal-incidence X-ray standing-wave study of copper phthalocyanine submonolayers on Cu(111) and Au(111), Phys. Rev. B 83 (2011), 195414.
- [KSS+10] I. Kröger, B. Stadtmüller, C. Stadler, J. Ziroff, M. Kochler, A. Stahl, F. Pollinger, T-L Lee, J. Zegenhagen, F. Reinert, and C. Kumpf, Submonolayer growth of copper-phthalocyanine on Ag(111), New J. Phys. 12 (2010), 083038.
- [KSW+11] I. Kröger, B. Stadtmüller, C. Wagner, C. Weiss, R. Temirov, F.S. Tautz, and C. Kumpf, Modeling intermolecular interactions of physisorbed organic molecules using pair potential calculations, J. Chem. Phys. 135 (2011), 234703.
- [KTH+06] A. Kraft, R. Temirov, S.K.M. Henze, S. Soubatch, M. Rohlfing, and F.S. Tautz, Lateral adsorption geometry and site-specific electronic structure of a large organic chemisorbate on a metal surface, Phys. Rev. B 74 (2006), 041402.
- [KUS04] L. Kilian, E. Umbach, and M. Sokolowski, Molecular beam epitaxy of organic films investigated by high resolution low energy electron diffraction (SPA-LEED): 3,4,9,10-perylenetetracarboxylicacid-dianhydride (PTCDA) on Ag(111), Surf. Sci. 573 (2004), 359 378.
- [LP12] D. Lüftner and P. Puschnig, private communication, 2012.
- [LWM⁺89] P. H. Lippel, R. J. Wilson, M. D. Miller, Ch. Wöll, and S. Chiang, High-Resolution Imaging of Copper-Phthalocyanine by Scanning-Tunneling Microscopy, Phys. Rev. Lett. 62 (1989), 171–174.

- [LYJ+12] S. Lee, J.S. Yeo, Y Ji, C. Cho, D.Y. Kim, S.-I Na, B.H. Lee, and T. Lee, Flexible organic solar cells composed of p3ht:pcbm using chemically doped graphene electrodes, Nanotechnology 23 (2012), 344013.
- [McK98] Neil B. McKeown, Phthalocyanine Materials, Cambridge University Press, 1998.
- [MEP+07] K. Manandhar, T. Ellis, K.T. Park, T. Cai, Z. Song, and J. Hrbek, A scanning tunneling microscopy study on the effect of post-deposition annealing of copper phthalocyanine thin films, Surf. Sci. 601 (2007), 3623 – 3631.
- [Mer12] Giuseppe Mercurio, Study of molecule-metal interfaces by means of the Normal Incidence X-ray Standing Wave technique, Ph.D. thesis, RWTH Aachen, 2012.
- [MF05] S. C. B. Mannsfeld and T. Fritz, Understanding organic inorganic heteroepitaxial growth of molecules on crystalline substrates: Experiment and theory, Phys. Rev. B 71 (2005), 235405.
- [MGS+06] H. Marchetto, U. Groh, Th. Schmidt, R. Fink, H.-J. Freund, and E. Umbach, Influence of substrate morphology on organic layer growth: PTCDA on Ag(111), Chem. Phys. 325 (2006), 178 – 184.
- [MLF05] S. Mannsfeld, K. Leo, and T. Fritz, Line-on-Line Coincidence: A New Type of Epitaxy Found in Organic-Organic Heterolayers, Phys. Rev. Lett. 94 (2005), 056104.
- [MMM+10] G. Mercurio, E. R. McNellis, I. Martin, S. Hagen, F. Leyssner, S. Soubatch, J. Meyer, M. Wolf, P. Tegeder, F. S. Tautz, and K. Reuter, Structure and Energetics of Azobenzene on Ag(111): Benchmarking Semiempirical Dispersion Correction Approaches, Phys. Rev. Lett. 104 (2010), 036102.
- [MS79] K.J. Miller and J. Savchik, A new empirical method to calculate average molecular polarizabilities, J. Am. Chem. Soc. 101 (1979), 7206–7213.
- [MZS+11] M. Marks, N. L. Zaitsev, B. Schmidt, C.H. Schwalb, A. Schöll, I.A. Nechaev, P.M. Echenique, E.V. Chulkov, and U. Höfer, Energy shift and wave function overlap of metal-organic interface states, Phys. Rev. B 84 (2011), 081301.
- [OLS+03] K. Oura, V.G. Lifshits, A.A. Saranin, A.V. Zotov, and M. Katayama, Surface Science - An Introduction, Springer, 2003.
- [OWB+10] A. Opitz, J. Wagner, W. Brütting, I. Salzmann, N. Koch, J. Manara, J. Pflaum, A. Hinderhofer, and F. Schreiber, Charge Separation at Molecular Donor-Acceptor Interfaces: Correlation Between Morphology and Solar Cell Perfor-

- mance, Selected Topics in Quantum Electronics, IEEE Journal of ${\bf 16}$ (2010), 1707 –1717.
- [PBF+09] P. Puschnig, S. Berkebile, A. J. Fleming, G. Koller, K. Emtsev, T. Seyller, J. D. Riley, C. Ambrosch-Draxl, F. P. Netzer, and M. G. Ramsey, Reconstruction of Molecular Orbital Densities from Photoemission Data, Science 326 (2009), 702–706.
- [Pen93] J.B. Pendry, *LEED and the crystallography of surfaces*, Surf. Sci. Rep. **19** (1993), 87 97.
- [Pen94] J.B. Pendry, Multiple scattering theory of electron diffraction, Surf. Sci. 299-300 (1994), 375 390.
- [PRU+11] P. Puschnig, E.M. Reinisch, T. Ules, G. Koller, S. Soubatch, M. Ostler, L. Romaner, F.S. Tautz, C. Ambrosch-Draxl, and M.G. Ramsey, Orbital tomography: Deconvoluting photoemission spectra of organic molecules, Phys. Rev. B 84 (2011), 235427.
- [RGW+10] P.C. Rusu, G. Giovannetti, C. Weijtens, R. Coehoorn, and G. Brocks, First-principles study of the dipole layer formation at metal-organic interfaces, Phys. Rev. B 81 (2010), 125403.
- [RLZ⁺12] V. G. Ruiz, W. Liu, E. Zojer, M. Scheffler, and A. Tkatchenko, Density-Functional Theory with Screened van der Waals Interactions for the Modeling of Hybrid Inorganic-Organic Systems, Phys. Rev. Lett. 108 (2012), 146103.
- [RNP+09] L. Romaner, D. Nabok, P. Puschnig, E. Zojer, and C. Ambrosch-Draxl, Theoretical study of PTCDA adsorbed on the coinage metal surfaces, Ag(111), Au(111) and Cu(111), New J. Phys. 11 (2009), 053010.
- [RTT07] M. Rohlfing, R. Temirov, and F.S. Tautz, Adsorption structure and scanning tunneling data of a prototype organic-inorganic interface: PTCDA on Ag(111), Phys. Rev. B 76 (2007), 115421.
- [SBS79] J. Shanker, P.S. Bakhshi, and L.P. Sharma, Analysis of the crystal binding and the anderson-gruneisen parameters in the halides of copper(I), silver(I) and thallium(I), J. Inorg. Nucl. Chem. 41 (1979), 1285–1288.
- [Sch11] A. Schöll, Invited Talk, ESPMI-Conference, Karlsruhe Germany, 2011.
- [Shi72] D.A. Shirley, High-Resolution X-Ray Photoemission Spectrum of the Valence Bands of Gold, Phys. Rev. B 5 (1972), 4709–4714.

- [SHK+09] C. Stadler, S. Hansen, I. Kröger, C. Kumpf, and E. Umbach, Tuning intermolecular interaction on longrange-ordered submonolayer organic films, Nature Physics 5 (2009), 153–158.
- [SHS+07] C. Stadler, S. Hansen, A. Schöll, T-L Lee, J. Zegenhagen, C. Kumpf, and E. Umbach, Molecular distortion of NTCDA upon adsorption on Ag(111): a Normal Incidence X-ray standing wave study, New J. Phys. 9 (2007), 50.
- [SK] B. Stadtmüller and C. Kumpf, to be published.
- [SKRK11] B. Stadtmüller, I. Kröger, F. Reinert, and C. Kumpf, Submonolayer growth of CuPc on noble metal surfaces, Phys. Rev. B 83 (2011), 085416.
- [SKZ⁺10] A. Schöll, L. Kilian, Y. Zou, J. Ziroff, S. Hame, F. Reinert, E. Umbach, and R.H. Fink, Disordering of an Organic Overlayer on a Metal Surface Upon Cooling, Science 329 (2010), 303–305.
- [SLQ+11] L. Sun, C. Liu, D. Queteschiner, G.r Weidlinger, and P. Zeppenfeld, Layer inversion in organic heterostructures, Phys. Chem. Chem. Phys. 13 (2011), 13382–13386.
- [SS65] R.A. Scott and H.A. Scheraga, Method for Calculating Internal Rotation Barriers, J. Chem. Phys. 42 (1965), 2209–2215.
- [SS12] C. Sauer and A. Schöll, private communication, 2012.
- [SSHT+01] F. Sellam, T. Schmitz-Hübsch, M. Toerker, S. Mannsfeld, H. Pröhl, T. Fritz, K. Leo, C. Simpson, and K. Müllen, LEED and STM investigations of organicorganic heterostructures grown by molecular beam epitaxy, Surf. Sci. 478 (2001), 113 – 121.
- [SSK+12] B. Stadtmüller, T. Sueyoshi, G. Kichin, I. Kröger, S. Soubatch, R. Temirov, F.S. Tautz, and C. Kumpf, Commensurate Registry and Chemisorption at a Hetero-organic Interface, Phys. Rev. Lett. 108 (2012), 106103.
- [SSK13] S. Schröder, B. Stadtmüller, and C. Kumpf, to be published, 2013.
- [SSM+08] C.H. Schwalb, S. Sachs, M. Marks, A. Schöll, F. Reinert, E. Umbach, and U. Höfer, Electron Lifetime in a Shockley-Type Metal-Organic Interface State, Phys. Rev. Lett. 101 (2008), 146801.
- [Sta09a] Christoph Stadler, Strukturuntersuchungen organischer Monolagen auf Ag(111), Ph.D. thesis, Universität Würzburg, 2009.
- [Sta09b] Benjamin Stadtmüller, Strukturuntersuchungen von CuPc auf verschiedenen Edelmetalloberflächen, Master's thesis, Universität Würzburg, 2009.

- [Ste02] T. Steiner, *The Hydrogen Bond in the Solid State*, Angewandte Chemie International Edition **41** (2002), 48–76.
- [SWR+12] B. Stadtmüller, M. Willenbockel, E.M. Reinisch, T. Ules, M. Ostler, F. Bocquet, S. Soubatch, P. Puschnig, G. Koller, M.G. Ramsey, F.S. Tautz, and C. Kumpf, Orbital tomography for highly symmetric adsorbate systems, EPL (Europhysics Letters) 100 (2012), 26008.
- [SWTT09] S. Soubatch, C. Weiss, R. Temirov, and F.S. Tautz, Site-Specific Polarization Screening in Organic Thin Films, Phys. Rev. Lett. 102 (2009), 177405.
- [SZJ⁺04] A. Schöll, Y. Zou, M. Jung, Th. Schmidt, R. Fink, and E. Umbach, Line shapes and satellites in high-resolution x-ray photoelectron spectra of large π -conjugated organic molecules, J. Chem. Phys. **121** (2004), 10260–10267.
- [Tau07] F.S. Tautz, Structure and bonding of large aromatic molecules on noble metal surfaces: The example of PTCDA, Prog. Surf. Sci. 82 (2007), 479 520.
- [TH85] J. Tersoff and D. R. Hamann, Theory of the scanning tunneling microscope, Phys. Rev. B **31** (1985), 805–813.
- [TKS+08] T. Darrah Thomas, Edwin Kukk, Rami Sankari, Hironobu Fukuzawa, Georg Prümper, Kiyoshi Ueda, Ralph Püttner, James Harries, Yusuke Tamenori, Takahiro Tanaka, Masamitsu Hoshino, and Hiroshi Tanaka, Recoil excitation of vibrational structure in the carbon 1s photoelectron spectrum of CF₄, J. Chem. Phys. 128 (2008), 144311.
- [TRH+10] A. Tadich, J. Riley, E. Huwald, R. Leckey, T. Seyller, and L. Ley, Full Hemisphere Fermi Surface Mapping Using A Novel Toroidal Electron Spectrometer, American Institute of Physics Conference Series (R. Garrett, I. Gentle, K. Nugent, and S. Wilkins, eds.), American Institute of Physics Conference Series, vol. 1234, 2010, pp. 943–946.
- [TSLT06] R. Temirov, S. Soubatch, A. Luican, and F.S. Tautz, Free-electron-like dispersion in an organic monolayer film on a metal substrate, Nature 44 (2006), 350.
- [VHWC86] M.A. Van Hove, W.H. Weinberg, and C.-M. Chan, Low energy electron diffraction, Springer, 1986.
- [WBB $^+$ 07] Th. Wagner, A. Bannani, C. Bobisch, H. Karacuban, and R. Möller, *The initial growth of PTCDA on Cu(111) studied by STM*, J. Phys.: Condens. Matter **19** (2007), 056009.

- [Wei05] Lothar Weinhardt, Elektronische und chemische Eigenschaften von Grenzflächen und Oberflächen in optimierten $Cu(In,Ga)(S,Se)_2$ Dünnschichtsolarzellen, Ph.D. thesis, Universität Würzburg, 2005.
- [WHS+12] M. Wießner, D. Hauschild, A. Schöll, F. Reinert, V. Feyer, K. Winkler, and B. Krömker, Electronic and geometric structure of the PTCDA/Ag(110) interface probed by angle-resolved photoemission, Phys. Rev. B 86 (2012), 045417.
- [Wie94] R. Wiesendanger, Scanning Probe Microscopy and Spectroscopy, Cambridge University Press, 1994.
- [WKG+10] C. Wagner, D. Kasemann, C. Golnik, R. Forker, M. Esslinger, K. Müllen, and T. Fritz, Repulsion between molecules on a metal: Monolayers and submonolayers of hexa-peri-hexabenzocoronene on Au(111), Phys. Rev. B 81 (2010), 035423.
- [WMPL07] K. Walzer, B. Maennig, M. Pfeiffer, and K. Leo, Highly Efficient Organic Devices Based on Electrically Doped Transport Layers, Chem. Rev. 107 (2007), 1233–1271.
- [Wol06] J. Wolberg, Data Analysis Using the Method of Least Squares: Extracting the Most Information from Experiments, Springer, 2006.
- [Woo98] D.P. Woodruff, Normal incidence X-ray standing wave determination of adsorbate structures, Prog. Surf. Sci. 57 (1998), 1 60.
- [Woo05] D.P. Woodruff, Surface structure determination using x-ray standing waves, Rep. Prog. Phys. **68** (2005), 743.
- [WSS+13] M. Willenbockel, B. Stadtmüller, K. Schönauer, E.M. Reinisch, T. Ules, M. Ostler, F. Bocquet, T. Seyller, C. Kumpf, P. Puschnig, G. Koller, S. Soubatch, M.G. Ramsey, and F.S. Tautz, Energy offsets within a molecular monolayer: The influence of the molecular environment, New. J. Phys. 15 (2013), 033017.
- [WW04] G. Witte and C. Wöll, Growth of aromatic molecules on solid substrates for applications in organic electronics, J. Mater. Res. 19 (2004), 1889–1916.
- [Zeg93] J. Zegenhagen, Surface structure determination with X-ray standing waves, Surf. Sci. Rep. 18 (1993), 202 – 271.
- [ZFS+10] J. Ziroff, F. Forster, A. Schöll, P. Puschnig, and F. Reinert, Hybridization of Organic Molecular Orbitals with Substrate States at Interfaces: PTCDA on Silver, Phys. Rev. Lett. 104 (2010), 233004.

- [ZHvH02] P. Zahl and M. Horn-von Hoegen, Third-generation conical spot profile analyzing low-energy electron diffraction, Rev. Sci. Instrum. 73 (2002), 2958–2962.
- [ZKS+06] Y. Zou, L. Kilian, A. Schöll, Th. Schmidt, R. Fink, and E. Umbach, Chemical bonding of PTCDA on Ag surfaces and the formation of interface states, Surf. Sci. 600 (2006), 1240 – 1251.
- [ZNEC12] N.L. Zaitsev, I.A. Nechaev, P.M. Echenique, and E.V. Chulkov, Transformation of the Ag(111) surface state due to molecule-surface interaction with ordered organic molecular monolayers, Phys. Rev. B 85 (2012), 115301.

List of Figures

2.1	(a) Cross section of a SPA-LEED instrument [HvH99] and modified Ewald	
	construction (b)	6
2.2	(a) PTCDA orbital (LUMO) for a free molecule in the gas phase (DFT calcu-	
	lation, B3LYP, basis set: LANL2DZ [FTS $^+$]). (b) 3D Fourier Transform of the	
	PTCDA LUMO wave function. The red dome represents a hemispherical cut	
	at constant $k=\sqrt{(2m/\hbar^2)\cdot E_{\rm kin}}$ for $E_{\rm kin}=35{\rm eV}$ (image created by Daniel	
	Lüftner, University of Graz). (c) Resulting constant binding energy map of the	
	PTCDA LUMO level	11
2.3	(a) Schematic overview of the ARPES experiment. (b) Illustration of an	
	ARPES data cube $I(k_x, k_y, E_b)$	12
2.4	Shape of the reflectivity profile for a perfect crystal as a function of the real	
	part η' of the parameter η [BC64]. The dashed curve (a) is obtained for zero	
	absorption while for (b) the adsorption of the standing wave field in the crystal	
	is considered	15
2.5	Argand diagram with hypothetical data demonstrating the Fourier analysis for	
	two different adsorption sites A and B which are equally occupied	17
2.6	(a) Schematic working principle of a scanning tunneling microscope. (b) Po-	
	tential diagram illustrating the quantum mechanic tunneling effect	18
2.7	Energy diagrams illustrating the role of the molecular orbitals for the tunneling	
	process. The energetic positions of the molecular energy levels are fixed with	
	respect to the substrate Fermi level. The sample bias is negative (a) zero (b)	
	and positive (c)	21
2.8	Illustration of the pair potential approach. (a) The relative displacement vector	
	${f r}$ between the center of masses of the molecules is shown as a black arrow, the	
	atomic distance r_{ij} used in the pair potential equation (2.22) as red arrow.	
	(b) Pair potential map for a constant rotation vector $\Theta = (\Theta_x, \Theta_y, \Theta_z)$ as a	
	function of the lateral displacement $\mathbf{r}=(\Delta X,\Delta Y,\Delta Z)$ with $\Delta Z=0.$	23
3.1	Chemical structure of PTCDA presented in a ball model. The molecule consists	
	of a perylene core which is terminated by two anhydride groups	26

3.2	(a) LEED pattern ($E_{\rm kin}=27.2{\rm eV}$) and (b) STM image ($U_{\rm Bias}=-0.34{\rm V}$, $I=0.2{\rm nA}$) of the PTCDA monolayer structure on Ag(111). The inset of panel (b) shows the lateral adsorption geometry of the PTCDA molecules in the unit cell. (c) Vertical adsorption geometry of PTCDA/Ag(111) [HTS ⁺ 10]. The molecule is shown in a front view along the molecular axes. (d) Schematic model of the interaction channels between PTCDA and the Ag(111) surface.	27
3.3	Shape of the PTCDA HOMO (a) and LUMO (b) calculated for a free molecule in the gas phase (DFT calculation, B3LYP, basis set: LANL2DZ [FTS ⁺]). Similar colors in the orbital surface refer to a similar sign of the orbital wave function. The corresponding momentum maps calculated for the PTCDA HOMO and LUMO are shown in panels (c) and (d) respectively	30
3.4	Constant binding energy (CBE) maps for the HOMO and LUMO of PTCDA molecules. In all panels the p3m1 symmetry of the substrate surface is considered, which causes a superposition of six different molecular orientations. In (a) and (b) this is performed for molecule A (aligned along $[\bar{1}01]$), in (c) and (d) for molecule B (77° with respect to $[\bar{1}01]$) (see also Ref. [SWR ⁺ 12])	31
3.5	Calculated (a,b) and measured (c,d) CBE maps of the LUMO and HOMO level, respectively, for the monolayer structure of PTCDA/Ag(111) (see also Ref. [SWR $^+$ 12]). Calculated maps consider surface symmetry and different molecular orientations (compare with Fig. 3.4). Experimental maps were recorded for $E_{\rm b}=0.3{\rm eV}$ (c) and $E_{\rm b}=1.6{\rm eV}$ (d). In panels (e) and (f) the experimental maps of the clean Ag(111) surface recorded at the same binding energies are included as a reference	33
3.6	Orbital projected density of states (PDOS) curves of the HOMO and LUMO level for both molecules in the PTCDA monolayer structure obtained by the orbital tomography analysis of the ARPES data (see also Ref. [SWR $^+$ 12]). While the dotted curves for the LUMOs show the fitting parameters a_i , the solid curves are divided by the Fermi distribution function for an effective temperature of 930 K. The gray-shadowed curve represents the ARPES data integrated over the ring in k -space which was used for fitting. Peak positions in the PDOS curves are indicated by vertical markers. Short thick and long thin lines mark the peak positions obtained from ARPES (this work) and STS (Ref. [KTH $^+$ 06]), respectively. In addition, the substrate parameter $b(E_b)$ and the offset $c(E_b)$ are also included	35
3.7	Chemical structure of CuPc shown in a top (left) and side view (right) of the	40

3.8	(a) LT-STM image of a disordered CuPc sub monolayer film ($U_{\rm Bias}=0.34{\rm V}$, $I=0.02{\rm nA},T_{\rm sample}=5{\rm K}$). (b) LEED pattern of the CuPc monolayer film on Ag(111) ($E_{\rm kin}=27.2{\rm eV}$). (c) Position of the unit cell corners for all p.o.l. superstructures in the coverage regime between $\Theta_{\rm CuPc}=0.89{\rm ML}$ and $\Theta_{\rm CuPc}=1.00{\rm ML}$ [Krö11]. (d) Vertical adsorption position of CuPc in the monolayer structure at RT. (e) Adsorption heights of all CuPc components as a function of CuPc coverage [Krö11] for LT films. (f) Schematic model of the interaction channels between CuPc and the Ag(111) surface. Panels (c) and (e) are taken from [Krö11]	42
3.9	Shape of the CuPc HOMO (a) and LUMO (b) level calculated for a free molecule in the gas phase (DFT calculation, B3LYP, basis set: LANL2DZ [FTS ⁺]). Similar colors in the orbital surfaces reefer to similar signs of the orbital wave function. The corresponding momentum maps calculated for the CuPc HOMO and LUMO level are shown in panels (c) and (d) respectively.	44
3.10	Calculated (a,b) and measured (c,d) CBE maps of the HOMO and LUMO level, respectively, for the monolayer structure of CuPc/Ag(111). Calculated maps account for the surface symmetry and the molecular orientations of CuPc reported by STM [MEP+07]. For the LUMO CBE maps, only one of the degenerated LUMO states is considered. Experimental maps were recorded for $E_{\rm b}=1.3{\rm eV}$ (c) and $E_{\rm b}=0.2{\rm eV}$ (d)	45
3.11	Work function Φ of the CuPc/Ag(111) metal-organic interface for different CuPc coverages. In the inset the same data are plotted versus the inverse coverage. The red line represents a linear least square fit to the experimental data	47
4.1	Schematic overview of the three different phases existing for different coverages of CuPc and PTCDA on Ag(111). The LEED patterns show the typical diffraction signature of the corresponding phase $(E_{\rm kin}=27.2{\rm eV})$	51
4.2	(a)-(e): Pair potential maps for different rotational orientations Θ_z between a CuPc and a PTCDA molecule. Red areas indicate regions of intermolecular repulsion and green/blue areas indicate attraction. Panel (f) shows radial line profiles along a line connecting the two molecules for different Θ_z cutting through the prominent potential minima	52
4.3	STM images of very low coverages of CuPc and PTCDA $\Theta < 0.2\mathrm{ML}$ ($U_\mathrm{Bias} = -0.34\mathrm{V},I = 0.1\mathrm{nA}$). The lattice of the PTCDA monolayer structure is indicated in red and the orientation of silver rows of the surface in white dashed lines. For this coverage no mixing of molecules could be achieved	54

4.4	SPA-LEED images recorded in-situ during the formation of the mixed organic films ($E_{\rm kin}=27.2{\rm eV},t_{\rm scan}=52{\rm s},T_{\rm sample}=300{\rm K}$). The left column shows the diffraction data of the initial CuPc layer with increasing coverage from top to bottom. The middle column shows the LEED image after half of the PTCDA coverage is deposited and the right one the final mixed structure. The total coverage of the right column is $\approx 1.0{\rm ML}.$	55
4.5	Evolution of the LEED pattern demonstrating the mixing process for CuPc deposited on a PTCDA precovered surface ($E_{\rm kin}=27.2{\rm eV}$). These films were annealed at the given sample temperature $T_{\rm sample}$ for 20 min	56
4.6	(a) Low energy electron diffraction pattern of Mixed Brick Wall structure recorded at $E_{\rm kin}=27.2{\rm eV}$. The blue circles in the lower part of the diffraction image model the brick wall structure. The spots not described by blue circles belong to the pure PTCDA monolayer structure. (b) Detailed STM image of the Mixed Brick Wall structure (80 Å × 80 Å, $U_{\rm Bias}=0.2{\rm V},I=0.01{\rm nA}$). The molecules within the unit cell (marked by red arrows) are drawn as ball models whereas the molecular orientation is indicated by white dotted lines	58
4.7	(a) Model of the MBW unit cell. The black grid represents the lattice of the Ag(111) surface calculated from the position of the superstructure unit cell vectors. (b) Pair potential optimized structural model for the MBW structure (more details about the calculation can be found in the text). The hydrogen atoms are displayed as dark green circles and the oxygens as red circles. The black ellipses mark the existing $O \cdots H$ interactions. (c) STM image of a similar mixture of one CuPc and two PTCDA molecules on Cu(111) ([BWBM03]). The unit cell is again marked with red arrows and the molecules are represented in a ball and stick model	59
4.8	Diffraction pattern of the occurring structures in the <i>Mixed One-to-One</i> phase. The point-on-line structure on the left side (a) can be transformed to the commensurate structure (b) by sample annealing. For both structures the relative position of the unit cell vectors are drawn on the hexagonal grid of the $Ag(111)$ surface (c). (d)+(e): Pair potential maps for both $M1^21$ structures. The optimized molecular orientations are indicates by ball models	61
4.9	STM data for the commensurate M1 ² 1 structure ($U_{\rm Bias} = 0.15 {\rm V}, I = 0.01 {\rm nA}$). (a) Island of the M1 ² 1 structure surrounded by disordered CuPc molecules. The edge of the mixed island is decorated with CuPc molecules. (b) High resolution STM image of the unit cell. The molecules are drawn as ball models, the dotted white lines mark the orientation of the molecules.	62

4.10	(a)+(b): Incommensurate MZZ structures with the smallest (a) and largest (b) unit cell size. (c) Commensurate MZZ structure. (d) Plot of all MZZ structures on the Ag(111) surface lattice. (e) Structural model for the molecular arrangement of the commensurate MZZ structure. The positions and rotational angels are optimized applying a pair potential calculation	63
4.11	Angle integrated UPS spectra of different mixed layer structures ($\hbar\omega=21.218\mathrm{eV}$, $\theta_{\mathrm{Emission}}=45^{\circ}$). (a): Spectra of the MBW structure with applied fitting model. (b): UPS spectra of different mixed structures. In addition, the spectra of the pure CuPc and PTCDA monolayer is shown	66
4.12	(a): Constant binding energy maps of the HOMO region recorded at different binding energies showing the HOMO level of PTCDA and CuPc embedded in different phases. (b): Projected DOS obtained by fitting $I_{\rm HOMO}(k_x,k_y,E_{\rm b})$ with the theoretical maps given in panel (c). (c): Theoretical angular momentum maps for all HOMO state involved in the fitting procedure	68
4.13	(a): Constant binding energy maps (CBE) of the Fermi edge region recorded for different binding energies. The LEED pattern identifies a coexistence of the MBW structure with islands of the PTCDA monolayer structure. (b) Theoretical CBE maps depicting the angular distribution of the LUMO orbital for CuPc and PTCDA included in both structures present on the surface	70
4.14	(a): Projected DOS for the LUMO energy region $(I_{\rm LUMO}(k_x,k_y,E_{\rm b}))$. The color code described in (a) holds for all other panels in this figure. (b)+(c): Radial line profiles cutting through the experimental CBE map at an angle of 60° with respect to [$\bar{1}10$]-direction. For comparison the same line profiles for the theoretical maps and the substrate (dotted line) are shown. The cutting direction for the theoretical maps is indicated in the inset of (a). (d): Circular line profile for $E_{\rm b}=0.44{\rm eV}~(r_{k,{\rm cirlce}}=1.75{\rm Å}^{-1})$. The insets indicates the cutting direction through the data. The dotted black lines represent the contribution of the substrate. The red curve shows the fit of the substrate and the molecular contribution to the experimental data	72
4.15	ARPES data for the M1 ² 1 structure. (a): Constant binding energy map (CBE) of the Fermi edge region recorded at $E_{\rm b}=0.47{\rm eV}$. (b): Projected DOS obtained by fitting the data cube $I_{\rm LUMO}(k_x,k_y,E_{\rm b})$ with the three theoretical maps shown in Fig. 4.13(b). (c): Radial line profile cutting through the experimental CBE map for $E_{\rm b}=0.47{\rm eV}$ at an angle of 60° with respect to $k_{[\bar{1}10]}$. For comparison the same line profiles for the theoretical maps (colored lines) and the clean substrate (dotted line) are shown. The cutting direction for the	
	theoretical maps is indicated in the inset of panel (b)	74

4.16	Work function Φ and binding energy positions of the molecular features for three mixed structures with different ratio of CuPc to PTCDA. In the panel depicting the work function changes, the green circles mark the work function of the mixed film and the blue circles the one for the pure CuPc film before the mixing process. The error of the experimental data is reflected by the size	
4.17	of the circles	76
	$(I=0.1\mathrm{nA})$, (b): M1 ² 1 structure $(I=0.03\mathrm{nA})$. The colored dots on the STM image in the inset of (a) and (b) mark the positions where the spectra of the same color code was taken	78
4.18	Background subtracted core level spectra of the carbon C1s, nitrogen N1s, oxygen O1s, and copper Cu2p emission arising from the molecules in the MBW structure. The spectra are obtained at an energy 4 eV below the Bragg energy. For C1s and O1s, the chemically different species are separated by the shown model. The Gaussian curve of the energy loss tail at high binding energies is	
4.19	not shown in those models	82
4.20	numbers given for the each species represent the fitting result this particular single XSW scan	85
4.21	diagram shown in (a)	88 89
5.1	High resolution LEED images ($E_{\rm kin}=27.2{\rm eV}$) for different CuPc coverages adsorbed on a closed layer PTCDA/ Ag(111) [SSK+12]. Images (a-c) are recorded at RT, image (d) at 100 K. Red and blue circles mark calculated positions of diffraction spots from the PTCDA monolayer structure and the CuPc/PTCDA Stacked-Bilayer structure, respectively. The figure is taken from [SSK+12]	99

5.2	(a-c): STM images of the SB phase at T=10 K (0.75 V, 18 pA) [SSK+12]. (a) A CuPc island (bright contrast) has condensed on a closed PTCDA monolayer on Ag(111). PTCDA and CuPc lattices are indicated by red and blue lines, respectively. (b) Close-up of the CuPc island. Six CuPc molecules (one unit cell) are shown as ball-and-stick models. (c) Dotted ellipses indicate the positions of PTCDA molecules under the CuPc layer. Bright STM contrast is found where CuPc wings lie above the PTCDA core. (d) Model of the PTCDA ML-structure. Adsorption sites of CuPc molecules are marked by red circles, the size of which indicate statistical errors. This figure is taken from [SSK+12].	. 102
5.3	(a)+(c): High resolution LEED images ($E_{\rm kin}=27.2{\rm eV}$) for the 1.4 ML and 1.0 ML CuPc on PTCDA. The insets enlarge k-space regions which reveal a slightly changed diffraction signature upon increasing the coverage. (b)+(d): CuPc thermal desorption signal of the corresponding layer. The green curve represents an exponential fit to the data in the relative temperature range of $T=455{\rm K}$ to $465{\rm K}$ and $T=570{\rm K}$ to $585{\rm K}$	104
5.4	(a):UPS data of CuPc/PTCDA/Ag(111) for different CuPc-coverages at RT (black circles, $\hbar\omega=21.218\mathrm{eV}$). Red curves represent least square fits to the data. For the lower- and uppermost curves the fitting model consisting of up to four independent peaks is shown, PTCDA and CuPc states are displayed in green and blue, respectively. For fitting the background we used a Fermi function which was broadened in order to account for the instrumental resolution, plus an exponential component (black curve). (b) Intensity of the PTCDA HOMO level as function of CuPc coverage. The red curve illustrates the exponential fitting curve. Panel (a) of this figure is taken from [SSK+12].	107
5.5	(a) Constant binding energy maps for three different binding energies of \approx 0.7 ML CuPc on PTCDA. The ARPES data were obtained using synchrotron radiation of $\hbar\omega=35\mathrm{eV}$ and recorded with a toroidal analyzer. (b) Projected density of states (PDOS) and substrate contribution $b(E_\mathrm{b})$ obtained by the orbital tomography analysis of the ARPES data. The theoretical momentum maps used for the fitting procedure are depicted below the corresponding curves in (b)	109
5.6	Work function Φ and binding energy positions of all molecular features identified for the hetero-organic interface CuPc/PTCDA on Ag(111) as a function of the CuPc coverage. All data have been obtained at RT using a photoemission setup with an energy resolution better than $30\mathrm{meV}$	111

5.7	UPS spectra of 0.6 ML CuPc on PTCDA at room (a) and at liquid nitrogen (b) temperatures, recorded with an emission angle of 45°. The Gaussian curves modeling the PTCDA peaks are displayed below the spectral data (for the color coding see text). The lateral order of the films is indicated by the corresponding SPA-LEED images	113
5.8	Background subtracted core level spectra of nitrogen N1s (a), copper Cu2p	
	(b) and oxygen O1s (c) emission arising from the CuPc/PTCDA bilayer with	
	a CuPc coverage of $\Theta_{\text{CuPc}} = 0.95 \text{ML}$ at RT. The insets of panel (a) and (b)	
	depict the line shape for a lower CuPc coverage of $\Theta_{\text{CuPc}} = 0.60 \text{ML}$. The red	
	line is the best fit using a fitting model consisting of one Gaussian profile for	
	the main peak (green area or in case of (c) green and blue solid lines) and at	
	least one more peak for satellites (dotted lines). For the oxygen emission the	
	model for the energy loss tail at higher binding energies is not displayed	116
5.9	Background subtracted C1s core level spectra for different coverages of CuPc on	
	PTCDA/Ag(111). The Voigt profiles in the photoemission spectra represent	
	the fitting models used to separate the chemical components of CuPc (blue	
	lines) and PTCDA (green peaks). Details of the fitting model are summarized	
	in table 5.2. For clarity, the profile of the energy loss tail at higher binding	
	energies is not displayed for all spectra	118
5.10	Partial yield curves of single XSW scans for all chemically different species in	
	the hetero-organic CuPc/PTCDA bilayer film for two different CuPc coverages	
	(left: $\Theta_{\text{CuPc}} = 0.60 \text{ML}$, right: $\Theta_{\text{CuPc}} = 0.95 \text{ML}$). The lowermost curves repre-	
	sent typical reflectivity profiles of the sample. Solid lines represent the curves	
	fitted to the data using <i>Torricelli</i> [Mer12]. Fitting results (coherent position	
	P^H and fraction F^H) are given for each single XSW scan. The error bars of	
	the yield curves are calculated by a Monte Carlo error analysis included in	120
5 11	CasaXPS [Fai11]	120
5.11	scan. ((a) $\Theta_{\text{CuPc}} = 0.60 \text{ML}$ and (b) $\Theta_{\text{CuPc}} = 0.95 \text{ML}$). The arrows indicate	
	the averaged results for the coherent position P^H and fraction F^H . The re-	
	sulting adsorption heights of all atomic species of the CuPc/PTCDA bilayer	
	are displayed in panel (c) including the reference data of the pure PTCDA	
	monolayer film [HTS ⁺ 10]	122
5.12	Model of the vertical adsorption geometry of the CuPc/PTCDA bilayer film	
	for $\Theta_{\rm CuPc}=0.60\rm ML$ and $\Theta_{\rm CuPc}=0.95\rm ML$ at room temperature. PTCDA is	
	depicted in its typical front view while for CuPc the heights are shown only	
	schematically. Colored circles mark the adsorption heights of the molecules in	
	the mixed film, gray circles the vertical positions of the pure PTCDA monolayer	
	$\operatorname{film}\ [HTS^+10]. \ldots \ldots \ldots \ldots \ldots \ldots \ldots \ldots \ldots $	124

5.13	(a): Partial yield curves of single XSW scans for all species in the SB film at LT $(0.60\mathrm{ML}\ \mathrm{CuPc},50\mathrm{K})$. Solid lines represent the curves fitted to the data with $Torricelli$ [Mer12]. Fitting results are given for each single XSW scan. The error bars of the yield curves are calculated by a Monte Carlo error analysis. (b): Argand diagram of the XSW fitting results for each single XSW scan. The arrows indicate the averaged results for the coherent position P^H and fraction F^H . The color code is identical in (a) and (b)	127
5.14	Vertical adsorption model illustrating the temperature induced phase transition from RT (a) to LT (b). The PTCDA molecules are shown as red and orange rectangles respectively and CuPc as blue ellipses. (c): Argand diagram of the total and partial carbon yield results for 0.60 ML CuPc/PTCDA at RT. The black arrows represent the vector sum which is used to estimate the damping factor for PTCDA below CuPc. (d): Argand diagram for the LT phase, illustrating the splitting of the PTCDA carbon yield into the vectors of the pure PTCDA monolayer and the PTCDA molecules in the SB structure	129
5.15	Model of the vertical adsorption geometry of $\Theta_{CuPc} = 0.60\mathrm{ML}$ CuPc at different temperatures. PTCDA is depicted in its typical front view, CuPc in a schematic view of the molecule. Colored circles mark the adsorption heights of the molecules in the mixed film, gray circles in a film with 0.95 ML CuPc on PTCDA at RT (see section 5.3.2)	131
5.16	Schematic model for the screening mechanism in organic films. (a) The effective charge in the PTCDA LUMO level creates and image charge in the metal in order to reduce the on-site U and the intermolecular repulsion V . (b)+(c) CuPc molecules on PTCDA are polarized and contribute to the screening of the charged PTCDA molecule. The polarizability of the CuPc layer depends on the molecular density and hence the CuPc coverage	134
5.17	(a) Low energy electron diffraction pattern of $\Theta_{\text{CuPc}}=0.50\text{ML}$ CuPc on PTCDA recorded at RT. (b) Desorption signal of CuPc (blue line) and PTCDA (red line) monitored during the desorption process of CuPc from the heterogranic bilayer. (c) Diffraction pattern after annealing at 600 K. The diffraction spots can be attributed to the laterally mixed MBW structure which has been presented in section 4.1.3. All diffraction data was recorded at $E_{\rm kin}=27.2{\rm eV}$.	137
6.1	SPA-LEED images recorded in real time during the deposition of 0.70 ML of PTCDA on the monolayer structure CuPc/Ag(111) ($E_{\rm kin}=27.2{\rm eV},t_{\rm scan}=52{\rm s},T_{\rm sample}=300{\rm K}).$	144

6.2	(a) LEED pattern of 0.70 ML PTCDA on CuPc/Ag(111) recorded at RT ($E_{\rm kin}=27.2{\rm eV}$). In the lower left part of the diffraction image, calculated diffraction spots are shown as blue circles. The corresponding superstructure matrix is also given in panel (a). (b) Radial intensity profiles recorded along the scan directions indicated in the inset of panel (b). (c) Three selected orientations of the PTCDA/CuPc unit cell vectors on the Ag(111) surface grid. The light gray and black unit cell vectors illustrate the maximum and minimum rotation of the unit cell with respect to the substrate. The superstructure matrix in panel (a) corresponds to the unit cell shown in dark gray	146
6.3	UPS data (a) of PTCDA/CuPc/Ag(111) for different PTCDA-coverages at RT (black circles, $\hbar\omega=21.218\mathrm{eV}$, photoelectron acceptance angle 30°). Red curves represent least square fits to the data. For the lower- and uppermost curves the fitting models consisting of up to three independent peaks are shown. The corresponding work functions are shown in panel (b). (c) Intensity of the CuPc and PTCDA HOMO level normalized to the corresponding signal at $\Theta_{\mathrm{PTCDA}}=0.4\mathrm{ML}$ as a function of PTCDA coverage. The red curve describes the exponential attenuation of a constant first layer UPS signal, the orange curve the one of a linearly increasing signal	148
6.4	Background subtracted core level spectra of the carbon C1s, and oxygen O1s emission arising from the molecules in the PTCDA/CuPc structure on Ag(111). The spectra are obtained at an energy 4 eV below the Bragg energy. All components of the models used for fitting the data are shown as colored lines, except the Gaussian of the energy loss tail at high binding energies	151
6.5	Yield curves of a single XSW scan for all chemically different species found for the PTCDA/CuPc bilayer film on Ag(111). The yield curves were obtained by fitting the core level data according to the models discussed in chapter 6.3.1. The solid lines represent fits to the yield curves performed with <i>Torricelli</i> [Mer12]. The numbers given for each species represent the fitting result of this particular single XSW scan	153
6.6	(a) Argand diagram showing the XSW results for all single XSW scans for the adsorption of $0.50\mathrm{ML}$ PTCDA on one monolayer $\mathrm{CuPc/Ag}(111)$ at $50\mathrm{K}$. The arrows indicate the averaged results for the coherent position P^H and fraction F^H . (b) Fourier-component analysis for the XSW results of CuPc . The vector sum is exemplary shown for the nitrogen species. It is assumed that the first layer CuPc molecules of the PTCDA/CuPc structure exhibit the same adsorption height as in the MBW structure (see section 4.3.2). The position of the 2nd layer CuPc molecules can then be calculated, see text. The	15.4
	color code for the different CuPc species is identical in both panels	154

6.7	Model of the vertical adsorption geometry of CuPc and PTCDA in the PTC-	
	DA/CuPc film on Ag(111). PTCDA is shown in the typical front view and	
	CuPc in a schematic side view. The colored circles mark the experimentally	
	obtained adsorption heights of the molecules in the mixed interface. The gray	
	circles indicate the vertical positions of the PTCDA and CuPc molecules in	
	the laterally mixed MBW structure (see section 4.3.2)	156

List of publications

- I. Kröger, **B. Stadtmüller**, C. Stadler, J. Ziroff, M. Kochler, A. Stahl, F. Pollinger, T.-L. Lee, J. Zegenhagen, F. Reinert and C. Kumpf Submonolayer growth of copper-phthalocyanine on Ag(111) New J. Phys. **12**, 083038, (2010)
- **B. Stadtmüller**, I. Kröger, F. Reinert and C. Kumpf Submonolayer growth of CuPc on noble metal surfaces Phys. Rev. B **83**, 085416, (2011)
- I. Kröger, **B. Stadtmüller**, C. Kleimann, P. Rajput and C. Kumpf Normal-incidence x-ray standing-wave study of copper phthalocyanine submonolayers on Cu(111) and Au(111)

 Phys. Rev. B **83**, 195414, (2011)
- I. Kröger, **B. Stadtmüller**, C. Wagner, C. Weiss, R. Temirov, F.S. Tautz and C. Kumpf *Modeling intermolecular interactions of physisorbed organic molecules using pair potential calculations*
- J. Chem. Phys. 135, 234703, (2011)
- **B. Stadtmüller**, T. Sueyoshi, G. Kichin, I. Kröger, S. Soubatch, R. Temirov, F.S. Tautz and C. Kumpf

 Commensurate Registry and Chemisorption at a Hetero-organic Interface

Phys. Rev. Lett. **108**, 106103, (2012)

B. Stadtmüller, M. Willenbockel, E.M. Reinisch, T. Ules, F.C. Boquect, S. Soubatch, P. Puschnig, G. Koller, M.G. Ramsey, F.S. Tautz and C. Kumpf Orbital tomography for highly symmetric adsorbate systems
EPL (Europhys. Lett.), 100, 26008, (2012)

I. Kröger, P. Bayersdorfer, **B. Stadtmüller**, C. Kleimann, G. Mercurio, F. Reinert and C. Kumpf

Submonolayer growth of H_2 -Phthalocyanine on Ag(111) Phys. Rev. B, **86**, 195412, (2012)

M. Willenbockel, **B. Stadtmüller**, K. Schönauer, E.M. Reinisch, T. Ules, M. Ostler, F.C. Boquect, C. Kumpf, P. Puschnig, G. Koller, S. Soubatch, M.G. Ramsey, F.S. Tautz *Energy offsets within a molecular monolayer: The influence of the molecular environment* New J. Phys. **15**, 033017, (2013)

B. Stadtmüller, D. Lüftner, M. Willenbockel, E.M. Reinisch, T. Sueyoshi, G. Koller, S. Soubatch, M.G. Ramsey, P. Puschnig, F.S. Tautz and C. Kumpf *More than the sum of its parts: Electronic coupling at heteromolecular hybrid interfaces* to be published

Curriculum Vitae

Benjamin Stadtmüller

born on August 4th, 1985 in Aschaffenburg, Germany.

Nationality: German.

Education

2005: Abitur at Friedrich Dessauer Gymnasium, Aschaffenburg, Germany.

2005-2008: Bachelor of Science study in Physics at Julius-Maximilians University Würzburg.

2008: Bachelor of Science degree.

 $The sis \ title: \ Untersuchung \ der \ Strukturbildung \ von \ TiOPc \ bei \ der \ Adsorption \ auf \ der \ Ag (111)$

 $Ober fl\"{a}che.$

Advisor: PD. C. Kumpf.

2007-2009: Master of Science studies in Fokus Physics at Julius-Maximilians University Würzburg.

2009: Master of Science with Honors degree.

 $The sis\ title:\ Strukturuntersuchungen\ von\ CuPc\ auf\ verschiedenen\ Edelmet all oberflächen.$

Advisor: PD. C. Kumpf.

2009-2012: PhD student at Peter Grünberg Institut (PGI-3), Forschungszentrum Jülich.

 $The sis\ title:\ Study\ of\ intermolecular\ interactions\ in\ hetero-organic\ thin\ films.$

Advisor: Prof. C. Kumpf.

 $\mathbf{since}\ \mathbf{11/2012} \mathbf{:}\ \mathbf{Postdoc}\ \mathbf{at}\ \mathbf{Peter}\ \mathbf{Gr\"{u}nberg}\ \mathbf{Institut}\ (\mathbf{PGI-3}), \mathbf{Forschungszentrum}\ \mathbf{J\"{u}lich}.$

Acknowledgements

This work would not have been possible without the assistance and contribution of many people. At this point, I would like to take the opportunity to thank

- first of all my PhD mentor Prof. Christian Kumpf for giving me the opportunity to work in his group. I am grateful for his support during the last years, for many stimulating discussions and the freedom to select my research interests.
- Prof. Matthias Wuttig for his interest in our work and for accepting to co-referee my PhD
 thesis. I also would like to thank Prof. Uwe Klemradt and Prof. Carsten Honerkamp
 who also agreed to be on the PhD board.
- Dr. Ingo Kröger for introducing me into the experimental work in surface science as well as for many helpful advices and discussions. It would also like to thank him for establishing the "4pm coffee break" in our institute.
- Dr. Sergey Subach for his scientific and experimental support in many projects. I am
 especially grateful for his huge contribution to our STM-experiments as well as to our
 orbital tomography project.
- Dr. Tomoki Sueyoshi for his contribution to our UPS study and the subsequent discussions
- Martin Willenbockel for spending many nights together with me at synchrotrons, for countless scientific and non-scientific discussions as well as for his good advices in any situation.
- Christoph Schmitz for his contribution to our SPA-LEED study in the framework of his Bachelor thesis.
- Dr. Ruslan Temirov and Georgy Kichin for their collaboration in carrying out STM experiments.
- Christoph Kleimann, Sonja Schröder, Kathrin Schönauer and Dr. Francois Bocquet for their assistance during many beamtimes at the ESRF and at BESSY II.
- Caroline Henneke and Dr. Thomas Duden for their support during my last attempts to work with our LEEM/PEEM microscope.

- Prof. F. Stefan Tautz, head of Peter Grünberg Institut-3, for the chance to work on my PhD thesis in his institute and for his support for my research projects during that time.
- all my colleagues from Peter Grünberg Institut-3 for creating a warm and friendly atmosphere at work.
- Dr. Jörg Zegenhagen, Dr. Blanka Detlefs and Dr. Julien Duvernay for their great support as local contacts during our beamtimes at the endstation ID 32 at the ESRF, France.
- our experimental collaborators from the University of Graz, namely Prof. Michael G. Ramsey, Prof. Georg Koller, Eva M. Reinisch, Thomas Ules and Hannes Offenbacher, for many joined beamtimes at BESSY II, Berlin, and for their support in analyzing and discussing our ARPES data.
- Prof. Peter Puschnig and Daniel Lüftner from the University of Graz, for supporting our ARPES studies with theoretical calculations as well as for stimulating discussions, especially concerning the orbital tomography analysis.
- Dr. Achim Schöll and Christoph Sauer from the University of Würzburg for stimulating discussions about the properties of hetero-organic thin films.
- Dr. Giuseppe Mercurio for his XSW analysis software *Torricelli* and Patrick Bayersdorfer for the SPA-LEED analysis software *Spotplotter*.
- finally my parents, Walter and Helma, my sister Natascha, all my friends, especially, Stephan, Sebastian, Valentin, and my girlfriend Annemarie, for their support as well as for the fun and joy they brought to my life.

Band / Volume 48

High Temperature Radio-Frequency Superconducting Quantum Interference Device System for Detection of Magnetic Nanoparticles

A. Pretzell (2012), 122 pp ISBN: 978-3-89336-814-3

Band / Volume 49

Study of Molecule-Metal Interfaces by Means of the Normal Incidence X-ray Standing Wave Technique

G. Mercurio (2012), XXII, 361 pp

ISBN: 978-3-89336-816-7

Band / Volume 50

5th Georgian-German School and Workshop in Basic Science

Tbilisi, Georgia/August 6 – 10, 2012. Batumi, Georgia/August 13 – 17, 2012.

Org. Committee: E. Abrosimova, A. Bakuridze, A. Kacharava, A. Kvitashvili, A.

Prangishvili, H. Ströher (2012): CD-ROM

ISBN: 978-3-89336-818-1

Band / Volume 51

Exploring the electronic properties of novel spintronic materials by photoelectron spectroscopy

A. Herdt (2012), ii, 126 pp ISBN: 978-3-89336-831-0

Band / Volume 52

Quantum Information Processing

Lecture Notes of the 44th IFF Spring School 2013 February 25 – March 8, 2013 Jülich, Germany D. DiVincenzo (Ed.) ca. 1000 pp

ISBN: 978-3-89336-833-4

Band / Volume 53

Real-Space Finite-Difference PAW Method for Large-Scale Applications on Massively Parallel Computers

P.F. Baumeister (2012), vi, 212 pp

ISBN: 978-3-89336-836-5

Band / Volume 54

Einfluss unkonventioneller Medien auf die Selektivität ThDP-abhängiger Enzyme

T. Gerhards (2013), XIV, 199 pp ISBN: 978-3-89336-846-4 Band / Volume 55

Aufbau einer Vierspitzen-Rastertunnelmikroskop/Rasterelektronenmikroskop-Kombination und Leitfähigkeitsmessungen an Silizid Nanodrähten

E. Zubkov (2013), 150 pp ISBN: 978-3-89336-848-8

Band / Volume 56

Interplay between magnetic and dielectric phenomena at transition metal oxide interfaces

D. Schumacher (2013), IV, 128 pp

ISBN: 978-3-89336-855-6

Band / Volume 57

Single NdPc₂ Molecules on Surfaces: Adsorption, Interaction, and Molecular Magnetism

S. Fahrendorf (2013), viii, 100 pp

ISBN: 978-3-89336-856-3

Band / Volume 58

Heyd-Scuseria-Ernzerhof Screened-Exchange Hybrid Functional for Complex Materials: All-Electron Implementation and Application

M. Schlipf (2013), XV, 170 pp ISBN: 978-3-89336-857-0

Band / Volume 59

Orbital-dependent exchange-correlation functionals in density-functional theory realized by the FLAPW method

M. Betzinger (2013), vi, 173 pp ISBN: 978-3-89336-858-7

Band / Volume 60

Structural influences on electrical transport in nanostructures

R. D. Frielinghaus (2013), viii, 190 pp

ISBN: 978-3-89336-867-9

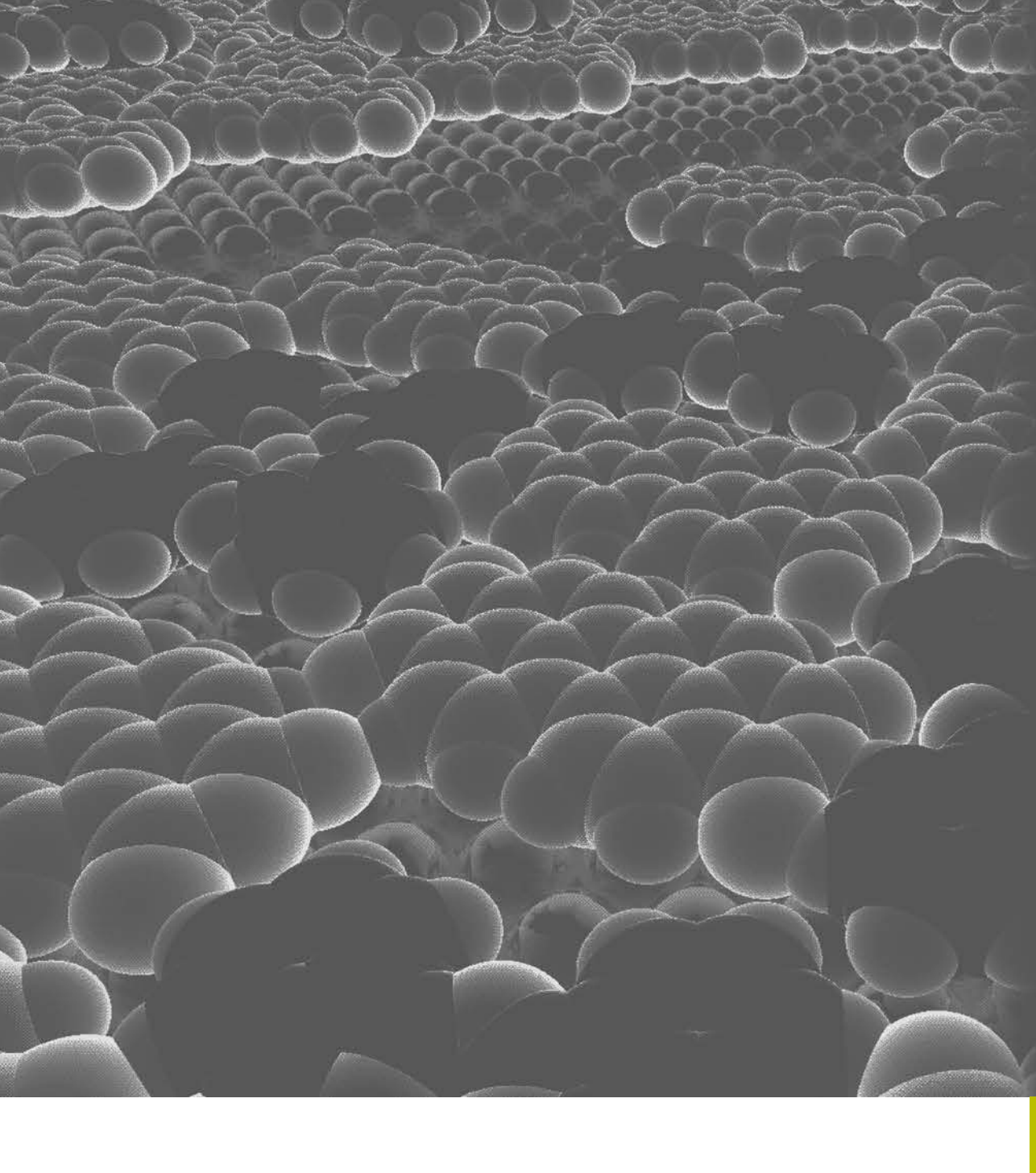
Band / Volume 61

Study of intermolecular interactions in hetero-organic thin films

B. Stadtmüller (2013), viii, 198 pp

ISBN: 978-3-89336-871-6

Weitere **Schriften des Verlags im Forschungszentrum Jülich** unter http://www.zb1.fz-juelich.de/verlagextern1/index.asp



Schlüsseltechnologien / Key Technologies Band / Volume 61 ISBN 978-3-89336-871-6

